



Modélisation de l'effet de nouvelles molécules anti-VHB chez la souris et chez l'homme

Antonio Gonçalves

► To cite this version:

Antonio Gonçalves. Modélisation de l'effet de nouvelles molécules anti-VHB chez la souris et chez l'homme. Médecine humaine et pathologie. Université Paris Cité, 2021. Français. NNT : 2021UNIP5228 . tel-04548582

HAL Id: tel-04548582

<https://theses.hal.science/tel-04548582>

Submitted on 16 Apr 2024

HAL is a multi-disciplinary open access archive for the deposit and dissemination of scientific research documents, whether they are published or not. The documents may come from teaching and research institutions in France or abroad, or from public or private research centers.

L'archive ouverte pluridisciplinaire **HAL**, est destinée au dépôt et à la diffusion de documents scientifiques de niveau recherche, publiés ou non, émanant des établissements d'enseignement et de recherche français ou étrangers, des laboratoires publics ou privés.

Université de Paris

Ecole doctorale 393 Pierre Louis de santé publique
Epidémiologie et sciences de l'information biomédicale

Laboratoire IAME – Infection, Antimicrobiens, Modélisation, Evolution
Equipe BIPID – Modélisation biostatistique, pharmacométrie et investigation clinique en maladies infectieuses

Modélisation de l'effet de nouvelles molécules anti-VHB chez la souris et chez l'homme

Antonio GONÇALVES

Thèse de doctorat de Biostatistiques et Biomathématiques

Dirigée par le Dr. Jérémie Guedj

Présentée et soutenue publiquement le 10 février 2021

Devant un jury composé de :

Madame Elisabeta VERGU	Rapporteur
Monsieur Slim FOURATI	Rapporteur
Madame Mélanie PRAGUE	Examinateur
Monsieur Fabien CRAUSTE	Examinateur
Monsieur Tarik ASSELAH	Examinateur
Monsieur Fabien ZOULIM	Examinateur
Monsieur Jérémie GUEDJ	Directeur de thèse
Madame Annabelle LEMENUEL-DIOT	Membre invité



Except where otherwise noted, this work is licensed under
<https://creativecommons.org/licenses/by-nd/3.0/fr/>

Remerciements

Cette thèse vient clore trois années de doctorat et onze années d'études universitaires, riches tant professionnellement que personnellement. Celle-ci n'a été rendue possible que par le concours de plusieurs personnes que je tenais à chaleureusement remercier aujourd'hui.

A mes rapporteurs, les Docteurs Elisabeta Vergu et Slim Fourati, pour le temps consacré à la lecture de ce manuscrit. Vos remarques et suggestions ont été des plus constructives et ont contribué à l'amélioration de ce manuscrit. Je remercie également les Docteurs Mélanie Prague, Annabelle Lemenuel-Diot et Fabien Crauste ainsi que les Professeurs Fabien Zoulim et Tarik Asselah d'avoir accepté d'évaluer mon travail de thèse sous l'angle de leur expertise respective.

A mon directeur de thèse, le Docteur Jérémie Guedj, pour avoir accepté de m'encadrer en stage de M2 puis en thèse il y a quatre ans. Je tiens à chaleureusement te remercier pour ta disponibilité, ton dynamisme et ton sens critique. Je garderai en mémoire ta grande rigueur scientifique et ton sens du détail qui m'accompagneront tout au long de ma carrière scientifique. Enfin, merci de m'avoir fait confiance en m'impliquant dans de nombreux projets originaux.

Au Docteur Annabelle Lemenuel-Diot, pour la qualité de son encadrement malgré la distance physique. Merci à toi et à Roche d'avoir accepté de financer et d'encadrer cette thèse. Merci pour tes conseils et nos échanges réguliers qui ont grandement contribué à chacun des projets présentés dans cette thèse. Tes qualités tant professionnelles que personnelles m'ont permis de grandir en tant que jeune scientifique.

Au Professeur France Mentré, de m'avoir accueilli au sein de l'équipe BIPID. Merci de m'avoir permis de réaliser une thèse dans des conditions de travail optimales. Je tiens à te remercier pour ton engagement auprès des jeunes chercheurs de l'équipe que tu ne cesses d'encourager et à qui tu communiques un dynamisme des plus encourageant et motivant. Mon passage au sein de ton équipe marquera mon parcours de jeune chercheur.

A membres « séniors » de l'équipe BIPID : Emmanuelle, Houda, Julie, Myriam, Thu-Thuy, Tram, Tiphanie, Cédric, Charles, François C., Jimmy, Lionel, Romain et Vincent. Merci pour nos nombreuses discussions et échanges informelles (déjeuner, pause café et autres) au cours de ces quatre années passées au sein de l'unité.

A Hervé, pour son aide considérable et sa patience pour nous expliquer le fonctionnement d'un « centre de calcul » et d'un « cloud ». Je me souviendrais également longtemps de ton amour pour la cuisine de Cappadoce.

A Houda, pour l'énergie et la bonne humeur dont tu fais preuve au quotidien. Ces qualités ont fait de toi une personne indispensable au bon déroulement de cette thèse.

Aux jeunes post-doctorants, doctorants, stagiaires, actuels et passés, que j'ai pu croiser au sein de l'unité : Alexandra, Claire, Coralie, Drifa, Emilie, Jinju, Marion, Mélanie, Nadège, Pauline,

Aurélien, François, Guillaume, Jérémy, Marc, Mathieu, Simon et Vincent. Une véritable dynamique de groupe s'est instaurée au fil des mois aussi bien au sein du labo qu'en dehors. Je garderai longtemps en mémoire nos sorties au cinéma et à l'Escale, nos discussions, nos fous rires et tous ces moments de légèreté qui ont rendu ses quatre années de labeur bien plus agréables.

Aux mes camarades du club des 5 : Emilie, François, Jérémy et Mathieu. Après une arrivée timide, nous avons su trouver nos marques au sein du labo. Depuis nous nous sommes unis aussi bien dans les moments de joie que dans l'adversité ! J'espère partager encore d'excellents moments à vos côtés à l'avenir !

A Emilie, pour ta positivité, ton aide, tes conseils et tes délicieux gâteaux. Alors même que je me plais à te contredire par plaisir de débattre, tu as en réalité très souvent raison. J'espère cependant réussir à te donner tort un jour ;)

A François et Jérémy. Un même parcours, un même amour de la pharmacométrie (qui nous le rend bien) et un quotidien partagé depuis le master PK. Depuis, pas une journée sans rire et se divertir. Vos rires dans le bureau risquent de me manquer pour un moment ! Prenez soin de vous les champions et courage pour la dernière ligne droite !

A mes camarades pharmaciens, les petits loups et les autres : Estelle, Eugénie, Hélène, Florian, François, Jérémy, Matthieu, Sophie, Claire Marine et Valentin, pour tous ses moments partagés aussi bien sur les bancs d'amphis que dans les bars.

A ma belle-famille : Myriam, Patrick et Matthieu. Merci pour vos encouragements et votre soutien répété au fil des années.

A Nadège, Robin et Noé, merci d'exister tout simplement. Les dimanches en famille avec vous ont été de vraies bouffées d'oxygène !

A mon frère Pedro pour son soutien inestimable. Les mots me manquent pour te dire combien je te remercie toi qui m'a toujours soutenu et accompagné tout au long de ces années. Mille et un merci pour tes encouragements, nos discussions et tes idées toujours nombreuses pour me changer les idées. J'espère qu'on pourra très vite se remettre à nos parties de squash !

Aos meus pais, obrigado por tudo o que têm feito nos últimos 30 anos. Nunca poderei agradecer-vos o suficiente. Espero que estejam orgulhosos dos vossos filhos. Este diploma também é vosso.

A Aurélie, merci de croire en moi plus que de raison.

« L'incertitude, en tant que part fondamentale de votre nature profonde, est absolument nécessaire au progrès scientifique »

Richard Feynman

Table des matières

Chapitre 1. L'hépatite B	1
1.1. Epidémiologie	1
1.2. Virologie.....	2
1.2.1. Le cycle de réPLICATION du VHB	2
1.2.2. Les produits viraux et sous-viraux de l'infection au VHB.....	4
1.3. Histoire naturelle de la maladie.....	5
1.4. Prophylaxie et traitements antiviraux.....	7
1.4.1. Prophylaxie vaccinale	7
1.4.2. « HBV cure » ou la complexe définition de l'objectif thérapeutique	7
1.4.3. Prise en charge thérapeutique.....	8
1.5. Nouvelles approches thérapeutiques	9
1.5.1. Immunomodulateurs.....	10
1.5.2. Inhibiteurs de capsidE.....	11
1.5.3. ARN interférents	12
1.5.4. Défis des nouveaux traitements.....	13
Chapitre 2. Modèles mathématiques et statistiques de la cinétique virale	14
2.1. Modélisation de la cinétique virale du VHB	14
2.1.1. Modèle mathématique standard de l'hépatite B	14
2.1.2. Modélisation de la relation concentration-efficacité des traitements	19
2.1.3. Rôle des modèles dans l'optimisation thérapeutique du VHC	21
2.1.4. Limites des modèles	21
2.1.5. Comment modéliser de nouvelles cibles thérapeutiques ?	22
2.2. Inférence et sélection de modèle	23
2.2.1. Modèles non-linéaire à effets mixtes	23
2.2.2. Sélection de modèles.....	28
2.2.3. Incertitude liée au modèle et <i>model averaging</i>	29
2.3. Objectifs de la thèse	30
Chapitre 3. Modélisation de l'effet des agonistes du TLR7 chez la souris et prédition de son efficacité chez l'homme	32
3.1. Résumé	32
3.2. Article 1: A modeling framework to understand the effect of TLR7 agonists against Hepatitis B virus and predict its efficacy in clinical trial	33
Chapitre 4. Modélisation de l'ARN VHB chez des patients traités par inhibiteurs de capsidE	68

4.1. Résumé	68
4.2. Article 2: What drives the dynamics of HBV RNA during treatment?	69
Chapitre 5. Le <i>model averaging</i> dans les modèles de cinétique virale	97
5.1. Résumé	97
5.2. Article 3: Model averaging in viral dynamic models.....	98
Chapitre 6. Discussion et conclusion	117
6.1. Discussion	117
6.2. Perspectives	120
6.3. Conclusion générale	122
Chapitre 7. Une thèse pendant l'épidémie de COVID-19.....	123
Chapitre 8. Bibliographie	158

Liste des abréviations

AAV : *adeno-associated virus*

ADN : acide désoxyribonucléique

ADV : adéfovir

AgHBC : antigène de capsid du VHB

AgHBe : antigène E du VHB

AgHBs : antigène de surface du VHB

AIC : *Akaike Information Criteria*

ALAT : alanine-amino transférase

ARN : acide ribonucléique

BIC : *Bayesian Information Criteria*

CAM : *capsid assembly inhibitors* – inhibiteurs de capsid

cccDNA : *covalently-closed circular DNA* – ADN circulaire superenroulé

EBE : *empirical Bayes estimates*

ETV : entecavir

FIM : *Fisher information matrix* – matrice d'information de Fisher

FO : *First Order*

FOCE : *First Order Conditional Estimation*

HCQ : hydroxychloroquine

IC : *information criteria* – critère d'information

IFN α : interféron-alpha

IWRES : *individual weighted residuals* – résidus individuels pondérés

LAM : lamivudine

LL : *log-likelihood* – log-vraisemblance

LRT : *likelihood ratio test* – test du rapport de vraisemblance

MA : *model averaging*

MNLEM: modèles non linéaires à effets mixtes

MS : *model selection*

npde : *normalized prediction discrepancy errors*

NTCP : cotransporteur sodium/taurocholate

NUC : analogue nucléot(s)idique

pcVPC : *prediction corrected visual predictive check*

pd : *prediction discrepancies*

PD1 : *programmed death receptor 1*

PDL1 : *programmed death ligand 1*

PegIFN α : interféron alpha pegylé

pgRNA : *pregenomic RNA* – ARN pré génomique

rcDNA : *relaxed-circular DNA* – ADN relâché circulaire

SAEM : *Stochastic Approximation Expectation Maximization*

SARS-CoV-2 : *severe acute respiratory syndrome coronavirus 2* – syndrome respiratoire
aigu sévère du au coronavirus 2

SE : *standard error* – erreur standard

siRNA : *silencing RNA* – ARN interférents

SVP : *subviral particles* – sous particules virales

TAF : ténofovir alafénamide

TBV : telbivudine

TDF : fumarate de ténofovir disoproxil

TLR7 : toll-like récepteur 7

VHB : virus de l'hépatite B

VHC : virus de l'hépatite C

VHD : virus de l'hépatite D

VIH : virus de l'immunodéficience humaine

VPC : *visual predictive check*

Production scientifique liée à la thèse

Articles publiés

GONÇALVES A, MENTRÉ F, LEMENUEL-DIOT A, GUEDJ J. Model Averaging in Viral Dynamic Models. *The American Association of Pharmaceutical Scientists*, 2020;22(2):48

GONÇALVES A, LEMENUEL-DIOT A, COSSON V, JIN Y, FENG S, BO Q, GUEDJ J. What drives the dynamics of HBV RNA during treatment? *Journal of Viral Hepatitis*, 2020;doi: 10.1111/jvh.13425

Article en préparation

GONÇALVES A, LEMENUEL-DIOT A, GAO L, DAI L, ALVAREZ-SÁNCHEZ R, GRIPPO JF, GUEDJ J. A modeling framework to understand the effect of TLR7 agonist against Hepatitis B Virus and to predict its efficacy in clinical trials.

Communications orales

GONÇALVES A, MENTRÉ F, LEMENUEL-DIOT A, GUEDJ J. Model Averaging in Viral Dynamic Models. *28th Population Approach Group in Europe (PAGE) conference*, Stockholm, Suède, Juin 2019.

GONÇALVES A, LEMENUEL-DIOT A, COSSON V, JIN Y, FENG S, BO Q, GUEDJ J. What drives the dynamics of HBV RNA during treatment? *4th workshop on viral dynamics*, Paris, France, Octobre 2019.

Communication affichée

GONÇALVES A, LEMENUEL-DIOT A, GAO L, DAI L, ALVAREZ-SÁNCHEZ R, GRIPPO JF, GUEDJ J. A modeling framework to understand the effect of TLR7 agonist against Hepatitis B Virus and to predict its efficacy in clinical trials. *27th Population Approach Group in Europe (PAGE) conference*, Montreux, Suisse, Juin 2018.

Production scientifique non liée à la thèse

Articles publiés

GONCALVES A, BERTRAND J, KE R, COMETS E, DE Lamballerie X, MALVY D, PIZZORNO A, TERRIER O, ROSA CALATRAVA M, MENTRÉ F, Smith P, PERELSON AS, GUEDJ J. Timing of antiviral treatment is critical to reduce SARS-CoV-2 viral loads. *CPT: Pharmacometrics and System Pharmacology*, 2020;9(9):509-14

MAISONNASSE P, GUEDJ J, CONTRERAS V, BEHILLIL S, SOLAS C, MARLIN R, NANINCK T, PIZZORNO A, LEMAITRE J, **GONCALVES A**, KAHLAOUI N, TERRIER O, FANG RHT, ENOUF V, DEREUDDRE-BOSQUET N, BRISSEBARRE A, TOURET F, CHAPON C, HOEN B, LINA B, CALATRAVA MR, VAN DER WERF S, DE LAMBALLERIE X, LE GRAND R. Hydroxychloroquine use against SARS-CoV-2 infection in non-human primates. *Nature*, 2020;585(7826):584-587

DODDS MG, KRISHNA R, **GONCALVES A**, RAYNER CR. Model-informed drug repurposing: Viral kinetic modelling to prioritize rational drug combinations for COVID-19. *Bristish journal of Clinical Pharmacology*, 2020;doi: 10.1111/bcp.14486

Articles en révision

GONÇALVES A, MAISONNASSE P, Donati F, Albert M, BEHILLIL S, CONTRERAS V, NANINCK T, MARLIN R, SOLAS C, PIZZORNO A, LEMAITRE J, KAHLAOUI N, TERRIER O, FANG RHT, ENOUF V, DEREUDDRE-BOSQUET N, BRISSEBARRE A, TOURET F, CHAPON C, HOEN B, LINA B, CALATRAVA MR, DE LAMBALLERIE X, MENTRÉ F, LE GRAND R, VAN DER WERF S, GUEDJ J. SARS-CoV-2 viral dynamics in non-human primates. *PLoS Computational Biology*

CZUPPON P, DÉBARRE F, **GONÇALVES A**, TENAILLON A, PERELSON AS, GUEDJ J, BLANQUART F. Success of prophylactic antiviral therapy for SARS-CoV-2: predicted critical efficacies and impact of different drug-specific mechanisms of action. *PLoS Computational Biology*

Chapitre 1. L'hépatite B

1.1. Épidémiologie

L'hépatite B est une infection virale du foie causée par le virus de l'hépatite B humain (VHB), un virus de la famille des *Hepadnaviridae*. En 2018, on estime à plus de 292 millions le nombre de patients chroniquement infectés par le VHB (Polaris Observatory Collaborators, 2018). Chaque année, près de 900 000 personnes décèdent des complications de l'infection comme la cirrhose ou le carcinome hépatocellulaire, faisant du VHB la première cause de cancer devant l'alcool et le tabac (Fan et al., 2013). De portage ubiquitaire, le virus connaît cependant une répartition géographique inégale (MacLachlan et Cowie, 2015). On distingue 3 zones géographiques distinctes :

- L'Afrique subsaharienne, la Chine et l'Asie du Sud-Est où la prévalence du virus est supérieure à 8%.
- Le Proche Orient, l'Europe du Sud et de l'Est ainsi que l'Amérique Centrale et du Sud montrent une prévalence intermédiaire comprise entre 2 et 7%.
- L'Europe du Nord et l'Amérique du Nord où la prévalence est inférieure à 2%.

Ces zones se distinguent également par différents modes de transmission (Hou et al., 2005). Dans les zones à forte prévalence, la transmission du VHB s'effectue principalement par contamination materno-fœtale ou périnatale (Kwon et Lee, 2011), par le sang maternel ou les sécrétions vaginales (Stevens et al., 1975). Plus la charge virale maternelle est importante, plus le risque de transmission est grand (Beasley et al., 1977; Stevens et al., 1979). La transmission sexuelle est responsable de la majorité des cas d'hépatite B dans les pays occidentaux (Inoue et Tanaka, 2016). Une transmission parentérale peut également avoir lieu des suites d'une transfusion sanguine. Dans les pays occidentaux, le risque transfusionnel est contrôlé (Pillonel et al., 1998) notamment grâce aux mesures d'éviction des donneurs de sang qui sont systématiquement dépistés depuis 1971. En revanche, l'utilisation de matériel souillé par les toxicomanes constitue encore aujourd'hui une voie importante de transmission. Enfin, une transmission horizontale, de personne à personne, est possible par tout liquide biologique rentrant en contact avec une peau lésée. Elle est favorisée par de mauvaises conditions

d'hygiène et particulièrement fréquente dans le cadre intrafamilial (d'un enfant contaminé à un enfant sain) et chez les enfants et adolescents vivant en collectivité.

1.2. Virologie

1.2.1. Le cycle de réPLICATION du VHB

Formellement identifié par David Dane dans les années 70, le virion mesure entre 40 et 48 nm de diamètre (Dane et al., 1970). Comme présenté dans la Figure 1, le virus se compose d'une enveloppe lipidique elle-même composée de 3 glycoprotéines de taille différente (S, Pré-S2 et Pré-S1) toutes dérivées d'un gène codant pour l'antigène de surface noté AgHBs (Bruss, 2007). Cette enveloppe renferme en son sein une capsule icosaédrique (ou nucléocapside) formée de l'antigène HBc (AgHBc) et contenant un ADN circulaire relâché (*relaxed-circular DNA*, *rcDNA*) partiellement double brin dont un brin de polarité négatif complet et un brin de polarité positive représentant 50 à 80% du génome (Figure 1).

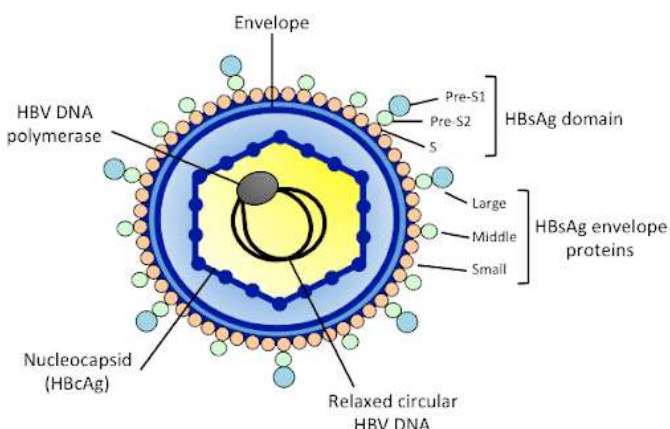


Figure 1: Représentation schématique du virus de l'hépatite B (Gonzalez, 2017)

Suite à l'entrée du virus dans les hépatocytes de l'hôte *via* le co-trasnsporteur sodium/taurocholate (NTCP) (Yan et al., 2012), la nucléocapside est transportée vers le noyau pour y relâcher le *rcDNA* (Figure 2). Celui-ci y est converti en ADN circulaire super-enroulé (*covalently-closed circular DNA*, *cccDNA*). Le *cccDNA* sert alors à la transcription des

nombreux ARN messagers, parmi lesquels l'ARN prégénomique (*pre-genomic RNA, pgRNA*) et les ARN codants pour les protéines S (région PréS/S) (Lucifora et Protzer, 2016). Au sein des nucléocapsides nouvellement formées, la transcriptase inverse produit une nouvelle particule de *rcDNA* à partir du *pgRNA*. Les particules de *rcDNA* sont ainsi conduites vers le réticulum endoplasmique pour y être enveloppées puis sécrétées dans la circulation générale (Seeger et Mason, 2000). Certaines particules peuvent cependant échapper à l'étape de sécrétion et retourner dans le noyau, formant ainsi une boucle d'amplification virale contribuant au maintien des niveaux de *cccDNA* dans les hépatocytes (Locarnini et Mason, 2006; Köck et al., 2010). Notons qu'au gré de cette amplification, le génome viral peut intégrer celui de l'hôte, contribuant au maintien de l'infection et à la transformation des hépatocytes (Levrero et Zucman-Rossi, 2016). En effet, une partie du *cccDNA* peut subir un processus d'intégration et être exprimée directement par l'hôte. Celui-ci est notamment responsable d'une partie de l'expression de l'AgHBs (Tu et al., 2017).

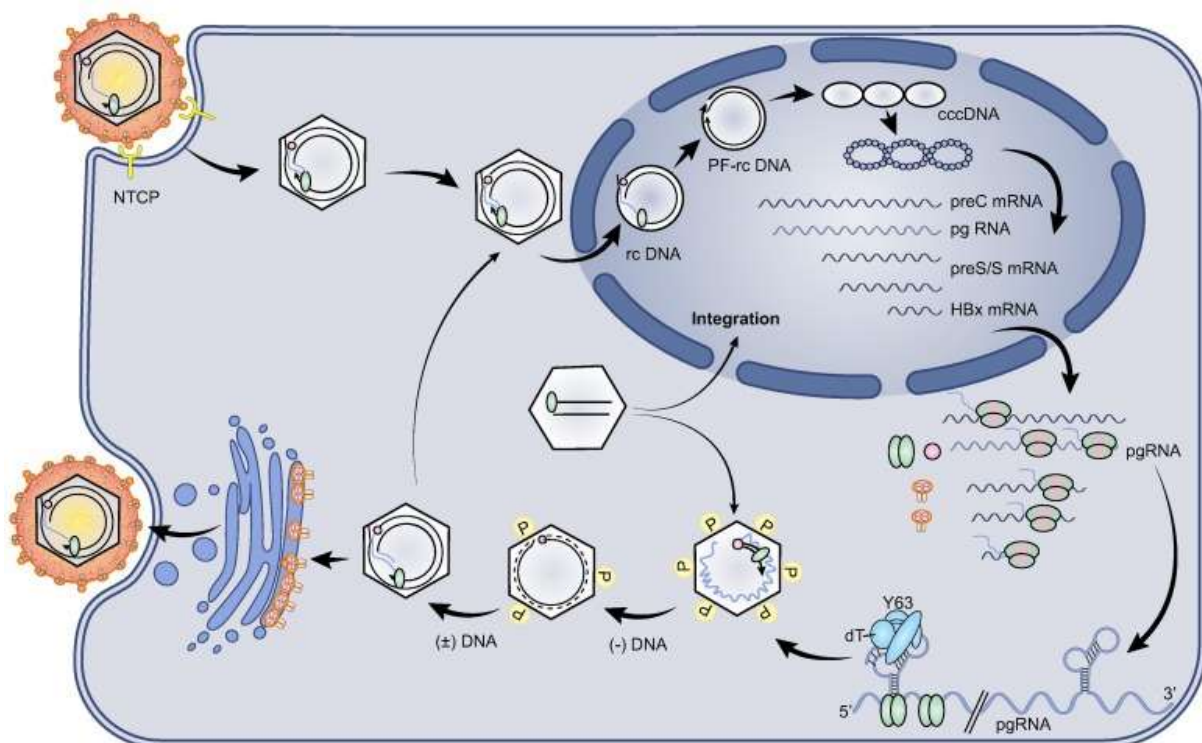


Figure 2: Représentation du cycle de réPLICATION du VHB (Tong et Revill, 2016)

1.2.2. Les produits viraux et sous-viraux de l'infection au VHB

Les virions complets

Les virions complets (ADN VHB) sont excrétés en grande quantité dans la circulation des patients infectés ($\approx 10^7 - 10^9$ copies/mL de sang) et sont à l'origine de nouvelles infections de cellules de l'hôte (Abe et al., 1999). Ces particules se définissent par la présence d'un double brin d'ADN partiel et de la transcriptase inverse encapsidés. Cependant, une dérégulation du processus de maturation peut conduire à la formation de nombreuses autres particules dites incomplètes (Hu et Liu, 2017). Celles-ci se définissent par l'absence de protéines de capsid et/ou de la particule de *rcDNA*.

Les sphères et filaments d'AgHBs

Des particules couvertes d'antigènes HBs (AgHBs) peuvent se former à partir des différentes protéines S et prennent la forme de filaments ou de sphères. Appelées sous particules virales (*subviral particles, SVP*), celles-ci sont vides de tout contenu génomique mais constituent l'entité majoritairement sécrétée dans la circulation sanguine de l'hôte. On estime qu'il y entre 1000 et 100 000 fois plus de SVP que d'ADN VHB dans la circulation ($\approx 10^{12} - 10^{14}$ SVP/mL) (Ganem et Prince, 2004). Produites par le *cccDNA* ou l'ADN intégré, elles sont recouvertes des mêmes protéines HBs que les virions et agissent comme unurre pour le système immunitaire de l'hôte, en monopolisant l'action des anticorps anti-AgHBs, rendant ces derniers moins disponibles pour lutter contre les virions (Rydell et al., 2017).

L'antigène E ou AgHBe

L'antigène HBe (AgHBe) est une protéine soluble dans le sérum des individus infectés et secrétée de façon précoce au cours de l'infection. Il résulte de l'épissage alternatif du gène codant pour la protéine de capsid. Protéine non essentielle à la réplication virale, elle joue cependant un rôle important dans la régulation de la réponse immunitaire. Elle permet notamment d'induire une immunotolérance de l'hôte envers le virus en réduisant la réponse des lymphocytes T (Hong et Bertoletti, 2017; Kramvis et al., 2018).

Les particules d'ARN VHB

Récemment, des particules contenant de l'ARN ont été détectées dans le sérum de patients infectés (Rokuhara et al., 2006; van Bömmel et al., 2015) à des niveaux 100 à 1000 fois inférieurs à ceux des virions complets ($10^6 - 10^7$ copies/mL) (Huang et al., 2010, 2015). L'hypothèse la plus répandue quant à la nature de ces particules est qu'elles sont constituées du couple *pgRNA/transcriptase inverse* encapsidé dans la nucléocapside. Elles seraient excrétées avant que la transcriptase inverse ait produit le double brin d'ADN des virions (Wang et al., 2016). L'ARN VHB étant détecté chez les patients traités par analogues nucléosidiques, il a été suggéré qu'il puisse être un reflet des quantités de *pgRNA* intracellulaires et donc un marqueur de l'activité transcriptionnelle du *cccDNA* (Giersch et al., 2017). Se faisant, une diminution de ce marqueur traduirait une diminution de l'activité virale et traduirait donc l'efficacité des traitements (Wang et al., 2016; Liu et al., 2020).

L'infectiosité de ces particules reste inconnue mais possible. Dans la mesure où elles contiennent tout le matériel nécessaire à la formation d'un virion complet, les particules d'ARN pourraient entrer dans une cellule, subir la transcription inverse, et donner lieu à la formation de nouveaux *cccDNA* (Wang et al., 2016).

1.3. Histoire naturelle de la maladie

L'hépatite B peut induire une infection aigüe avec des manifestations cliniques très variables, allant de l'absence totale de symptômes (portage asymptomatique) à des troubles hépatiques comme l'ictère (McMahon et al., 1985). Dans 0,1 à 0,5% des cas, les troubles hépatiques peuvent dégénérer et engendrer une hépatite fulminante. Ce risque est accru lorsque les patients sont co-infectés aux virus de l'hépatite C (VHC) ou de l'hépatite Delta (VHD) (Smedile et al., 1982; Féray et al., 1993). Dans 90 à 95% des cas, l'infection aigüe se résout spontanément, procurant à son hôte une immunité protectrice. Les autres personnes infectées développent une forme chronique de l'infection. L'infection chronique se définit par la persistance de l'AgHBs dans les six mois suivant la déclaration de l'infection aigüe. Le risque de chronicité dépend de l'âge et de l'immunité de l'hôte : 5 à 10% des personnes adultes et immunocompétentes développent une maladie chronique contre 90% chez les nouveau-nés ou les personnes immunodéprimées (Hyams, 1995).

On distingue 4 phases de l'infection chronique au VHB reposant sur les concentrations des marqueurs sériques du VHB (AgHBe, AgHBs et virions) et/ou la présence d'une maladie hépatique (Figure 3). Ainsi, la première phase dénommée « infection chronique AgHBe positive » (anciennement phase immunotolérante) se caractérise par des titres d'AgHBe, AgHBs et virions élevés, traduisant une forte activité réplicative du virus et une absence de troubles hépatiques comme en témoigne les concentrations d'ALAT (Alanine-Amino-Transférase), normales au décours de cette phase. L'infection peut alors évoluer vers le stade « hépatite chronique AgHBe positive » au cours de laquelle les troubles hépatiques apparaissent. Les marqueurs sériques y restent élevés mais s'accompagnent d'une augmentation des ALAT traduisant une inflammation ou une fibrose hépatique. La suite de l'infection est variable. Certains patients parviennent à contrôler l'infection en développant des anticorps anti-AgHBe, et rentrent dans une phase de portage inactif ou « Infection chronique AgHBe négative ». Au cours de cette phase, l'activité transcriptionnelle est faible et associée à des concentrations virales inférieures à 2000 UI/mL. Enfin, une partie des patients au stade d'« hépatite chronique AgHBe positive » peuvent ne jamais contrôler l'infection, mais perdent cependant l'AgHBe : on parle d'hépatite chronique AgHBe négative.

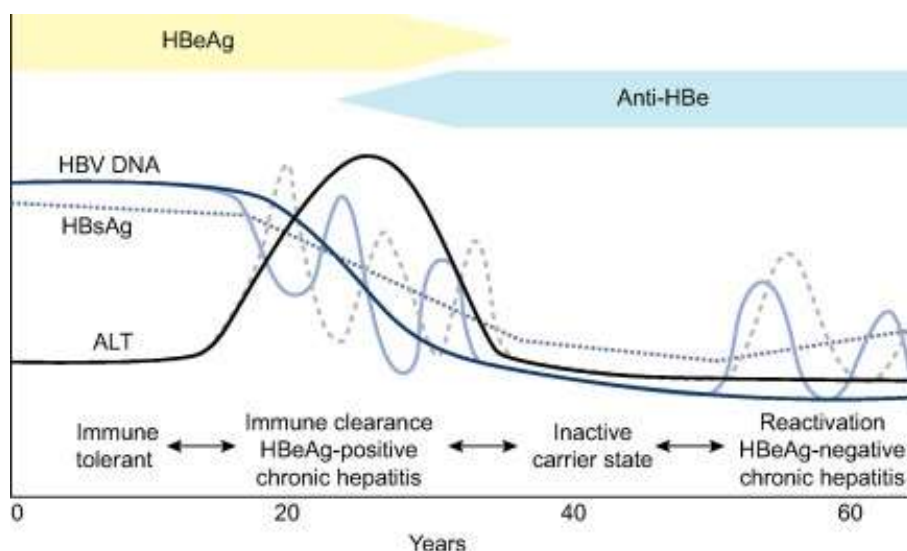


Figure 3: Les quatre phases de l'infection chronique au VHB en histoire naturelle (Lok et al., 2017)

1.4. Prophylaxie et traitements antiviraux

1.4.1. Prophylaxie vaccinale

Malgré le développement de nouvelles thérapies, la vaccination de la population mondiale reste la solution la plus efficace pour éradiquer le virus et réduire les comorbidités associées à l'infection au VHB (Luo et al., 2012). Initialement développé dans les années 1970, le vaccin se constituait de particules virales vides de leur contenu génomique mais recouvertes de protéines de surface. Difficile à produire, ce vaccin a été remplacé par des vaccins dits recombinants (Michel et al., 2001) conférant une immunité protectrice chez 95 à 98% des vaccinés et mesurable par dosage des anticorps anti-AgHBs. On parle d'effet protecteur des anti-AgHBs si les concentrations sont supérieurs à 10 UI/mL. En France, depuis 2018, la vaccination est obligatoire chez tous les nourrissons âgés de 2 mois et fortement recommandée en rattrapage chez les adolescents de moins de 15 ans.

1.4.2. « HBV cure » ou la complexe définition de l'objectif thérapeutique

La guérison complète de la maladie ou « HBV cure » se définit par une élimination du virus permettant l'arrêt du traitement sans risque de rebond virologique ou d'évolution vers des complications hépatiques (Lok et al., 2017). Derrière cette définition générique de la guérison de la maladie, il existe trois objectifs thérapeutiques intégrant la disparition d'un ou plusieurs marqueurs du VHB. Le premier d'entre eux est l'éradication stérilisante du virus. Elle se définit par une disparition de l'ADN VHB, de l'AgHBs mais également des formes intracellulaires du virus telles que le *cccDNA* et de l'ADN intégré. Or, même chez les sujets ayant guéris d'une infection aigue au virus, ses formes sont détectées dans les cellules et peuvent être à l'origine d'une réactivation de l'infection.

Ainsi, un objectif plus réaliste consiste à atteindre la guérison fonctionnelle de la maladie. Elle se définit par un ADN VHB et un AgHBs demeurant indétectables après l'arrêt du traitement : on parle de réponse virologique et sérologique, respectivement. Notons que la perte de l'AgHBs peut s'accompagner de l'apparition d'anticorps anti-AgHBs : c'est la séroconversion.

Enfin, il existe un troisième objectif consistant en une guérison partielle de la maladie. Elle se définit par un AgHBs détectable mais une réponse virologique persistante après l'arrêt du

traitement (Lampertico et al., 2017; Lok et al., 2017). Cet objectif constitue le critère minimal à atteindre pour les traitements puisque la réponse virologique est associée à une diminution de la fibrose hépatique et une amélioration histologique du foie (Chang et al., 2010).

1.4.3. Prise en charge thérapeutique

Actuellement, nous disposons de deux classes thérapeutiques pour traiter les patients chroniquement infectés par le virus de l'hépatite B : l'interféron α et les analogues nucléos(t)idiques, administrés seuls ou en combinaison.

Interféron α

L'interféron α (IFN α) est une molécule endogène produite par les cellules dendritiques plasmacytoïdes en réponse aux infections virales (Cantell, 1998). L'IFN α agit principalement de façon indirecte en stimulant la production de gènes immunomodulateurs (Gibbert et al., 2013). Il possède par ailleurs une activité antivirale directe en inhibant la transcription du virus. Actuellement, l'interféron utilisé dans l'hépatite B est produit par génie génétique et commercialisé sous une forme pegylée (Peg-IFN α). Le traitement par Peg-IFN α repose sur une administration hebdomadaire de 180 µg pendant 48 semaines entraînant une réponse virologique persistante et une restauration de l'immunité au long cours (Janssen et al., 2005; Lau et al., 2005). Chez les patients AgHBe positifs, une réponse virologique persistant six mois après l'arrêt du traitement est observée dans 20 à 30% des cas. La perte de l'AgHBs est observée chez 5% des patients après un an de traitement (Janssen et al., 2005). Chez les patients AgHBe négatifs, le taux de réponse virologique est plus élevé et de l'ordre de 60% (Marcellin et al., 2004). Chez 12% des patients, cette réponse est associée à une perte de l'AgHBs au cours des 5 ans suivant l'arrêt du traitement (Marcellin et al., 2012).

Analogues nucléos(t)idiques

Actuellement, les analogues nucléos(t)idiques (NUC) constituent le traitement de référence pour les patients chroniquement infectés par le VHB. En Europe, on distingue actuellement 6 molécules approuvées dans le traitement du VHB : la lamivudine (LAM), l'adefovir (ADV), la telbivudine (TBV), l'entecavir (ETV), le tenofovir disoproxil fumarate (TDF) et le tenofovir alafenamide (TAF). Les NUC agissent par inhibition de la polymérase virale entraînant une

diminution de la réPLICATION virale et de la virémie (Papatheodoridis et al., 2002). Ces molécules présentent l'avantage d'être mieux tolérées que le Peg-IFN α et constituent la seule option thérapeutique chez les patients souffrant de cirrhose décompensée ou ayant été transplantés (Lok et al., 2016). L'entecavir et les esters de ténofovir offrent une haute barrière à la mutagénèse et sont aujourd'hui le traitement de référence. Les essais contrôlés randomisés ont montré une réponse virologique persistante jusqu'à 6 mois après l'arrêt du traitement chez 21 et 76% des patients AgHBe positifs selon le NUC utilisé (Marcellin et al., 2008). Chez les patients AgHBe négatifs, ces chiffres atteignent jusqu'à 90%. Après 5 ans de traitement, 100% des patients atteignent une charge virale indétectable (Lampertico et al., 2013; Luo et al., 2013). Dans de rares cas, une perte de l'AgHBs est observée sous un traitement au long cours (<2% par an) (Chang et al., 2006; Chen et al., 2018).

En résumé, les traitements actuels permettent un contrôle virologique de l'infection mais ne ciblent ni l'ADN intégré ni le *cccDNA*. Par ailleurs la guérison fonctionnelle demeure un évènement rare et l'arrêt du traitement est rarement possible (Lau et al., 2005; Chang et al., 2006). Ainsi, dans la suite de cette introduction nous présenterons les différentes pistes thérapeutiques actuellement à l'étude afin de pallier à ces limites.

1.5. Nouvelles approches thérapeutiques

Il existe différentes pistes thérapeutiques intervenant au cours de chacune des étapes du cycle de réPLICATION du VHB (Figure 4). Dans cette section nous nous focaliserons sur les trois principales classes thérapeutiques actuellement à l'étude : les immunomodulateurs, les inhibiteurs de capside et les ARN interférents.

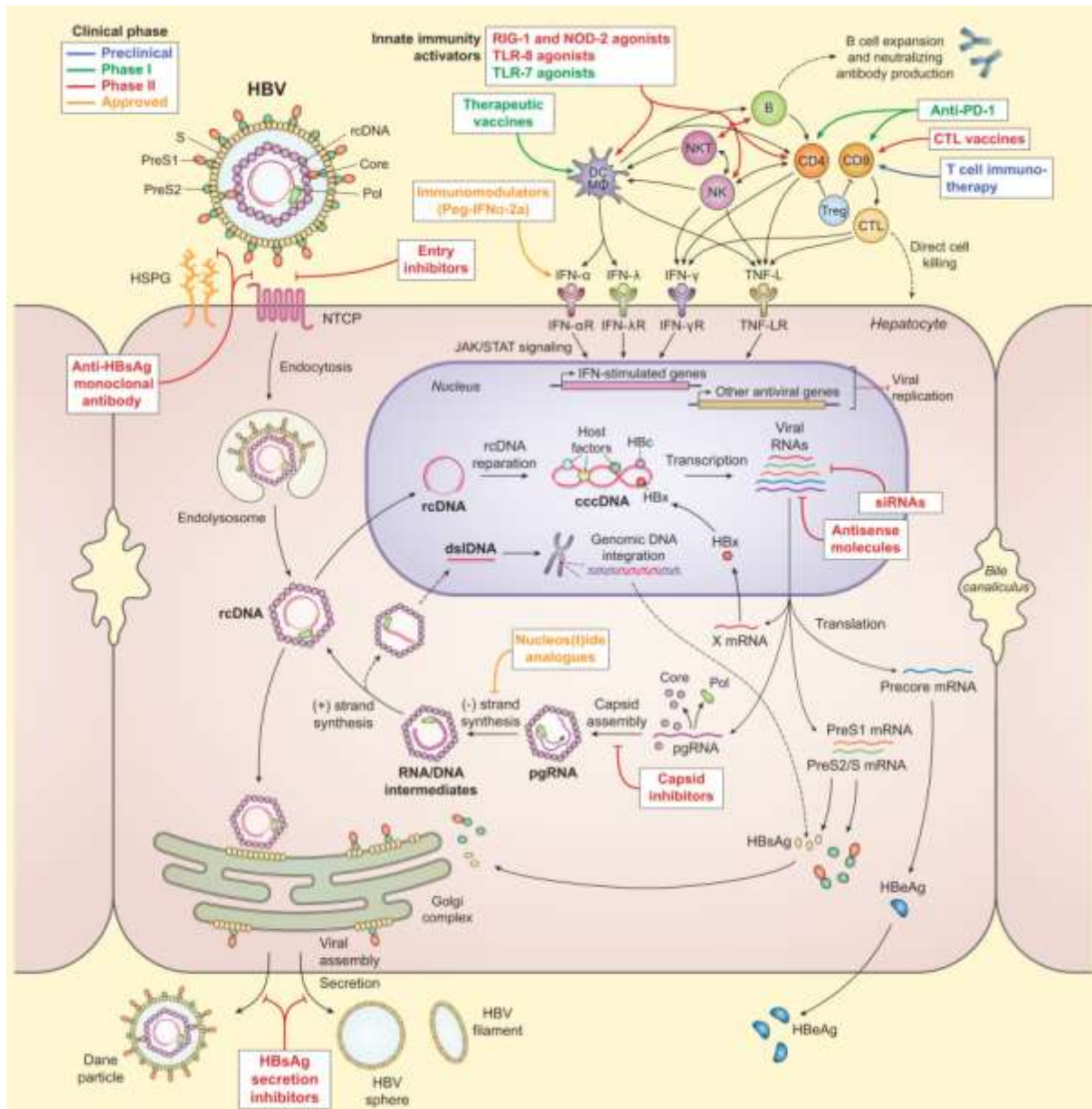


Figure 4 : Les approches thérapeutiques en développement contre l'infection au VHB
(Mouzannar et Liang, 2020)

1.5.1. Immunomodulateurs

Une des pistes thérapeutiques actuellement à l'étude consiste à restaurer l'immunité contre le VHB afin de favoriser à terme l'élimination des particules virales : on parle d'immunomodulateurs (Bertoletti et Ferrari, 2012). Cette classe thérapeutique agit par l'activation du système immunitaire inné impliqué dans la gestion de l'infection (Zoulim et al., 2013). Parmi eux, les agonistes du *toll-like* récepteur 7 (TLR7) entraînent une stimulation des

cellules dendritiques plasmacytoïdes produisant l'IFN α , des cellules NK et des lymphocytes cytotoxiques, tous contribuant à l'instauration d'une réponse immunitaire innée et adaptative (Niu et al., 2018). Il existe plusieurs candidats issus de cette classe thérapeutique en essais cliniques, notamment le GS-9620 et le RO7020531. Chez le singe, outre l'augmentation des concentrations d'IFN α et des niveaux cytokiniques, le GS-9620 a montré une diminution des concentrations d'ADN VHB, d'AgHBe et d'AgHBs ainsi qu'une apparition d'anticorps anti-AgHBs (Lanford et al., 2013). En clinique chez le patients avirémique traités par TDF, aucun effet sur l'AgHBs n'a pu être observé. Cela peut être dû aux doses faibles utilisées : environ 5 fois plus faible que chez l'homme d'après les relations allométriques standards.

Le RO7020531, que nous étudierons en détail dans le Chapitre 3, a montré dans un modèle souris une forte diminution des concentrations d'ADN VHB et d'AgHBs (Dai et al., 2018). Chez l'homme, des données de phase I chez le volontaire sain ont montré que la molécule était bien tolérée et induisait une augmentation dose-dépendante des concentrations d'INF α (Luk et al., 2020). Actuellement, des études cliniques de phase I/II sont en cours en combinaison avec un inhibiteur de capsid.

Plus récemment, des agonistes du TLR8 sont entrés en essais cliniques. Ces molécules stimulent la production de cytokines intrahépatiques comme l'IL-12 ou l'IL-18 et engendrent une réponse immunitaire de type T via l'IFN- γ (Schurich et al., 2013; Jo et al., 2014). Les anti- *programmed death receptor-1* (PD1) ou anti-PDL1 sont également à l'étude. Chez le hamster, l'administration d'un inhibiteur de PDL1 a permis la restauration d'une réponse immunitaire de type T associé à un contrôle de la virémie (Balsitis et al., 2018).

1.5.2. Inhibiteurs de capsid

Les inhibiteurs de capsid (*capsid assembly inhibitors, CAM*) agissent par blocage de l'étape d'encapsidation du pgRNA. Il existe deux classes de *CAM* se distinguant par un mécanisme d'action différent. Les *CAM* de classe I entraînent la formation hétéro-dimères de protéines de capsid aberrantes (*core protein allosteric modulators*), rendant l'encapsidation impossible (Deres et al., 2003) alors que les *CAM* de classe II entraînent la formation précoce de nucléocapsides vides de tout contenu viral (*capsid assembly modulators*) (Feld et al., 2007). Dans son article de 2017, Berke et al. rapporte un double mécanisme d'action des *CAM in vitro*

(Berke et al., 2017). Outre leur action par blocage de l'encapsidation, les *CAM* bloqueraient également le désassemblage des protéines de capside lors de l'entrée de l'ADN viral dans le noyau réduisant ainsi le réservoir de *cccDNA* et donc la production de l'ensemble des marqueurs vitaux.

In vitro, de nombreuses molécules ont été étudiées et ont montré une forte réduction de la production intracellulaire d'ARN et d'ADN viral ainsi que de l'AgHBs sécrété allant jusqu'à 90% (Lahlali et al., 2018). Dans cette thèse nous étudierons le RG7907. Cette molécule réduit l'ADN VHB, et l'AgHBs chez la souris de $2 \log_{10}$ en 4 semaines de traitement (Zhou et al., 2018). Chez l'homme, ce CAM de classe I est bien tolérée et diminue l'ADN et l'ARN VHB de 3 et $2,5 \log_{10}$ copies/mL (Gane et al., 2018, 2019). Cependant la molécule n'a pas montré de diminution de l'AgHBs. Les CAM de classe II ont montré des efficacités similaires les trois marqueurs (Yuen et al., 2019c; Zoulim et al., 2020).

Actuellement une étude de phase II évaluant l'ABI-H0371 en combinaison avec de l'ETV a montré un bénéfice par rapport à l'ETV en monothérapie tant d'un point virologique (ADN et ARN VHB) que sérologique (AgHBs) bien que la diminution maximale d'AgHBs observée n'excède pas $0.5 \log_{10}$ IU/mL (Ma et al., 2019). Actuellement six CAM sont en cours d'investigation dans des essais cliniques de phase I ou II (Fanning et al., 2019).

1.5.3. ARN interférents

Les ARN interférents (*silencing RNA, siRNA*) sont de petites molécules composées d'une vingtaine de nucléotides se fixant sur des ARN messagers et entraînant un blocage de l'expression de ceux-ci (Chen et al., 2008). Compte-tenu du nombre d'ARN messagers impliqués dans l'hépatite B, cette approche connaît un succès important. Des études *in vitro* et chez la souris transgénique ont montré une diminution importante des concentrations d'AgHBs dans le sang associée à une diminution des ARN messagers et de l'ADN viral au niveau intrahépatique (Wu et al., 2005). Des essais cliniques de Phase Ib ou II évaluant le JNJ-3989 ont montré une diminution de l'AgHBs supérieure à $1 \log_{10}$ UI/mL chez les 40 patients traités dont 88% avaient des concentrations d'AgHBs inférieures à $2 \log_{10}$ IU/mL après 24 semaines de traitement (Yuen et al., 2019b; van den Berg et al., 2020). En bloquant simultanément l'expression des gènes du *cccDNA* et de l'ADN intégré, les *siRNA* diminuent significativement les concentrations d'AgHBs (Wooddell et al., 2017). La magnitude de la diminution ou la durée

pendant laquelle les AgHBs doivent être indétectables pour permettre une guérison fonctionnelle demeurent des inconnues auxquelles les essais cliniques de phase II actuellement en cours devraient répondre.

1.5.4. Défis des nouveaux traitements

Les nouveaux traitements présentés précédemment ont des mécanismes d'action originaux pouvant permettre la diminution de nombreux marqueurs et acteurs de l'infection dont l'AgHBs. Cependant, la caractérisation de ces marqueurs sous traitement est à ce jour peu décrite. Le développement de modèles mathématiques de la cinétique virale a permis de soutenir et d'accompagner la révolution des antiviraux anti-VHC, en permettant d'optimiser les relations doses-effets, de prédire les durées de traitements optimales, ou encore de mieux comprendre les déterminants de la résistance (Guedj et Perelson, 2011). Cette approche a aussi été proposée dans le VHB, pour le moment de manière beaucoup moins systématique étant donné la complexité de son cycle de réPLICATION et son interaction avec le système immunitaire.

Chapitre 2. Modèles mathématiques et statistiques de la cinétique virale

2.1. Modélisation de la cinétique virale du VHB

2.1.1. Modèle mathématique standard de l'hépatite B

Modèle de référence

Le modèle utilisé pour décrire le VHB est identique à celui utilisé dans le cadre d'infections chroniques comme l'infection par le virus d'immunodéficience humaine (VIH) ou l'infection par le virus de l'hépatite C (VHC) (Ho et al., 1995; Neumann et al., 1998). Il repose sur la traduction des mécaniques biologiques en lien avec la réPLICATION du virus en un système d'équations différentielles:

$$\frac{dT}{dt} = s - dT - \beta VT$$

$$\frac{dI}{dt} = \beta VT - \delta I$$

$$\frac{dV}{dt} = pI - cV$$

où T représentent les cellules cibles, I les cellules infectées et V les virions. Dans ce modèle les cellules cibles sont produites à une vitesse s et éliminées à une vitesse d soit une demi-vie des cellules cibles $t_{1/2} = \frac{\ln(2)}{d}$. Ces cellules cibles deviennent des cellules infectées par contact avec les particules virales circulantes V à un taux β traduisant l'infectiosité du virus. Les cellules infectées I ainsi produites peuvent produire de nouveaux virus à un taux p ou être éliminées à un taux δ . Enfin, les particules virales V sont éliminés dans la circulation systémique à un taux c (Figure 5). Il est possible, comme dans les modèles épidémiologiques, de définir le taux de reproduction de base R_0 correspondant au nombre de cellules infectées engendrées par une cellule infectée au début de l'infection. Dans ce modèle, R_0 est donné par $R_0 = \frac{p\beta s}{d\delta c}$.

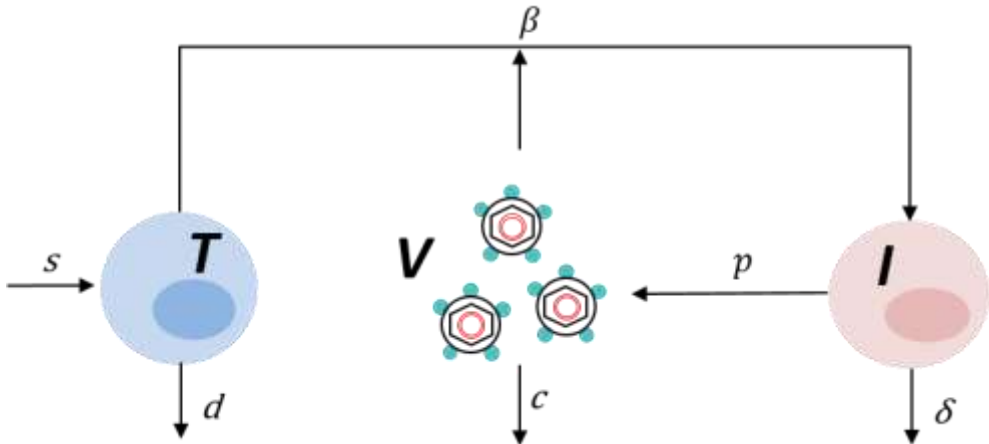


Figure 5: Modèle de référence de l'interaction hôte-virus dans les infections virales chroniques

Au bout d'un certain temps, le modèle prédit l'arrivée au stade d'infection chronique où les cellules et le virus sont à l'état d'équilibre. Pour le virus cela se traduit par une production de virions égale à son élimination soit $pI = cV$. Cependant cet équilibre peut être rompu par l'initiation d'un traitement : l'élimination devient importante que la production virale, révélant ainsi les mécanismes de décroissance du virus. Les mécanismes les plus communs par lesquels un traitement antiviral agit sont : la diminution de l'infection du virus avec une efficacité η et la réduction de la production virale avec une efficacité ε .

En pratique, les traitements antiviraux ne conduisent pas à une suppression virale totale mais peuvent réduire suffisamment la réPLICATION au point de mener à une réDUCTION continue du virus. Pour cela, l'efficacité d'un traitement doit dépasser un seuil critique valant $\varepsilon_c = \left(1 - \frac{1}{R_0}\right)$. Compte-tenu du $R_0 \approx 10$ estimé dans l'infection au VHB (Whalley et al., 2001), l'efficacité nécessaire pour atteindre la clairance du virus sont importantes et de l'ordre de 90%.

En supposant que i) les efficacités du traitement sont toutes deux compris entre 0 et 1 et que ii) les cellules cibles sont dans un état de quasi-équilibre tel que $T_0 = \frac{c\delta}{\beta p}$, il existe une solution analytique permettant de décrire l'évolution de la charge virale après initiation du traitement :

$$V(t) = V_0 [A e^{-\lambda_1(t-\tau)} + (1-A) e^{-\lambda_2(t-\tau)}]$$

$$\text{où } \lambda_{1,2} = \frac{1}{2} [c + \delta \pm \sqrt{(c - \delta)^2 + 4(1 - \varepsilon)(1 - \eta)c\delta}] \text{ et } A = \frac{\varepsilon c - \lambda_2}{\lambda_1 - \lambda_2}.$$

La perturbation d'un système biologique des suites du traitement révèle les mécanismes sous-jacents de l'infection et permet d'en estimer les paramètres clés. Ainsi, l'équation révèle une cinétique de déclin bi-exponentielle où la première pente de décroissance est λ_1 et la seconde λ_2 . En présence d'un traitement bloquant la production virale avec une efficacité supérieure à 90% et $c > \delta$, alors les deux pentes de déclin sont c la clairance du virus et δ la perte de cellules infectées, respectivement (Figure 6).

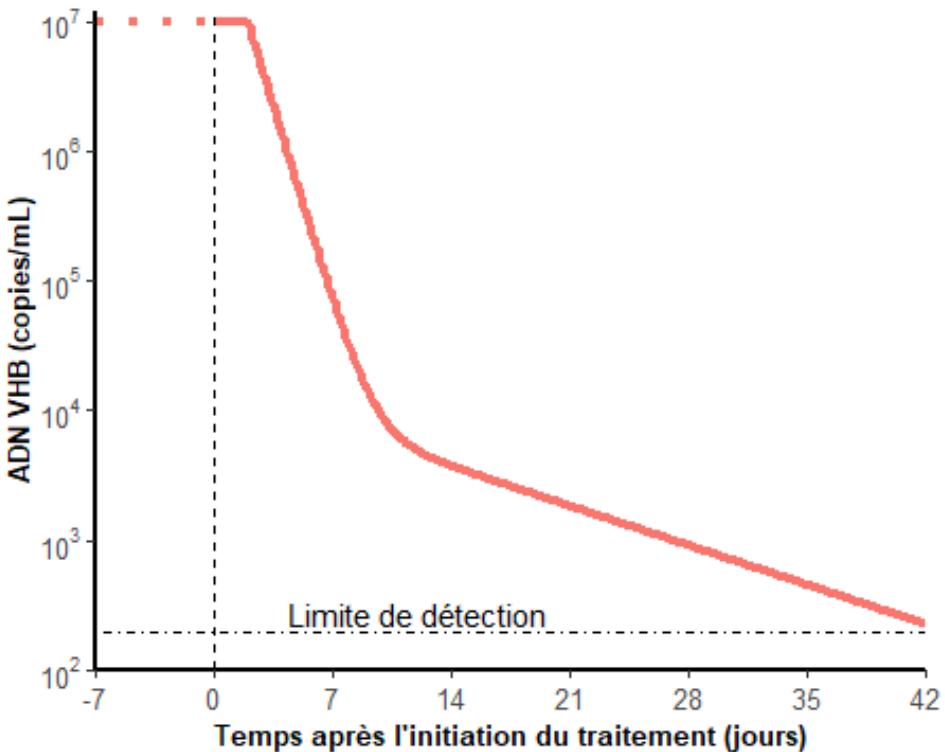


Figure 6 : Profil typique de l'ADN VHB sous traitement. Avant le traitement, l'ADN VHB est à l'équilibre (pointillés rouges). L'initiation d'un traitement à $t=0$ entraîne après un délai de quelques heures, un premier déclin rapide du virus avec une vitesse proche de la clairance du virus dans le sang. Cette phase dure environ 10 jours et mène à un déclin de la charge virale proportionnelle à l'efficacité du traitement (ici, par exemple le déclin de 3 log10 reflète un blocage de la production virale de **99.9%**). Par la suite, le virus entame une seconde phase de déclin, plus lente, qui reflète l'élimination progressive des cellules infectées.

Apports du modèle

Ce modèle a été utilisé dans de nombreuses études cliniques afin de déterminer l'efficacité des traitements ainsi que la demi-vie du virus et des cellules infectées. Les estimations des paramètres varient en fonction des études, des molécules et de la durée de suivi des patients (Table 1 et 2) .

Table 1 : Estimation des paramètres de cinétique virale en monothérapie

TraITEMENT	N	AgHBe	DURÉE (semaines)	Efficacité	$t_{1/2} V$ (jours)	$t_{1/2} I$ (jours)	Etude
PEG-IFN	24	-	6	-	-	10,4	Colombatto et al., 2006
	18	-	4	0,93	0,53	9,6	Sypsa et al., 2005
	5	+/-	-	0,77	0,40	10,3	Ribeiro et al., 2010
médiane				0,85	0,47	10,3	
LAM	8	-	4	0,83	0,53	5,8	Sypsa et al., 2005
	24	-	6	0,87	0,38	12,9	Colombatto et al., 2006
	9	+	12	0,94	2	43	Lau et al., 2000
	15	+	12	0,95	1,2	2,4 - 120	Lewin et al., 2001
	20	+	4	0,96	1	16	Nowak et al., 1996
	10	+	4	0,94	0,99	15,5	Wang et al., 2004
	21	+	4	0,94	0,54	7,3	Wolters et al., 2002a
	12	+	4	0,93	0,67	9	Wolters et al., 2002c
médiane				0,94	0,99	NA	
ADV	32	+	12	0,995	1,35	12,5	Leung et al., 2009
	13	+	12	0,993	1,1	18,2	Tsiang et al., 1999
médiane				0,994	1,22	15,4	
ETV	33	+	12	0,999	0,6	8,9	Leung et al., 2009
	21	+	12	0,992	0,86	9,2	Suh et al., 2010
	10	+/-	4	0,96	0,66	10,7	Wolters et al., 2002b
médiane				0,992	0,66	9,2	

LAM +	8	+/-	8	0,98	1	9,4	Mihm et al., 2005
ADV	9	+/-	4	0,94	0,53	12,4	Ribeiro et al., 2010
médiane				0,96	0,77	10,9	
LAM +	24	-	6	0,87	0,34	9,8	Colombatto et al., 2006
PEG	18	-	4	0,96	0,53	2,7 - 75	Sypsa et al., 2005
	7	+/-	4	0,95	1,0	6,7	Ribeiro et al., 2010
médiane				0,95	0,53	NA	

Alors que le PEG-IFN fournit un efficacité de 85% environ, l'apparition des analogues nucléos(t)idiques, notamment la lamivudine a permis d'obtenir une efficacité supérieure à 90% en médiane (Table 1). Notons que chez les individus AgHBe négatifs, l'efficacité rapportée est plus faible que chez les individus AgHBe positifs. La combinaison (Sypsa et al., 2005; Colombatto et al., 2006). Les stratégies alliant LAM et PEG-IFN en combinaison fournissent des efficacités similaires à celle sous LAM en monothérapie (Sypsa et al., 2005; Colombatto et al., 2006).

L'apparition de résistance au traitement par LAM a conduit les firmes pharmaceutiques au développement de nouveaux NUC montrant moins de résistance dont l'adefovir (ADV) et l'entecavir (ETV) (Zoulim, 2011). Ces NUC présentent une efficacité accrue qui atteint jusqu'à 99,9% pour l'ETV. Sa grande barrière génétique à l'apparition de résistance (1,2% de patients montrant une résistance après 5 ans de traitement) et sa grande efficacité font de l'ETV le NUC de référence dans le traitement du VHB (Zoulim et Locarnini, 2009).

Outre l'efficacité du traitement, les travaux de modélisation présentés ci-dessus rapportent les demi-vies de virus et des cellules infectées. On note une constance de la demi-vie du virus dont l'ordre de grandeur est d'environ 1 jour quel que soit le traitement utilisé. En revanche, on observe une grande variabilité de la demi-vie des cellules infectées, comprise entre 2,4 et plus d'une centaine de jours. L'origine de cette variabilité pourrait être la difficulté à observer la seconde pente de déclin. En effet, les méthodes de dose de l'ADN VHB ont des limites de détection diverses, lesquelles ne permettent pas toujours d'observer la seconde pente de déclin.

2.1.2. Modélisation de la relation concentration-efficacité des traitements

Outre la cible thérapeutique du traitement étudié, qui va définir le mécanisme d'action par lequel l'efficacité du traitement sera modélisée, la relation concentration-effet joue un rôle important. En monothérapie, l'effet traitement limitant la production virale ε est considéré constant tout au long de la durée de l'étude et varie entre 0 (pas d'effet de la molécule) et 1 (suppression totale de la production virale). Or, cette hypothèse d'efficacité thérapeutique constante est souvent remise en question par la nature des profils observés. En effet, les cinétiques virales observées chez les patients traités peuvent varier suite aux fluctuations des concentrations de médicament au cours du temps. Une façon de prendre en compte ces observations consiste à modéliser l'efficacité d'un traitement comme une fonction dépendant de la cinétique des concentrations de médicament dans le sang ou le site d'action de la molécule d'après l'équation suivante (Talal et al., 2006) :

$$\varepsilon(t) = \frac{C(t)^n}{C(t)^n + EC_{50}^n}$$

Où $C(t)$ est la concentration de médicament au temps t , n est le paramètre de raideur de la relation concentration-effet et EC_{50} est la concentration générant une efficacité de 50%. Dans cette équation, l'efficacité varie au gré des concentrations de médicament : plus les concentrations sont élevées par rapport à l' EC_{50} plus l'efficacité est importante (Figure 7).

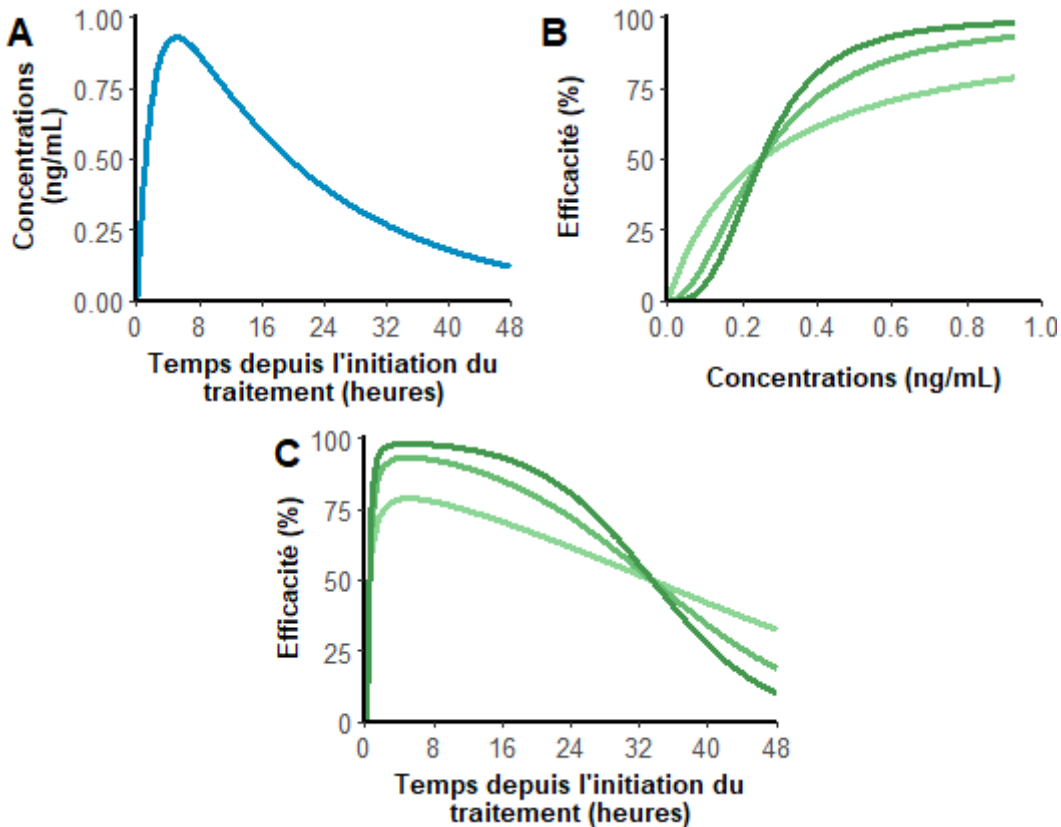


Figure 7 : Représentation de la relation concentration-efficacité. Exemple de profil pharmacocinétique d'une molécule administrée par voie orale (A). Plus les concentrations sont élevées par rapport à l' EC_{50} (ici $EC_{50} = 0,25 \text{ ng/mL}$) plus l'efficacité est grande (B). L'efficacité change au cours du temps en suivant les variations de concentrations. Elle est maximale au moment où les concentrations le sont ($t_{max} = 5 \text{ h}$). L'efficacité varie d'autant plus vite que n est grand (ici $n = 1 ; 2$ ou 3 en vert clair, vert et vert foncé, respectivement)

En l'absence de données pharmacocinétiques, des modèles empiriques permettent de décrire une efficacité variant au cours du temps. Par exemple, on peut prendre en compte l'augmentation de l'efficacité suite à des prises successives du médicament par la fonction suivante :

$$\varepsilon(t) = \varepsilon_1 + (\varepsilon_2 - \varepsilon_1)(1 - e^{-kt})$$

où ε_1 est l'efficacité initiale, ε_2 l'efficacité finale (à l'équilibre) et k la vitesse avec laquelle cet équilibre pharmacologique est atteint (Guedj et Perelson, 2011).

2.1.3. Rôle des modèles dans l'optimisation thérapeutique du VHC

La modélisation a joué un rôle important dans le développement, l'optimisation et l'individualisation des traitements antiviraux dans le contexte du VHC.

En 2010, Snoeck et al. ont montré qu'un modèle simple combinant la pharmacocinétique du Peg-IFN α ± ribavirine et la cinétique virale pouvait reproduire la réponse observée chez 1200 patients pendant et après traitement, permettant ainsi de mieux comprendre les déterminants de la réponse virologique (Snoeck et al., 2010). En caractérisant la cinétique virale sous antiprotéases, ces approches ont ensuite permis de guider le développement thérapeutiques des antiviraux du VHC et les durées optimales de traitement (Guedj et Perelson, 2011).

La modélisation a également permis une meilleure compréhension des mécanismes d'action des nouveaux traitements. En intégrant des processus intracellulaires du cycle de réPLICATION du VHC, il a été montré que le daclatasvir avait un double mécanisme d'action sur la réPLICATION virale et la sécrétion du virus (Guedj et Perelson, 2011). Enfin, ces modèles ont montré qu'ils pouvaient de manière prospective anticipé l'impact du choix de la dose dans le taux de SVR (Nguyen et al., 2014). Ces analyses sont désormais recommandées par la *Food and Drug Administration* pour justifier de la dose de médicament utilisée dans les phases ultérieures du développement du médicament (Food and Drug Administration, 2017).

2.1.4. Limites des modèles

Le modèle de référence permet une bonne compréhension des mécanismes élémentaires régissant la dynamique de déclin de la virémie sous traitement et a permis le développement de traitements contre d'autres infections virales comme le VHC. Cependant, la complexité de l'infection au VHB et la variété des cibles thérapeutiques révèlent les limites du modèle standard. Dans cette section nous exposons les limites des modèles actuels et introduisons des modèles alternatifs tentant de pallier à celles-ci.

Alors que la première pente de déclin s'interprète comme la clairance du virus, des observations semblent contredire ce résultat. En effet, on note que la demi-vie du VHB est d'environ 1 jour contre 1 à 6 heures pour le VHC ou le VIH (Nowak et al., 1996; Guedj et al., 2013). Par analogie avec l'infection au VHC, la mort des cellules infectées se détermine à partir de la seconde phase de déclin de la virémie. D'après cette pente, on estime que 99% des cellules infectées seraient

éliminées en moins de 3 ans. Or dans le même temps l’AgHBs, lui-même produit par les cellules infectées, décline de $0.007 \log_{10} \text{UI/mois}$ uniquement ; ce qui correspondrait à une élimination totale en plus de 50 ans (Chevaliez et al., 2013). Ainsi, quel que soit le phénomène observé et menant à la seconde pente de déclin de l’ADN VHB, il ne peut s’agir uniquement de mort cellulaire.

2.1.5. Comment modéliser de nouvelles cibles thérapeutiques ?

Le modèle de référence ne prend en compte que certaines pièces du « puzzle » de l’infection au VHB (Neumann, 2005). Compte-tenu des mécanismes d’action des molécules (action sur l’immunité, production d’anticorps anti-AgHBs, inhibition de l’étape d’encapsidation), les futurs modèles doivent intégrer plus d’étapes du cycle de réPLICATION du virus et davantage de marqueurs.

A l’initiation de cette thèse, certains travaux tentaient déjà d’apporter un nouveau degré de complexité au modèle du VHB. Lewin et al. ont notamment proposé un modèle prenant en compte la perte naturelle du *cccDNA* par une cellule infectée (Lewin et al., 2001). Ils expriment la perte globale de cellules infectées δ comme la somme de la mort cellulaire se produisant à une vitesse δ' et le mécanisme de perte du *cccDNA* se produisant une vitesse ϱ tel que $\delta = \delta' + \varrho$. Cependant, l’estimation du paramètre ϱ requiert des mesures répétées du *cccDNA* lesquelles sont difficiles à obtenir. Ce modèle apporte un degré supplémentaire de compréhension de mécanismes menant à la seconde pente de déclin de la charge virale en dissociant les processus cytolytiques et non-cytolytiques.

Murray et al. ont proposé un modèle intégrant l’export des virions dans la circulation (Murray et al., 2005). De ce modèle l’ADN intracellulaire est produit proportionnellement au nombre de cellules infectées à une vitesse a et sécrété dans la circulation systémique à une vitesse ρ . Le modèle s’écrit alors:

$$\begin{aligned}\frac{dI}{dt} &= \beta VT - \delta I \\ \frac{dD}{dt} &= aI - \rho D - \delta D \\ \frac{dV}{dt} &= \rho D - cV\end{aligned}$$

En appliquant ce modèle à des données de chimpanzés infectés par le VHB, Murray et al. ont montré que le lent déclin de la virémie observé à l'initiation du traitement est dû à une vitesse de sécrétion du virus lente plutôt qu'une longue demi-vie d'élimination du virus. En effet, ils estiment une demi-vie de sécrétion comprise entre 0.6 et 1.1 jour, cohérente avec les estimations précédentes de la première phase de déclin. La demi-vie d'élimination du virus est quant à elle estimée à 4.4 heures, soit une estimation plus faible que celle fournit par le modèle de référence, mais cohérente avec les demi-vies du VHC ou du VIH (Perelson et al., 1996; Neumann et al., 1998; Ramratnam et al., 1999).

Certains travaux menés dans le cadre de l'infection aigüe au VHB ont initié l'étude d'autres marqueurs comme l'AgHBs (Ciupé et al., 2014; Shekhtman et al., 2020). Dans leur article, Ciupé et al. proposent un modèle distinguant la production d'ADN VHB et de sous particules virales (voir section 1.2.2.). En prenant en compte la présence d'AgHBs à la surface des virions et des sous particules virales, ils intègrent la stimulation de la production des anticorps anti-AgHBs. Dans leur étude ils concluent que la résolution spontanée de l'infection n'est possible qu'à deux conditions : soit les anticorps sont présents en grand quantité, soit les sous particules virales sont présentes en faible quantité, permettant tout de même au système immunitaire de prendre en charge l'infection. Cependant, les conclusions présentées se focalisent sur l'infection aigüe et n'intègrent pas la modélisation de données réelles.

Dans la suite de cette thèse nous étendrons davantage le modèle de référence en nous appuyant sur les données générées au cours du développement des nouveaux antiviraux. La section suivante présente la méthodologie utilisée pour développer ces modèles.

2.2. Inférence et sélection de modèle

2.2.1. Modèles non-linéaire à effets mixtes

L'analyse des données longitudinales requiert l'utilisation de modèles statistiques complexes. Une méthode consiste à utiliser une approche de population, particulièrement adaptée aux mesures répétées au cours du temps (Davidian et Giltinan, 1995), et reposant sur des modèles non linéaires à effets mixtes (MNLEM).

Modèle statistique

Le modèle statistique dit à effets mixtes permet de prendre en compte l'ensemble des cinétiques individuelles où l'observation y_{ij} de l'individu i au temps j et s'écrit :

$$y_{ij} = f(t_{ij}, \theta_i) + g(t_{ij}, \theta_i) \times \epsilon_{ij}$$

Avec la fonction $f(t_{ij}, \theta_i)$ correspondant au modèle structural utilisé pour décrire les données et la fonction $g(t_{ij}, \theta_i) \times \epsilon_{ij}$ décrivant le modèle d'erreur résiduelle où ϵ_{ij} est supposé suivre une loi normale d'espérance 0 et de variance 1.

La fonction f dépend du temps et du vecteur de paramètres individuels θ_i . Elle est commune à tous les individus cependant le vecteur de paramètres θ_i varie d'un individu à l'autre. Il se décompose en un vecteur d'effets fixes μ , représentant le paramètre de position soit la valeur « typique » du paramètre pour l'ensemble des individus et un effet aléatoire η_i spécifique à chaque individu. On peut alors écrire $\theta_i = \mu + \eta_i$ si un paramètre suit une loi normale ou $\theta_i = \mu \times e^{\eta_i}$ dans le cas plus fréquent en biologie où un paramètre est strictement positif et suit ainsi une loi log-normale. On note également $logit(\theta_i) = logit(\mu) + \eta_i$ si un paramètre est contraint entre 0 et 1. Les effets aléatoires η_i suivent une loi normale de moyenne 0 et de matrice de variance-covariance Ω .

Une partie de la variabilité interindividuelle peut s'expliquer par un ensemble de caractéristiques individuelles ou covariables (âge, poids, génotype du virus). Pour un paramètre suivant une loi log-normale on note alors :

$$\theta_i = \mu \times e^{\eta_i} \times e^{\beta' z_i}$$

Où β' est le vecteur des effets de covariables et z_i le vecteur de covariables de l'individu i .

La fonction g caractérise la forme du modèle d'erreur résiduelle et s'écrit :

$$g(t_{ij}, \theta_i) = a + b \times f(t_{ij}, \theta_i, z_i)$$

Avec a et b les termes d'erreur additif et proportionnel, respectivement.

Enfin, on note Ψ le vecteur de paramètres de population à estimer se composant des effets fixes μ , des éléments de la matrice de variance-covariance Ω , des effets des covariables β ainsi que des paramètres d'erreur résiduelle a et b

Estimation des paramètres

La plupart des méthodes disponibles sont basées sur la maximisation de la vraisemblance (Dartois et al., 2007). On note alors $L(\Psi; y)$ la vraisemblance de l'ensemble des données observées. Chaque individu étant indépendant, la vraisemblance résulte du produit des vraisemblances individuelles. Chaque vraisemblance individuelle se traduit par la probabilité de l'observation (y) conditionnellement aux paramètres du modèle. Cette probabilité est calculée par intégration des données par rapport à la distribution des paramètres individuels tel que :

$$L(\Psi; y) = \prod_{i=1}^N L(\Psi; y_i) = \prod_{i=1}^N p(y_i | \Psi) = \prod_{i=1}^N \int p(y_i | \eta_i, \Psi) p(\eta_i, \Psi) d\eta_i$$

avec L la vraisemblance et $p(y_i | \eta_i, \Psi)$ la probabilité de l'observation y_i conditionnellement aux effets aléatoires η_i et au vecteur de paramètres de population Ψ à estimer. Du fait de la non linéarité du modèle structural, l'intégrale dans la fonction de vraisemblance n'a pas d'expression analytique. Celle-ci doit alors être approximée par des algorithmes complexes.

Les premières méthodes développées consistent à approximer la vraisemblance par un développement de Taylor d'ordre 1 permettant de linéariser le modèle structural et d'en calculer la vraisemblance. Il existe plusieurs méthodes de linéarisation du modèle, la première méthode dite FO (*First-Order*) (Sheiner et al., 1972), linéarise le modèle en l'espérance des effets aléatoires alors que la méthode FOCE (*First-Order Conditional Estimate*) (Lindstrom et Bates, 1990) le linéarise autour des estimations individuelles des effets aléatoires. Combinées à un algorithme itératif tel que l'algorithme de minimisation de Newton-Raphson (minimiser la log-vraisemblance revient à maximiser la vraisemblance), ces méthodes permettent de calculer la vraisemblance par rapport à un vecteur de paramètres donné et de converger vers les estimations finales des paramètres de population. Cependant ces méthodes peuvent produire des estimateurs biaisés des paramètres de population notamment lorsque la variance des effets aléatoires est grande (Ge et al., 2004). Pour pallier à cette limite, une méthode de calcul de la vraisemblance par approximation de Laplace a été proposée (Wolfinger, 1993). Ces méthodes sont toutes implémentées dans les logiciels NONMEM® (Sheiner et Beal 1998), SAS® et R au travers des packages nlme et lme4 (Pinheiro et Bates, 2000).

Ces trois méthodes partagent le même inconvénient : elles maximisent une vraisemblance approchée par linéarisation du modèle. Plus récemment, des méthodes de calcul plus précises de la vraisemblance ont été proposées, notamment par approximation numérique ou stochastique. Ces méthodes présentent néanmoins l'avantage d'être moins dépendantes des valeurs initiales et de fournir des estimations plus précises des paramètres mais au prix d'un temps de calcul accru. L'une d'entre elles est l'algorithme itératif SAEM (*Stochastic Approximation Expectation Maximization*) développé par Delyon et al. en 1999 puis implémenté dans le logiciel MONOLIX® (Kuhn et Lavielle, 2005). La première étape dite E (*expectation*) se compose d'une simulation des effets aléatoires par une procédure de Markov de Monte-Carlo (étape S) suivie d'un calcul de l'espérance de la vraisemblance par approximation stochastique (étape A). Enfin, une deuxième étape dite M (*maximisation*) consiste à déterminer un vecteur de paramètres maximisant l'espérance de la vraisemblance et à l'utiliser lors de l'itération suivante (Delyon et al., 1999). L'algorithme SAEM figure parmi les algorithmes les plus performants et robustes bien que l'estimation soit sensible aux paramètres initiaux fournis (Plan et al., 2012). L'algorithme SAEM tel qu'implémenté dans MONOLIX a été utilisé pour estimer les paramètres des modèles développés dans le cadre de cette thèse.

Paramètres individuels

Une fois les paramètres de population obtenus, les paramètres individuels peuvent être calculés par une approche bayésienne (Casella, 1985). Dans cette approche, les paramètres des distributions *a priori* des paramètres individuels sont les paramètres de population lesquels sont combinés aux données individuelles afin de fournir une distribution *a posteriori*. La valeur individuelle du paramètre considéré ou EBE (*Empirical Bayes Estimate*) correspond le plus souvent au mode ou à la moyenne de la distribution *a posteriori*. Les prédictions du modèle structural effectuées avec ces paramètres permettent de reconstituer les profils individuels. Cependant, le manque de données individuelles donne plus de poids aux distributions *a priori* rapprochant artificiellement les estimations individuelles de celle de la population, on parle de régression vers la moyenne (η -shrinkage) (Savic et Karlsson, 2009).

Incertitude des paramètres

L'incertitude autour des paramètres estimés constitue un élément central de la construction d'un modèle. Cette incertitude se mesure au travers des erreurs standard (*standard errors*, SE) lesquels se calculent à partir de la matrice d'information de Fisher (*Fisher Information Matrix*, FIM). La FIM est la dérivée seconde de la vraisemblance observée tel que :

$$FIM(\Psi) = E \left\{ \frac{\partial LL(y; \psi)}{\partial \Psi} \frac{\partial LL(y; \psi)}{\partial \Psi}' \right\}$$

Les racines carrées des éléments diagonaux de FIM^{-1} donnent les SE des paramètres du modèle. De ces SE, les intervalles de confiance (IC) autour des paramètres sont données par la formule suivante :

$$IC_\alpha = [\hat{\theta} \pm z_{1-\alpha/2} SE(\hat{\theta})]$$

où $z_{1-\alpha/2}$ est le $(1 - \alpha/2)$ quantile d'une distribution normale. Les IC calculés à partir des SE données par la FIM sont symétriques car l'incertitude des paramètres suit une distribution normale. Bien que cela soit asymptotiquement le cas, certains modèles non linéaires peuvent s'éloigner des conditions asymptotiques de normalité, conduisant à des estimations des erreurs standard biaisées.

Evaluation du modèle

Pendant la construction d'un modèle, aussi bien structural que statistique, un modélisateur doit s'assurer d'une description adéquate des données par le modèle. Pour cela, divers outils et métriques diagnostiques ont été développés et appliqués aux modèles non linéaires à effets mixtes (Brendel et al., 2006). Les plus simples d'entre eux sont les outils graphiques qui permettent de détecter les manquements du modèle et d'orienter sur les causes sous-jacentes à ce manquement. Le premier examen à effectuer est celui des prédictions individuelles obtenues à partir des paramètres individuels (Simon, 2011). Une dynamique individuelle prédite proche des observations indique des bonnes performances du modèle. Cependant, les prédictions individuelles peuvent tendre vers les observations (η -shrinkage ou régression vers la moyenne) rendant la capture des données individuelles à elle seule insuffisante pour s'assurer de l'adéquation du modèle. On peut dès lors s'intéresser aux écarts entre les prédictions individuelles et les observations, appelés résidus. Les résidus peuvent être pondérés par la

matrice de variance-covariance et l'erreur résiduelle. On parle alors de IWRES (*Individual weighted residuals*) calculés pour chaque individu et à chaque temps tel que :

$$IWRES_{ij} = \frac{y_{ij} - f(t_{ij}, \theta_i, z_i)}{g(t_{ij}, \theta_i, z_i)}$$

Une représentation des IWRES en fonction du temps et des prédictions permet de détecter des tendances concernant l'erreur d'estimation (Lavielle, 2014).

Il existe d'autres méthodes d'évaluation de modèles basées sur la simulation. Le plus répandu est le VPC (*visual predictive check*) (Nguyen et al., 2017) qui représente les observations et les percentiles des simulations au cours du temps. Cependant, les VPC ne sont valables que lorsque l'ensemble de la population est décrit par les mêmes modalités d'une variable indépendante (dose, ethnique, sexe). Ainsi, une stratification des VPC pour chaque modalité de variable indépendante est possible (hommes vs. femmes, ...) mais entraîne une perte de puissance. Une alternative consiste à normaliser les VPC par la variabilité introduite par chaque variable indépendante : on parle alors de pcVPC (Bergstrand et al., 2011). Il existe d'autres métriques comme le pd (*prediction discrepancies*) (Mentré et Escolano, 2006) et les npde (Brendel et al., 2006) qui ne requièrent aucune stratification.

2.2.2. Sélection de modèles

Tests statistiques

Certaines métriques permettent de comparer des modèles et de sélectionner celui fournissant la meilleure description des données. Elles peuvent par ailleurs s'associer à un test statistique.

En effet, en considérant deux modèles se différenciant par un paramètre β , il est possible d'utiliser plusieurs tests pour conclure à l'avantage d'un modèle à l'autre. Sous l'hypothèse nulle on note : $H_0: \beta = 0$ et sous l'hypothèse alternative $H_1: \beta \neq 0$.

On détaillera ci-dessous deux tests : le test de Wald et le test du rapport de vraisemblance.

Le test de Wald se définit par sa statistique de test $W = \frac{\hat{\beta}}{SE(\hat{\beta})}$ où $\hat{\beta}$ est l'estimation de β et $SE(\hat{\beta})$ son erreur standard estimée. L'hypothèse nulle H_0 est rejetée si $|W| > \phi^{-1}(1 - \alpha/2)$ où ϕ^{-1} est la fonction quantile de la loi normale centrée-réduite.

Le test du rapport de vraisemblance (noté LRT pour *likelihood ratio test*) est défini par $LRT = -2[LL(\hat{\theta}_0) - LL(\hat{\theta})]$ avec respectivement $LL(\hat{\theta}_0)$ et $LL(\hat{\theta})$ les fonctions de log-vraisemblance du modèle de référence et du modèle alternatif à tester. Sous l'hypothèse nulle, ce test suit asymptotiquement un loi du χ^2 à m degré de liberté où m est le nombre de paramètres différents entre les deux modèles. Il est à noter que le LRT nécessite d'ajuster les données sous deux modèles entraînant un temps de calcul important. Dans le logiciel MONOLIX, le calcul de la vraisemblance s'effectue par *Importance Sampling* permettant d'estimer l'erreur standard de la log-vraisemblance. Le test de Wald et le LRT font figures de tests de référence pour comparer deux modèles emboîtés mais ceci constitue également leur principale limite.

Critères d'information

Pour comparer deux modèles qui ne sont pas emboîtés, on utilise généralement des critères d'information dérivés de la log-vraisemblance. Deux d'entre eux sont couramment utilisés dans les modèles non linéaires à effets mixtes : l'AIC et le BIC. L'AIC (*Akaike's Information Criteria*) se définit par $AIC = -2LL(\hat{\theta}) + 2n_{par}$ avec n_{par} le nombre de paramètres du modèle considéré. Le BIC (*Bayesian Information Criteria*) emploie une pénalisation de la vraisemblance plus complexe dépendant du nombre total de sujets N considérés tel que : $BIC = -2LL(\hat{\theta}) + n_{par} \log(N)$. De façon générale, le modèle fournissant le critère d'information le plus petit dans l'absolu est meilleur. Il est cependant couramment admis qu'une différence de moins de deux points entre deux modèles ne justifie pas l'utilisation d'un modèle plutôt qu'un autre (Raftery, 1995). Il est à noter que le BIC a tendance à sélectionner des modèles plus parcimonieux que l'AIC.

2.2.3. Incertitude liée au modèle et *model averaging*

Bien que l'utilisation de modèles non linéaires à effets mixtes ait facilité l'estimation des paramètres des modèles de cinétique virales, ceux-ci se caractérisent souvent par un manque d'identifiabilité théorique ou pratique (Guedj et al., 2007; Lavielle et Mentré, 2007). De plus, l'utilisation d'algorithmes d'estimation de plus en plus performants s'est accompagnée d'une augmentation de la complexité des modèles, laquelle n'est pas toujours justifiée au regard des données disponibles (Ganusov, 2016).

En cinétique virale, une façon de diminuer le nombre de paramètres à estimer consiste à fixer certains paramètres à des valeurs de la littérature et d'évaluer subséquemment l'impact des valeurs retenues sur les estimations de paramètres au travers d'une analyse de sensibilité. D'autre part, des modèles de complexité variable faisant différentes hypothèses biologiques peuvent aussi être utilisés pour décrire un même jeu de données. Dans les deux cas, l'approche courante consiste à sélectionner le modèle fournissant le plus faible AIC ou BIC, et de l'utiliser à des fins de prédiction. Cette approche, en se focalisant sur un unique modèle, ignore l'incertitude liée aux différents modèles testés ce qui peut conduire à des prédictions erronées ou à un trop grand degré de confiance dans les paramètres estimés (Boulesteix, 2015; Kirk et al., 2015).

Pour pallier à ces limites et prendre en compte l'incertitude liée aux modèles testés il est possible d'utiliser le *model averaging* (MA) (Buckland et al., 1997). Cette approche consiste à pondérer les modèles en fonction d'un critère d'information IC (voir section Critères d'information) tel que :

$$w_m = \frac{e^{\frac{-IC_m}{2}}}{\sum_1^M e^{\frac{-IC_m}{2}}}$$

avec w_m le poids que l'on accorde au modèle m compte tenu de son critère d'information IC_m (Aoki et al., 2017; Buatois et al., 2018). Les poids ainsi déterminés rendent compte de la vraisemblance du modèle. En effet, le modèle candidat fournissant l' IC le plus faible sera associé au poids le plus important. Pondérer ainsi les différents modèles candidats permet de calculer les intervalles de confiance de paramètres en prenant en compte l'incertitude liée au modèle. De plus, MA connaît des applications dans les études de recherche de dose et rend compte de l'incertitude liée au choix d'une dose efficace (Schorning et al., 2016; Bornkamp et al., 2017).

2.3. Objectifs de la thèse

L'objectif principal de cette thèse est d'étudier l'effet de thérapies antivirales innovantes. Pour cela nous avons développé des modèles mécanistiques du VHB, plus proches de sa physiopathologie et permettant la prise en compte des marqueurs autres que l'ADN VHB. Nous

avons étudié deux nouvelles classes thérapeutiques : un agoniste du TLR7, qui interfère avec la réponse immunitaire par la voie de l'IFN α , ainsi qu'un inhibiteur de capsid, ciblant les particules encapsidées. Enfin cette thèse aura aussi pour objectif de répondre à la complexité croissante des modèles de cinétique virale en développant des aspects méthodologiques permettant de prendre en compte l'incertitude liée au modèle.

Dans un premier temps, nous étudierons l'effet des agonistes de TLR7 chez la souris (Chapitre 3). Nous développerons la construction d'un modèle complexe reposant sur plusieurs marqueurs : l'ADN viral, les sous-particules virales et les anticorps anti-AgHBs. Après validation, le modèle sera utilisé pour fournir des prédictions des effets attendus dans les premières études chez l'homme.

Dans un second temps, nous présenterons les résultats de la modélisation simultanée des particules d'ARN et d'ADN chez des patients traités par RG7907, un inhibiteur de capsid actuellement testé chez l'homme. Nous fournirons une compréhension mécanistique des déclins d'ADN et d'ARN observés sous traitement ainsi qu'une évaluation de l'efficacité de cette molécule (Chapitre 4).

Enfin, nous présenterons le *model averaging*, une approche prenant en compte l'incertitude inhérente aux modèles utilisés en cinétique virale. Les estimations des paramètres et performances prédictives du *model averaging* seront comparées à celles fournies classiquement par la sélection de modèle (Chapitre 5).

La suite de ce manuscrit présente ces trois travaux de thèse et les articles qui leur sont associés. Une discussion mettant en perspective cette thèse prendra place dans le Chapitre 6.

Chapitre 3. Modélisation de l'effet des agonistes du TLR7 chez la souris et prédition de son efficacité chez l'homme

3.1. Résumé

Dans l'infection au VHB, le système immunitaire de l'hôte est déficient et incapable de prendre en charge seul l'infection. En cause, les sous particules virales (SVP) produites en large excès qui agissent comme leurre auprès du système immunitaire. Les agonistes du *toll-like* récepteur 7 (TLR7) sont des immunomodulateurs qui, en induisant la production d'interféron- α , restaureraient un contrôle de l'infection menant à une diminution de la virémie et de l'AgHBs.

Dans ce projet, nous avons étudié les effets du RO7020531, un agoniste du TLR7 testé chez la souris. Dans un premier temps, nous avons estimé les effets antiviraux chez 118 souris traitées par RO7020531 et/ou entecavir (ETV) pendant une période comprise entre 6 à 9 semaines. Dans le modèle développé, l'agoniste du TLR7 induit non seulement une diminution de la production d'ADN VHB (comme les NUC), mais il agit aussi directement sur la production de SVP, avec une efficacité estimée supérieure à 98%. De plus, l'agoniste du TLR7 conduit à une stimulation spécifique du système immunitaire, menant à une augmentation des concentrations d'anticorps anti-HBs qui deviennent détectables après 7 semaines de traitement. Le modèle murin utilisé est un modèle d'adénovirus transfecté par le VHB dit modèle AAV/HBV (Huang et al., 2011; Yang et al., 2014). Contrairement au modèle uPA-SCID, les souris sont immunocompétentes ce qui permet l'étude de la réponse immunitaire sous traitement. Cependant ce modèle possède des limites qui ne permettent pas de transposer les résultats obtenus directement à l'homme. Contrairement à l'infection humaine, l'ensemble des cellules hépatiques des souris sont infectées dès l'initiation de l'expérimentation et les virus produits *de novo* ne peuvent pas infecter de nouvelles cellules saines.

Afin de pallier à ces limites nous avons dans un second temps décrit l'infection humaine chez des patients traités par Peg-IFN pendant 48 semaines pour lesquels nous disposions des données de virémie et d'AgHBs. Le modèle développé se distingue du modèle standard de cinétique virale (voir section 2.1.1.) en intégrant deux populations de cellules infectées. Nous distinguons

les cellules I_1 productrices de virus et de *SVP* disposant d'ADN intégré et de *cccDNA* et les cellules I_2 qui ont perdu leur *cccDNA* et ne produisant que des *SVP*. Le modèle ainsi développé permet de capturer les différences de cinétique entre la virémie et l'AgHBs. En effet, nous avons estimé une demi-vie de 23,6 jours pour les cellules I_1 contre 170 jours pour les cellules I_2 , expliquant ainsi la persistance de l'AgHBs au long cours.

En supposant la même relation concentration-effet que chez la souris, nous avons simulé l'effet de cette nouvelle molécule chez l'homme seule ou en combinaison. Nous montrons notamment que la combinaison ETV+TLR7 pourrait conduire à des titres d'AgHBs indétectables chez 22% des patients en 1 an contre 8% seulement chez les patients traités par ETV. Par ailleurs, une simulation des cinétiques au long cours montre que les agonistes du TLR7 peuvent conduire à un déclin supplémentaire de la virémie et de l'AgHBs *via* l'augmentation des titres d'anticorps.

L'article décrivant ces travaux est finalisé et fera l'objet d'une soumission dans un journal de pharmacométrie au courant du premier trimestre 2021.

3.2. Article 1: A modeling framework to understand the effect of TLR7 agonists against Hepatitis B virus and predict its efficacy in clinical trial

A modeling framework to understand the effect of TLR7 agonist against Hepatitis B Virus and to predict its efficacy in clinical trials

Antonio Gonçalves¹, Annabelle Lemenuel-Diot², Lu Gao³, Lue Dai³, Ruben Alvarez-Sánchez
R.², Joseph F. Grippo⁴, and Jérémie Guedj¹

¹INSERM, IAME, UMR 1137, F-75018 Paris, France; Université Paris Diderot, Sorbonne Paris
Cité, Paris, France

²Roche Pharmaceutical Research and Early Development, Pharmaceutical Sciences, Roche
Innovation Center Basel

³Roche Pharmaceutical Research and Early Development, Disease Therapeutic Area Infectious
Diseases, Roche Innovation Center Shanghai

⁴Roche Pharmaceutical Research and Early Development, Pharmaceutical Sciences, Roche
Innovation Center New York

Corresponding author: Antonio Gonçalves, antonio.goncalves@inserm.fr

INSERM U1137,
16 rue Henri Huchard 75018, Paris, France
Tel: +33 1 57 27 75 39

Abstract

One of the main obstacles to cure Hepatitis B virus (HBV) is its ability to escape the host immune system through the release of subviral particles (SVPs). Toll-like receptor 7 (TLR7) agonists have developed to boost the immune response and increase the elimination of SVPs. Here, we modelled the effects of TLR7 agonist (aTLR7) administered in mice using a viral dynamic model. We found that aTLR7, unlike current therapies, can inhibit SVPs production and directly stimulate antibody production. We then plugged the parameters of aTLR7 efficacy into a model of HBV pathogenesis in human estimated in a large historical clinical database. Using this model, we predict that aTLR7 could lead to loss of HBsAg in about 20% of patients after a year of treatment, assuming that the effective concentration remains above 10% of their value in mice.

Introduction

Nearly 240 million people worldwide are chronically infected with hepatitis B virus (HBV)¹, and about 1 million people die from HBV-related liver disease, in particular cirrhosis and hepatocellular carcinoma². With the current recommended treatment of nucleosidic reverse transcriptase inhibitors (NRTIs), viremia is controlled in a large majority of patients but other viral products (in particular HBsAg) continue to be produced³, which shows that infected cells remain transcriptionally active. Therefore, treatment needs to be taken lifelong to avoid viral resurgence and progression of the disease.

The difficulty to cure HBV is due to the presence of viral DNA that either integrates the cell genome or forms covalently closed circular DNA (*cccDNA*), both of which can code for various viral products and are not targeted by NRTIs. These viral products, including HBsAg, are produced in large excess compared to viral DNA. Those viral products can form subviral particles (SVPs) which are poorly or not infectious but act as a decoy for the immune system⁴.

Antiviral research in HBV is very active and several new therapeutic approaches are currently being developed. One promising area of research is to develop drugs that stimulate the immune response (immunomodulators) to reduce its tolerance to HBV and possibly destabilize *cccDNA*. We here focus on an agonist of the toll-like receptor 7 (aTLR7), which stimulates the innate

immune system and induces the production of type I interferons and cytokines⁵. This stimulation may also, directly or indirectly, stimulate B lymphocytes and induce the production of anti-HBsAg. GS-9620, a previous and first in class TLR7 agonist, showed promising results in a chimpanzee and in a woodchuck model, with a prolonged reduction of HBV DNA⁶, a reduction in HBsAg levels and an induction of immune effector cells. Unfortunately, these effects could not be confirmed in clinical trials, and no significant changes in HBsAg or HBV DNA levels were observed⁷.

Following what has been done in other chronic viral infections⁸, important insights on a drug mechanism of action (MoA) and translation of preclinical findings can be obtained by mathematically modelling the response to treatment. Here we propose the first model describing the effect of a novel TLR7 agonist using data obtained in mice either in monotherapy or in combination with entecavir (ETV). To allow translation of these results, key parameter of HBV pathogenesis in humans are estimated using a database of 255 individuals treated with pegylated interferon (Peg-IFN). The understanding of HBV pathogenesis in human was then used to bridge the preclinical data and predict the kinetics of HBV DNA, HBsAg and anti-HBsAg in humans exposed to different exposure levels of aTLR7, alone or in combination with ETV.

Material & methods

Data

Mice

AAV/HBV model. We used the AAV/HBV mice model, where immunocompetent C57BL/6 mice are infected by a hepatotropic adeno-associated virus harboring a replicable HBV genome, allowing infection of virtually all hepatocytes⁹ and large levels of production of virions, HBs and HBe antigens. As mice lack NTCP receptor, the released virions cannot infect cells, and thus, there are no *de novo* infections.

Study designs. Studies were conducted by Roche Pharmaceutical Research and Early Development (pRED) in 4 separate experiments, leading to a total of 118 mice (Figure 1). Different dosing regimens of aTLR7 in monotherapy were tested (30 and 100 mg.kg⁻¹, every

week, QOD and 100 and 300 mg.kg⁻¹, every other day, QW). Two dosing regimens were tested for ETV (0.03 mg.kg⁻¹ QD or 0.3 mg.kg⁻¹ QOD) either alone or in combination with aTLR7. The treatment periods ranged from 42 to 63 days and the follow-up periods from 42 to 91 days.

Virology and serology. HBV DNA and HBsAg were measured once a week throughout the study duration (Figure 2A). HBV DNA was quantified by quantitative PCR (qPCR) using a Taqman qPCR machine, LC480, (Roche, Basel), with an associated lower limit of quantification (LLOQ) equal to 4.3 log₁₀ copies.mL⁻¹, and HBsAg was quantified by chemiluminescence immunoassay kits (CLIA) from Autobio (Zhengzhou, China), LLOQ = 1.8 log₁₀ ng.mL⁻¹. Anti-HBsAg antibodies were dosed once a week by CLIA starting from week 3. The LLOQ of the assay was 100 ng.mL⁻¹.

Pharmacokinetics. We assumed that drug concentrations were constant over dosing interval and we derived average concentrations, noted \tilde{C} , as follows. For ETV, \tilde{C} was obtained using published data in rats where the PK was found linear and doses of 0.105 mg.kg⁻¹ QD led to average concentrations 2.187 ng.mL⁻¹¹⁰. Accordingly we assumed that doses of 0.03 mg/kg QD and 0.3 mg/kg QOD led to \tilde{C} equal to 0.625 and 3.125 ng.mL⁻¹, respectively. Regarding aTLR7, pharmacokinetic data were available in 32 animals and were obtained at either 0.25, 0.5, 1 or 4 hours post administration, at both days 14 and 42, allowing us to calculate \tilde{C} for each dosing regimen. These values were assumed to be similar for all animals receiving the same dosing regimen, namely 71, 108, 108, and 243 ng.mL⁻¹ in animals treated with 100 mg.kg⁻¹ QW, 30 mg.kg⁻¹ QOD, 300 mg.kg⁻¹ QW, and 100 mg.kg⁻¹ QOD, respectively.

Human

Study design. The clinical trial (NCT00048945) was conducted by Roche Pharmaceutical Research and Early Development (pRED) in 255 HBV chronic and HBeAg positive patients whom received 180 µg of Peg-IFN QW during 48 weeks and were followed for 26 weeks after treatment cessation.

Population characteristics and results. Baseline characteristics of the patients are reported in Supplementary Table S1. Undetectable HBV DNA was obtained in 24.2% of patients at the end of treatment, but only 12.1% had undetectable viremia at the end of the follow-up period. No patient achieved undetectable level of HBsAg during the study.

Modélisation de l'effet des agonistes du TLR7 chez la souris et prédition de son efficacité chez l'homme

Virology and serology. HBV DNA was measured using a Taqman qPCR machine, LC480, Roche, LLOQ = 1.57 log₁₀ copies.mL⁻¹. HBsAg was quantified by CLIA, with LLOQ = 0.05 ng.mL⁻¹ whereas anti-HBsAg antibodies were not measured during the study. As none of the patient achieved undetectable HBsAg, we considered that anti-HBsAg remained undetectable throughout the study period. A subset of observed individual profiles, randomly selected, are presented in Figure 2B.

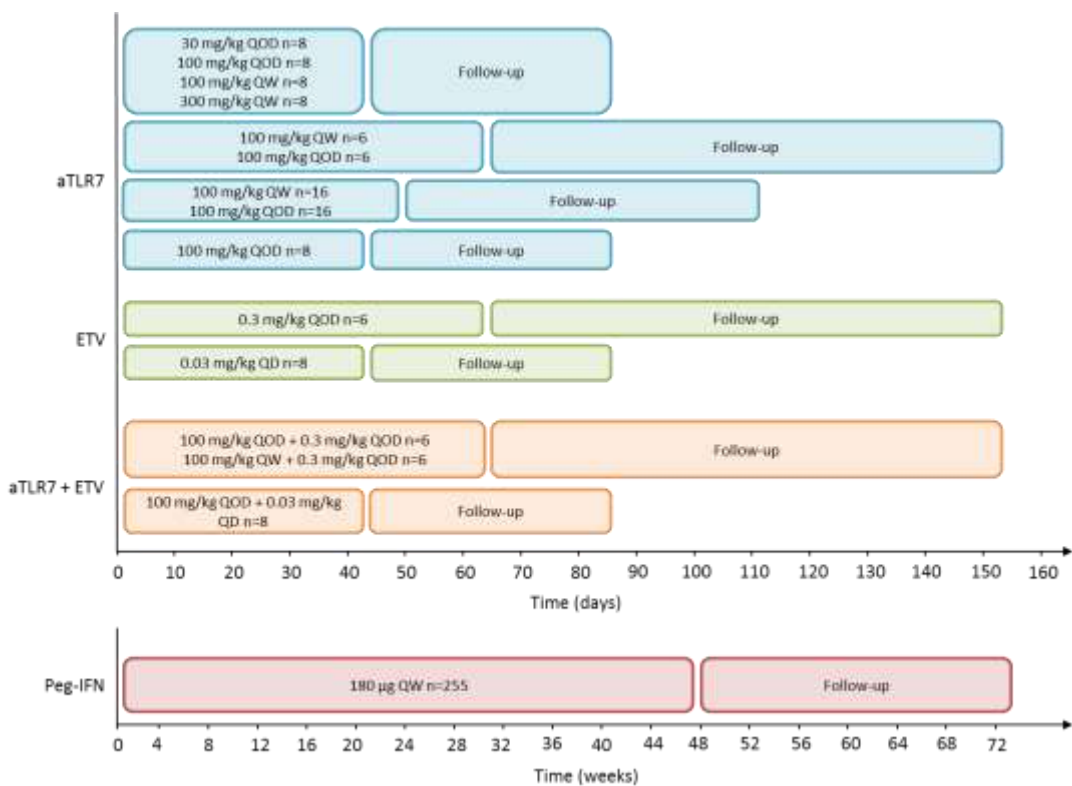


Figure 1. Design of the studies used for modeling in mice (top) and humans (bottom).

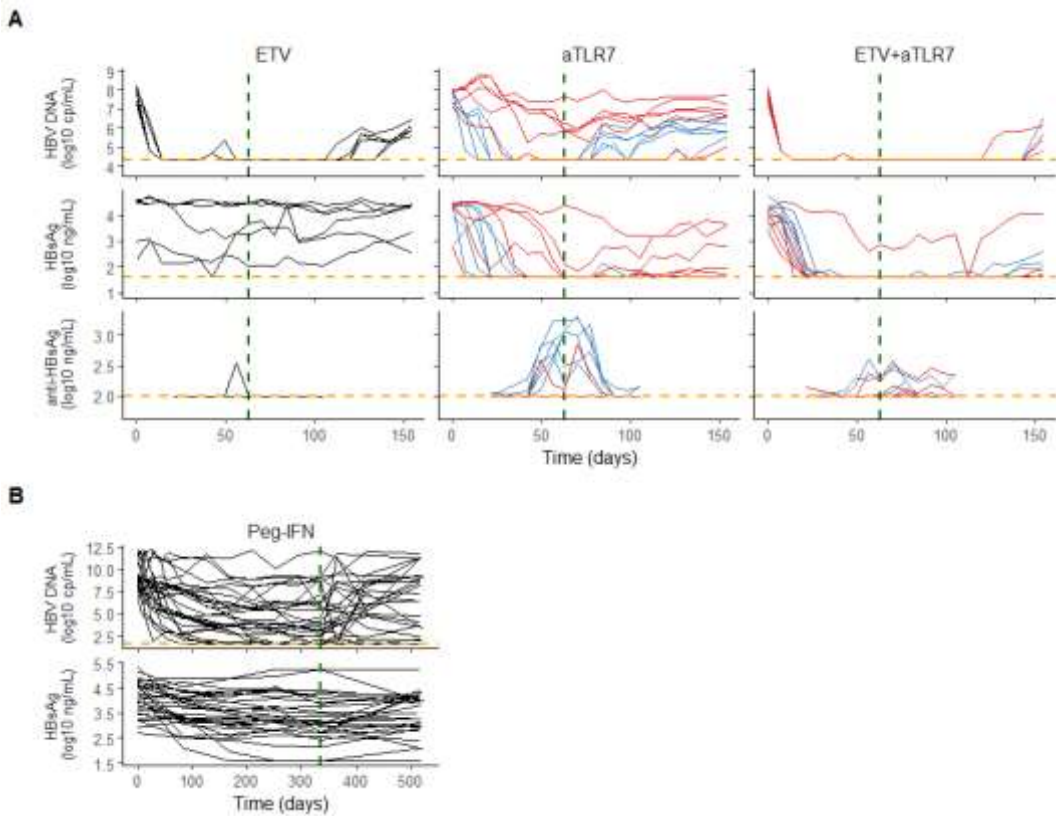


Figure 2. Observed kinetics of HBV markers. A. HBV DNA, HBsAg and anti-HBsAg in AAV infected mice treated with ETV (left column), aTLR7 (middle) and aTLR7+ETV (right). Colors represent the different dose levels of aTLR7 (red, 100 mg/kg QW; blue, 100 mg/kg QOD). B. Longitudinal changes in HBV DNA and HBsAg in representative individuals treated with Peg-IFN for 48 weeks. Dotted green line indicates the end of the treatment period; dotted orange line indicates the lower limit of quantification (LLOQ).

Data analysis

Viral dynamic model

Viral dynamics during and after treatment was characterized using a model inspired from Ciupé et al¹¹. The model considers uninfected hepatocytes (T) that can be infected (I) at rate β , and I are then cleared with rate δ . The loss rate of uninfected cells was assumed to be negligible and set to 0 given the long half-life of hepatocytes. We assumed that all cells can proliferate at rate r , and we assumed that proliferation of one infected cell led to one uninfected cell and one

infected cell¹². Infected cells produce both viral and subviral particles (noted V and S, respectively) at rates p_V and p_S , respectively. Free V and S are cleared at similar rate c . Further, antibodies (noted A) are produced at an antigen dependent rate ρ and bind to V or S, leading to the formation of V-A and S-A complexes, noted X_V and X_S , at a rate γ . Free antibodies can be cleared from circulation at a rate σ whereas X_V and X_S complexes can either be eliminated at a similar rate c_A or dissociate with rate k . A particularity of HBV resides in the fact that intermediate forms of HBV DNA can integrate the host genome¹³ that also contribute to the production HBsAg^{14,15}. As the integration process starts rapidly after infection¹⁴ we supposed that all infected cells harbored both *cccDNA* and integrated DNA at time of treatment initiation. Under treatment, the *cccDNA* can be lost or partially silenced through the action of IFN- α ¹⁶ at a rate δ_2 thus leading to cells which can still produce S but not complete virions. We supposed 3 hypothetical mechanisms of action for ETV and aTLR7: 1) reduce viral production (with efficacy ε_V) ; 2) reduce S production (with efficacy ε_S) and 3) stimulate antibody production (with efficacy ε_A). The model dynamics is summarized by the following equations:

$$\begin{aligned}
 \frac{dT}{dt} &= r(T + I + I_2) \left(1 - \frac{(T + I + I_2)}{T_{max}}\right) - \beta V T \\
 \frac{dI}{dt} &= \beta V(T + I_2) - \delta I - \delta_2 I \\
 \frac{dI_2}{dt} &= \delta_2 I - \beta V I_2 - \delta I_2 \\
 \frac{dV}{dt} &= p_V(1 - \varepsilon_V)I - cV - \gamma A V + k X_V \\
 \frac{dS}{dt} &= p_S(1 - \varepsilon_S)(I + I_2) - cS - \gamma A S + k X_S \\
 \frac{dA}{dt} &= \rho(V + S) + \varepsilon_A \left(1 - \frac{A}{A_{max}}\right) A - \gamma A(V + S) + k(X_V + X_S) - \sigma A \\
 \frac{dX_V}{dt} &= -k X_V + \gamma A V - c_A X_V
 \end{aligned} \tag{1}$$

$$\frac{dX_S}{dt} = -kX_S + \gamma AS - c_A X_S$$

Approximated steady-state equilibrium solutions (1) are given in Supplementary Material 1 and a schematic representation of the model is provided in Figure 3.

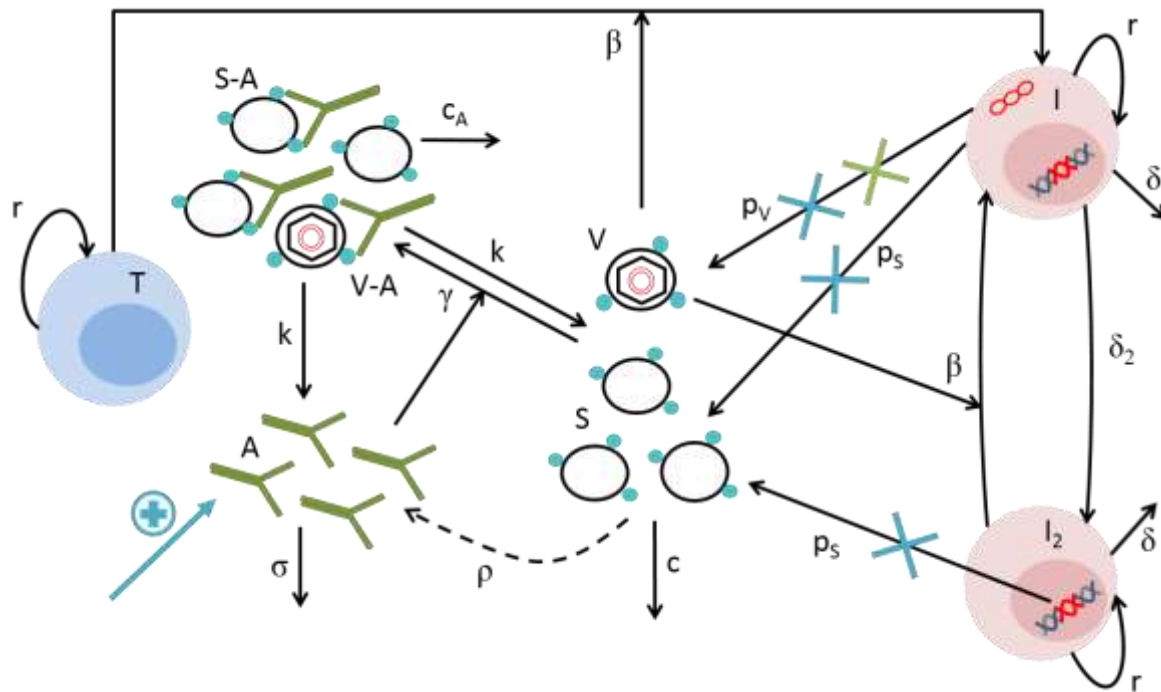


Figure 3. Schematic representation of the mechanistic model of HBV. Uninfected hepatocytes, T, are infected at rate β . Once infected (I), cells produce both viral (V) and subviral particles (S) at rates p_V and p_S , respectively, which are then cleared with rate c . Anti-HBsAg antibodies, A are produced at an antigen dependent rate ρ and bind to V or S, leading to the formation of V-A and S-A complexes, at a rate γ , that are then cleared with rate c_A or dissociate with rate k . During treatment cccDNA can be lost or silenced with rate δ_2 , leading to cells (I₂) that only produce subviral particles but not complete virions. Blue crosses represent the action of the TLR7 agonist on blocking the viral and subviral production and stimulating the production of antibodies. Green cross represents the action of ETV blocking the viral production.

Adjusting the viral dynamic model to the AAV mice model

Since the virus is injected in large excess, we assumed that all hepatocytes were infected at the initiation of treatment, *i.e.*, $T_0=0$ and $I_0=10^6$ cells.mL⁻¹ (corresponding to mice liver size¹⁷) and

that no *de novo* infection occurred ($\beta=0$, see above). The low signal on interferon stimulating genes (ISG, see Supplementary Materials 2) and the return of HBV DNA and HBsAg to their pre-treatment levels suggested that there was no permanent loss of *cccDNA*. Hence, we set δ_2 to 0. Parameter δ was estimated by linear regression in the vehicle group using both HBV DNA and HBsAg kinetics, i.e., 0.0056 d^{-1} (not shown). Steady-state equilibrium solutions of this simplified model are presented in Supplementary Materials 1.

Conversion factors to fit the model to HBsAg data

We assumed that V and S harbored 96 molecules of HBsAg at their surface⁴. Therefore the total number of circulating HBsAg in ng per mL of serum is given by $H=96\times(V+S)$. We then used the molecular mass of one HBsAg molecule ($24,000\text{ g.mol}^{-1}$) and the Avogadro constant (6.022×10^{23}) to convert to the data units.

Drug efficacy

ETV & aTLR7 treatment. ETV was assumed to act only on HBV DNA production with efficacy $\varepsilon_V^{ETV} = \frac{\tilde{C}}{\tilde{C} + EC_{50,V}^{ETV}}$, where $EC_{50,V}^{ETV}$ is the ETV concentration leading to half the maximal effect. As ETV did not act on HBsAg and anti-HBsAg, we set $\varepsilon_S^{ETV} = \varepsilon_A^{ETV} = 0$.

For aTLR7, we assumed 3 putative independent mechanisms of action:

aTLR7 blocks HBV DNA production, with an effectiveness $\varepsilon_V^{TLR7} = \frac{\tilde{C}}{\tilde{C} + EC_{50,V}^{TLR7}}$.

aTLR7 blocks S production, ps, with an effectiveness $\varepsilon_S^{TLR7} = \frac{\tilde{C}}{\tilde{C} + EC_{50,S}^{TLR7}}$.

aTLR7 stimulates B-cell production and induces the production of antibodies with effectiveness $\varepsilon_A^{TLR7} = \frac{E_{max}\tilde{C}}{\tilde{C} + EC_{50,A}^{TLR7}}$.

where $EC_{50,V}^{TLR7}$, $EC_{50,S}^{TLR7}$ and $EC_{50,A}^{TLR7}$ are the drug concentrations leading to half the maximal effect. Of note, since the proliferation is a biological mechanism, we assumed that it could not exceed a level noted E_{max} . In a second step, we verified that hill coefficients did not improve

the data fitting (see Model building section below). Further a lag-effect was included to take into account the delay between initiation and effect of the treatment, noted $T_{lag,V}$ and $T_{lag,S}$ for the effects on V and S production, respectively.

Peg-IFN treatment. Peg-IFN blocked the viral production with an efficacy noted ε_V^{Peg} comprised between 0 and 1. In order to take into account the time needed for Peg-IFN pharmacokinetics to achieve steady-state we used the following empirical model to account for an increasing time-dependent effect $\varepsilon_V^{Peg}(t) = \varepsilon_{max}^{Peg} \times (1 - e^{-k_i t})$ with k_i the rate of increase in drug efficacy and ε_{max}^{Peg} is the maximal efficacy that can be achieved.

Drug efficacy after the end of treatment. We assumed that all drug concentrations declined exponentially after treatment cessation¹⁸, leading to $\frac{\varepsilon e^{-\alpha(t-t_{end})}}{1 - \varepsilon + \varepsilon e^{-\alpha(t-t_{end})}}$ where ε is the drug efficacy at the end of treatment, t_{end} , and α is the drug specific clearance rate, estimated on the data.

Drug combination. Combination of ETV and aTLR7 on viral production was modelled using a Loewe additivity model¹⁹.

Fixed parameter values

Given the fact that only few animals had detectable anti-HBsAg and that no antibody data were seen in humans, a number of antibody-related parameters were fixed to ensure identifiability. The dissociation rate constant of complexes k was set equal to 10 d^{-1} ¹¹. Parameter c_A was fixed to 4 times the value of the viral clearance noted c ¹¹, reflecting that the elimination of complexes was faster than the elimination of unbound viral or subviral particles. A_{max} is the maximal amount of anti-HBsAg that can be produced under stimulation of aTLR7. Assuming that no more than 10% of total antibodies in circulation can be HBsAg specific¹¹, that the titer of antibodies in C57BL/6 mice is about 4 mg/mL ²⁰ and 10 mg/mL ¹¹ in humans and the molecular mass of an antibody is $150000 \text{ g.mol}^{-1}$ we obtained that $A_{max} = 1.6 \cdot 10^{15} \text{ molecules.ml}^{-1}$ in mice and $4 \cdot 10^{15} \text{ molecules.ml}^{-1}$ in humans. Parameters γ and σ which were fixed to 10^{-12} d^{-1} and 0.1 d^{-1} , respectively^{11, 21} (Table 1).

Parameter estimation

The model for the observation was given by:

$$Y_{ijk} = f(t_{ijk}, \theta_i) + \varepsilon_{ijk}$$

Where Y_{ijk} is the log-concentration of the k^{th} biomarker ($k=1,2,3$) for subject i at the j -th timepoint, t_{ijk} . θ_i is the vector of individual parameters which follows a log-normal distribution with mean μ and variance ω_i^2 to account for between-individuals variability. For effectiveness parameters, logit-normal distributions were used to constraints parameters between 0 and 1. The residual error ε_{ijk} was assumed to follow a normal distribution centered on zero and constant variance σ_k^2 .

Modelling building strategy in mice

First, we estimated the hill coefficients (n_V^{ETV}, n_V, n_S and n_A) associated to the concentration effect relationships of ETV and aTLR7. If the estimated CI_{95%} of the parameter included 1, we set them to 1. The following set of parameters was finally estimated using mice studies: $\theta_{mice} = \{c, \delta, p_V, p_S, \rho, EC_{50,V}^{ETV}, n_V^{ETV}, EC_{50,V}^{TLR7}, n_V, EC_{50,S}^{TLR7}, EC_{50,A}^{TLR7}, E_{max}, \alpha_V, \alpha_S, \alpha_A, T_{lag,V},$

and $T_{lag,S}\}$. A forward selection was used to select hill coefficients and random effects and the procedure stopped once the Bayesian Information Criteria (BIC) did not decrease by more than 2 points. After the most parsimonious model was found, we tested correlation between drug-related parameters ($EC_{50,V}^{ETV}, EC_{50,V}^{TLR7}, EC_{50,S}^{TLR7}, EC_{50,A}^{TLR7}$). We first screened all potential correlations on the EBEs using a Spearman correlation test. When the p-value was below 0.2, we implemented the correlations in the model and retained the correlation when the BIC was lowered by more than 2 points. Because the correlation coefficient between $EC_{50,V}^{TLR7}$ and $EC_{50,S}^{TLR7}$ was greater than 0.8, we parameterized $EC_{50,S}^{TLR7} = \lambda \cdot EC_{50,V}^{TLR7}$. Finally, we tested a potential difference in efficacy parameters between mice treated with aTLR7 alone and those treated with aTLR7+ETV. Consistent with what was done for the random effects, we first screened the EBEs of the parameters in individuals treated with monotherapy and those receiving combination. When the p-value of the Wilcoxon test was below 0.2, we tested in the model a potential combination effect on the efficacy related parameters using a Wald test. A similar strategy was used to estimate viral dynamic parameters in humans treated with Peg-IFN and the following parameters were estimated $\theta_{humans} = \{r, R_0, \delta, \delta_2, p_V, p_S, \varepsilon^{Peg}, k_i \text{ and } \alpha_V\}$ where R_0 the basic reproduction number associated to the model, i.e. $R_0 = \frac{\delta c}{\beta p_V T_{max}}$.

Final models evaluation relied on graphical diagnosis such as individual predicted profiles, individual weighted residuals (IWRES) and normalized prediction distribution errors (NPDE) versus time and predictions. A subset of individual profiles were randomly selected before the analysis of the data to serve as illustration of the quality of the data fitting. Prediction corrected visual predictive checks (pcVPC) were performed for each biomarker and for each study²².

Simulations of aTLR7 effect in humans

We simulated time course profiles of virions, HBsAg and anti-HBsAg under 3 strategies: ETV alone, aTLR7 alone or aTLR7+ETV during 2 years. For that purpose we used the disease parameter values estimated during Peg-IFN treatment and drug related parameters of aTLR7 and ETV estimated in mice (Table 1). In order to evaluate the effect of lower or less frequent dosing regimen of aTLR7 in humans as compared to what was used in mice, we considered 4 different levels of drug concentrations (or, more precisely, 4 different values for the ratio of the plasma concentration to the drug EC₅₀) and equal to \tilde{C}_{mice} , $\tilde{C}_{\text{mice}}/2$, $\tilde{C}_{\text{mice}}/5$ and $\tilde{C}_{\text{mice}}/10$ where \tilde{C}_{mice} is the average drug concentration in mice treated with the highest dosing regimen (eg, 100 mg.kg⁻¹ QOD). For ETV, we used $\tilde{C}=0.617 \text{ ng.mL}^{-1}$ which corresponds to the average concentration at the recommended dose of 0.05 mg QD²³. For each scenario 200 trials of 50 individuals were simulated and we reported the median and 90% prediction interval (IP_{90%}) of the percentage of patients that will reached undetectable HBV DNA, HBsAg, with undetectability defined as <1.57 log₁₀ copies.mL⁻¹ and <0.05 ng.mL⁻¹ respectively, and detectable anti-HBsAg (>100 ng.mL⁻¹).

Table 1. Parameter estimates used for simulations

	Parameter	Description	Fixed effect	SD random effect
Parameters fixed from mice experiments	$EC_{50,V}^{ETV}$ (ng.mL ⁻¹)	Concentration producing 50% of the effect of ETV on viremia	6.05.10 ⁻⁵	1.72
	n_V^{ETV}	Hill coefficient of the ETV concentration-effect relationship for viremia	1.19	-
	$EC_{50,V}^{TLR7}$ (ng.mL ⁻¹)	Concentration producing 50% of the effect of aTLR7 on viremia	3.23	2.70
	n_V^{TLR7}	Hill coefficient of the aTLR7 concentration-effect relationship for viremia	1.17	-
	λ	Scaling factor ($EC_{50,V} \rightarrow EC_{50,S}$)	0.0954	3.15
	ρ (molecules.d ⁻¹)	Antigen-dependent production rate of antibodies	0.00126	-
	E_{max}	Maximal effect of aTLR7 on antibodies	0.361	-
	$EC_{50,A}^{TLR7}$ (ng.mL ⁻¹)	Concentration producing 50% of maximal aTLR7 effect on antibodies	177	1.08
	$T_{lag,V}$ (d)	Lag time of aTLR7 on viremia	5.22	1.53
Parameters fixed from individuals treated with Peg-IFN	$T_{lag,S}$ (d)	Lag time of aTLR7 on SVPs	14.6	1.69
	r (d ⁻¹)	Hepatocyte maximum proliferation rate	0.186	1.85
	R_0	Basic reproduction number	121	4.51
	δ_1 (d ⁻¹)	Loss rate of infected cells	0.00395	1.35
	δ_2 (d ⁻¹)	<i>cccDNA</i> loss rate	0.025	0.59
	p_V (virion.cell ⁻¹ .d ⁻¹)	Viral production rate	156	3.87
	p_S (SVP.cell ⁻¹ .d ⁻¹)	Subviral particles production rates	1.96.10 ⁵	1.05
Fixed from literature	Corr p_V-p_S	Correlation between production rates	0.555	-
	c (d ⁻¹) ^a	Viral clearance rate	0.7	-
	A_{max} (molecules.mL ⁻¹) ^a	Antibody carrying capacity	4.10 ¹⁵	-
	k (d ⁻¹) ^a	Antibody dissociation rate	10	-
	c_A (d ⁻¹) ^a	Complex degradation rate	4c	-
	γ (d ⁻¹) ^a	Antibody binding rate	10 ⁻¹²	-
	σ (d ⁻¹) ^b	Antibody degradation rate	0.1	-

Graphical and computational methods

Parameters were estimated with the SAEM algorithm implemented in Monolix® software version 2016R1 64-bits. Likelihood was estimated by importance sampling and the Fisher Information Matrix (FIM) was calculated by stochastic approximation. Graphical and statistical analyses were performed using R version 3.3.3.

Results

HBV viral dynamics in mice treated with aTLR7 +/- ETV

The selected model could well fit the viral kinetics in all dosing regimen groups (Figure 4), with no detection of misspecification (see Supplementary Figures S1, S2 and S3). Parameter estimates are presented in Supplementary Table S2.

Both ETV and aTLR7 led to a reduction of HBV DNA. As expected, ETV led to a profound reduction of HBV DNA with $EC_{50,V}^{ETV} = 6.05 \cdot 10^{-5} \text{ ng.mL}^{-1}$ and $n_V^{ETV} = 1.19$, which corresponds to a reduction of nearly $5 \log_{10}$ in HBV DNA ($\varepsilon_V^{ETV} = 0.99998$ and 0.999998 at the dose of 0.03 mg.kg^{-1} QD and 0.3 mg.kg^{-1} QOD, respectively) but had no significant effect on S production or antibody stimulation. In contrast, aTLR7 had a lower efficacy on HBV DNA against ETV, with a $EC_{50,V}^{TLR7}$ of 3.23 ng.mL^{-1} and $n_V = 1.17$, corresponding to an efficacy of 98.4% and 99.4% at doses of 100 mg.kg^{-1} QW and 100 mg.kg^{-1} QOD, respectively. Unlike ETV, aTLR7 also reduced subviral production with an estimated $EC_{50,S}^{TLR7}$ equal to 0.308 ng.mL^{-1} , corresponding to an effect of 99.71% and 99.87% at doses of 100 mg.kg^{-1} QW and 100 mg.kg^{-1} QOD, respectively, and leading to a 2.5 log reduction in HBsAg levels after few weeks of treatment. Boxplots of individual efficacies per dose groups and biomarkers are reported in SM1 Figure S4.

Modélisation de l'effet des agonistes du TLR7 chez la souris et prédiction de son efficacité chez l'homme

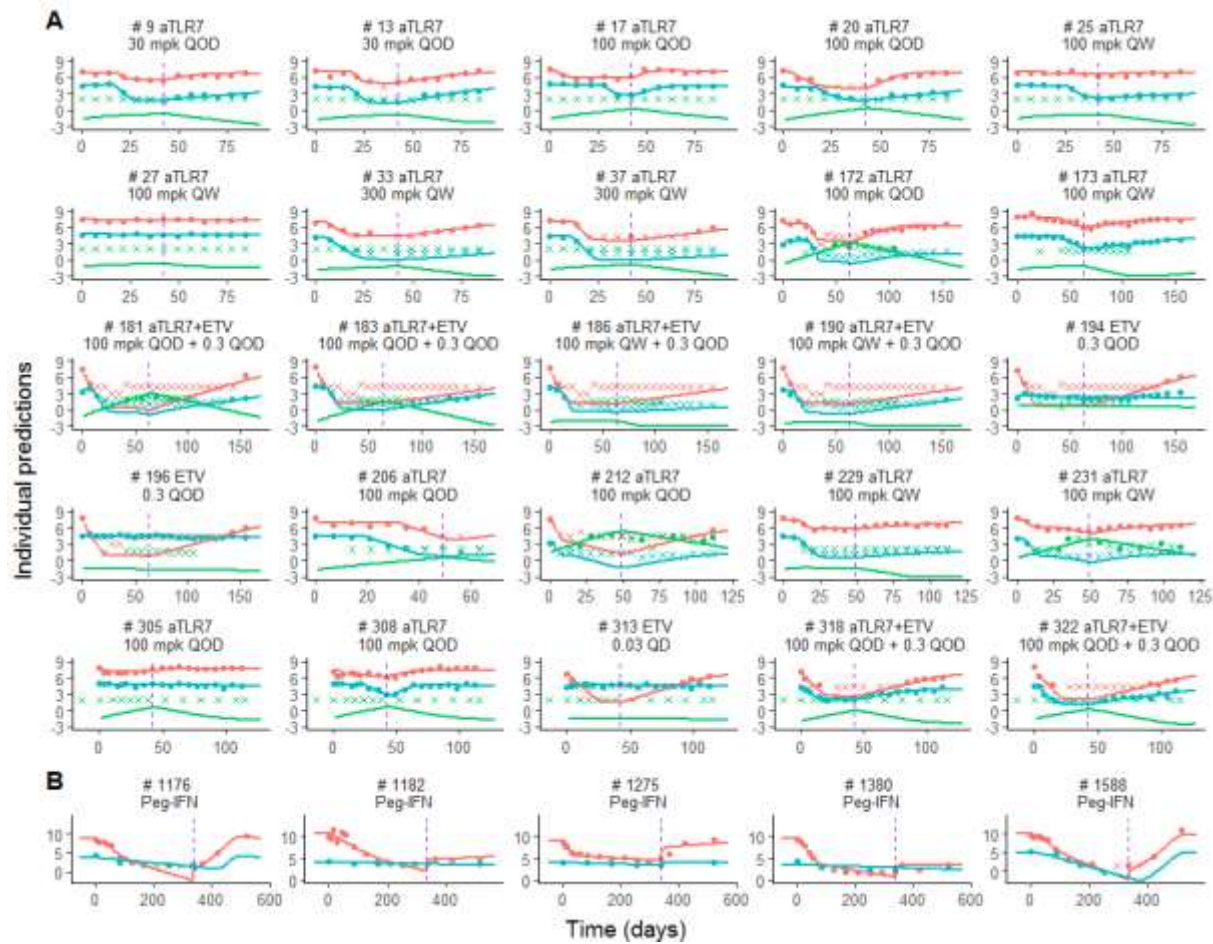


Figure 4. Individual predictions for representative individuals. A: in aTLR7 studies; B: in Peg-IFN study. Dots represent the observed data; crosses represent data below the limit of quantification (LOQ). In red, HBV DNA (\log_{10} copies/mL); in blue, HBsAg (\log_{10} IU/mL); in green the anti-HBsAg antibody, in purple the end of the treatment period.

Further aTLR7 also induced a stimulation of the anti-HBsAg. Given the limited amount of data, only a limited number of parameters could be estimated (E_{\max} , ρ and $EC_{50,A}^{TLR7}$), with no inter-individual variability on E_{\max} . The natural production of antibodies through V and S, ρ , was equal to 0.00126 d^{-1} , and the drug related parameters $EC_{50,A}^{TLR7}$ and E_{\max} were equal to 177 ng.mL^{-1} and 0.361 respectively. At the doses of 100 mg.kg^{-1} QW and QOD those parameters means that aTLR7 treatment stimulate the production of anti-HBsAg with a proliferation rate equal to 0.136 and 0.208 d^{-1} , respectively.

Next we could use the model to predict the effect of longer-term treatment duration. We predicted that a continuous increase in antibody could be obtained by prolonging treatment up

to 24 weeks and could drive a further decline in HBV DNA and HBsAg by about 3 \log_{10} (Figure 5).

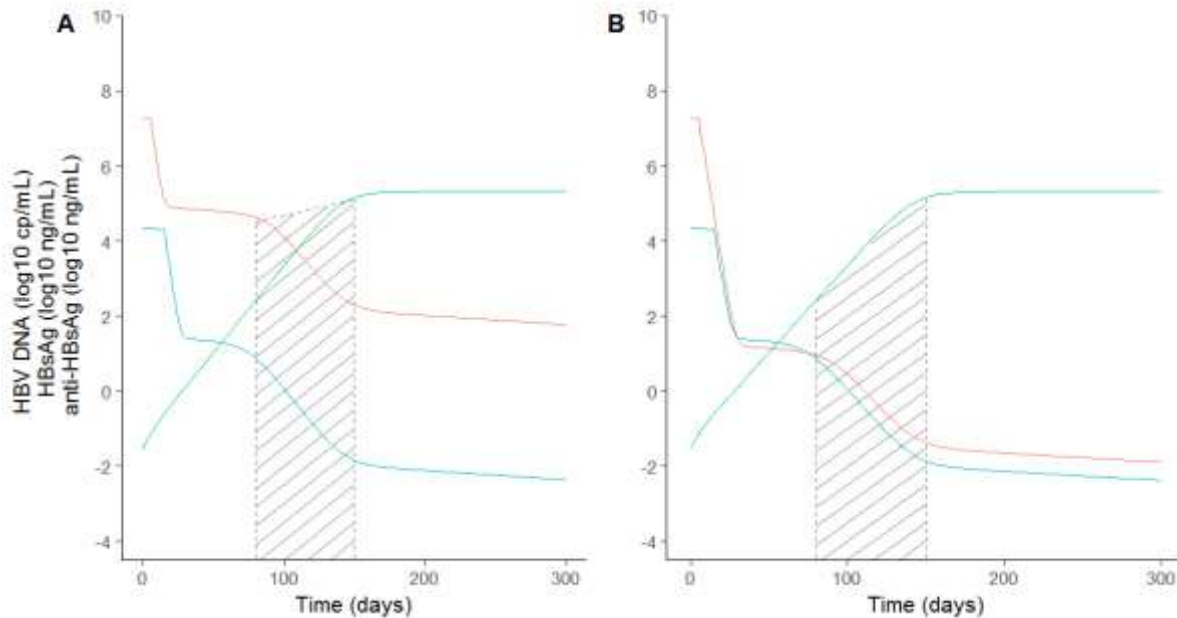


Figure 5. Long-term predicted kinetics in aTLR7 at the dose of 100 mg/kg QOD in monotherapy (A) or combination with ETV (B). In red, HBV DNA; in blue, HBsAg; in green, anti-HBsAg antibody. Hashed area represents the renewed decline of HBV DNA and HBsAg due to the increase in anti-HBsAg antibodies from W8 up to W20. This could lead to an additional decline in HBV DNA and HBsAg of more than 3 logs at the highest dose.

HBV viral dynamics in humans

The model developed could well characterize the kinetics of Peg-IFN in humans (Figures S5, S6, S7). The first phase of HBV DNA decline was profound with a maximal effectiveness of Peg-IFN ε_{max}^{Peg} equal to 99.9%, and no effect on HBsAg production. Then, the second phase of HBV DNA decline was more rapid than that of HBsAg. This suggests that the pool of cells capable of producing HBsAg was largely unaffected by treatment but that there are less and less cells capable of producing HBV DNA over time. This was captured in our model by assuming that the rate at which cell lose their capability to produce HBV DNA (through loss or silencing of *cccDNA* for instance), noted δ_2 , was equal to 0.025 d^{-1} . However these cells continue to produce HBsAg, suggesting that they are still transcriptionally active (in case of integration of virus genome for instance), and the loss rate of infected hepatocytes, δ , was equal to only

0.0040 d⁻¹. Albeit limited, this loss rate combined with lower quantities of HBV DNA in circulation led to a slow decline in HBsAg of 0.05 log₁₀ ng.mL⁻¹.month⁻¹ during treatment.

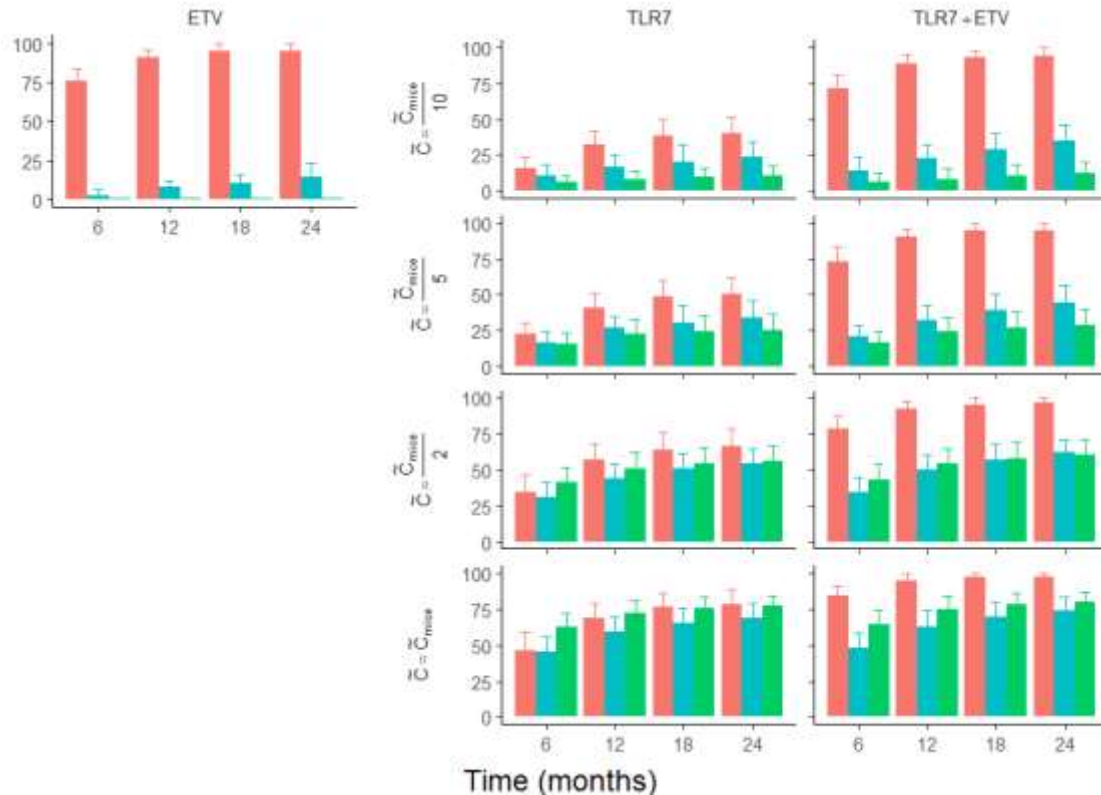


Figure 6. Predicted proportion of patients achieving clinical endpoint after 6, 12, 18 and 24 months of treatment with ETV monotherapy, aTLR7 monotherapy or ETV+aTLR7. Results are given for four proposed concentration levels of aTLR7. \tilde{C}_{mice} indicates the effective concentrations obtained in mice experiments at 100 mg/kg QOD. Red: HBV DNA undetectable (<300 copies/mL); Blue: undetectable HBsAg (<0.05 IU/mL); Green: anti-HBsAg detectable (>100 ng/mL).

Simulations of aTLR7 effect in human.

Next, we used this model to predict the effect of aTLR7 and ETV in humans. In the case of ETV monotherapy at the clinical dose of 0.05 mg QD (Figure 6), our model predicted, as observed in clinical trials^{24,25,26}, that 90.5% of patients achieve undetectable levels of HBV DNA after a year of treatment (IP_{90%}=82.2-95.7%), but the loss of HBsAg remains minimal,

equal to 8% ($IP_{90\%}=2-10\%$). In contrast, aTLR7 monotherapy may achieve up to 44% loss of HBsAg after 1 year treatment if drug concentrations are at least 50% of those achieved in mice at doses of 100 mg.kg^{-1} QOD ($\tilde{C} = \tilde{C}_{\text{mice}} / 2$). In combination with ETV, the rate of HBV DNA undetectability could be obviously improved, from 57% to more than 90%. Even at concentration ($\tilde{C} = \tilde{C}_{\text{mice}} / 10$), our model still predicted that 22% of patients could achieve undetectable HBsAg after 1 year of treatment, i.e., about three times as much what can be obtained with ETV monotherapy in this model.

Discussion

We developed here a model to characterize the effect of a TLR7 agonist on HBV dynamics. Unlike ETV, that only act on viral production, the model suggests that aTLR7 has three distinct mechanisms of action, two that are directly related to its antiviral effect (blocking viral and subviral production with effectiveness of 99.4% and 99.87%, respectively) and one that was indirect through the stimulation of anti-HBsAg antibodies production. Assuming similar concentrations in humans than what was obtained in mice, our model would predict that 12 months of treatment with aTLR7+ETV could lead to a large proportion of patients achieving undetectable HBV DNA and HBsAg, as well as detectable levels of anti-HBsAg antibodies. Obviously, those results in humans will be contingent on the dose (and hence exposure) that will be used. In the case of GS-9620, the doses used in humans led to 2 to 10 times lower exposures than in woodchucks, where a strong antiviral was observed^{7, 27, 28}. Assuming lower effective concentration such as $\tilde{C} = \tilde{C}_{\text{mice}}/10$, the model predicted that about 20% of patients could achieve undetectable HBsAg levels, which is higher than typically observed with ETV (2-6%)^{29,30} or Peg-IFN (2-7%)^{31,32}.

The model developed is to our knowledge the first attempt to model the effect of immunomodulatory agents against HBV. For that purpose, we extended prior models by uncoupling the production of virus and of subviral particles within infected cells and accounting for the antigen- and drug-dependent B-cell stimulation on anti-HBsAg antibodies. Despite its complexity, our model does not include important aspects of HBV dynamics, such as the different forms of subviral particles (RNA virions, empty virions), and important steps of intra-cellular replication (*cccDNA* recycling, HBeAg production). In that respect, the growing availability of HBV markers such as HBcrAg or HBV RNA should be helpful to construct more

models that are realistic and understand in details the effect of immunomodulatory agents on the complex virus lifecycle.

Although our results predict that aTLR7 could be a relevant candidate for testing in humans, several limitations of the model need to be pointed out. First, we could not identify a significant loss of infected cells during the treatment period (up to 8 weeks) and, consequently, our model predicted that viral and subviral production would return to pre-treatment value after treatment cessation. Consistent with the lack of effect of aTLR7 on *cccDNA*, the levels of HBeAg, another marker of viral activity, remained unchanged during treatment (not shown). Whether aTLR7 can partially silence *cccDNA* from the infected cells and not only transiently limit its transcriptional activity will be key to lead to a functional cure in humans. Although aTLR7 are thought to stimulate the IFN system, we could not identify a significant correlation between the viral kinetic parameters of the model and the levels of IFN activity, as measured by plasma cytokines and interferon-stimulating genes (see Supplementary Materials 2). One possibility is that the timing of measure (day 26) was too late and/or that plasma levels may not reflect liver activity but it could also indicate that the pathways of aTLR7 in mice may be different from those in humans, and jeopardize translations from mice to humans.

In summary, our model identifies three separate mechanisms of action for aTLR7 based on mice data. Its effect on anti-HBsAg in mice make it potentially more effective than current treatments. Future analyses considering longer treatment durations and combinations with other drugs in development will be needed to confirm the potential of this class of drugs in the fight for an HBV cure.

Study highlights

What is the current knowledge on the topic?

Several toll-like receptor 7 agonists are in development against Hepatitis B virus, aiming to restore/boost the immune response. Mathematical models can help better understand virus pathogenesis and assess the mechanism of action of antiviral drugs.

What question did this study address?

We developed the first model of HBV dynamics during treatment with TLR7 agonists using mice data. The model was then bridged to humans to predict the effects in future clinical trials.

What does this study add to our knowledge?

TLR7 agonists in mice have a triple mechanism of action through the inhibition of viral and subviral particles, as well as through the stimulation of the antibody production.

How might this change drug discovery, development, and/or therapeutics?

TLR7 agonists could be a valuable candidate for testing in clinical trials. The model provides a framework to characterize the effects of other immunomodulatory drugs.

Author contributions

A.G., A.L.D., and J.G. wrote the manuscript; L.G. designed the research; A.G., A.L.D., and J.G. performed the research; A.G. analyzed the data.

References

1. Hou, J., Liu, Z., Gu, F. & others Epidemiology and prevention of hepatitis B virus infection. *Int J Med Sci* **2**, 50–57 (2005).
2. Lavanchy, D. Worldwide epidemiology of HBV infection, disease burden, and vaccine prevention. *J. Clin. Virol. Off. Publ. Pan Am. Soc. Clin. Virol.* **34 Suppl 1**, S1–3 (2005).
3. Zeisel, M. B. *et al.* Towards an HBV cure: state-of-the-art and unresolved questions—report of the ANRS workshop on HBV cure. *Gut* **64**, 1314–1326 (2015).
4. Patient, R., Houroux, C. & Roingeard, P. Morphogenesis of hepatitis B virus and its subviral envelope particles. *Cell. Microbiol.* **11**, 1561–1570 (2009).
5. Liang, T. J. *et al.* Present and future therapies of hepatitis B: From discovery to cure: VIRAL HEPATITIS. *Hepatology* **62**, 1893–1908 (2015).
6. Lanford, R. E. *et al.* GS-9620, an Oral Agonist of Toll-Like Receptor-7, Induces Prolonged Suppression of Hepatitis B Virus in Chronically Infected Chimpanzees. *Gastroenterology* **144**, 1508–1517.e10 (2013).
7. Janssen, H. L. A. *et al.* Safety, efficacy and pharmacodynamics of vesatolimod (GS-9620) in virally suppressed patients with chronic hepatitis B. *J. Hepatol.* **68**, 431–440 (2018).

8. Nguyen, T. & Guedj, J. HCV Kinetic Models and Their Implications in Drug Development: HCV Kinetic Models and Their Implications. *CPT Pharmacomet. Syst. Pharmaal.* **4**, 231–242 (2015).
9. Huang, Y.-H. *et al.* A murine model of hepatitis B-associated hepatocellular carcinoma generated by adeno-associated virus-mediated gene delivery. *Int. J. Onal.* **39**, 1511–1519 (2011).
10. Jiang, Q. *et al.* Simultaneous determination of entecavir and lamivudine in rat plasma by UPLC-MS/MS and its application to a pharmacokinetic study. *RSC Adv.* **6**, 70990–70998 (2016).
11. Ciupe, S. M., Ribeiro, R. M. & Perelson, A. S. Antibody responses during hepatitis B viral infection. *PLoS Comput Biol* **10**, e1003730 (2014).
12. Goyal, A., Ribeiro, R. M. & Perelson, A. S. The Role of Infected Cell Proliferation in the Clearance of Acute HBV Infection in Humans. *Viruses* **9**, (2017).
13. Nagaya, T. *et al.* The mode of hepatitis B virus DNA integration in chromosomes of human hepatocellular carcinoma. *Genes Dev.* **1**, 773–782 (1987).
14. Tu, T., Budzinska, M. A., Shackel, N. A. & Urban, S. HBV DNA Integration: Molecular Mechanisms and Clinical Implications. *Viruses* **9**, (2017).
15. Hu, J. & Liu, K. Complete and Incomplete Hepatitis B Virus Particles: Formation, Function, and Application. *Viruses* **9**, 56 (2017).
16. Liu, F. *et al.* Alpha-Interferon Suppresses Hepadnavirus Transcription by Altering Epigenetic Modification of *cccDNA* Minichromosomes. *PLoS Pathog.* **9**, (2013).
17. Carrillo-Bustamante, P. *et al.* Determining Ribavirin's mechanism of action against Lassa virus infection. *Sci. Rep.* **7**, 11693 (2017).
18. Guedj, J., Dahari, H., Shudo, E., Smith, P. & Perelson, A. S. Hepatitis C viral kinetics with the nucleoside polymerase inhibitor mericitabine (RG7128). *Hepatology* **55**, 1030–1037 (2012).
19. Guedj, J. *et al.* Analysis of hepatitis C viral kinetics during administration of two nucleotide analogues: sofosbuvir (GS-7977) and GS-0938. *Antivir. Ther.* **19**, 211–220 (2014).
20. Klein-Schneegans, A. S., Kuntz, L., Trembleau, S., Fonteneau, P. & Loor, F. Serum concentrations of IgM, IgG1, IgG2b, IgG3 and IgA in C57BL/6 mice and their congenics at the nu(nude)locus. *Thymus* **16**, 45–54 (1990).
21. Vieira, P. & Rajewsky, K. The half-lives of serum immunoglobulins in adult mice. *Eur. J. Immunol.* **18**, 313–316 (1988).

22. Bergstrand, M., Hooker, A. C., Wallin, J. E. & Karlsson, M. O. Prediction-Corrected Visual Predictive Checks for Diagnosing Nonlinear Mixed-Effects Models. *AAPS J.* **13**, 143–151 (2011).
23. Scott, L. J. & Keating, G. M. Entecavir. *Drugs* **69**, 1003–1033 (2009).
24. Wang, J. Clinical utility of entecavir for chronic hepatitis B in Chinese patients. *Drug Des. Devel. Ther.* **8**, 13–24 (2013).
25. Matthews, S. J. Entecavir for the treatment of chronic hepatitis B virus infection. *Clin. Ther.* **28**, 184–203 (2006).
26. Woo, G. *et al.* Tenofovir and Entecavir Are the Most Effective Antiviral Agents for Chronic Hepatitis B: A Systematic Review and Bayesian Meta-analyses. *Gastroenterology* **139**, 1218-1229.e5 (2010).
27. Menne, S. *et al.* Sustained efficacy and seroconversion with the Toll-like receptor 7 agonist GS-9620 in the Woodchuck model of chronic hepatitis B. *J. Hepatol.* **62**, 1237–1245 (2015).
28. Lopatin, U. *et al.* Safety, pharmacokinetics and pharmacodynamics of GS-9620, an oral Toll-like receptor 7 agonist. *Antivir. Ther.* **18**, 409–418 (2013).
29. Yapali, S., Talaat, N. & Lok, A. S. Management of Hepatitis B: Our Practice and How It Relates to the Guidelines. *Clin. Gastroenterol. Hepatol.* **12**, 16–26 (2014).
30. Chang, T.-T. *et al.* A Comparison of Entecavir and Lamivudine for HBeAg-Positive Chronic Hepatitis B. *N. Engl. J. Med.* **354**, 1001–1010 (2006).
31. Marcellin, P. *et al.* Combination of Tenofovir Disoproxil Fumarate and Peginterferon α-2a Increases Loss of Hepatitis B Surface Antigen in Patients With Chronic Hepatitis B. *Gastroenterology* **150**, 134-144.e10 (2016).
32. Lau, G. K. *et al.* Peginterferon Alfa-2a, lamivudine, and the combination for HBeAg-positive chronic hepatitis B. *N. Engl. J. Med.* **352**, 2682–2695 (2005).

Supplementary tables and figures

Table S1. Patients' characteristics at baseline in Peg-IFN study

Characteristic	Value
Age (years) ^a	32 (18-77)
Treatment duration (weeks) ^a	47.9 (38.7-51.6)
HBV DNA (log ₁₀ copies/mL) ^a	9.2 (3.8-15.4)
HBsAg (IU/mL) ^a	34058.5 (2.0-249751.0)
HBeAg (NCU/mL) ^a	766.7 (0.2-5470.4)
ALT (ng/mL) ^a	160.4 (15.6-1740.8)
Race^b	
Caucasian	226 (88.6)
African	4 (1.6)
Oriental or Asian	21 (8.2)
Other	4 (1.6)
Fibrosis status^b	
0	99 (38.8)
1	31 (12.2)
2	32 (12.5)
3	79 (31.0)
4	14 (5.5)
Genotype^b	
A	154 (60.5)
B	21 (8.2)
C	8 (3.1)
D	71 (27.8)
Other	1 (0.4)
Response status^b	
Non-responders	174 (68.2)
Responders	81 (31.8)

Table S2. Parameter estimates of the selected model under the Loewe additivity hypothesis for combination effect

Parameters	Fixed effects estimates (RSE%)	Standard deviation of random effects (RSE%)
HBV DNA associated parameters		
c (d^{-1})	0.582 (5)	0.40 (12)
p_v (copies. $mL^{-1}.d^{-1}$)	11.1 (12)	0.91 (10)
δ (d^{-1})	5.60×10^{-2} (-) ^a	
$EC_{50,V}^{ETV}$ (ng. mL^{-1})	6.05×10^{-5} (73)	1.72 (39)
n_V^{ETV}	1.19 (5)	
$EC_{50,V}^{TLR7}$ (ng. mL^{-1})	3.23 (25)	2.70 (10)
n_V	1.17 (1)	
$T_{lag,V}$ (d^{-1})	5.22 (25)	1.53 (15)
α_v (d^{-1})	0.136 (11)	0.81 (11)
Residual error (copies. mL^{-1})	0.481 (3)	
SVPs associated parameters		
p_s (copies. $mL^{-1}.d^{-1}$)	3.39×10^3 (10)	0.94 (8)
λ	9.54×10^{-2} (36)	3.15 (12)
$T_{lag,S}$ (d^{-1})	14.6 (13)	1.69 (11)
α_s (d^{-1})	5.66×10^{-2} (17)	1.26 (14)
Residual error (IU. mL^{-1})	0.318 (3)	
Anti-HBsAg associated parameters		
ρ (d^{-1})	1.26×10^{-3} (102)	4.15 (17)
σ (d^{-1})	0.1 (-) ^a	
γ (d^{-1})	10^{-12} (-) ^a	
A_{max} (molecules. mL^{-1})	1.60×10^{15} (-) ^a	
α_A (d^{-1})	0.741 (16)	
k (d^{-1})	10 (-) ^a	
c_A (d^{-1})	2.62 (-) ^b	
E_{max}	0.357 (4)	
$EC_{50,A}$ (ng. mL^{-1})	177 (27)	1.08 (30)
Residual error (ng. mL^{-1})	0.623 (6)	

^a: parameters were fixed to a plausible value from literature

^b: c_A was set equal to 4 times the viral clearance c

Table S3. Parameter estimates of the Peg-IFN VK model

Parameters	Fixed effects estimates (RSE%)	Standard deviation of random effects (RSE%)
r (d^{-1})	0.186 (55)	1.85 (16)
R ₀	121 (41)	4.51 (7)
c (d^{-1})	0.7 (-) ^a	-
p _v (copies.mL ⁻¹ .d ⁻¹)	156 (27)	3.87 (6)
p _s (SVPs.mL ⁻¹ .d ⁻¹)	1.96.10 ⁵ (10)	1.05 (8)
δ ₁ (d^{-1})	0.0040 (15)	1.35 (11)
δ ₂ (d^{-1})	0.025 (7)	0.59 (11)
ρ (d^{-1})	0.003 (-) ^a	-
σ (d^{-1})	0.1 (-) ^a	-
γ (d^{-1})	10 ⁻¹² (-) ^a	-
ε _{max} ^{Peg}	0.999 (<1)	-
k _i (d^{-1})	0.0778(17)	2.11 (7)
α _v (d^{-1})	0.0615 (15)	1.93 (15)
Residual errors		
HBV DNA (copies.mL ⁻¹)	1.13 (1)	
HBsAg (IU.mL ⁻¹)	0.427 (3)	

^a: parameters were fixed to a plausible value from literature

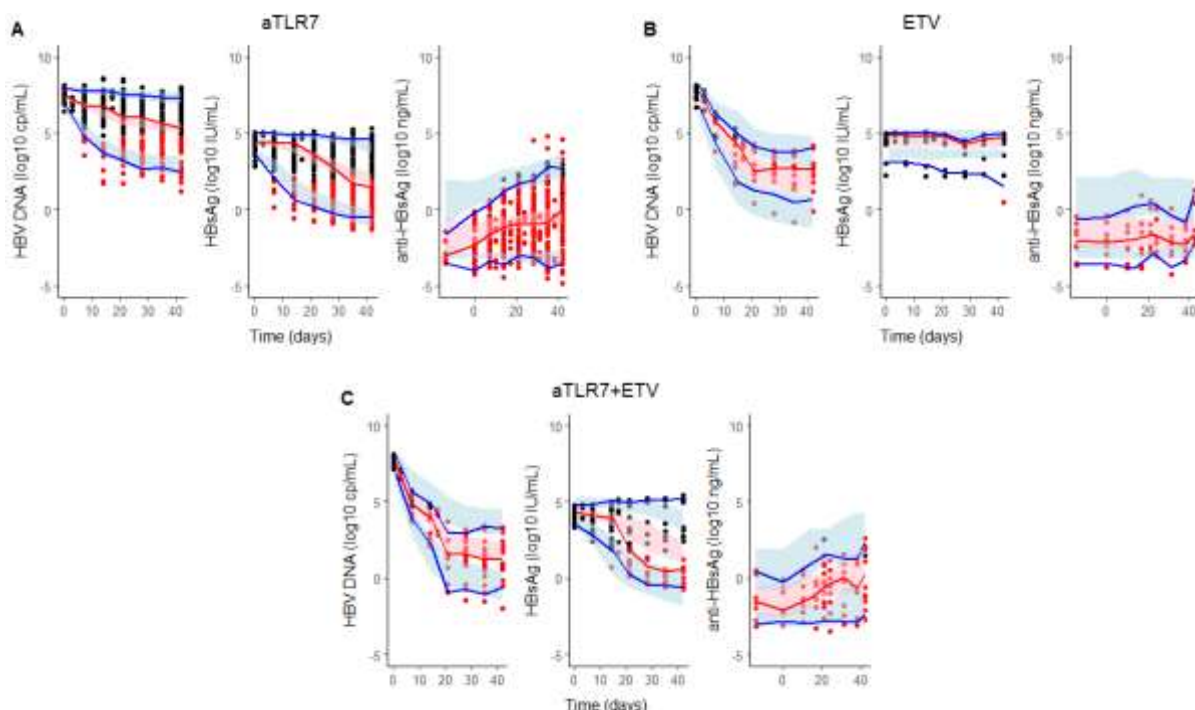


Figure S1. Mice model: Prediction-corrected visual predictive checks (pcVPC)

Modélisation de l'effet des agonistes du TLR7 chez la souris et prédiction de son efficacité chez l'homme

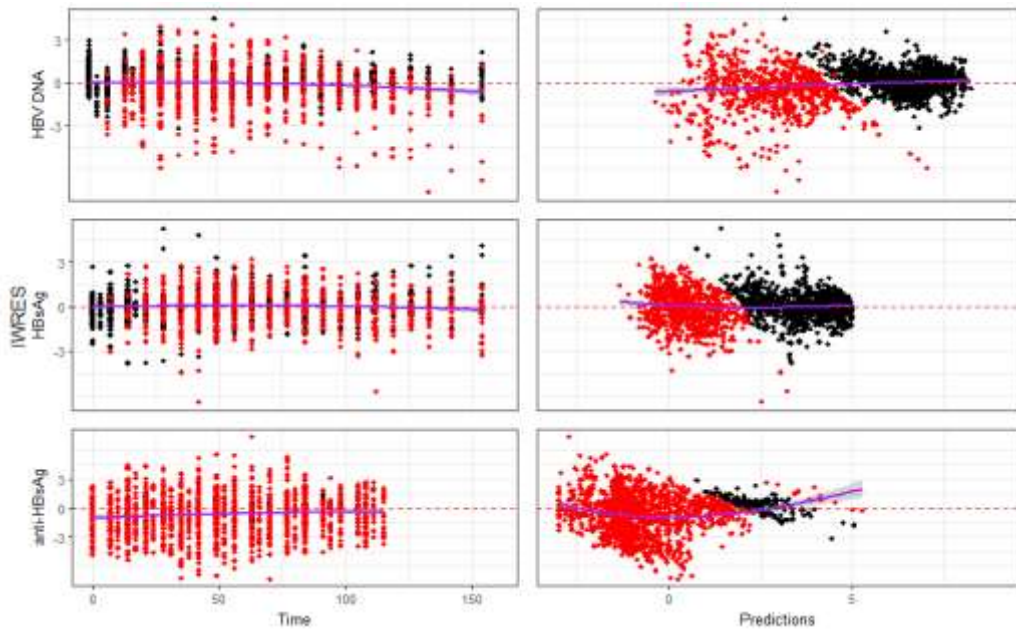


Figure S2. Mice model: Individual weighted residuals (IWRES) versus time and predictions. Red dots: BLQ observation points

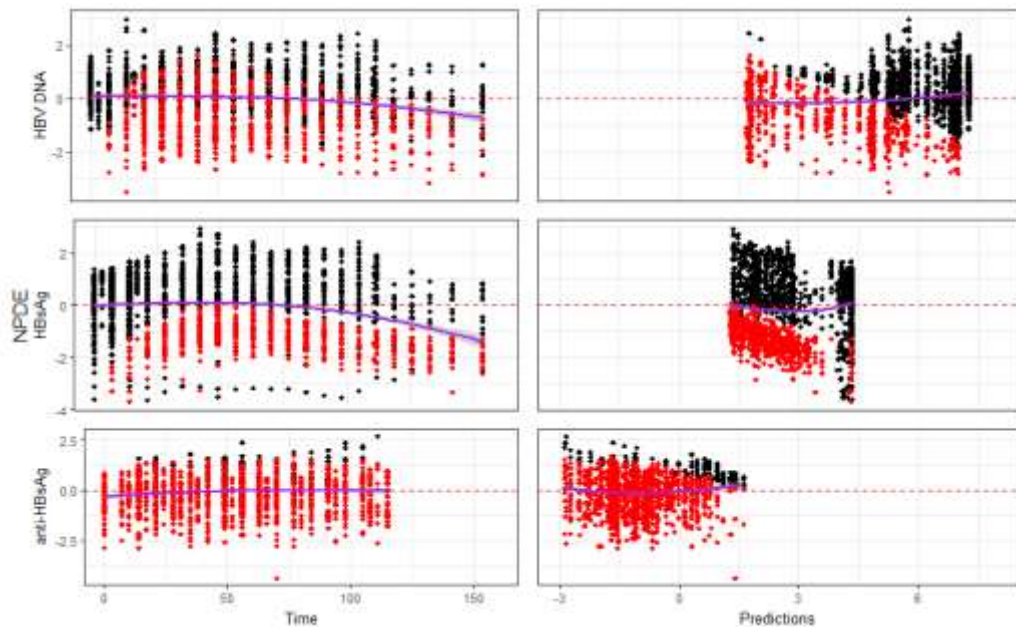


Figure S3. Mice model: Normalized prediction distribution errors (NPDE) versus time and predictions. Red dots: BLQ observation points

Modélisation de l'effet des agonistes du TLR7 chez la souris et prédiction de son efficacité chez l'homme

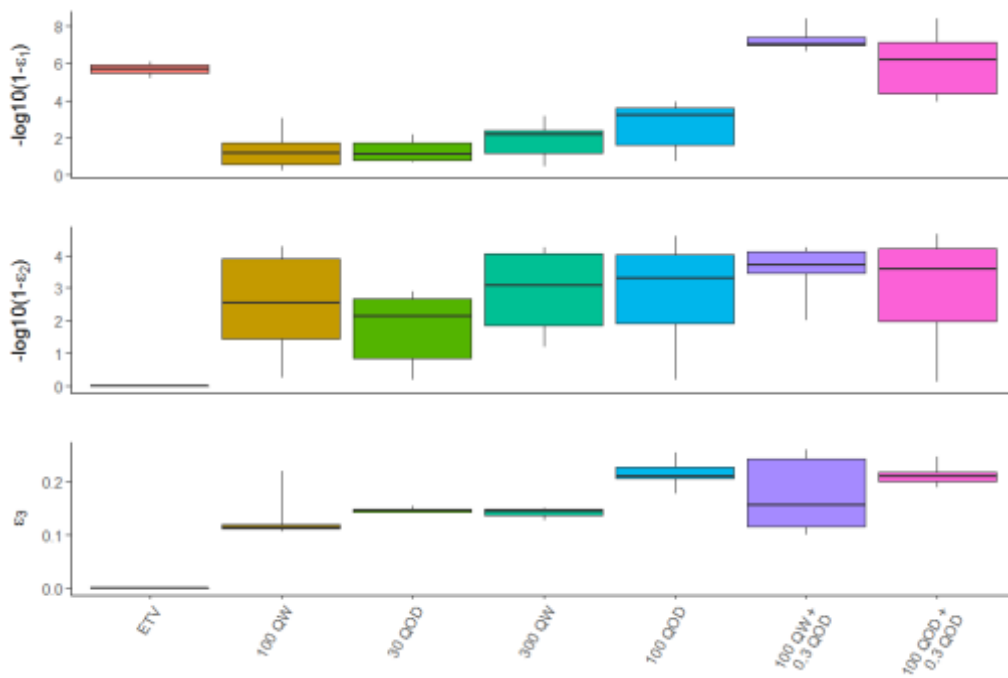


Figure S4. Individual efficacy distribution by dose group and marker determined by empirical Bayes approach in the mice model

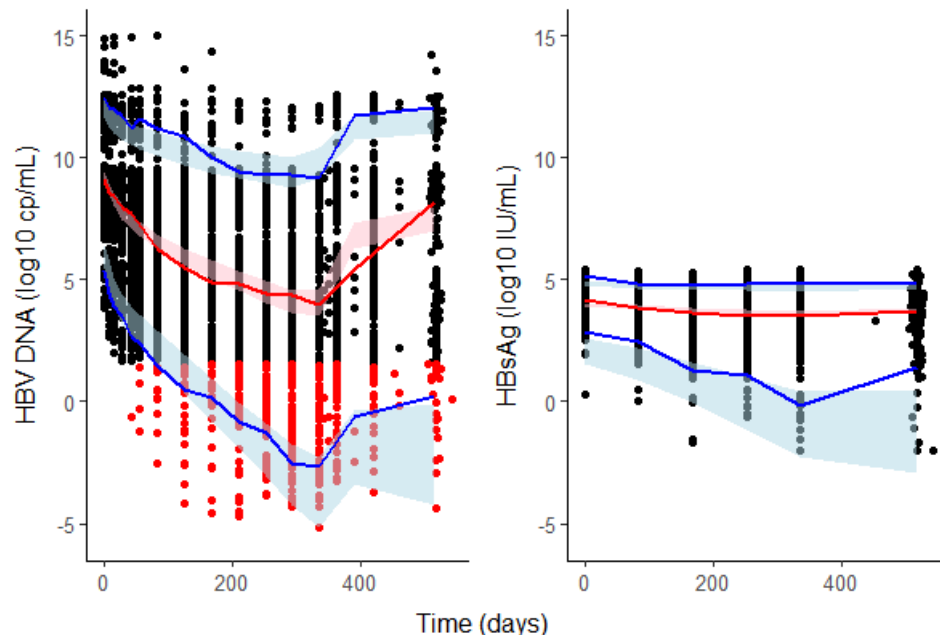


Figure S5. Peg-IFN model: Visual predictive checks (VPC) of Peg-IFN VK model

Modélisation de l'effet des agonistes du TLR7 chez la souris et prédiction de son efficacité chez l'homme

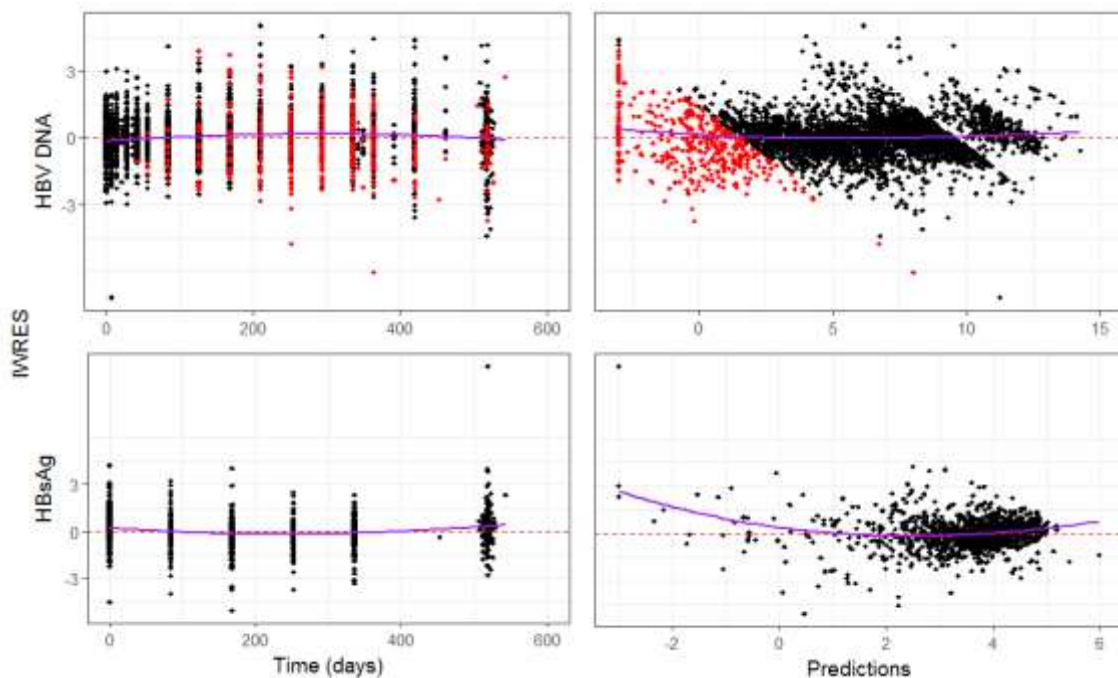


Figure S6. Peg-IFN model: Individual weighted residuals (IWRES) versus time and predictions.

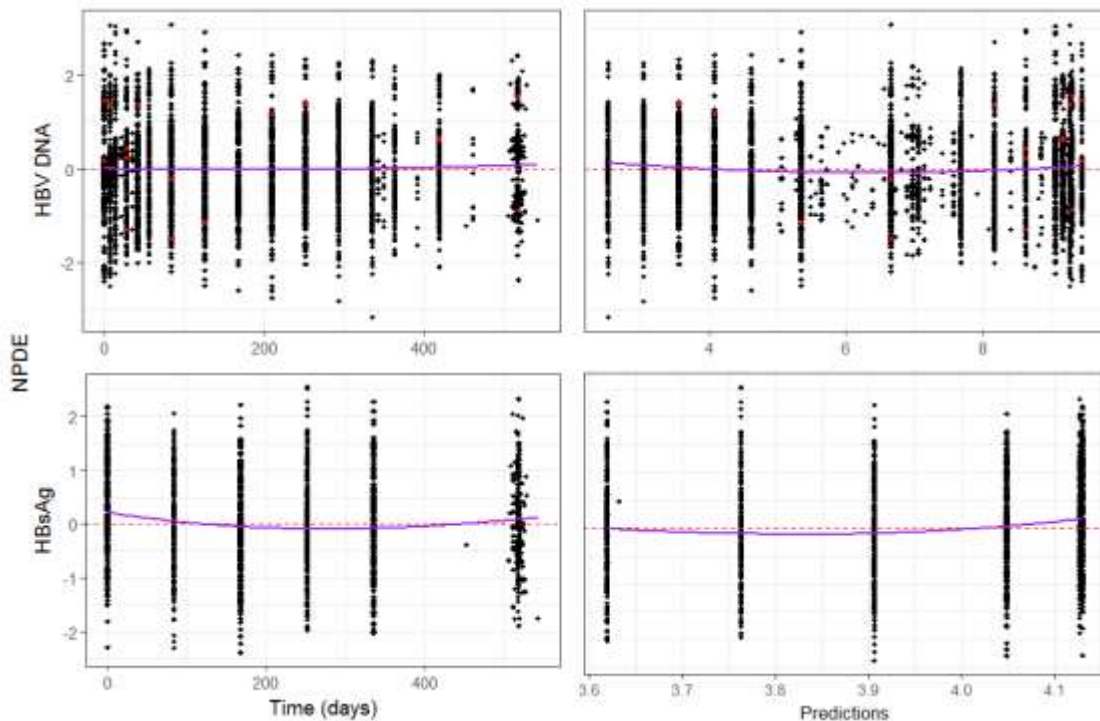


Figure S7. Peg-IFN model: Normalized prediction distribution errors versus time and predictions (NPDE)

Supplementary material 1: Model steady states

Human model

The ODE system (1) admitted the following solutions:

$$\begin{aligned} T_0 &= \frac{\delta(c + aA_0)}{p_V\beta} \\ I_0 &= \frac{\beta V_0 T_0}{\delta} \\ I_{2_0} &= 0 \\ V_0 &= \frac{\sigma p_V A_0}{(p_V + p_S)(\rho - aA_0)} \\ S_0 &= \frac{p_S}{p_V} V_0 \\ X_{V_0} &= \frac{\gamma V_0 A_0}{K} \\ X_{S_0} &= \frac{\gamma S_0 A_0}{K} \end{aligned}$$

A_0 is the unique real and positive root of the following 3nd degree polynomial:

$$\begin{aligned} &A^3(rab^2) + A^2 \left[\left(\frac{\beta\sigma p_V}{p_V + p_S} - rb \right) caR_0 - (cb + 2a\rho)br \right] \\ &+ A \left[\left(\frac{\beta\sigma p_V}{p_V + p_S} + rb - ra \right) c\rho R_0 - r\rho(cb + ca + \rho a) \right] + (R_0 - 1)cr\rho^2 = 0 \end{aligned}$$

With $K = k + c_A$; $a = \gamma \left(1 - \frac{k}{K} \right)$; $b = \frac{\beta\sigma p_V}{\delta(p_V + p_S)} - a$ and $R_0 = \frac{\beta p_V T_m}{\delta c}$.

Since the term $A^3(rab^2)$ is negligible, with regard to the range of possible values for all parameters, A_0 was defined as the positive root of the 2nd degree polynomial and then equal to:

$$\begin{aligned} B &= \left(\frac{\beta\sigma p_V}{p_V + p_S} - rb \right) caR_0 - (cb + 2a\rho)br \\ C &= \left(\frac{\beta\sigma p_V}{p_V + p_S} + rb - ra \right) c\rho R_0 - r\rho(cb + ca + \rho a) \\ D &= (R_0 - 1)cr\rho^2 \\ \Delta &= C^2 - 4BD \end{aligned}$$

And $A_0 = -\frac{C - \sqrt{\Delta}}{2B}$. The approximated state-state equilibrium is presented in Figure A.

Adjusted viral dynamic model to the AAV mice model

$$\begin{aligned}
 \frac{dI}{dt} &= -\delta I \\
 \frac{dV}{dt} &= p_V I - c_V V - \gamma_V A V + k_V X_V \\
 \frac{dS}{dt} &= p_S I - c_S S - \gamma_S A S + k_S X_S \\
 \frac{dA}{dt} &= \rho(V + S) - \gamma_V A V - \gamma_S A S + k_V X_V + k_S X_S - \sigma A \\
 \frac{dX_V}{dt} &= k_V X_V + \gamma_V A V - c_{AV} X_V \\
 \frac{dX_S}{dt} &= k_S X_S + \gamma_S A S - c_{AS} X_S
 \end{aligned} \tag{2}$$

The ordinary differential equations (2) admitted the following solutions:

$$I_0 = 10^6$$

$$\begin{aligned}
 V_0 &= \frac{p_V I_0 K}{(c + \gamma A_0)K - k\gamma A_0} \\
 S_0 &= \frac{p_S I_0 K}{(c + \gamma A_0)K - k\gamma A_0} \\
 X_{V_0} &= \frac{\gamma V_0 A_0}{K} \\
 X_{S_0} &= \frac{\gamma S_0 A_0}{K}
 \end{aligned}$$

With $K = k + c_A$ and A_0 is the unique positive root of the following 2nd degree polynomial:

$$A^2(\sigma\gamma k - \sigma\gamma K) + A[k\gamma I_0(p_V + p_S) - \sigma c K - \gamma I_0 K(p_V + p_S)] + \rho I_0 K(p_V + p_S) = 0$$

We could define:

$$B = \sigma\gamma(k - K)$$

$$C = \gamma I_0(p_V + p_S)(k - K) - \sigma c K$$

$$D = \rho K I_0(p_V + p_S)$$

$$\Delta = C^2 - 4BD$$

Therefore, $A_0 = -\frac{C-\sqrt{\Delta}}{2B}$. The steady-state equilibrium are presented in Figure B.

Modélisation de l'effet des agonistes du TLR7 chez la souris et prédiction de son efficacité chez l'homme

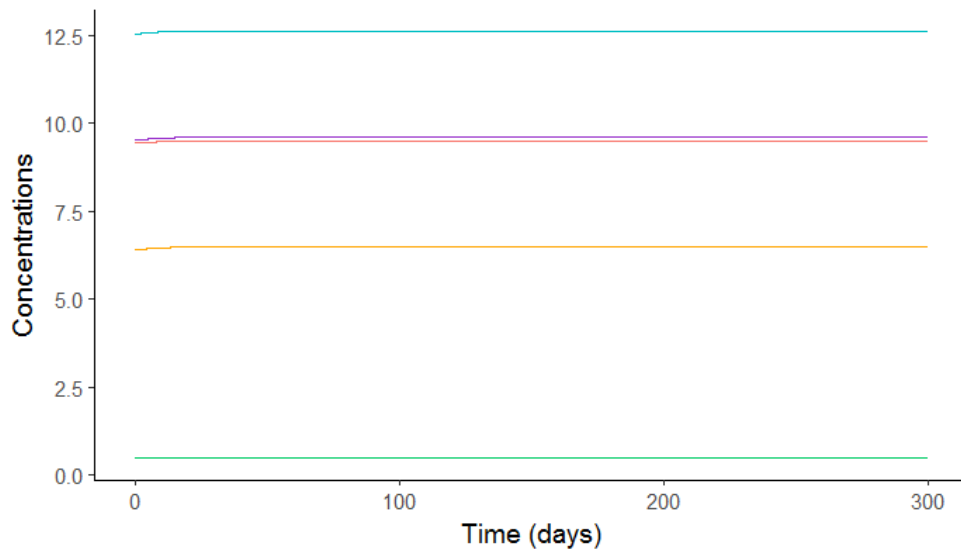


Figure A. Approximated steady-state equilibrium in the human model computed with the final parameter estimates. Red: viremia in $\log_{10}(\text{copies/mL})$; Blue: SVPs count in $\log_{10}(\text{SVPs/mL})$; Green: anti-HBsAg in $\log_{10}(\text{ng/mL})$; Orange: Complexes V-AB in $\log_{10}(\text{cpx/mL})$ and Purple: Complexes S-AB in $\log_{10}(\text{cpx/mL})$.

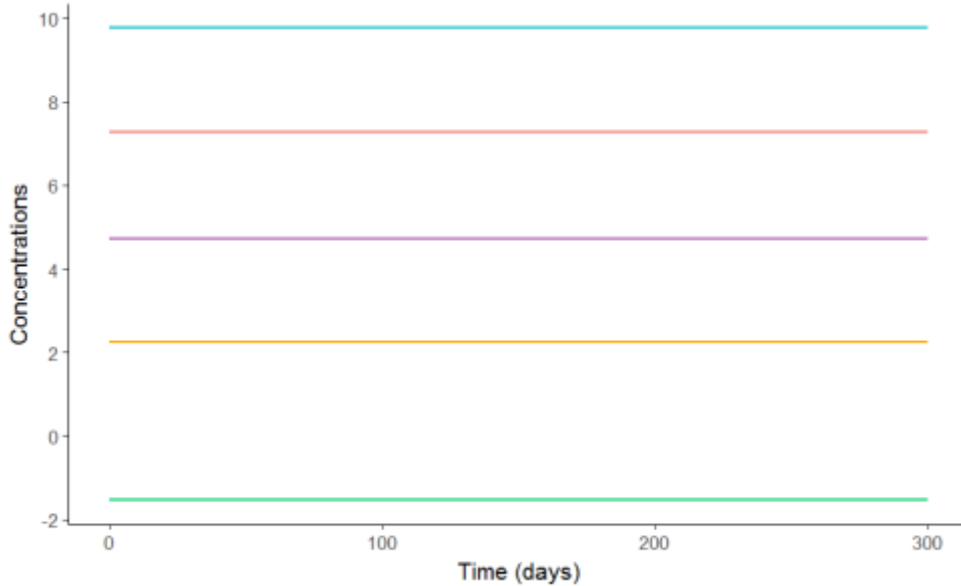


Figure B. Steady-state equilibrium in the mice model computed with the final parameter estimates. Red: viremia in $\log_{10}(\text{copies/mL})$; Blue: SVPs count in $\log_{10}(\text{SVPs/mL})$; Green: anti-HBsAg in $\log_{10}(\text{ng/mL})$; Orange: Complexes V-AB in $\log_{10}(\text{cpx/mL})$ and Purple: Complexes S-AB in $\log_{10}(\text{cpx/mL})$.

Supplementary material 2: Correlations between predicted effects and ISG or cytokine levels

The expression level of 4 interferon-stimulated genes (ISG) and 7 cytokines were measured 6h post the dose of day 28, in 40 mice from study 1 (8 from the vehicle group and 8 from each of the 4 dose groups of aTLR7). The genes measured were ISG 15, mycoma resistance protein 1 (Mx1), 2'-5' oligoadenylate synthase 1 (OAS1a) and tumor necrosis factor superfamily member 10 (TNFSF10). Cytokines measured were the following: IFN- α , IFN- γ , IL-6, IP-10, IL12-p40, MIP-1b and TNF- α . Associations between effects on virions (ε_1) or SVPs (ε_2) versus ISG expression levels or cytokines were tested using Spearman correlation (Figure C).

Since aTLR7 induced innate immune activity, we evaluated whether the elevation of interferon stimulating genes (ISG) and other cytokines could be related to the antiviral activity of the drug using a Spearman correlation test. In Figures C, D and E we represented the correlations between 4 different ISG and 7 cytokines involved in TLR7 pathway. Regarding the effect on virions or SVPs, we could not establish any significant link with ISG levels (Figure C). However, a trend was observed as efficacies increased. An explanation might be that even though ISG and cytokines are involved in innate immune activation on aTLR7 therapy, the relationship linking those markers to the effect might not be quantitative. Indeed, ISG and cytokines clearly participate to the innate immune system activation but their level might not be a direct reflect of the effect on viral markers. No association was found with normalized cytokine levels (Figures D and E).

Modélisation de l'effet des agonistes du TLR7 chez la souris et prédiction de son efficacité chez l'homme

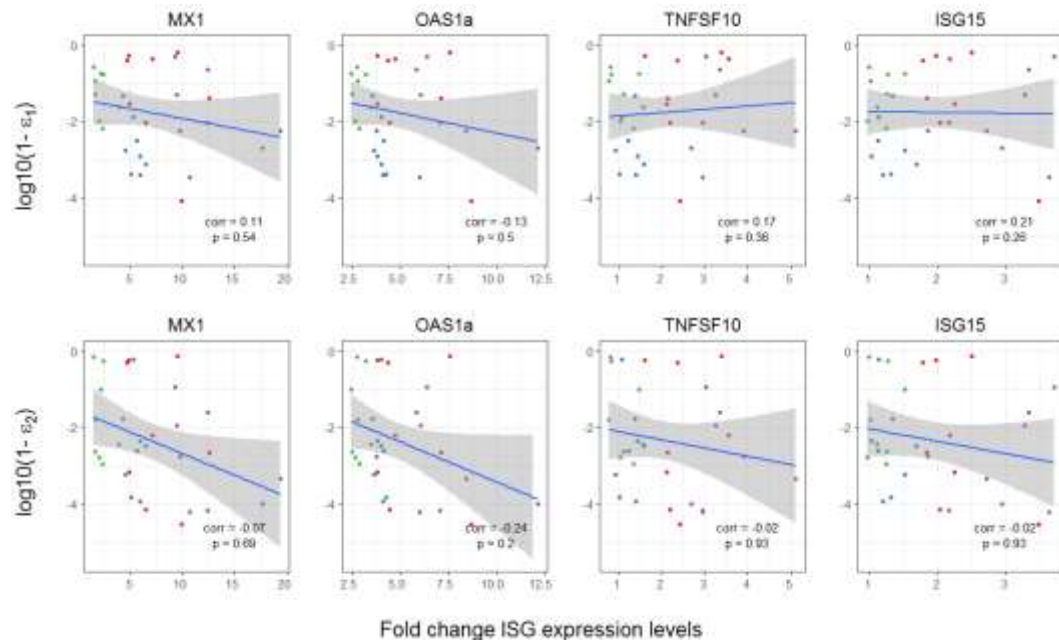


Figure C. Correlation between the estimated effects (on virions ε_1 and SVPs ε_2) and normalized ISG expression levels. Red dots: 100 mg/kg QW dose; blue dots: 100 mg/kg QOD dose; green dots: 30 mg/kg QW; purple dots: 300 mg/kg QOD.

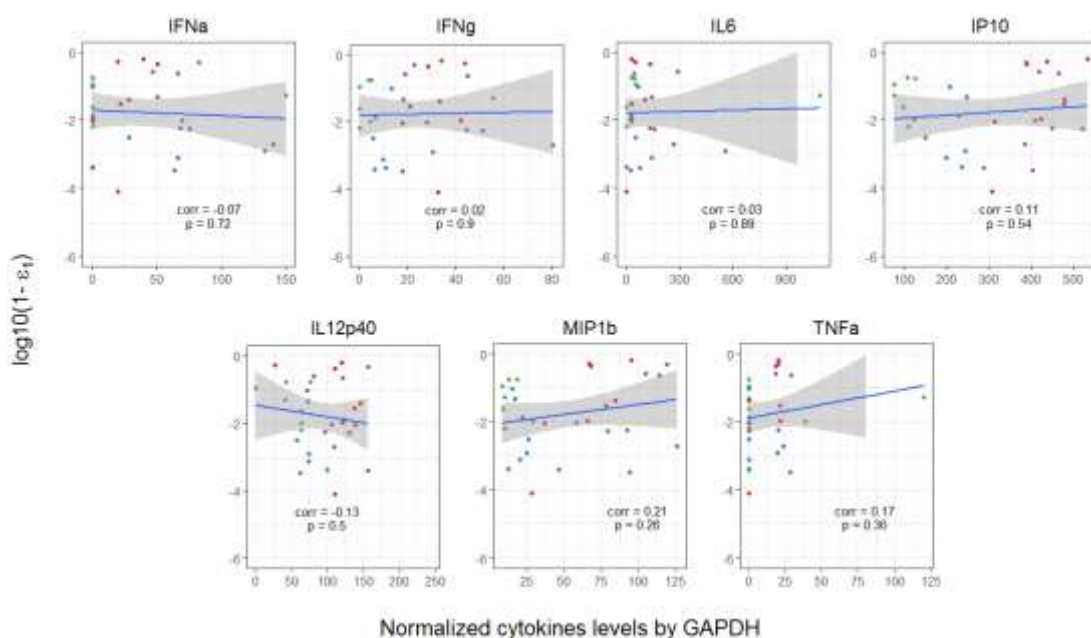


Figure D. Correlation between the estimated effects on virions (ε_1) and normalized cytokine titers. Red dots: 100 mg/kg QW dose; blue dots: 100 mg/kg QOD dose; green dots: 30 mg/kg QW; purple dots: 300 mg/kg QOD.

Modélisation de l'effet des agonistes du TLR7 chez la souris et prédiction de son efficacité chez l'homme

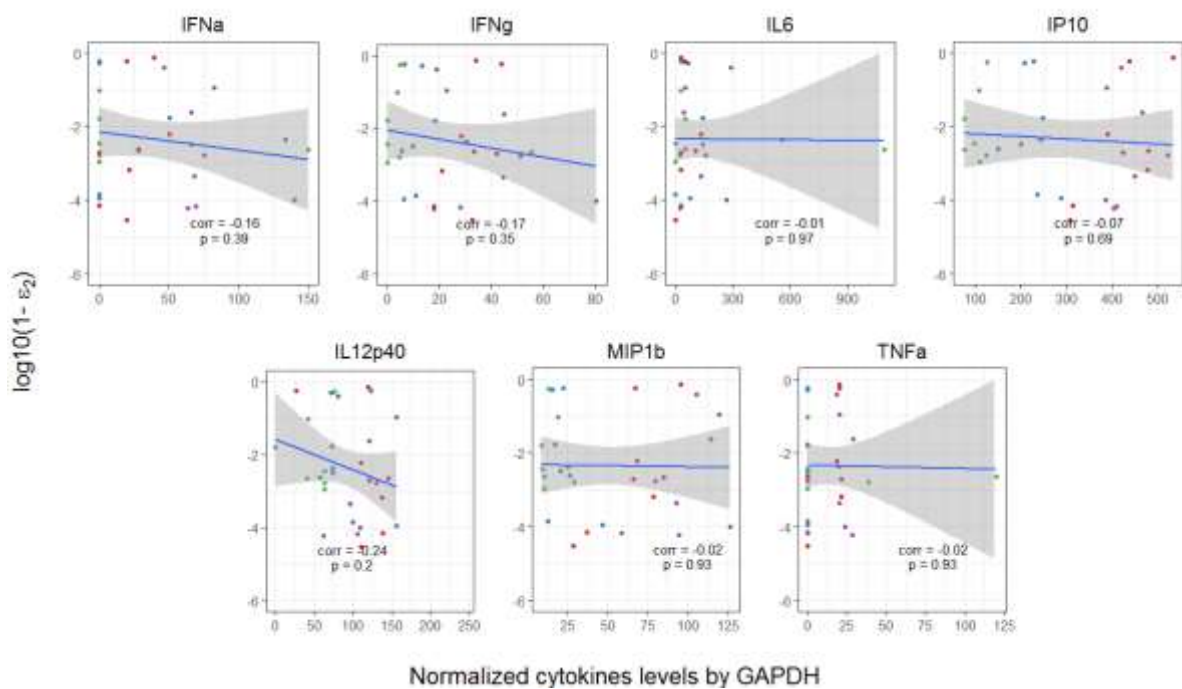


Figure E. Correlation between the estimated effects on SVPs (ε_2) and normalized cytokine titers. Red dots: 100 mg/kg QW dose; blue dots: 100 mg/kg QOD dose; green dots: 30 mg/kg QW; purple dots: 300 mg/kg QOD

Chapitre 4. Modélisation de l’ARN VHB chez des patients traités par inhibiteurs de capsidé

4.1. Résumé

Précédemment, nous avons développé un nouveau modèle de cinétique virale décrivant la cinétique de l’ADN viral, de l’AgHBs et des anticorps associés chez des souris traitées par un agoniste du TLR7. Il existe cependant un autre marqueur : l’ARN VHB sécrété conjointement aux virions et aux sous particules virales et qui demeure détectable en dépit du traitement (Liu et al., 2019).

Dans ce second travail, nous avons étudié l’effet du RG7907, un inhibiteur de capsidé (CAM) actuellement en phase II. Le RG7907 est une molécule prometteuse qui en bloquant l’étape d’encapsidation, réduit la production d’ADN et d’ARN VHB. Cependant, nous manquons actuellement de modèle permettant de caractériser conjointement la cinétique des deux marqueurs et d’estimer l’efficacité de ce nouveau traitement. Pour répondre à ces questions nous avons dans un premier temps analysé les données de phase Ib recueillies chez 35 patients en infection chronique et naïfs de traitement antérieur. Nous avons développé un modèle multi-échelle intégrant des étapes ignorées jusqu’alors comme la transcription de l’ARN en ADN au niveau intracellulaire et le taux de sécrétion des particules virales (voir section 1.2.1.). Dans ce modèle, l’ARN pré-génomique (*pgRNA*) est encapsidé au sein des cellules infectées à une vitesse α et subit la transcription inverse à une vitesse π pour donner naissance aux particules d’ADN intracellulaires, les *rcDNA*. La sécrétion se produit à une vitesse ρ donnant lieu à l’ARN et l’ADN VHB circulants. Le modèle ainsi développé décrit correctement les données d’ADN et d’ARN observées sous CAM. L’efficacité du RG7907 sur le blocage de l’encapsidation est de 99% et se traduit par un déclin biphasique de l’ARN et d’ADN VHB chez l’ensemble des individus. L’analyse de covariables montre qu’outre des niveaux de production d’ARN encapsidés plus faible, les individus AgHBe négatifs sont plus sensibles à RG7907 : l’efficacité de 99,3% contre 98,3% chez les individus HBe positifs. Une prédiction du modèle est que l’ARN décroît plus rapidement que l’ADN. En effet, le blocage de l’encapsidation des *pgRNA* par les inhibiteurs de capsidé entraîne un déclin rapide des concentrations d’ARN dans le sang à une vitesse proche de leur vitesse de clairance c . A l’initiation du traitement, les particules

rcDNA sont quant à elles sécrétées plus lentement à une vitesse ρ limitant le déclin observé d'ADN. Après cette décroissance initiale, les deux marqueurs déclinent de façon parallèle à une vitesse commune δ traduisant la vitesse d'élimination des cellules infectées ($t_{1/2} \cong 6 \pm 0,8$ jours). Les prédictions sous CAM ont dans un second temps été comparées à celles obtenues sous NUC. Pour cela, le modèle a été appliqué aux données de 51 patients traités par ténofovir pendant 4 semaines (Agarwal et al., 2015). Compte-tenu du fait que seules les données d'ADN VHB étaient disponibles, nous avons utilisé les paramètres précédemment estimés sous inhibiteurs de capsid et estimé l'efficacité du ténofovir sur le blocage de transcriptase inverse. Outre une efficacité de 99,99%, le modèle prédit que le ténofovir conduit à une augmentation transitoire des concentrations d'ARN VHB au cours de la première semaine de traitement alors que l'ADN suit une décroissance biphasique similaire à celle observée sous CAM.

En conclusion, ce travail présente le premier modèle de cinétique virale prenant en compte simultanément la dynamique de l'ARN et de l'ADN VHB. Le modèle met en évidence les différences de cinétique attendues entre les deux marqueurs chez des patients traités par CAM ou NUC. Il montre l'utilité des inhibiteurs de capsid pour réduire l'ARN VHB et suggère que l'utilisation des deux molécules en combinaison permettrait de réduire fortement l'ADN et l'ARN VHB. Ce travail a fait l'objet d'un article accepté en octobre 2020 dans *Journal of Viral Hepatitis* et présenté ci-dessous.

4.2. Article 2: What drives the dynamics of HBV RNA during treatment?



What drives the dynamics of HBV RNA during treatment?

Antonio Gonçalves¹ | Annabelle Lemenuel-Diot² | Valérie Cosson² | Yuyan Jin³ | Sheng Feng³ | Qingyan Bo⁴ | Jérémie Guedj¹

¹Université de Paris, INSERM, IAME, Paris, France

²Pharmaceutical Sciences, Roche Pharmaceutical Research and Early Development, Roche Innovation Center, Basel, Switzerland

³Clinical Pharmacology, Pharmaceutical Sciences, Roche Pharma Research & Early Development, Roche Innovation Center Shanghai, Shanghai, China

⁴I2O DTA, Roche Pharma Research & Early Development, Roche Innovation Center Shanghai, Shanghai, China

Correspondence

Antonio Gonçalves, Université de Paris, IAME INSERM U1137, 16 rue Henri Huchard 75018, Paris, France.
Email: antonio.goncalves@inserm.fr

Funding information

Roche Pharmaceutical Research and Early Development

Abstract

Hepatitis B virus RNA (HBV RNA)-containing particles are encapsidated pre-genomic RNA (pgRNA) detectable in chronically infected patients in addition to virions (HBV DNA) that have been suggested as a marker of the treatment efficacy. This makes promising the use of core protein allosteric modulators, such as RG7907, which disrupt the nucleocapsid assembly and profoundly reduce HBV RNA. Here, we developed a multiscale model of HBV extending the standard viral dynamic models to analyse the kinetics of HBV DNA and HBV RNA in 35 patients treated with RG7907 for 28 days. We compare the predictions with those obtained in patients treated with the nucleotide analog tenofovir. RG7907 blocked 99.3% of pgRNA encapsidation (range: 92.1%–99.9%) which led to a decline of both HBV DNA and HBV RNA. As a consequence of its mode of action, the first phase of decline of HBV RNA was rapid, uncovering the clearance of viral particles with half-life of 45 min. In contrast, HBV DNA decline was predicted to be less rapid, due to the continuous secretion of already formed viral capsids ($t_{1/2} = 17 \pm 6$ h). After few days, both markers declined at the same rate, which was attributed to the loss of infected cells ($t_{1/2} = 6 \pm 0.8$ days). By blocking efficiently RNA reverse transcription but not its encapsidation, nucleotide analog in contrast was predicted to lead to a transient accumulation of HBV RNA both intracellularly and extracellularly. The model brings a conceptual framework for understanding the differences between HBV DNA and HBV RNA dynamics. Integration of HBV RNA in viral dynamic models may be helpful to better quantify the treatment effect, especially in viral-suppressed patients where HBV DNA is no longer detectable.

KEY WORDS

core protein allosteric modulators, HBV RNA, hepatitis B, viral kinetics

1 | INTRODUCTION

Chronic infection with hepatitis B virus (HBV) affects nearly 260 million people worldwide and is the major cause of liver damage.^{1,2} Current treatments, such as pegylated interferon or nucleosidic analogs (NA), can effectively induce the loss of hepatitis B e-antigen (HBeAg) and result in the suppression of HBV DNA (virologic response in what are called virologically suppressed patients) and a normalization of liver transaminase enzymes (biochemical response).

However, these treatments do not achieve a high rate of clinical cure, defined as a sustained loss of HBsAg with or without seroconversion (also referred to as functional cure).³ This is particularly true for NA, which do not target the cccDNA, and therefore need to be taken life-long to keep the viral load undetectable and avoid a resurgence of the virus.

In virologically suppressed patients, an important question is the level of residual activity of the cccDNA.⁴ It has been suggested that hepatitis B virus RNA (HBV RNA)-containing particles could be a

good a marker of the residual activity of the virus and may therefore be predictive of disease evolution.^{5,6} These particles are made of encapsidated pre-genomic RNA (pgRNA) that are secreted by hepatocytes before the action of the reverse transcriptase, and are therefore not targeted by NA.^{5,7} Recently, two 4-week clinical trials investigating the effect of core protein allosteric modulators (CpAM) showed a profound decline of both HBV RNA and HBV DNA.^{8,9} Although longer duration studies are needed to assess the effect of CpAM on HBsAg loss, current data offer the opportunity to better understand the dynamics of HBV RNA in the perspective of a cure.

Following what has been done in other chronic infections, mathematical tools can be used to get insights on viral markers.^{12,13} To date, viral dynamic models of HBV have focused on the kinetics of HBV DNA in patients treated by nucleosidic analogs, but did not incorporate the kinetics of HBV RNA.¹⁴⁻¹⁶ In this paper, we developed a multiscale model of HBV integrating both intra- and extracellular processes of the infection to unravel the determinants of the kinetics of both HBV DNA and HBV RNA. The model was sequentially applied to two clinical trials with patients receiving either RG7907, a CpAM, or tenofovir, a nucleosidic analog.

2 | MATERIAL AND METHODS

2.1 | Ethical statement

The data used in this study are part of a multi-centre randomized, placebo-controlled, double-blinded clinical trial NCT02952924. The study protocol was approved by the institutional review boards and/or ethics committees of each study centre. The study was conducted in full conformance with the ICH E6 guideline for Good Clinical Practice and the principles of the Declaration of Helsinki, or the laws and regulations of the country in which the research was conducted. All participants have signed an informed consent form prior to their participation in the study.

2.2 | A multiscale model of HBV RNA and HBV DNA viral dynamics

We developed a model to describe the kinetics of HBV DNA and HBV RNA that extends previous models of HBV dynamics and takes into account the intracellular dynamics of HBV replication. The pool of target cells (of maximal size T_{max}) are infected by HBV DNA, noted V , at a rate β leading to the production of infected cells, I , that produce multiple messenger RNAs, in particular pre-genomic RNA (pgRNA). After nucleus export, pgRNAs are encapsidated at a constant rate α and form the pool of encapsidated pgRNA, noted R_{int} . They can then either be degraded at rate μ_R , transcribed into complete virions V_{int} by the polymerase at a rate π or secreted into bloodstream at a rate ρ_R to form the circulating HBV RNA, noted R .^{17,18} Similarly, V_{int} can be degraded at a rate μ_V or secreted as circulating HBV DNA particles at a rate ρ_V . Finally, both circulating HBV

DNA and HBV RNA can be cleared from bloodstream at rates c_V and c_R . Therapeutic agents disturbing this system are useful to tease out the determinants of the kinetics of viral products.¹⁹⁻²¹ We consider two types of treatments acting on different targets of the replication life cycle of HBV, namely core protein allosteric modulators (CpAM) and nucleosidic analogs (NA). CpAM act mainly by blocking the production of encapsidated pgRNA with an efficacy noted ϵ_{CpAM} . It has also shown that CpAM could inhibit de novo cccDNA formation, albeit with a much lower efficacy,^{11,22} and this effect was neglected in the following. NA act by blocking the production of complete virions with an efficacy ϵ_{NA} . Importantly as none of these two treatments has shown a significant drop of HBsAg or HBcrAg in the period of our study (see Supplemental File 1 Figure S1), these markers were not considered in the model. The multiscale model combining the intracellular and extracellular processes leading to the formation of HBV DNA and HBV RNA is given by the system of partial differential equations in Supplemental file 2.

In order to perform parameter estimation, this model was transformed into an ordinary differential equation (ODE) model following the methodology of Kitagawa et al^{23,24} and yields to Equations 1-5:

$$\frac{dI}{dt} = \beta V (T_{max} - I) - \delta I \quad (1)$$

$$\frac{dP}{dt} = (1 - \epsilon_{CpAM}) \alpha I - (\mu_R + \rho_R + \pi (1 - \epsilon_{NA}) + \delta) P \quad (2)$$

$$\frac{dQ}{dt} = (1 - \epsilon_{NA}) \pi P - (\mu_V + \rho_V + \delta) Q \quad (3)$$

$$\frac{dR}{dt} = \rho_R P - c_R R \quad (4)$$

$$\frac{dV}{dt} = \rho_V Q - c_V V \quad (5)$$

where P and Q are the total amount of intracellular RNA (R_{int}) and DNA (V_{int}), respectively (see Supplemental File 2). This model admits a basic reproduction number, defined as the number of cells infected by a single infected cell at the beginning of the infection, $R_0 = \beta T_{max} \alpha \pi \rho / (c \delta (\delta + \rho + \pi) (\delta + \rho))$. Both PDE and ODE models yield mathematically identical solutions (Supplemental File 2 Figure S1). Of note, an approximated analytical solution for V and R can be obtained by neglecting the number of new infections after treatment initiation (Supplemental File 2).

2.3 | RG7907 viral kinetics data

Model parameters were estimated using viral dynamics observed in a phase Ib study in 35 non-cirrhotic patients chronically infected by hepatitis B (see Supplemental File 1 Table S1).²⁵ Patients were treated during 28 days either by RG7907 ($n = 30$), with 5 different doses: 200, 600 or 1000 mg once daily (QD) or 200, 400 mg twice

daily (BID), or by placebo ($n = 5$). Patients were followed until day 112 after treatment initiation. Blood samples were taken pre-dose at days 7, 14, 21, 28, 35, 56, 84 and 112 after treatment initiation to measure HBV DNA, HBV RNA, HBsAg, HBeAg and HBcrAg (see Supplemental File 1 Figure S1).

2.4 | RG7907 pharmacokinetics

Samples for plasma pharmacokinetic of RG7907 and its metabolite were collected on day 1 at pre-dose and 1, 2, 3, 4, 6, 8 and 12 h post-dose and on day 28 at pre-dose and 1, 2, 3, 4, 6, 8 and 24 h post-dose. Pre-dose samples were also collected on days 2, 3, 4, 8, 15 and 22. After 28 days of dosing, RG7907 showed no accumulation in plasma (see Supplemental File 1 Figure S2 and S3). A mechanistic population PK model already developed was used using plasma PK data to predict the plasma concentrations and infer the liver quantities, noted AL by accounting for the known active and saturable liver uptake (see Supplemental File 1 Figure S4).

2.5 | Modelling the antiviral activity of RG7907

As liver is RG7907 site of action, we assumed that the drug effectiveness, noted $\epsilon_{CPAM}(t)$, depended on liver amounts of RG7907 and was given by:

$$\epsilon_{CPAM}(t) = \frac{A_L(t)}{EA_{50} + A_L(t)} \quad (6)$$

with EA_{50} the liver amount needed to achieve an effectiveness of 50%.

The individual average effectiveness, $\bar{\epsilon}_{CPAM}$, over a dosing time interval $[t_i, t_j]$ was defined as $\bar{\epsilon}_{CPAM} = 1/(t_j - t_i) \int_{t_i}^{t_j} \epsilon_{CPAM}(t) dt$.

2.6 | Modelling strategy

2.6.1 | Fixed parameter values

We supposed that clearance, secretion and degradation rates were similar for DNA- and RNA-containing particles, such that $c_R = c_V = c$, $\rho_R = \rho_V = \rho$ and $\mu_R = \mu_V = \mu$ (Figure 1). In our model, only the quantity $\mu + \rho$ can be identified. Thus, we assumed $\mu = 0$ and only estimated ρ . Because the clearance rate, c , could not be estimated due to lack of data on the very first days of treatment, we tested values of 1, 2, 5, 10 and 20 d^{-1} according to the range of values proposed in the literature.^{26–28} The value providing the lowest Bayesian information criteria (BIC) was kept and moved forward in the rest of the analysis. We used model averaging to take into account the uncertainty related to the value of c (see Supplemental File 3).²⁹ The pool of target cells available for infection was fixed to $1.3 \cdot 10^7 \text{ cells ml}^{-1}$.³⁰

2.6.2 | Statistical model

The structural model used to describe the observations Y_{ik} of the k th biomarker ($k = 1$ for HBV DNA and $k = 2$ HBV RNA) of subject i at time t_{ik} is

$$Y_{ik} = f(\theta_i, t_{ik}) + e_{ik} \quad (7)$$

where θ_i is the vector of parameters of subject i and e_{ik} the residual error.

Individual parameters θ_i followed a log-normal distribution or a logit-normal distribution (e.g., treatment effect parameters, ϵ_{NA}):

$$\theta_i = \mu \times \exp(\eta_i) \quad (8)$$

$$\theta_i = \frac{\exp(\mu + \eta_i)}{1 + \exp(\mu + \eta_i)} \quad (9)$$

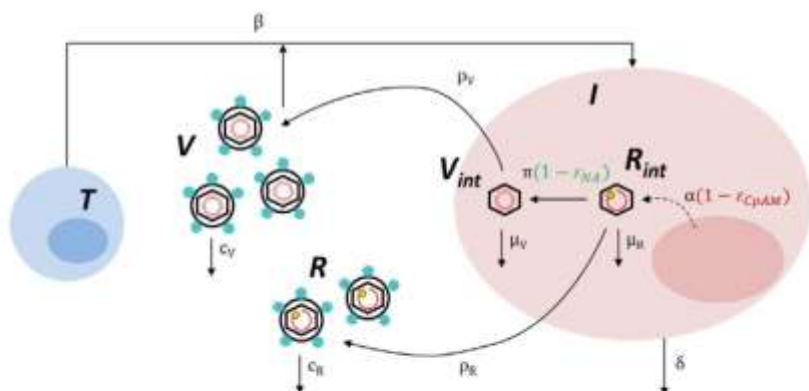


FIGURE 1 Schematic representation of the multiscale model of HBV. Target cells T (blue cell) are infected by viruses V at a rate β and give an infected cell I (red cell). While I are lost with rate δ , they produce intracellular RNA R_{int} at a rate α . R_{int} are either secreted into bloodstream at a rate ρ , degraded at a rate μ or converted into complete DNA particle V_{int} intracellularly. After secretion circulating DNA and RNA (V and R) die at a per capita rate c .

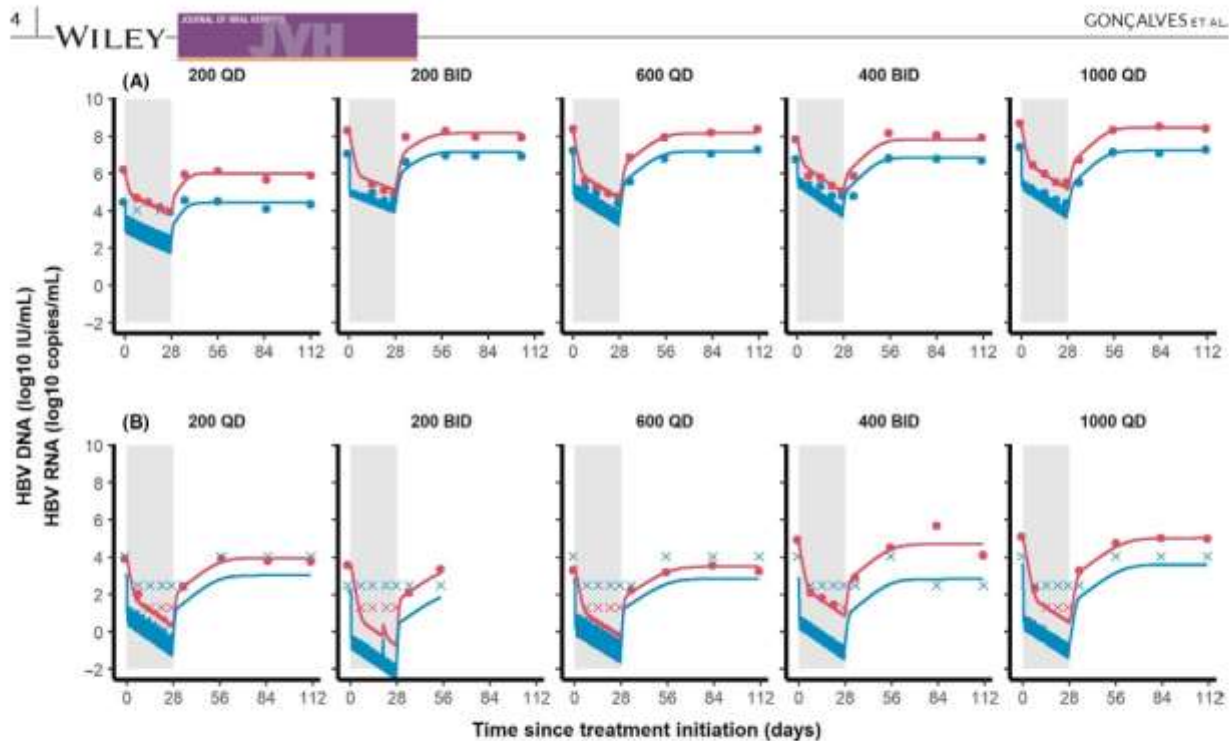


FIGURE 2 Individual fits of HBV DNA (red) and HBV RNA (blue) in randomly selected individuals during on-treatment (grey area) and follow-up period (white area). (A) HBeAg-positive patients. (B) HBeAg-negative patients. Full dots are the observed measurements while crosses are the measurements below the limit of detection. Lines are the individual predictions obtained with the model. Viral load oscillation is due to varying drug concentrations over time. Individuals were selected by drawing randomly one ID per dose and HBeAg group

where μ indicates the fixed effects and η_i indicates the random effects, supposed to follow a normal distribution of mean zero and standard deviation ω . The residual error e_{ik} is assumed to follow a normal distribution of mean zero and constant standard deviation σ_k . A backward procedure was performed to select the random effects and was stopped once the BIC did not decrease anymore. Then, we screened the random effects for correlations based on the empirical Bayes estimates (EBE). Only correlations with a Pearson's coefficient > 0.8 were implemented in the model.

2.6.3 | Covariate model

To build our covariate model, a 2-step procedure was used. In the first step, we screened for association between covariates and individual parameters using the Kruskal-Wallis, Wilcoxon's or Pearson's correlation tests, and only association with p -values $< .1$ were retained. In the second step, a forward procedure was used to build the covariate model and only covariates leading to a more than 2 points decrease in the Bayesian information criteria (BIC) were kept. At the end of the selection procedure, we verified the significance of all covariates and we provided p -values obtained by Wald test for each covariate. Among the five covariates tested, four were categorical (ethnicity, gender, e-antigen status and HBV genotype) and one was continuous (body mass index). For categorical covariates,

classes White, male, e-antigen positive and genotype C were considered as reference groups.

2.7 | Estimation of NA efficacy

To assess the efficacy of NA given by our model, we digitized the individual data (using Plot Digitizer v.2.6.8.) of a phase 1b study where tenofovir (TAF or TDF) was administered to 51 patients. In this study, only HBV DNA was assessed through a frequent sampling schedule on days 1, 2, 5, 8, 10, 15, 19, 22 and 29.³¹ Patients were randomly allocated in 5 groups to receive either TAF in doses of 8, 25, 40 and 120 or TDF at the dose of 300 mg. Since we did not have access to dynamics of HBV RNA, nor the patients' covariates in this study, we fixed disease-related parameters to their estimates given by the CpAM model without covariates (see Supplemental File 4 Table S1) and estimated the efficacy ϵ_{NA} .

2.8 | Simulations of the kinetics of HBV DNA and HBV RNA in patients treated by CpAM, NA or the combination

Using the model parameter estimates, we simulated the time course of HBV DNA and HBV RNA in 1000 individuals treated by CpAM,

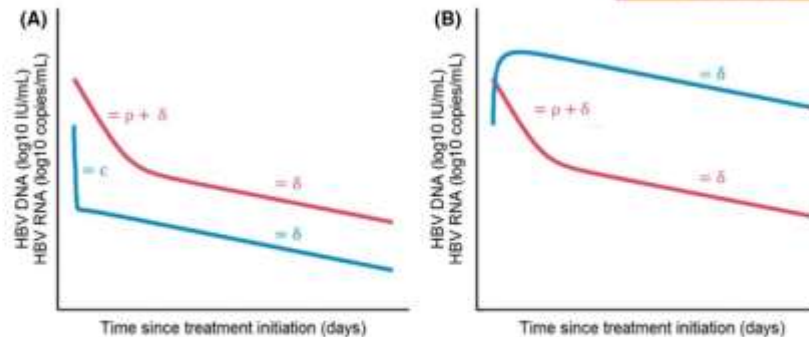


FIGURE 3 Theoretical profiles of HBV DNA (red) and HBV RNA (blue) in HBeAg-positive patients treated by CpAM or NA supposing that $c \neq \rho$. (A) During CpAM therapy, both HBV DNA and HBV RNA follow a biphasic decline. However, mechanism of the first decline differs for both markers: viral c for HBV RNA and secretion plus loss rate of infected cells $\rho + \delta$ for HBV DNA. (B) During NA therapy, HBV DNA follows the same dynamics as in NA-treated patients but due to a blocking of the reverse transcription, HBV RNA can accumulate within a cell. To generate those profiles, we supposed that the treatments are sufficiently potent to neglect the number of novel infections

NA or CpAM + NA during 28 days. Design and baseline characteristics were identical to those in the CpAM study. For each group, the median and the 90% prediction interval of HBV DNA and HBV RNA in HBeAg-positive and HBeAg-negative patients were reported.

2.9 | Parameter estimation

Parameters were estimated with the SAEM algorithm implemented in MONOLIX® software version 2018R2 allowing to handle the left censored data.³² Likelihood was estimated using the importance sampling method, and the Fisher information matrix (FIM) was calculated by stochastic approximation. Graphical and statistical analyses were performed using R version 3.4.3.

3 | RESULTS

3.1 | CpAM drug efficacy

To describe the dynamics of HBV RNA decline during and after treatment, we developed a model that incorporates the essential processes of HBV RNA and HBV DNA production. The model was first applied to a phase Ib study of chronically infected patients treated during 28 days by RG7907. At all doses investigated, RG7907 showed a robust decline for both HBV DNA and HBV RNA with a median reduction of 2.7 to 3.0 log₁₀ IU/ml and 2.1 to 2.6 copies/ml, respectively, over the 4-week period²³ (see Supplemental File 1 Figure S2).

All patients from all dosing groups were well fitted with both HBV DNA and HBV RNA following a biphasic decline during the 28 days of treatment by RG7907 (Figure 2 and Supplemental File 1 Figures S5 and S6). Antigen-e (HBeAg) status of patients was significantly associated with three parameters, namely α , the production rate of encapsidated pgRNA; EA₅₀, the in vivo liver amount of RG7907 leading to 50% of effectiveness; and R_0 , the basic reproduction number

(see Supplemental File 4 for details). First, we found that HBeAg-positive patients produced more encapsidated pgRNA than HBeAg-negative patients (522 vs. 0.55 copies cell⁻¹ d⁻¹, $p = 4.10^{-14}$). Of note, the HBV DNA/HBV RNA ratio at baseline is constant in HBeAg-positive and HBeAg-negative patients and given by π and estimated to 98.2 d⁻¹. Second, the EA₅₀ was higher in HBeAg-positive patients than in HBeAg-negative patients (251 vs. 53.4 ng, $p = 1.10^{-2}$). Using an in-house pharmacokinetic model of both RG7907 and its metabolite, we predicted at all doses, high individual liver amounts of RG7907 (Supplemental File 1 Figure S4), 40- to 1000-fold larger than the estimated EA₅₀, thus leading to an effectiveness of 98.3 and 99.3% on average, in HBeAg-positive and HBeAg-negative patients, respectively.

Finally, in all patients, both plasma HBV DNA and HBV RNA returned to pretreatment equilibria few weeks after the end of treatment. The rate at which this new equilibrium is reached mostly depends on R_0 . In our study, HBeAg-positive patients were associated with a greater R_0 as compared to HBeAg-negative patients (3.17 vs. 2.05, $p = 2.10^{-3}$), thus leading to a faster rebound.

3.2 | Kinetics of HBV DNA and HBV RNA during CpAM

How to interpret the prediction that HBV RNA decline is more rapid than HBV DNA? With CpAM efficiently blocking the formation of encapsidated pgRNA and pgRNA being rapidly converted into DNA (at a rate α), treatment leads to an immediate blocking of HBV RNA particles. Thus, circulating HBV RNA declines rapidly with a rate close to its natural clearance rate, c (Figure 3A). Given the lack of data in the first 7 days of treatment, c could not be precisely estimated and different values were tested, with the best fit obtained with c equal to 20 d⁻¹ ($t_{1/2} = 45$ min). However, models with viral clearances of 10 or 5 d⁻¹ could also well describe the data (BIC within 2-point difference with the best model, see Supplemental File 3), supporting the conclusion of a rapid viral clearance of the virus.

HBV DNA was predicted to decline more slowly, due to the presence of intracellular DNA that is secreted with rate ρ after treatment initiation. Thus, the decline of HBV DNA after treatment initiation was attributed to the secretion rate of DNA particles, with a rate ρ estimated to 1 d^{-1} .

After few days, a novel equilibrium is reached for the intracellular viral levels of both R_{int} and V_{int} . At the circulation level, this corresponds to the second phase of the virus where both HBV DNA and HBV RNA decline in parallel with a rate $\delta = 0.13 \text{ d}^{-1}$ corresponding to a half-life of infected cells of 5.3 days.

3.3 | Viral dynamics in patients treated with NA

Next, we analysed the predictions of our model in patients receiving a nucleosidic analog, namely TAF or TDF. The trial included both HBeAg-positive ($n = 24$) and HBeAg-negative ($n = 27$) patients, and showed a dose-independent decline of HBV DNA ranging from -2.2 to $-2.8 \log_{10} \text{ IU/ml}$ over a 4-week period.³¹ Since parameters related to intracellular viral production could not be estimated based on HBV DNA data only, they were fixed to estimates obtained previously (Table 1). The model provided good individual predictions of HBV DNA decline during treatment (up to $-2 \log_{10} \text{ copies ml}^{-1}$). We

estimated the effectiveness of tenofovir, r_{NA} , to 0.9999.

Although the data used here were only HBV DNA, we used the model to infer the kinetics of HBV RNA and we predicted a

transient increase in HBV RNA levels during the first week of therapy (Figure 4), of $1.9 \log_{10} \text{ copies ml}^{-1}$. The difference between HBV RNA kinetics during CpAM and NA treatment relies on the different mechanism of action of both drugs. In contrast to CpAM, NA do not block encapsidated pgRNA, leading to an accumulation of HBV RNA intracellularly, that eventually leads to an increased level in circulation (Figure 3B). However, both treatments have similar effects on HBV DNA, leading to a reduced production and a decline with a rate $-\rho$ corresponding to the progressive secretion into the circulation of the remaining intracellular HBV DNA particles.

3.4 | Predicted viral dynamics in patients treated with CpAM + NA combination

Finally, using the parameters obtained during CpAM and NA therapy, we simulated the time course of HBV DNA and HBV RNA in 1,000 HBeAg-positive or HBeAg-negative patients treated either by CpAM, NA or CpAM + NA during 28 days. Assuming that the two drugs have the same efficacy in combination as in monotherapy, the model predicts that CpAM + NA could lead to a larger drop of HBV DNA after 28 days of treatment in HBeAg-negative and HBeAg-positive patients as compared to each monotherapy, with drops of 6.0 ± 1.3 and $5.3 \pm 1.4 \log_{10}$, respectively (Figure 5). The effect on HBV RNA would be less pronounced in combination as compared to CpAM monotherapy with a drop of 2.0 ± 1.1 to $1.3 \pm 1.2 \log_{10}$ after 28 days of treatment in HBeAg-negative and HBeAg-positive patients, respectively.

TABLE 1 Parameter estimates of the multiscale model with covariates

Parameters	Fixed effects		Between-subject variability ω (%) (RSE, %)
	Estimates (RSE, %)		
R_0 (HBeAg positive)	3.17 (12)	26.0 (23)	
R_0 (HBeAg negative) [*]	2.05 (9.1)		
α (HBeAg positive) (copies cell ⁻¹ d ⁻¹)	522 (67)	263 (13)	
α (HBeAg negative) (copies cell ⁻¹ d ⁻¹) ^{**}	0.55 (62)		
π (d ⁻¹)	98.2 (24)	81.7 (18)	
ρ (d ⁻¹)	1.00 (18)	0 (-)	
c (d ⁻¹)	20.0 (-)	0 (-)	
δ (d ⁻¹)	0.13 (7)	25.8 (26)	
EA_{50} (HBeAg positive) (ng)	251 (43)	147 (18)	
EA_{50} (HBeAg negative) (ng) ^{***}	53.4 (54)		
σ_{DNA}	0.327 (5)		
σ_{RNA}	0.365 (7)		

* $P = 2.10^{-3}$.

** $P = 4.10^{-14}$.

*** $P = 1.10^{-2}$.

4 | DISCUSSION

HBV RNA is a marker that has gained a lot of interest, particularly as a potential marker of the intrahepatic transcriptional activity. Here, we introduced a model allowing to tease out the mechanisms driving the kinetics of both HBV DNA and HBV RNA that can be used to understand the effects of drugs having different mechanisms of action. We used this model to compare the viral kinetics in patients treated with RG7907, a CpAM, and tenofovir alafenamide, a nucleosidic analog.

For all the doses investigated, CpAM achieved a high effectiveness in blocking the formation of capsids, with an efficacy estimated to 98.3% and 99.3% in HBeAg-positive and HBeAg-negative patients, respectively. This leads to a biphasic decline of both HBV RNA and HBV DNA during treatment, but the first phase of decline of each marker was different and directly related to the drug mechanism of action. We predict that CpAM leads to a rapid decline of HBV RNA in bloodstream with a half-life of ~ 1 h. In contrast, CpAM does not affect already formed HBV DNA. Thus, we predict that HBV DNA declines more slowly with a rate that reflects the secretion of virus particles into the circulation with a half-life of ~ 17 h ($\log(2)/1$, see Table 1). After this initial decline, both HBV RNA and HBV DNA declined at a slower rate, reflecting the progressive loss of productively infected cells, with a half-life of 5.3 days.

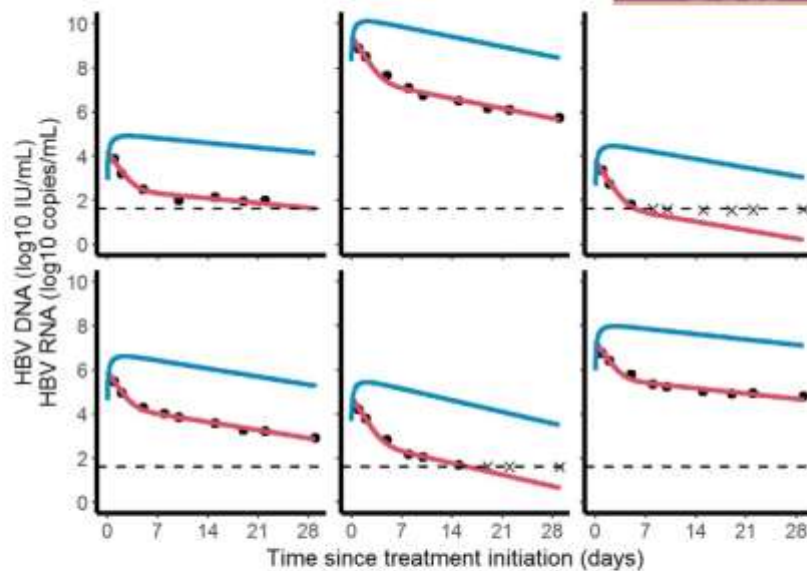


FIGURE 4 Individual predicted profiles of HBV DNA (red) and HBV RNA (blue) in tenofovir-treated patients (digitized data from Agarwal et al.³¹). Full dots are the observed data, and crosses are the data below the limit of detection (dashed line)

The model was also used to fit the viral dynamics in patients treated with tenofovir, a nucleosidic analog. With high level of efficacy in blocking the transcription ($\epsilon_{NA} = 99.99\%$), we found that tenofovir leads to a rapid decline of HBV DNA similar to what was found during CpAM treatment, while HBV RNA was predicted to increase in the circulation. This finding, consistent with the observed measurements in vitro and in transgenic mice,⁵ enhances the current knowledge of HBV RNA kinetics under NA therapy. In particular, we show that HBV RNA may transiently increase in the first days of treatment reflecting the accumulation of pgRNA in infected cells before decreasing in the long run as shown by Liu et al.³³ Our model also predicted that NA treatment leads to an increase in the ratio of HBV RNA/HBV DNA, from 0.01 at baseline to up to 100 after a couple of weeks (Figure 5).^{5,7} Interestingly, we predicted that this increase was also likely to occur during treatment combination of CpAM + NA.

Thus, unlike standard models of HBV,^{20,34} our model suggests that the slow initial decline of HBV DNA observed during NA or CpAM treatment does not reveal a fundamentally slower clearance rate of the virus as compared to other viruses, such as HCV or HIV. In fact, our model suggests that the clearance rate of HBV could be similar to what was found for these viruses, approximately ~ 1 h.^{21,35} This prediction is not novel and was already proposed by other models of HBV intracellular replications.^{26,27} As explained above, the fact that HBV DNA declines much more slowly than HCV RNA may be due to the fact that current drugs do not directly perturb its secretion (as found for instance with HCV NS5A inhibitors¹³). Consequently, large quantities of HBV DNA, that are already pre-formed, continue to be secreted after treatment initiation. One prediction of the model is that HBV RNA declines with the viral clearance rate and hence faster than HBV DNA which declines at the pace of the secretion.

Interestingly, data obtained with other CpAM, such as NVR-3378, JNJ-6379 or ABI H-2158, a similar rate of decline for HBV DNA and HBV RNA thanks to early time point measurements.^{10,36} This discrepancy may be due to the drug pharmacokinetic properties. In fact, these drugs have a slow accumulation rate as compared to RG7907. When adjusting for the increasing drug efficacy in the first days of treatment to mimic the PK accumulation,³⁷ our model well reproduces a slower HBV RNA decay rate comparable to the one of HBV DNA (Supplemental File 2 Figure S3). Still, more frequent data in the first week of treatment are needed to validate this finding.

The model was also used to provide insights on the influence of HBeAg status on viral dynamic parameters. HBeAg-negative patients had a lower rate of production of encapsulated pgRNA (522 and 0.55 copies cell⁻¹ d⁻¹ in HBeAg-positive and HBeAg-negative patients, respectively, $p < 10^{-6}$). This difference is consistent with the fact that HBeAg-positive patients have greater number of copies of cccDNA per cell than HBeAg-negative patients.^{17,27,38} Further HBeAg-positive patients had a larger basic reproduction number R_0 as compared to HBeAg negative patients, consistent with the fact that HBeAg is a marker of infectivity and of transcriptional activity of HBV.³⁹ As a consequence of its presumably higher rate of secondary infection, HBeAg-positive patients had a faster viral rebound after treatment cessation than HBeAg-negative patients. No difference was found for the rate of encapsulated pgRNA transcription into intracellular DNA particles that was found rapid and equal to 98.2 d⁻¹, consistent with the fact that HBV DNA are ~ 100 times larger in circulation than HBV RNA.

The model can also be used for clinical application to understand the long-term virological decline. After few days of treatment, HBV DNA and HBV RNA decayed with a rate δ equal to 0.13 d⁻¹ that was similar for both treatment. This value is

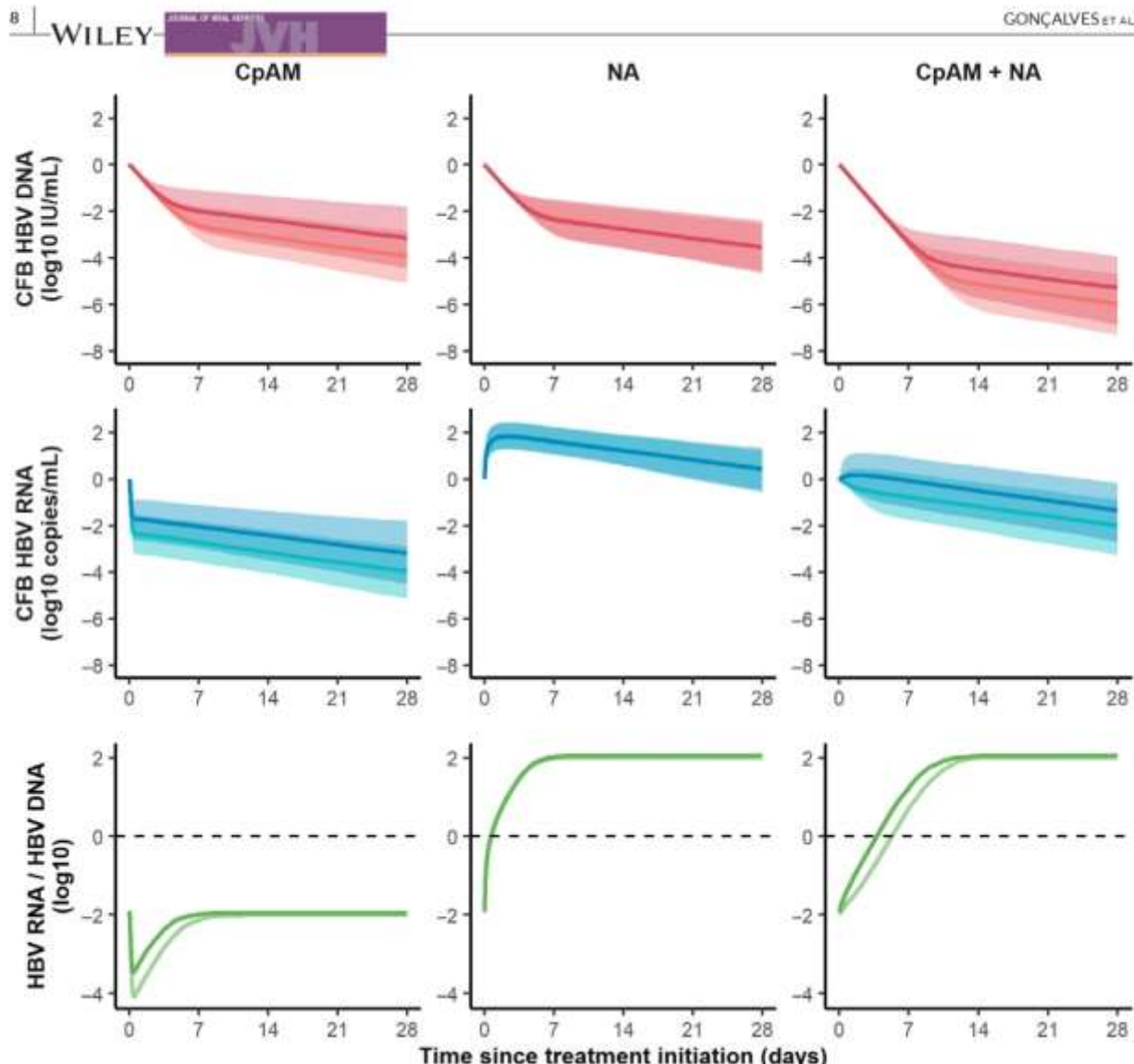


FIGURE 5 Simulated changes from baseline (CFB) of HBV DNA (red) and HBV RNA (blue), as well as evolution of HBV RNA/HBV DNA ratio (green) in CpAM-, NA- or CpAM + NA-treated patients. Dark and light lines represent the simulated outcome in HBeAg-positive and HBeAg-negative patients, respectively. Areas represent the 95% confidence interval around the predictions

consistent with what was found in other studies.^{20,40} However, long-term decay rate of HBV DNA and HBsAg is low under NA therapy ($\sim 0.01 \text{ d}^{-1}$),^{41,42} suggesting that this rate may rapidly slow down due to various reasons. There exist various hypotheses to explain why the long-term decay rate of virus is slow, such as the presence of integrated DNA (producing mainly HBsAg) differently affected by NA therapy. Another hypothesis suggested by our model could be that HBV RNA particles, that contain the material necessary for replication (i.e., a copy of the pgRNA and the viral polymerase), contribute to cell infection and maintain the residual levels of DNA and HBsAg in the long run. In that respect, it will be interesting to see whether combination of NA with CpAM would increase the long-term decline of HBV DNA and increase the rates of HBsAg seroclearance.

CONFLICT OF INTEREST

Jérémie Guedj has served as a consultant for F. Hoffmann-La Roche.

ORCID

Antonio Gonçalves <https://orcid.org/0000-0002-8759-2429>

REFERENCES

1. Hou J, Liu Z, Gu F. Epidemiology and prevention of hepatitis B virus infection. *Int J Med Sci.* 2005;2(1):50-57, others
2. Zeisel MB, Lucifora J, Mason WS, et al. Towards an HBV cure: state-of-the-art and unresolved questions—report of the ANRS workshop on HBV cure. *Gut.* 2015;64(8):1314-1326. <https://doi.org/10.1136/gutjnl-2014-308943>
3. Lampertico P, Agarwal K, Berg T, et al. EASL 2017 Clinical Practice Guidelines on the management of hepatitis B virus

- infection. *J Hepatol.* 2017;67(2):370-398. <https://doi.org/10.1016/j.jhep.2017.03.021>
4. Wang J, Yu Y, Li G, et al. Relationship between serum HBV-RNA levels and intrahepatic viral as well as histologic activity markers in entecavir-treated patients. *J Hepatol.* 2018;68(1):16-24. <https://doi.org/10.1016/j.jhep.2017.08.021>
 5. Wang J, Shen T, Huang X, et al. Serum hepatitis B virus RNA is encapsidated pregenome RNA that may be associated with persistence of viral infection and rebound. *J Hepatol.* 2016;65(4):700-710. <https://doi.org/10.1016/j.jhep.2016.05.029>
 6. Wang J, Yu Y, Li G, et al. Natural history of serum HBV-RNA in chronic HBV infection. *J Viral Hepat.* 2018;25(9):1038-1047. <https://doi.org/10.1111/jvh.12908>
 7. Jansen L, Kootstra NA, van Dord KA, Takkenberg RB, Reesink HW, Zaaijer HL. Hepatitis B virus pregenomic RNA is present in virions in plasma and is associated with a response to pegylated interferon Alfa-2a and Nucleos(t)ide analogues. *J Infect Dis.* 2016;213(2):224-232. <https://doi.org/10.1093/infdis/jiv397>
 8. Liang TJ, Block TM, McMahon BJ, et al. Present and future therapies of hepatitis B: from discovery to cure: VIRAL HEPATITIS, Hepatology. 2015;62(6):1893-1908. <https://doi.org/10.1002/hep.28025>
 9. Wang X-Y. Emerging antivirals for the treatment of hepatitis B. *WJG.* 2014;20(24):7707. <https://doi.org/10.3748/wjg.v20.i24.7707>
 10. Yuen MF, Gane EJ, Kim DJ, et al. Antiviral activity, safety, and pharmacokinetics of capsid assembly modulator NVR 3-778 in patients with chronic HBV infection. *Gastroenterology.* 2019;156(5):1392-1403.e7. <https://doi.org/10.1053/j.gastro.2018.12.023>
 11. Zoulim F, Lenz O, Vandebosch JJ, et al. JNJ-56136379, an HBV capsid assembly modulator, is well-tolerated and has antiviral activity in a phase 1 study of patients with chronic infection. *Gastroenterology.* 2020;159(2):521-533.e9. <https://doi.org/10.1053/j.gastro.2020.04.036>
 12. Nguyen T, Guedj J. HCV kinetic models and their implications in drug development: HCV kinetic models and their implications. *CPT Pharmacometrics Syst Pharmacol.* 2015;4(4):231-242. <https://doi.org/10.1002/psp4.28>
 13. Guedj J, Dahari H, Rong L, et al. Modeling shows that the NSSA inhibitor daclatasvir has two modes of action and yields a shorter estimate of the hepatitis C virus half-life. *PNAS.* 2013;110(10):3991-3996. <https://doi.org/10.1073/pnas.1203110110>
 14. Murray JM, Wieland SF, Purcell RH, Chisari FV. Dynamics of hepatitis B virus clearance in chimpanzees. *Proc Natl Acad Sci USA.* 2005;102(49):17780-17785.
 15. Sypsa V-A, Mimidis K, Tassopoulos NC, et al. A viral kinetic study using pegylated interferon alfa-2b and/or lamivudine in patients with chronic hepatitis B/HBeAg negative. *Hepatology.* 2005;42(1):77-85. <https://doi.org/10.1002/hep.20738>
 16. Tsiang M, Rooney JF, Toohey JJ, Gibbs CS. Biphasic clearance kinetics of hepatitis B virus from patients during adefovir dipivoxil therapy. *Hepatology.* 1999;29(6):1863-1869. <https://doi.org/10.1002/hep.510290626>
 17. Lesmana CRA, Jackson K, Lim SG, et al. Clinical significance of hepatitis B virion and SVP productivity: relationships between intrahepatic and serum markers in chronic hepatitis B patients. *United European Gastroenterol J.* 2014;2(2):99-107. <https://doi.org/10.1177/2050640614525151>
 18. Liu S, Zhou B, Valdes JD, Sun J, Guo H. Serum hepatitis B virus RNA: A new potential biomarker for chronic hepatitis B virus infection. *Hepatology.* 2019;69(4):1816-1827. <https://doi.org/10.1002/hep.30325>
 19. Neumann AU, Lam NP, Dahari H, et al. Hepatitis C viral dynamics in vivo and the antiviral efficacy of interferon-alpha therapy. *Science.* 1998;282(5386):103-107.
 20. Nowak MA, Bonhoeffer S, Hill AM, Boehme R, Thomas HC, McDade H. Viral dynamics in hepatitis B virus infection. *Proc Natl Acad Sci.* 1996;93(9):4398-4402.
 21. Ho DD, Neumann AU, Perelson AS, Chen W, Leonard JM, Markowitz M. Rapid turnover of plasma virions and CD4 lymphocytes in HIV-1 infection. *Nature.* 1995;373(6510):123-126. <https://doi.org/10.1038/373123a0>
 22. Berke JM, Dehertog P, Vergauwen K, et al. Capsid assembly modulators have a dual mechanism of action in primary human hepatocytes infected with hepatitis B virus. *Antimicrob Agents Chemother.* 2017;61(8):e00560-17. <https://doi.org/10.1128/AAC.00560-17>
 23. Kitagawa K, Nakao S, Asai Y, Watashi K, Iwami S. A PDE multiscale model of hepatitis C virus infection can be transformed to a system of ODEs. *J Theor Biol.* 2018;448:80-85. <https://doi.org/10.1016/j.jtbi.2018.04.006>
 24. Kitagawa K, Kuniya T, Nakao S, Asai Y, Watashi K, Iwami S. Mathematical analysis of a transformed ODE from a PDE multiscale model of hepatitis C virus infection. *Bull Math Biol.* 2019;81(5):1427-1441. <https://doi.org/10.1007/s11538-018-00564-y>
 25. Gane E, Yuen M-F, Bo Q, et al. RO7049389, a core protein allosteric modulator, demonstrates robust decline in HBV DNA and HBV RNA in chronic HBV infected patients. *J Hepatol.* 2019;70(1):e491. [https://doi.org/10.1016/S0022-1828\(19\)30964-8](https://doi.org/10.1016/S0022-1828(19)30964-8)
 26. Murray JM, Purcell RH, Wieland SF. The half-life of hepatitis B viruses. *Hepatology.* 2006;44(5):1117-1121. <https://doi.org/10.1002/hep.21364>
 27. Dandri M, Murray JM, Lutgehetmann M, Volz T, Lohse AW, Petersen J. Virion half-life in chronic hepatitis B infection is strongly correlated with levels of viremia. *Hepatology.* 2008;48(4):1079-1086. <https://doi.org/10.1002/hep.22469>
 28. Ribeiro RM, Germanidis G, Powers KA, et al. Hepatitis B virus kinetics under antiviral therapy sheds light on differences in hepatitis B e antigen positive and negative infections. *J Infect Dis.* 2010;202(9):1309-1318. <https://doi.org/10.1086/656528>
 29. Gonçalves A, Mentré F, Lemenuel-Diot A, Guedj J. Model averaging in viral dynamic models. *AAPS J.* 2020;22(2):48. <https://doi.org/10.1208/s12248-020-0426-7>
 30. Sherlock S, Dooley J. Diseases of the Liver and Biliary System, 11th edn. John Wiley & Sons; 2008.
 31. Agarwal K, Fung SK, Nguyen TT, et al. Twenty-eight day safety, antiviral activity, and pharmacokinetics of tenofovir alafenamide for treatment of chronic hepatitis B infection. *J Hepatol.* 2015;62(3):533-540. <https://doi.org/10.1016/j.jhep.2014.10.035>
 32. Samson A, Lavielle M, Mentré F. Extension of the SAEM algorithm to left-censored data in nonlinear mixed-effects model: Application to HIV dynamics model. *Comput Stat Data Anal.* 2006;51(3):1562-1574. <https://doi.org/10.1016/j.csda.2006.05.007>
 33. Liu S, Liu Z, Li W, et al. Factors associated with the biphasic kinetics of serum HBV RNA in patients with HBeAg-positive chronic hepatitis B treated with nucleos(t)ide analogues. *Aliment Pharmacol Ther.* 2020;52(4):692-700. <https://doi.org/10.1111/apt.15890>
 34. Neumann AU. Hepatitis B viral kinetics: A dynamic puzzle still to be resolved. *Hepatology.* 2005;42(2):249-254. <https://doi.org/10.1002/hep.20831>
 35. Ramratnam B, Bonhoeffer S, Binley J, et al. Rapid production and clearance of HIV-1 and hepatitis C virus assessed by large volume plasma apheresis. *Lancet.* 1999;354(9192):1782-1785. [https://doi.org/10.1016/S0140-6736\(99\)02035-8](https://doi.org/10.1016/S0140-6736(99)02035-8)
 36. Gane E, Schwabe C, Evançik M, et al. LBP-12-Phase 1a study of the safety, tolerability and pharmacokinetics of ABI-H, a novel second-generation HBV core inhibitor, healthy volunteers. *J Hepatol.* 2019;70(1):e146-e147. [https://doi.org/10.1016/S0022-1828\(19\)30258-0](https://doi.org/10.1016/S0022-1828(19)30258-0)
 37. Conway JM, Perelson AS. A hepatitis C virus infection model with time-varying drug effectiveness: solution and analysis. *Antia R, ed.*

- PLoS Comput Biol. 2014;10(8):e1003769. <https://doi.org/10.1371/journal.pcbi.1003769>
38. Ishida Y, Chung TL, Imanura M, et al. Acute hepatitis B virus infection in humanized chimeric mice has multiphasic viral kinetics. *Hepatology*. 2018;68(2):473-484. <https://doi.org/10.1002/hep.29891>
39. Gish RG, Given BD, Lai C-L, et al. Chronic hepatitis B: Virology, natural history, current management and a glimpse at future opportunities. *Antiviral Res*. 2015;121:47-58. <https://doi.org/10.1016/j.antiviral.2015.06.008>
40. Lewin SR, Ribeiro RM, Avihingsanon A, et al. Viral dynamics of hepatitis B virus DNA in human immunodeficiency virus-1-hepatitis B virus coinfecting individuals: Similar effectiveness of lamivudine, tenofovir, or combination therapy. *Hepatology*. 2009;49(4):1113-1121. <https://doi.org/10.1002/hep.22754>
41. Hadziyannis SJ, Tassopoulos NC, Heathcote EJ, et al. Adefovir dipivoxil for the treatment of hepatitis B e antigen-negative chronic hepatitis B. *N Engl J Med*. 2003;348(9):800-807. <https://doi.org/10.1056/NEJMoa021812>
42. Marcellin P, Lau GKK, Bonino F, et al. Peginterferon Alfa-2a alone, lamivudine alone, and the two in combination in patients with HBeAg-negative chronic hepatitis B. *N Engl J Med*. 2004;351(12):1206-1217. <https://doi.org/10.1056/NEJMoa040431>

SUPPORTING INFORMATION

Additional supporting information may be found online in the Supporting Information section.

How to cite this article: Gonçalves A, Lemuel-Diot A, Cosson V, et al. What drives the dynamics of HBV RNA during treatment?. *J Viral Hepat*. 2020;00:1-10. <https://doi.org/10.1111/jvh.13425>

Supplemental file 1**Supplementary Table S1: Baseline characteristics**

	200mg BID n=6	400mg BID n=6	200mg QD n=6	600mg QD n=6	1000mg QD n=7*	Placebo n=6*
Age, median (range)	41 (29-54)	35 (21-54)	34 (27-60)	43 (23-57)	47 (41-59)	46 (35-50)
Male, n (%)	5 (83.3%)	3 (83.3%)	5 (83.3%)	4 (66.7%)	3 (42.9%)	3 (50.0%)
BMI, median (range)	24.7 (29-54)	21.9 (29-54)	23.0 (29-54)	24.0 (29-54)	22.3 (29-54)	27.2 (29-54)
Race, n (%)						
Asian	5 (83.3%)	5 (83.3%)	5 (83.3%)	5 (83.3%)	7 (100%)	5 (83.3%)
White	1 (16.7%)	0	1 (16.7%)	1 (16.7%)	0	0
Other	0	1 (16.7%)	0	0	0	1 (16.7%)
HBeAg positive, n (%)	3 (50.0%)	3 (50.0%)	5 (83.3%)	2 (33.3%)	1 (14.3%)	2 (33.3%)
HBV DNA \log_{10} IU/mL, mean (SD)	4.85 (2.24)	6.83 (1.89)	6.75 (1.92)	5.34 (2.38)	5.35 (1.55)	6.35 (1.58)
HBsAg \log_{10} IU/mL, mean (SD)	3.61 (0.72)	4.31 (0.55)	3.69 (1.51)	3.47 (1.17)	3.16 (0.99)	3.39 (0.75)
HBV RNA \log_{10} copies/mL, mean (SD)	4.30 (1.80)	5.73 (2.00)	5.81 (1.62)	4.52 (2.06)	4.39 (1.63)	5.20 (1.42)

*: One patient discontinued on day 2 due to non-safety reason

Supplementary Table S1: Baseline characteristics (continued)

	200mg BID n=6	400mg BID n=6	200mg QD n=6	600mg QD n=6	1000mg QD n=7*	Placebo n=6*
ALT						
≤ 1.25 x ULN	6 (100%)	4 (66.7%)	5 (83.3%)	6 (100%)	7 (100%)	4 (66.7%)
1.25 – 10 x ULN	0	2 (33.3%)	1 (16.7%)	0	0	1 (16.7%)
> 10 x ULN	0	0	0	0	0	1 (16.7%)
HBV Genotype						
A	1 (16.7%)	0	0	0	0	0
B	0	2 (33.3%)	2 (33.3%)	4 (66.7%)	6 (85.7%)	3 (50.0%)
C	4 (66.7%)	3 (50.0%)	4 (66.7%)	1 (16.7%)	1 (14.3%)	3 (50.0%)
D	0	1 (16.7%)	0	0	0	0
Indeterminate	1 (16.7%)	0	0	1 (16.7%)	0	0

*: One patient discontinued on day 2 due to non-safety reason

Viral kinetics data

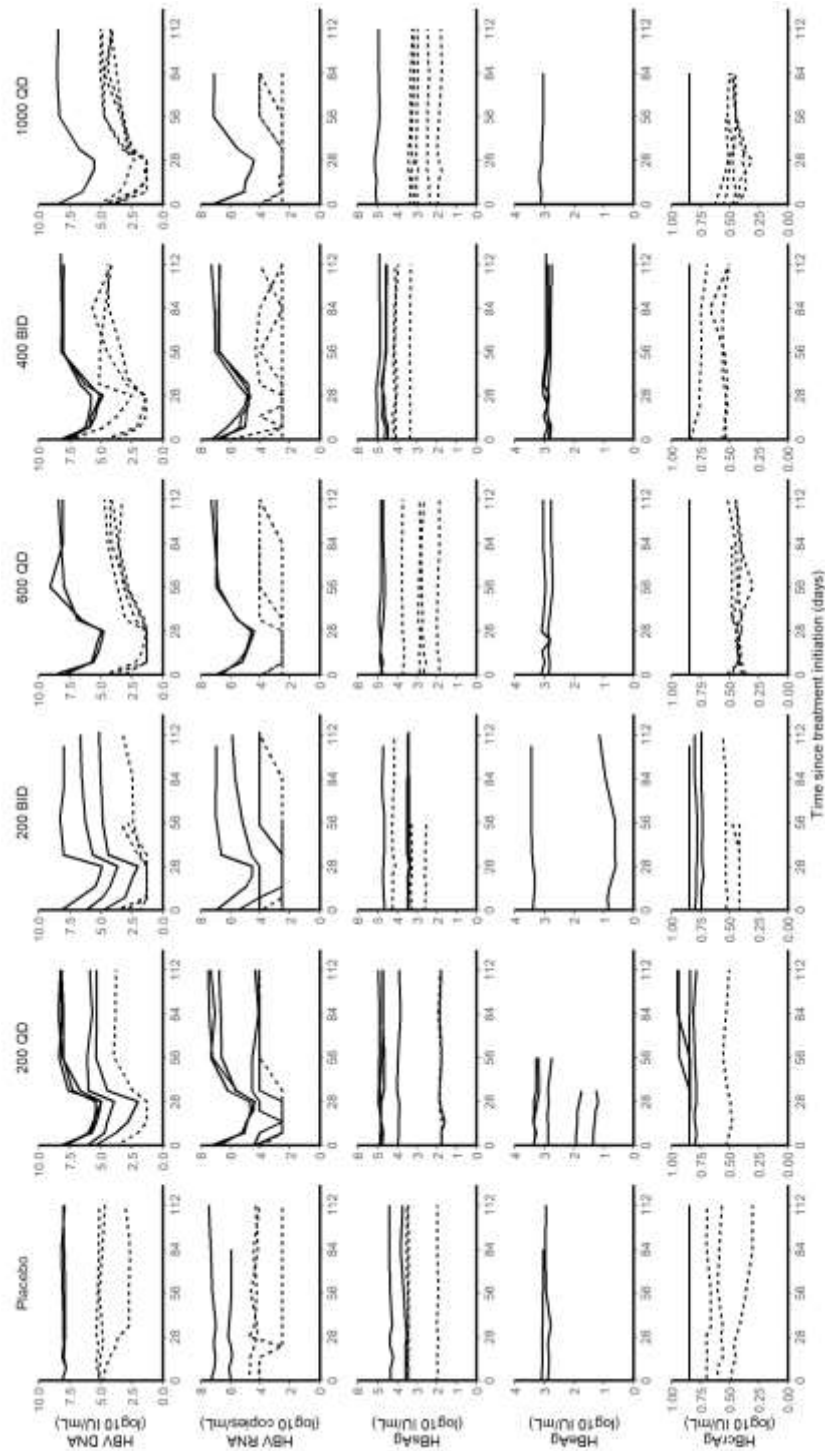


Figure S1: Individual time course of HBV DNA, HBV RNA, HBsAg, HBeAg and HBcAg during RG7907 trial. Solid lines represent HBeAg positive patients and dashed lines represent HBeAg negative patients. During the 28 first days (treatment duration) only HBV DNA and HBV RNA declined. HBsAg, HBeAg and HBcAg remained stable along the study duration.

RG7907 plasma concentrations

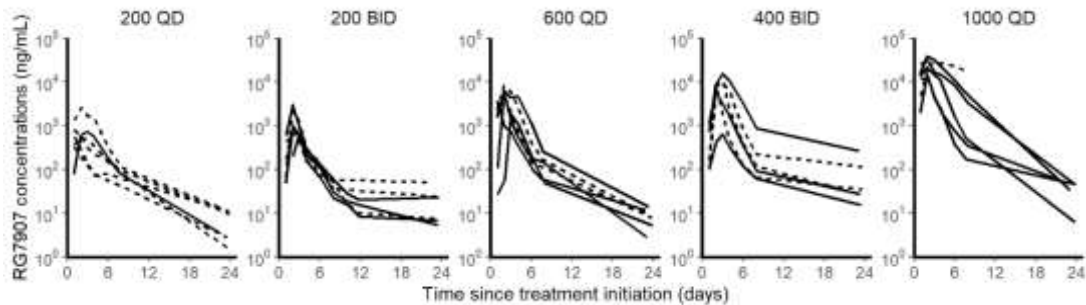


Figure S2: Individual RG7907 plasma concentrations at day 1. Solid lines represent HBeAg positive patients and dashed lines represent HBeAg negative patients.

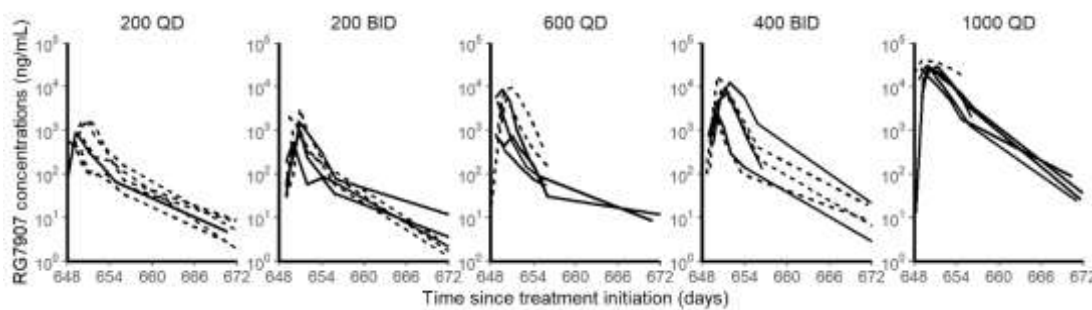


Figure S3: Individual RG7907 plasma concentrations at day 28. Solid lines represent HBeAg positive patients and dashed lines represent HBeAg negative patients. Concentration at day 28 remained similar to those at day 1 suggesting that absence of accumulation in plasma.

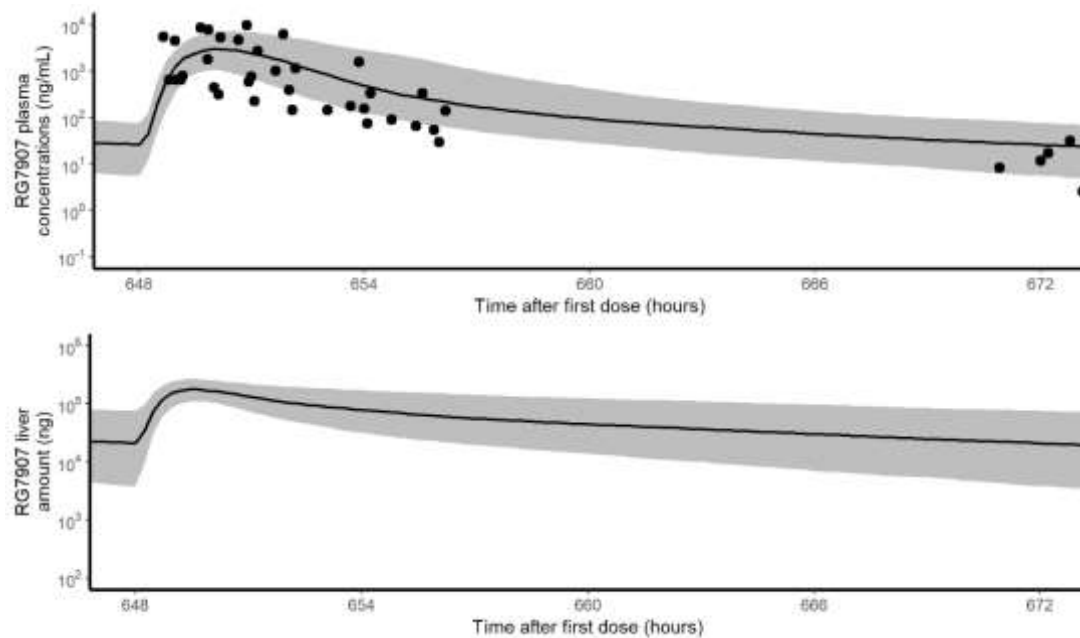


Figure S4: RG7907 simulated plasma concentration (top) and liver amount (bottom) at a dose of 600 mg QD at steady-state (Day28). Grey area represents the 90% prediction interval given by the PK model. Black dots are the observed PK data at day 28. The model well captures the plasma concentrations and allowed to simulate the liver amounts of RG7907.

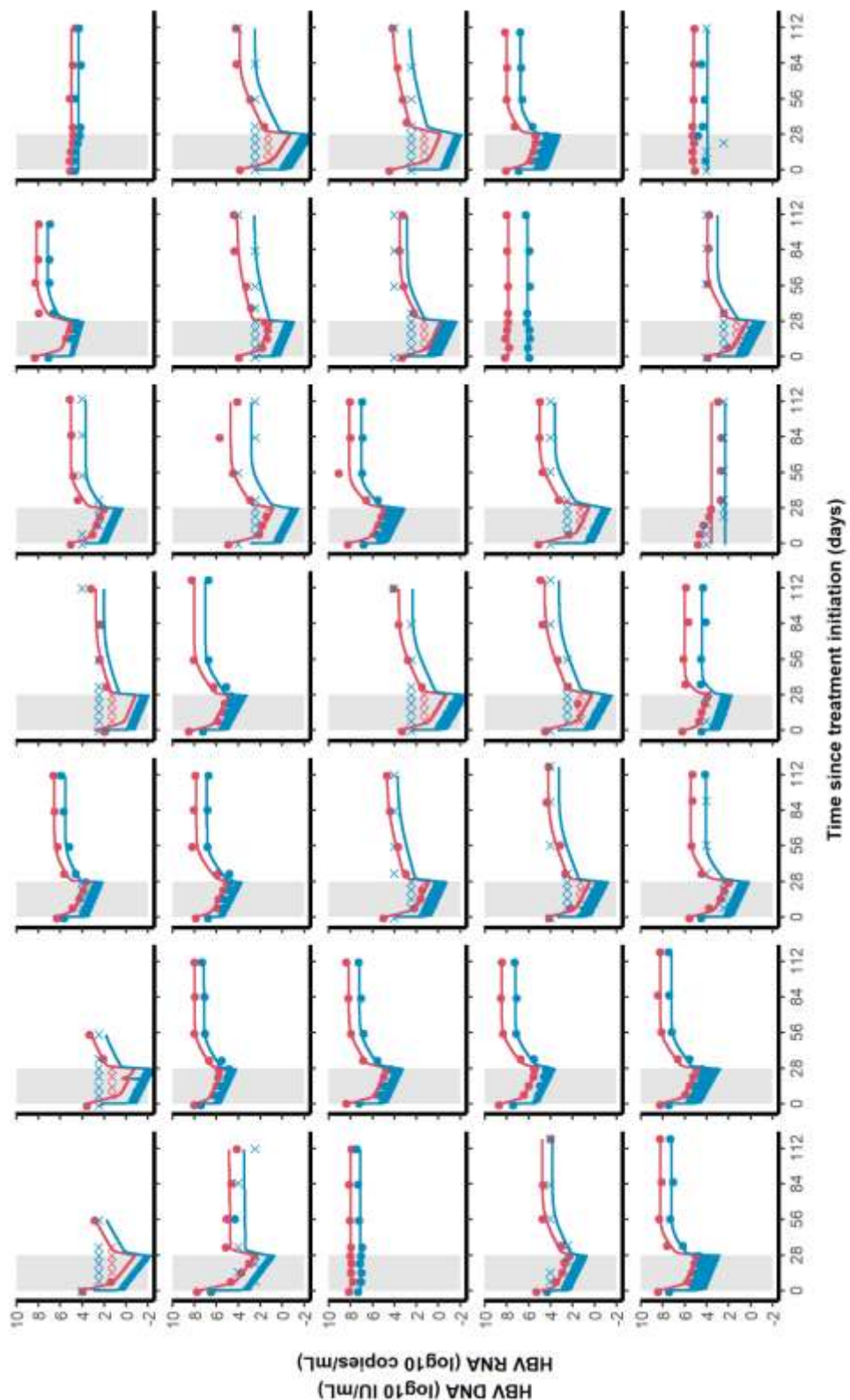


Figure S5: Individual fits of HBV DNA (red) and HBV RNA (blue). Full dots are the observed measurements while crosses are the measurements below the limit of detection. Lines are the individual predictions obtained with the model.

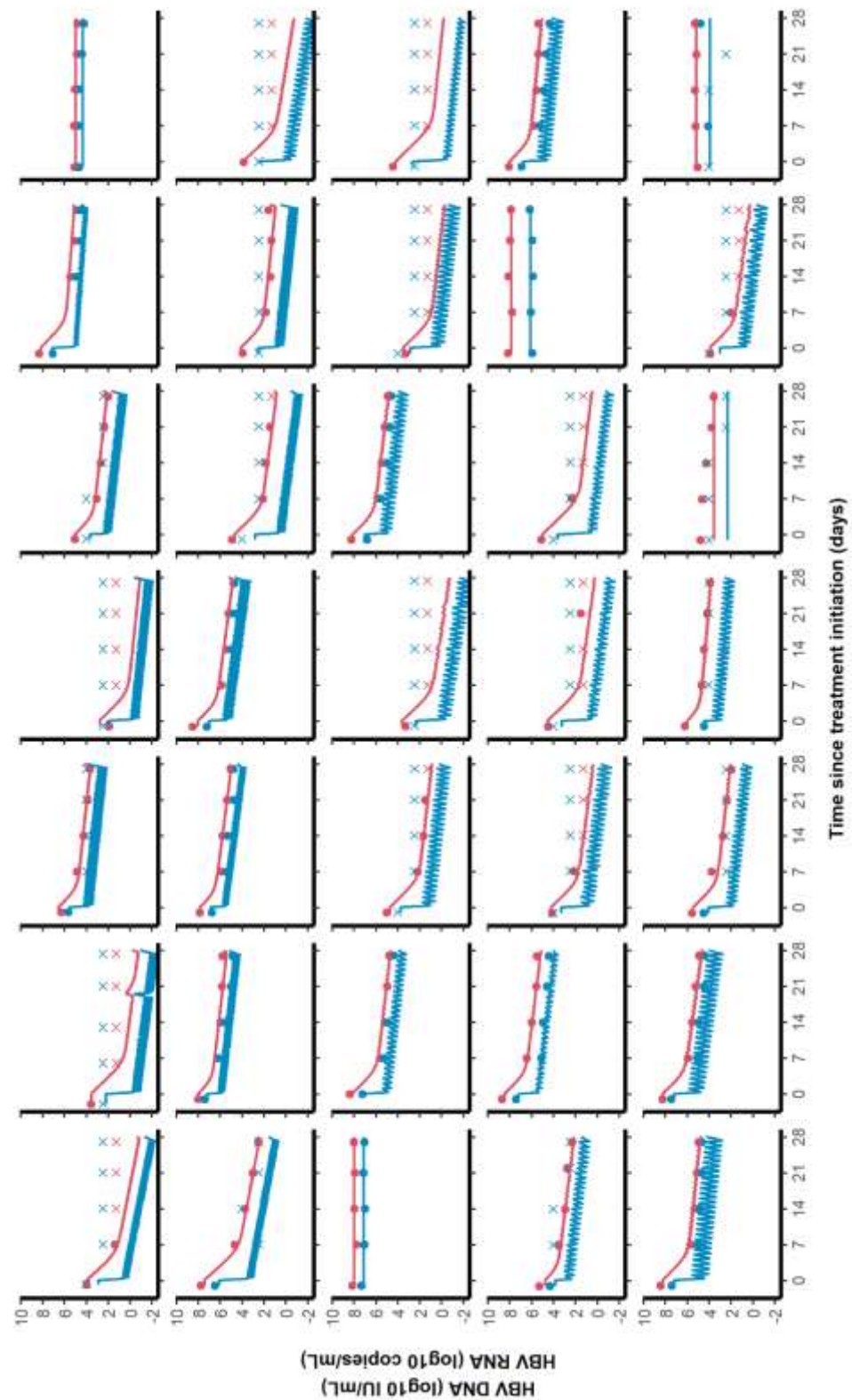


Figure S6: Individual fits of HBV DNA (red) and HBV RNA (blue) during the treatment period (28 days). Full dots are the observed measurements while crosses are the measurements below the limit of detection. Lines are the individual predictions obtained with the model.

Supplemental file 2

The PDE model is given by equations 1-5:

$$\frac{\partial I}{\partial t} + \frac{\partial I}{\partial a} = -\delta I(a, t) \quad (1)$$

$$\frac{\partial R_{int}}{\partial t} + \frac{\partial R_{int}}{\partial a} = (1 - \varepsilon_{CpAM})\alpha - \mu_R R_{int} - \rho_R R_{int} - (1 - \varepsilon_{NA})\pi R_{int} \quad (2)$$

$$\frac{\partial V_{int}}{\partial t} + \frac{\partial V_{int}}{\partial a} = (1 - \varepsilon_{NA})\pi R_{int} - \mu_V V_{int} - \rho_V V_{int} \quad (3)$$

$$\frac{dR}{dt} = \rho_R \int_0^\infty R_{int}(a, t)I(a, t)da - c_R R \quad (4)$$

$$\frac{dV}{dt} = \rho_V \int_0^\infty V_{int}(a, t)I(a, t)da - c_V V \quad (5)$$

with a the time since the cell has been infected, t the time since treatment initiation and the following boundary conditions $I(0, t) = \beta V(t) \left(T_{max} - \frac{\beta V_0 T_{max}}{\beta V_0 + \delta} \right)$, $I(a, 0) = I_0(a)$, $R_{int}(0, t) = 0$, $V_{int}(0, t) = 0$, $R(a, 0) = R_0(a)$ and $V(a, 0) = V_0(a)$, where $I_0(a)$, $R_0(a)$ and $V_0(a)$ are the pre-treatment steady-state distributions.

The PDE can be transformed into an ODE model as presented in main text. In the ODE model P and Q are the total amount of intracellular RNA and DNA given by:

$$P(t) = \int_0^\infty R_{int}(a, t)I(a, t)da \text{ and } Q(t) = \int_0^\infty V_{int}(a, t)I(a, t)da$$

The PDE model can be translated into an ODE. Both yield to the same steady states given by figure S1. Equations 6 – 10 present analytical forms of the steady states given by the ODE model.

$$V_{t=0} = \frac{\rho \pi \alpha T_{max}}{c(\delta + \rho)(\delta + \rho + \pi)} - \frac{\delta}{\beta} \quad (6)$$

$$I_{t=0} = \frac{\beta V_{t=0} T_{max}}{\beta V_{t=0} + \delta} \quad (7)$$

$$Q_{t=0} = \frac{c V_{t=0}}{\rho} \quad (8)$$

$$P_{t=0} = \frac{\alpha I_{t=0}}{\delta + \rho + \pi} \quad (9)$$

$$R_{t=0} = \frac{\rho P_{t=0}}{c} \quad (10)$$

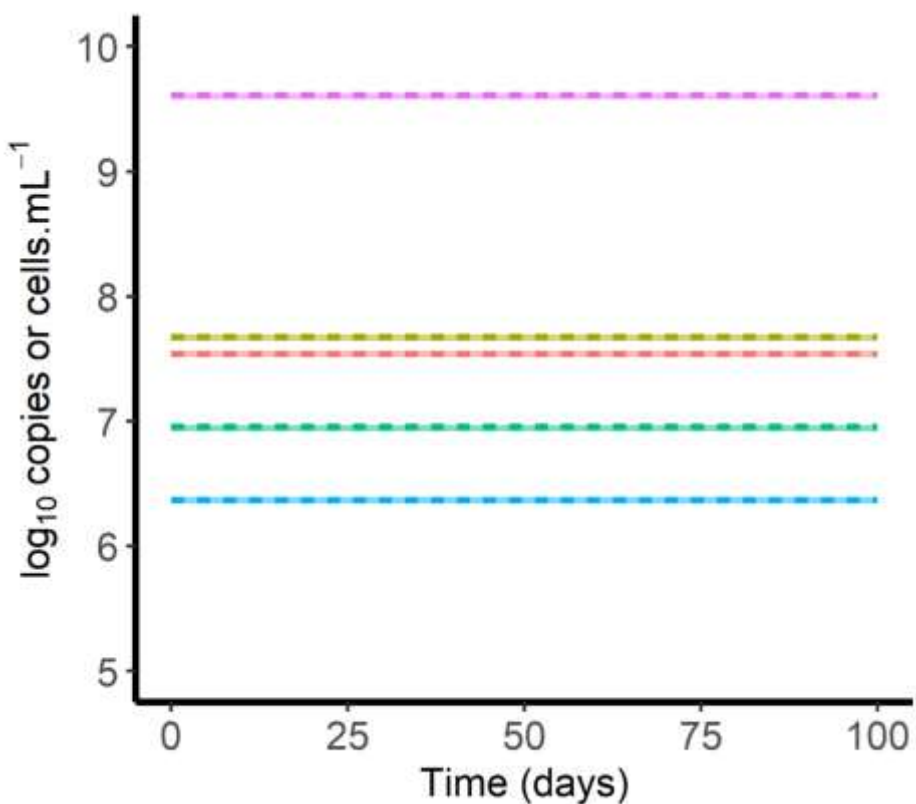


Figure S1: Steady-state equilibriums of PDE and ODE solutions. Full lines are the steady-state solutions given by the ODE model. Dashed lines are the solutions given by the PDE model. In red $V(t)$; in blue $R(t)$; in green $I(t)$; in purple $Q(t)$ ad in yellow $P(t)$.

Supposing that $\mu = 0 \text{ d}^{-1}$ and that a treatment is sufficiently effective to neglect the formation of new infected cells this model admits an analytical solution given by equation 12 and 13.

$$R(t) = Ae^{-ct} + Be^{-(\pi+\rho+\delta)t} + Ce^{-\delta t} \quad (12)$$

$$V(t) = De^{-ct} + Ee^{-(\rho+\pi+\delta)t} + Fe^{-(\rho+\delta)t} + Ge^{-\delta t} \quad (13)$$

With:

$$A = \frac{\rho\alpha I_0}{c(\rho + \pi)} - \frac{\rho K_1}{c - \rho - \pi(1 - \varepsilon_{NA}) - \delta} - \frac{\rho K_2}{(c - \delta)} \quad (14)$$

$$B = \frac{\rho K_1}{c - \rho - \pi(1 - \varepsilon_{NA}) - \delta} \quad (15)$$

$$C = \frac{\rho K_2}{(c - \delta)} \quad (16)$$

$$D = \frac{\rho\pi\alpha T_{max}}{c(\delta + \rho)(\delta + \rho + \pi)} - \frac{\rho\pi(1 - \varepsilon_{NA})K_1}{(\rho - \pi(1 - \varepsilon_{NA}))(c - \rho - \pi(1 - \varepsilon_{NA}) - \delta)} \\ - \frac{\rho\pi(1 - \varepsilon_{NA})K_2}{\rho(c - \delta)} - \frac{\rho K_3}{c - \rho - \delta} - \frac{\delta}{\beta} \quad (17)$$

$$E = \frac{\rho K_3}{c - \rho - \delta} \quad (18)$$

$$F = \frac{\rho\pi(1 - \varepsilon_{NA})K_1}{(\rho - \pi(1 - \varepsilon_{NA}))(c - \rho - \pi(1 - \varepsilon_{NA}) - \delta)} \quad (19)$$

$$G = \frac{\pi(1 - \varepsilon_{NA})K_2}{(c - \delta)} \quad (20)$$

where

$$K_1 = R_{int|t=0} - \frac{(1 - \varepsilon_{CAM})\alpha I_{t=0}}{\rho + \pi(1 - \varepsilon_{NA})} \quad (21)$$

$$K_2 = \frac{(1 - \varepsilon_{CAM})\alpha I_{t=0}}{\rho + \pi(1 - \varepsilon_{NA})} \quad (22)$$

$$K_3 = V_{int|t=0} + (1 - \varepsilon_{NA})\pi \left(\frac{K_1}{\pi(1 - \varepsilon_{NA})} + \frac{K_2}{\rho} \right) \quad (23)$$

Depending on the values of parameters, not all the declines might be observed at the same time.

From steady-states and the baseline of HBV DNA and HBV RNA, one can find that $\frac{V_{t=0}}{R_{t=0}} =$

$\frac{\pi}{\rho+\delta} \approx 100$. Since $\rho + \delta \approx 1$, this implies that $\pi \approx 100$. Therefore terms in $e^{-(\pi+\rho+\delta)t}$ in (12)

and (13) are in practice too fast and never observed.

Furthermore, if $c \gg \rho$ (i.e., clearance occurs faster than secretion of viral particles), equations 12 and 13 can be simplified into biphasic equations with different expressions according to the type of treatment used:

$$\text{CpAM: } \begin{cases} R(t) = Ae^{-ct} + Ce^{-\delta t} \\ V(t) = Ee^{-(\rho+\delta)t} + Fe^{-\delta t} \end{cases} \text{ and NA: } \begin{cases} R(t) = -Be^{-(\rho+\delta)t} + Ce^{-\delta t} \\ V(t) = Ee^{-(\rho+\delta)t} + Fe^{-\delta t} \end{cases} \quad (24)$$

For both CpAM and NA, $V(t)$ initially declines at the same rate $\rho+\delta$ while $R(t)$ will decrease at a rate c for CpAM and increase at rate depending on $\rho+\delta$ in NA treated patients.

Otherwise, if $\rho \gg c$, equations 12 and 13 can further be simplified, arising to equations (25). Those equations give biphasic profiles, for both CpAM and NA, depending on the viral clearance c and the loss rate of infected cells δ :

$$\text{CpAM: } \begin{cases} R(t) = Ae^{-ct} + Ce^{-\delta t} \\ V(t) = De^{-ct} + Fe^{-\delta t} \end{cases} \text{ and NA: } \begin{cases} R(t) = -Ae^{-ct} + Ce^{-\delta t} \\ V(t) = De^{-ct} + Fe^{-\delta t} \end{cases} \quad (25)$$

With CpAM and NA, the decline of HBV DNA attributed to the clearance of the virus c . Interestingly with CpAM, HBV RNA declines in a parallel to HBV DNA at a rate c while with NA, HBV RNA still tends to accumulate (see below).

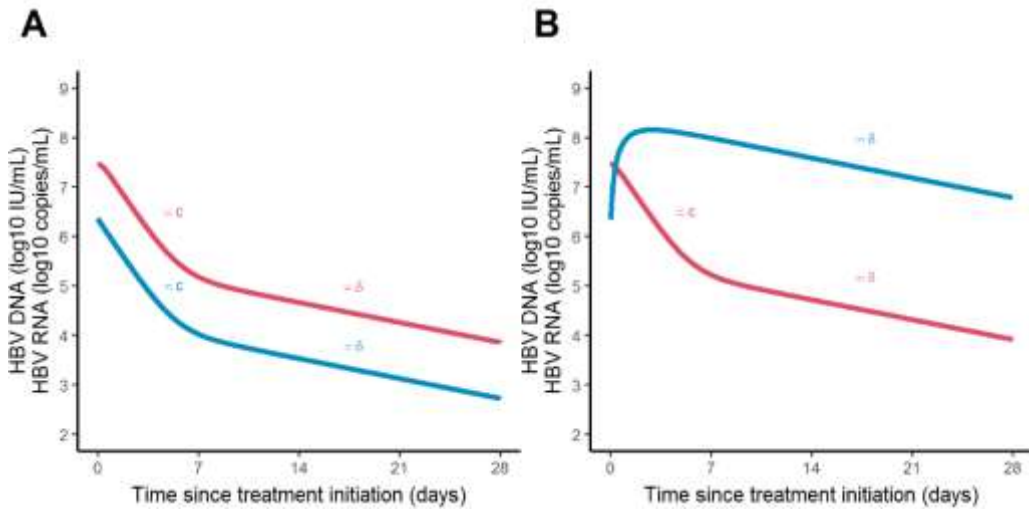


Figure S2: Typical profiles of HBV DNA and HBV RNA in HBeAg positive patients treated by CpAM (A) or NA (B) supposing that $\rho \gg c$. To generate those profiles we supposed that the treatments are sufficiently potent to neglect the number of novel infections.

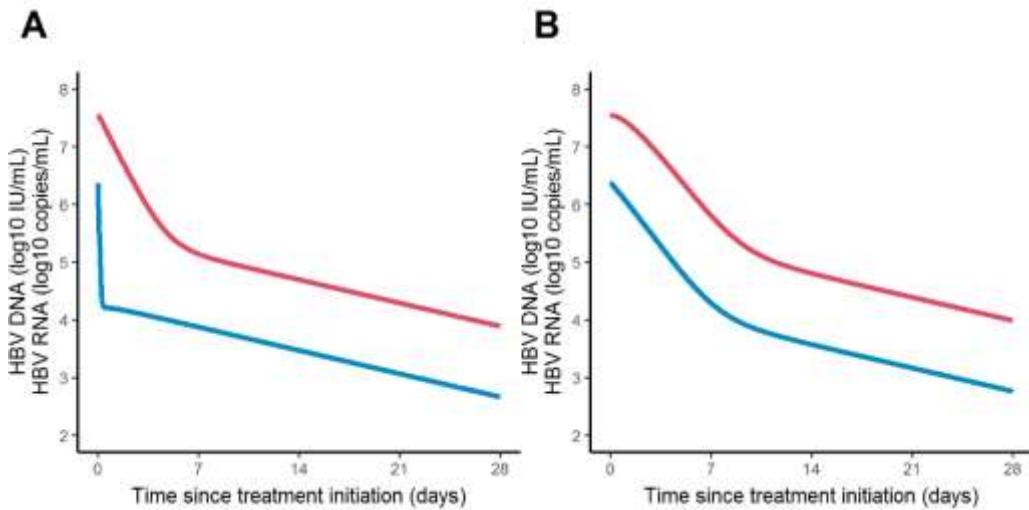


Figure S3: HBV DNA (red) and HBV RNA declines (blue) over 28 days of treatment. (A) Declines supposing the effectiveness of a drug is high and maximal at treatment initiation (see main text). (B) Declines supposing that the effect of a drug increases over time and is maximal at the end of the first week of dosing.

Supplemental file 3: Model averaging

The model developed integers in high number of parameters and not all can be estimated. For example the value of the viral clearance c , which drives the first phase of HBV DNA decline, might be difficult to estimate. Thus, we tested values of 1, 2, 5, 10 and 20 d^{-1} according to the range of values proposed in the literature (Murray et al., 2006; Dandri et al., 2008; Ribeiro et al., 2010). The value providing the lowest Bayesian Information Criteria (BIC) was kept and moved forward in rest of the analysis. However, we here propose to use model averaging (Gonçalves et al., 2020) to take into account the uncertainty related to the value of c . Depending on the information criteria provided by each model (here, the AIC) one can compute weights w associated to each candidate model (Figure 1). Then, we simulated 10,000 individual time courses of HBV DNA and HBV RNA under each model and represented the median profile expected for each model. One can also randomly draw w individual from each model to built the median profile in model averaging (Figure 2). Finally, based on the simulations, we calculated the time needed for HBV DNA and HBV RNA to be lower than 1 copies/mL (Table I).

The model where $c=20 \text{ d}^{-1}$ is the model providing the lowest BIC and therefore the most weighted model was the model with $c=20 \text{ d}^{-1}$ ($w=0.76$). Thus, the median model averaged profile was largely identical to the one obtained with $c=20 \text{ d}^{-1}$ (Figure 2). Similarly, the predicted times to reach HBV DNA and HBV RNA titers lower than 1 copies/mL were largely comparable between the model selected ($c=20 \text{ d}^{-1}$) and in model averaging (Table I). In HBeAg negative patients and using MA, we found that we would need 51.8 [48.0-55.6] and 51.0 days [47.0-54.6] to reach HBV DNA and HBV RNA titers lower than 1 copies/mL, respectively. On

the other hand for HBeAg positive patients we predict that 61.0 [55.0-69.5] and 60.3 days [54.0-69.0] are needed.

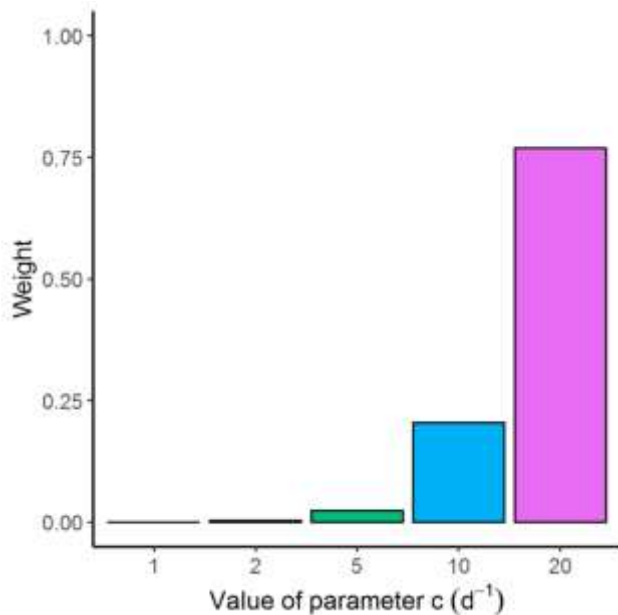


Figure S4: Weights obtained based on the AIC of each model

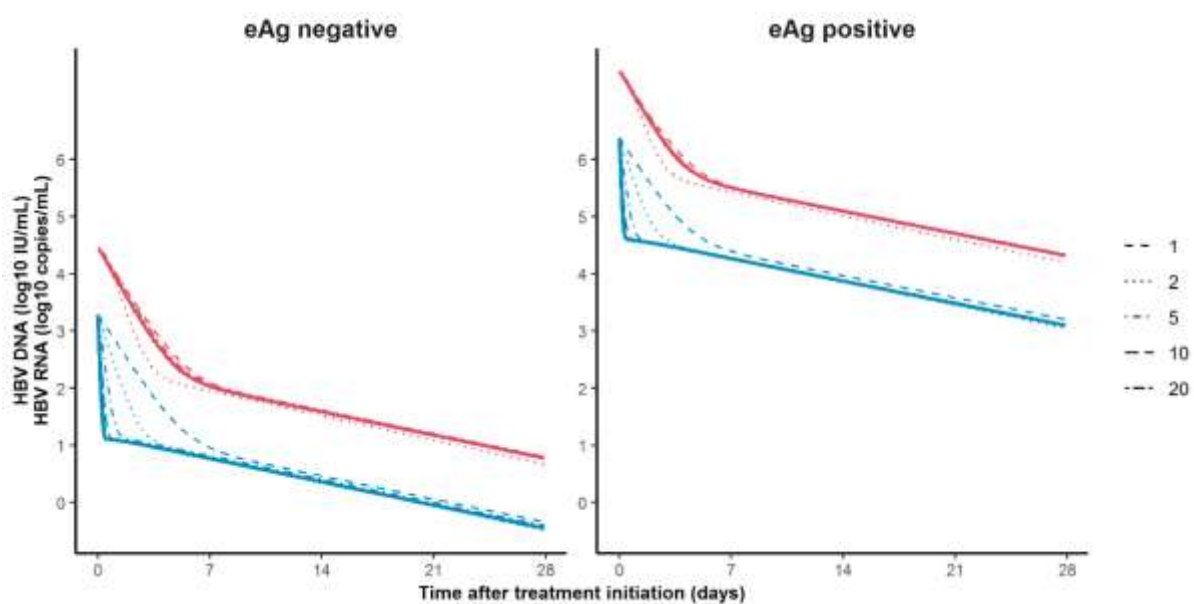


Figure S5: Typical individual profiles in function of the value at which the viral clearance c was fixed (dashed lines) and “model averaged” profile (solid line).

Table 2: Median time [IC95%] needed to reach HBV DNA and HBV RNA titers lower than 10 copie/mL

c (d ⁻¹)	HBeAg status	Median time for HBV DNA < 1 copies/mL	Median time for HBV RNA < 1 copies/mL
1	Negative	53.0 [49.0-56.5]	52.5 [49.0-56.5]
2		49.0 [46.0-52.0]	48.5 [45.0-52.0]
5		52.0 [48.0-56.5]	51.0 [47.0-55.5]
10		51.5 [48.0-55.5]	50.5 [47.0-54.5]
20		52.0 [48.5-56.5]	51.0 [47.5-55.5]
MA		51.8 [48.0-55.6]	51.0 [47.0-54.6]
1	Positive	62.3 [55.5-70.5]	62.0 [55.5-70.1]
2		58.0 [52.5-65.0]	57.8 [52.0-65.0]
5		61.5 [54.5-69.1]	60.5 [54.0-68.1]
10		60.8 [54.5-69.0]	60.0 [53.5-68.0]
20		61.0 [55.0-69.5]	60.0 [54.0-69.0]
MA		61.0 [55.0-69.5]	60.3 [54.0-69.0]

References

1. Murray JM, Purcell RH, Wieland SF. The half-life of hepatitis B virions. Hepatology. 2006;44:1117–21.
2. Dandri M, Murray JM, Lutgehetmann M, Volz T, Lohse AW, Petersen J. Virion half-life in chronic hepatitis B infection is strongly correlated with levels of viremia. Hepatology. 2008;48:1079–86.
3. Ribeiro RM, Germanidis G, Powers KA, Pellegrin B, Nikolaidis P, Perelson AS, et al. Hepatitis B Virus Kinetics under Antiviral Therapy Sheds Light on Differences in Hepatitis B e Antigen Positive and Negative Infections. The Journal of Infectious Diseases. 2010;202:1309–18.
4. Gonçalves A, Mentré F, Lemenuel-Diot A, Guedj J. Model Averaging in Viral Dynamic Models. AAPS J. 2020;22:48.

Supplemental file 4: covariate selection

Based on the the model described by equations 1-5, we evaluated the links between model random effects and covariates. At this stage, covariates were retained if the p-value<0.1. Candidate covariates were then formally included in the model in a forward procedure. The covariate model with the lowest BIC was kept and moved forward in the analysis. When a covariate model was selected, we checked the significance of each covariate coefficient using a Wald test. The covariate selection was stopped once the BIC did not decrease by more than 2 points. Table S2 presents the model before covariate inclusion. Table S2 presents the BIC of the best model at each step and the p-value of the covariate coefficients.

Table S1: Parameter estimates of the multiscale model without covariates

Parameters	Fixed effects	Between-subject variability
	Estimates (RSE, %)	ω (%) (RSE, %)
R_0	2.5 (9)	32.5 (23)
α (copies.cell $^{-1}$.d $^{-1}$)	13.2 (77)	4.52 (12)
π (d $^{-1}$)	96.9 (21)	82.4 (18)
ρ (d $^{-1}$)	1.00 (15)	0 (-)
c (d $^{-1}$)	20.0 (-)	0 (-)
δ (d $^{-1}$)	0.13 (8)	30.4 (23)
EA $_{50}$ (ng)	103 (36)	168 (18)
σ_{DNA}	0.323 (5)	
σ_{RNA}	0.358 (7)	

Table S2: BIC of the model at each step of the covariate selection

Model	P-value (Wald test)	BIC
Without covariates	-	812.1
HBeAg status on α	$4 \cdot 10^{-15}$	780.7
HBeAg status on α + HBeAg status on R_0	$5 \cdot 10^{-14}$ $7 \cdot 10^{-3}$	778.9
HBeAg status on α , HBeAg status on R_0 and HBeAg status on EA ₅₀	$2 \cdot 10^{-13}$ $2 \cdot 10^{-3}$ 0.01	774.3

Chapitre 5. Le *model averaging* dans les modèles de cinétique virale

5.1. Résumé

Précédemment nous avons développé deux modèles de cinétique virale caractérisant le mécanisme d'action de deux nouvelles molécules anti-VHB. Ces modèles contribuent à une meilleure compréhension de la relation hôte-pathogène et pourraient être utilisés pour le développement et l'optimisation de ces traitements. Le développement de tels modèles a été possible grâce à l'utilisation d'algorithmes puissants permettant d'obtenir des estimations précises des paramètres d'intérêt ainsi qu'une caractérisation de la variabilité au sein de la population étudiée. La multiplicité des marqueurs étudiés s'accompagne d'un accroissement du nombre de paramètres, lesquels ne sont pas toujours soutenus par les données. On parle alors d'un manque d'identifiabilité du modèle ou des paramètres. Une solution consiste à fixer les paramètres peu identifiables à plusieurs valeurs probables et à en étudier l'impact sur les estimations et conclusions fournies par le modèle au travers d'une analyse de sensibilité. De plus, il existe une incertitude liée aux différentes hypothèses biologiques testées. Cependant l'approche actuellement utilisée, consistant à sélectionner le modèle fournissant le meilleur critère statistique (*model selection*, MS), ignore l'incertitude liée aux différents modèles testés et peut mener à des fausses conclusions.

Dans ce troisième travail, nous nous proposons d'évaluer une approche alternative à la sélection de modèle dite de *model averaging* (MA). Cette approche permet de prendre en compte l'incertitude liée au modèle en pondérant chaque modèle testé par son adéquation aux données (*i.e.* leur critère statistique). Dans un premier temps, nous avons étudié la précision d'estimation des paramètres fournis par MS et MA au travers d'un modèle d'infection aigüe limitée par le nombre de cellules cibles avec phase d'éclipse. Dans ce modèle, la charge virale initiale V_0 et la vitesse de la phase d'éclipse k sont deux paramètres que les données de virémie seules ne permettent pas de distinguer. Dans plus de 30 à 60% des cas, MS conduit à la sélection d'un modèle ayant un V_0 et un k différents de ceux utilisés pour générer les données. Nous avons par la suite calculé le taux de couverture associé aux paramètres du modèle. Cela correspond au

nombre de fois où la valeur de simulation est comprise dans l'intervalle de confiance du paramètre estimé. Alors que MS fournit de faibles taux de couverture, MA fournit des estimations justes au risque de première espèce α . Ceci traduit le fait que les intervalles de confiance des paramètres estimés par MS sont trop étroits (Matériel supplémentaire article 3).

Dans un second temps, nous avons étudié l'incertitude liée à différents modèles de réponse immunitaire. On note que dans plus de 10% des cas, nous sélectionnons un modèle incluant une réponse immunitaire alors que le modèle utilisé pour simuler n'en contient pas. En somme, MS peut conduire à des conclusions erronées quant à la nature des phénomènes biologiques mis en jeu lors de l'infection pouvant mener à des prédictions erronées ou peu précises lorsque l'on utilise le modèle pour effectuer des prédictions.

Ce travail montre les limites des approches par sélection de modèle en présence de modèles complexes et faiblement identifiables. Il illustre également la possibilité de fournir des estimations plus justes en prenant en compte l'incertitude liée au modèle en appliquant le *model averaging*. Ce travail a fait l'objet d'un article publié dans *The American Journal of Pharmaceutical Scientists* en février 2020.

5.2. Article 3: Model averaging in viral dynamic models



Research Article

Model Averaging in Viral Dynamic Models

Antonio Gonçalves,^{1,3} France Mentré,¹ Annabelle Lemenuel-Diot,² and Jérémie Guedj¹

Received 4 October 2019; accepted 16 January 2020

Abstract. The paucity of experimental data makes both inference and prediction particularly challenging in viral dynamic models. In the presence of several candidate models, a common strategy is model selection (MS), in which models are fitted to the data but only results obtained with the “best model” are presented. However, this approach ignores model uncertainty, which may lead to inaccurate predictions. When several models provide a good fit to the data, another approach is model averaging (MA) that weights the predictions of each model according to its consistency to the data. Here, we evaluated by simulations in a nonlinear mixed-effect model framework the performances of MS and MA in two realistic cases of acute viral infection, i.e., (1) inference in the presence of poorly identifiable parameters, namely, initial viral inoculum and eclipse phase duration, (2) uncertainty on the mechanisms of action of the immune response. MS was associated in some scenarios with a large rate of false selection. This led to coverage rate lower than the nominal coverage rate of 0.95 in the majority of cases and below 0.50 in some scenarios. In contrast, MA provided better estimation of parameter uncertainty, with coverage rates ranging from 0.72 to 0.98 and mostly comprised within the nominal coverage rate. Finally, MA provided similar predictions than those obtained with MS. In conclusion, parameter estimates obtained with MS should be taken with caution, especially when several models well describe the data. In this situation, MA has better performances and could be performed to account for model uncertainty.

KEY WORDS: model selection; model averaging; viral dynamics; infectious diseases.

INTRODUCTION

Since 1995 and the two seminal papers providing an estimate of the half-life of HIV particles in blood [1, 2], the use of viral dynamic models has considerably expanded. Applications have been summarized in a recent issue of Immunological Reviews [3], showing their relevance for understanding the host-pathogen interactions in both chronic and acute infections [4–6]. In the last decade, parameter estimation of these models has increasingly relied on nonlinear mixed-effect models (NLMM), a statistical approach that improves both precision and accuracy of estimates by explicitly taking into account the between-subject variability in the model [7, 8]. This is particularly true in the case of antiviral drug development, where NLMM have become

central to support optimal treatment strategies in the presence of a large variability in the response [9, 10].

Although inference has been greatly facilitated by the use of NLMM, viral dynamic models remain often characterized by a lack of theoretical or practical identifiability [7, 8]. In fact, the availability of powerful algorithms for inference has mechanically led to the development of increasingly complex models, questioning the reliability of viral kinetic parameter estimates. In order to improve identifiability of these models, a commonly used strategy is to fix parameters to plausible values and then to check the impact of these choices by conducting sensitivity analyses. For instance in acute viral infection, one can fix the initial viral inoculum or the eclipse phase duration, two parameters that can hardly be estimated using only viral load data [11, 12]. Data fitting can also be used to evaluate the plausibility of different biological assumptions. In that case, the usual approach is model selection (MS), where a predefined set of candidate models are fitted to the data and the model providing the best fit to the data (based on Akaike or Bayesian information criteria) is selected and carried forward in the analysis. In both contexts, these approaches, by focusing the predictions on a single model, ignore the model uncertainty and may lead to wrong predictions [13] and potentially inaccurate biological conclusions [14–16].

Electronic supplementary material The online version of this article (<https://doi.org/10.1208/s12248-020-0426-7>) contains supplementary material, which is available to authorized users.

¹Université de Paris, IAME, INSERM, Henri Huchard, F-75018, Paris, France.

²Roche Pharmaceutical Research and Early Development, Pharmaceutical Sciences, Roche Innovation Center, Basel, Switzerland.

³To whom correspondence should be addressed. (e-mail: antonio.goncalves@inserm.fr)



In this paper, we propose to use model averaging (MA) as an alternative approach to MS in viral dynamics. MA is a conceptually simple approach, where the uncertainty related to each candidate model is taken into account and predictions associated to each model are weighted based on their consistency with the data [17, 18]. Through an extensive simulation study, we compare parameter estimates and predictive performances of model averaging versus model selection. We discuss the benefits and limits of model averaging compared with model selection. Simulations are inspired from recent works in Zika and Ebola virus dynamics [19, 20], representing two typical settings encountered in viral dynamic modeling, i.e., (1) a set of parameters are fixed to arbitrary values of a given biological model to ensure identifiability; (2) model selection relies on the comparison of fitting criterion of a set of pre-defined different biological models.

MATERIAL AND METHODS

Model Selection and Model Averaging

Model for the Observations

Let Y_{ijm} denote the j th log viral load measurement of subject i at time t_j , and suppose that $m=1,\dots,M$ candidate models can be used to simulate the data. The model for the observations is defined as:

$$Y_{ijm} = \log_{10}[V_m(t_j, \theta_{im})] + e_{ijm} \quad (1)$$

where V_m is the viral load prediction function given by model m , θ_{im} is the vector of individual parameters under model m , t_j is the time of viral load measurement, assumed to be similar for all patients and all models, and e_{ijm} is the residual error. Individual parameters θ_{im} are log normally distributed and depend on the vector of fixed effects μ_m and the vector of random effects $\eta_{im} \sim \mathcal{N}(0, \Omega_m)$ with $\theta_{im} = \mu_m + \eta_{im}$. The variance-covariance matrix Ω_m is assumed to be diagonal. Residual errors are assumed to be independent and normally distributed $e_{ijm} \sim \mathcal{N}(0, \sigma_m^2)$. Each biological model m is therefore associated with a set of population parameters, Ψ_m , of dimension $p_m = \dim(\mu_m, \Omega_m, \sigma_m)$.

Inference and Model Selection

For each candidate model, one can estimate the parameters using maximum likelihood estimates, providing, for each model, an estimate of the population parameters, noted $\hat{\Psi}_m$. One can also provide the confidence intervals of the parameters of interest under each model. This can be done using the asymptotic approximation, where the density function of the estimated parameter, $\hat{\Psi}_m$, $p(\hat{\Psi}_m)$, is assumed to be Gaussian with a variance-covariance matrix given by the inverse of the Fisher information matrix (FIM⁻¹).

Then, the most common approach is to select the model that best describes the data. This can be done using various criteria that rely on penalizations of the log-likelihood (LogL), such as the Akaike information criteria (AIC), the consistent Akaike (CAIC), or the Bayesian information criteria (BIC) [21–24]. In line with

previous analysis [25, 26], we relied on AIC given by $AIC_m = -2\text{LogL}(\hat{\Psi}_m) + 2p_m$. The analysis then focuses on the results (i.e., parameter estimates, confidence intervals, and predictions) obtained with the “best” model, i.e., the model associated with the lowest AIC among the m candidate models, noted AIC_{\min} , with parameter estimates noted $\hat{\Psi}_{MS}$.

Model Averaging

As explained above, MS is limited in the sense that it ignores the uncertainty associated with each model and only focuses on a post hoc selected model [14]. Alternatively, one can use MA to take into account the fact that several candidate models may provide a reasonable fit to the data. In this approach, a weight is attributed to each candidate model, w_m , proportional to AIC, such as $w_m = \frac{e^{-\Delta AIC_m}}{\sum_{m=1}^M e^{-\Delta AIC_m}}$ where $\Delta AIC_m = AIC_m - AIC_{\min}$ [14, 17, 18]. In that case, the MA estimator of Ψ_m is given by $\hat{\Psi}_{MA}$, with a density function given by $p(\hat{\Psi}_{MA}) = \sum_{m=1}^M w_m p(\hat{\Psi}_m)$. Another approach could be to consider only the models that are responsible for the majority of the weight (0.9 or 0.8) and equally average them (see “DISCUSSION” section).

Viral Dynamic Settings

Our objective is to compare model selection and model averaging in two typical contexts of viral dynamic models. In the first setting, we focus on the issue arising from using model selection when some parameters of the model cannot be identified and are fixed to arbitrary values. In the second setting, we focus on the issue arising from using model selection when several different biological models can be proposed to fit the data.

Setting I: Viral Dynamic Models in the Presence of Poorly Identifiable Parameters

Here, we focus on the standard target cell limited (TCL) model given by:

$$\frac{dT}{dt} = -\beta TV \quad (2)$$

$$\frac{dI_1}{dt} = \beta TV - kI_1 \quad (3)$$

$$\frac{dI_2}{dt} = kI_1 - \delta I_2 \quad (4)$$

$$\frac{dV}{dt} = \pi I_2 - cV \quad (5)$$

$$T_{t=0} = T_0; I_{1,t=0} = 0; I_{2,t=0} = 0; V_{t=0} = V_0$$

where T is the target cells, I_1 is the infected cells in eclipse phase, I_2 is the productive infected cells, and V is the

Table I. Expected Standard Error (SE) of the Fixed-Effect Parameters Using a Target Cell Limited Model when the Estimated Parameters Include or Do Not Include the Initial Inoculum, V_0 , and the Eclipse Rate, k . Expected Standard Errors Were Calculated Using PFIM Software and for a Study Design Including 30 Subjects Sampled Every 3 days from Day 3 to Day 18

Parameter (units)	Estimation of R_0 , δ , V_0 , k , and π			Estimation restricted to R_0 , δ , and π		
	Estimate	SE	Relative SE (%)	Estimate	SE	Relative SE (%)
R_0	12	62.0	516	12	0.84	7.0
δ (day $^{-1}$)	1	0.10	10	1	0.063	6.3
π (copies cell $^{-1}$ day $^{-1}$)	6,000	3,625	604	6,000	1,446	24.1
V_0 (copies mL $^{-1}$)	10^{-4}	29.7	743	10^{-4} (fixed)	-	-
k (day $^{-1}$)	4	38.9	971	4 (fixed)	-	-
c (day $^{-1}$)	20 (fixed)	-	-	20 (fixed)	-	-
T_0 (cells mL $^{-1}$)	10^8 (fixed)	-	-	10^8 (fixed)	-	-

SE, standard error

viral load in plasma. The model depends on the following disease parameters: β , the infectivity rate constant; k , the eclipse rate; δ , the infected cell elimination rate; π , the viral production rate constant; c , the clearance of free virus; T_0 , the initial number of target cells; and V_0 , the initial viral load. For the ease of interpretation and fitting, we reparametrized the model as $R_0 = \frac{\beta c T_0}{\delta}$, the basic reproductive ratio, instead of β , where R_0 represents the number of secondary infection caused by one infected cell when the target cells are abundant. For the sake of simplicity, we focused here on a simple, exponentially distributed, duration for the eclipse phase, but more complex models can be considered [27].

Not all parameters of the TCL model can be uniquely identified when only the viral load data are available [28–30], and this issue is not circumvented when parameters are estimated using NLMEM. This can be shown by analyzing the expected standard errors obtained with the approximated Fisher information matrix (<http://www.pfim.biostat.fr/>; see more details in [31]). Table I provides the expected standard errors obtained with 30 individuals sampled every 3 days from day 3 up to day 18 post-infection using typical parameter values close to those found during Zika infection in nonhuman primates [19]. Although being theoretically identifiable, several parameters are associated with a very large expected standard error. This can be corrected by fixing V_0 and k to some arbitrary values, leading to expected relative standard errors lower than 30% for all parameter values. We, here, aim to evaluate the impact of the choice of k and V_0 on parameter estimates.

We also conducted a sensitivity analysis on the parameters variability of setting I ($k=4$ day $^{-1}$ and $V_0=10^{-4}$ copies mL $^{-1}$). We reported the influence of lower and higher variabilities ($\omega=0.1$ and $\omega=1$, respectively) on the performances of MS and MA.

Setting II: Viral Dynamic Models Including the Immune Response

In order to evaluate the impact of testing different biological assumptions in parameter estimates and predictions, we considered 4 additional models integrating the role of innate or adaptive immune response in the control of viral replication and inspired from the models used to describe Ebola infection in nonhuman primates [20]. These models extend the TCL model with an additional compartment, noted as F . This compartment is not observed and can therefore represent any biological entity involved in viral clearance, such as cytokine, macrophages, T cell, or antibodies [5, 32, 33]. We assumed that F is produced at a rate q proportional to the number of productively infected cells, I_2 , and is eliminated at a rate d_F [20]. Thus, F could either (1) increase the number of refractory infected cells (refractory model, R), (2) decrease the viral production (production inhibition model, PI), (3) increase the clearance of productive infected cells (cytotoxic model, C), or (4) increase the clearance of the virus (virus-killing model, V). In all models, the effects of F followed an E_{max} relationship with ϕ the maximal effect of F and θ the sensitivity parameter. Table II

Table II. Differential Equations System of Immune Response Models. At $t=0$, We Have $T_{t=0}=T_0$; $I_{1, t=0}=0$; $I_{2, t=0}=0$ and $V_{t=0}=V_0$

	Target cell limited	Refractory	Production inhibition	Cytotoxic	Virus-killing
$\frac{dT}{dt} =$	$-\beta TV$	$-\beta TV - \frac{\phi F}{\theta + \phi}$	$-\beta TV$	$-\beta TV$	$-\beta TV$
$\frac{dI_1}{dt} =$	$\beta TV - kI_1$	$\beta TV - kI_1$	$\beta TV - kI_1$	$\beta TV - kI_1$	$\beta TV - kI_1$
$\frac{dI_2}{dt} =$	$kI_1 - \delta I_2$	$kI_1 - \delta I_2$	$kI_1 - \delta I_2$	$kI_1 - \delta I_2 - \frac{\phi F}{\theta + \phi}$	$kI_1 - \delta I_2$
$\frac{dV}{dt} =$	$\pi I_2 - cV$	$\pi I_2 - cV$	$\pi \left(1 - \frac{\phi F}{\theta + \phi}\right) I_2 - cV$	$\pi I_2 - cV$	$\pi I_2 - cV - \frac{\phi F}{\theta + \phi}$
$\frac{dF}{dt} =$	$qI_2 - d_F F$	$qI_2 - d_F F$	$qI_2 - d_F F$	$qI_2 - d_F F$	$qI_2 - d_F F$

displays the four model equations.

Simulations and Parameter Estimation

For each setting, the simulation procedure and parameter estimation under both MS and MA are described below.

Parameter Values

In the first setting, we aimed to evaluate the impact of fixing the two poorly identifiable parameters, k and V_0 , in the target cell limited model. For that purpose, we defined a set of $M=9$ candidate models with values for V_0 and k equal to $V_0=10^{-5}, 10^{-4}$, or 10^{-3} copies mL^{-1} and $k=1, 4$, or 20 day^{-1} . The other parameter values are given in Table III. Figure 1a shows that viral load is biphasic with a peak close to $10 \log_{10}$ copies mL^{-1} in all 9 scenarios, but the time to peak depends on k and V_0 to a lesser extent.

In the second setting, V_0 and k were fixed to 10^{-4} copies mL^{-1} and 4 day^{-1} , respectively. To ensure a fair comparison between the models, parameters were chosen to predict a similar contribution of the immune response to viral control, as measured by the area under the curve (AUC) of the \log_{10} viremia from 0 to 20 days. Thus, in all four models, the parameter values were such that $\text{AUC}=100 \log_{10}$ copies.days mL^{-1} while assuming $\phi^*=0$ would lead to $\text{AUC}=120 \log_{10}$ copies.days mL^{-1} (i.e., the absence of an immune system would lead to a 20% increase in AUC) (Fig. 1b). The values of the TCL model were chosen to lead to a similar $\text{AUC}=100 \log_{10}$ copies.days mL^{-1} .

We assumed that R_0 , δ , π , θ , and ϕ were the estimated fixed effects. Those parameters, with the exception of θ , where associated to an intermediate between-subject variability, ω , is equal to 0.3. Other parameters were assumed to be known with values given in Table III.

Data Simulation

For each model, we simulated $S=300$ datasets of $N=30$ individuals using the same population parameter values, Ψ_m^* , given in Table III. Therefore, $S \times M = 2700$ datasets were simulated in the setting I, and 1500 datasets were simulated in the setting II. We assumed that measurements were made at days 3, 6, 9, 12, 15, and 18, with a lower limit of quantification (LLOQ) of 1 \log_{10} copies mL^{-1} [20], and a measurement error term, σ , equal to $0.7 \log_{10}$ copies mL^{-1} .

Parameter Estimation

Each of the $s=1, \dots, S$ dataset, was fitted using the M candidate models of each setting. The set of parameter estimates obtained on the dataset s using the model m , namely R_0 , δ , π , θ , and ϕ , and their corresponding between-subject variabilities if specified, was noted without loss of generality $\hat{\Psi}_m^s$. Parameter estimates were obtained by maximization of the likelihood using the SAEM algorithm implemented in the MONOLIX software (version 2018, release 2). We used $k_1=800$ and $k_2=200$ iterations for the exploratory and smoothing phases, respectively. We used the asymptotic approximation to derive the probability density function of $\hat{\Psi}_m^s$, noted $p(\hat{\Psi}_m^s)$, assumed to be Gaussian with a variance-covariance matrix given by the inverse of the FIM[†]. The FIM was computed by stochastic approximation with at least 100 and up to 800 iterations. Of note, among the M models used to fit the data, only one is the true model (noted TM), i.e., the model used to generate the data, and we note $\hat{\Psi}_{\text{TM}}^s$ the parameter estimates obtained by fitting the dataset s with TM.

For MA, 95% confidence intervals of $\hat{\Psi}_{\text{MA}}^s$ was then calculated by sampling 10,000 values in the mixture distribu-

Table III. Parameter Values Used for Simulation

Parameter (units)	Setting I		Setting II				
	Target cell limited		Target cell limited	Refractory	Production Inhibition	Cytotoxic	Virus-killing
R_0	12		12	12	12	12	12
δ^* (day $^{-1}$)	1		1	1	1	1	1
π^* (copies. cell $^{-1}$ day $^{-1}$)	6,000		250	6,000	6,000	6,000	6,000
ϕ^*	-		-	1	0.99	0.9	36.5
θ	-		-	2,200	325,000	3	0.001
V_0 (copies.day $^{-1}$)	$[10^{-5}, 10^{-4}, 10^{-3}]$		10^{-4}	10^{-4}	10^{-4}	10^{-4}	10^{-4}
k (day $^{-1}$)	$[1; 4; 20]$		4	4	4	4	4
c (day $^{-1}$)	20		20	20	20	20	20
T_0 (cells.mL $^{-1}$)	10^8		10^8	10^8	10^8	10^8	10^8
q (day $^{-1}$)	1		1	1	1	1	1
d_F (day $^{-1}$)	0.4		0.4	0.4	0.4	0.4	0.4
SD of the additive error	0.7		0.7	0.7	0.7	0.7	0.7

[†]Parameter for which inter-individual variability $\omega=0.3$

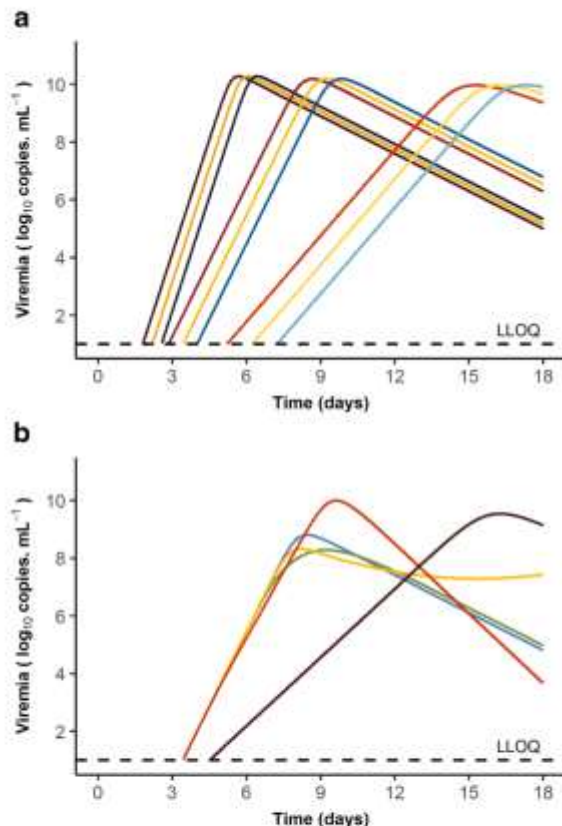


Fig. 1. Viral kinetics profiles obtained with the population parameters for each candidate model. **a** and **b** correspond to the simulation settings I and II, respectively. In panel **a**, curves are regrouped by 3. At left, the first 3 curves correspond to models with $k = 20 \text{ day}^{-1}$; center, models with $k = 4 \text{ day}^{-1}$ and right, models with $k = 1 \text{ day}^{-1}$. Within each group, red curves correspond to models with $V_0 = 10^0 \text{ copies mL}^{-1}$, yellow curves to models with $V_0 = 10^{-3} \text{ copies mL}^{-1}$, and blue curves to models with $V_0 = 10^{-5} \text{ copies mL}^{-1}$.

tion $p(\hat{\Psi}_{\text{MA}}^k) = \sum_{m=1}^M w_m^k p(\hat{\Psi}_m^k)$ and computing the associated 2.5th and 97.5th percentiles [14, 18, 34].

Performances of Model Averaging and Model Selection for Estimation

Model Selection

For each scenario, we reported the distribution weight of each candidate model as well as the proportion of simulations where each candidate model was selected (based on AIC, see above).

Parameter Estimates and Comparison with True Parameter Value

For each scenario, we reported the coverage rate obtained for each parameter with estimator based on MS, MA, or TM, defined as the proportion of simulated

datasets for which the true value of the parameter was contained in 95% confidence interval of the estimated parameter. The coverage rates were compared with the prediction interval of a binomial distribution with $p = 0.95$ and $S = 300$, i.e., [0.923; 0.973] and were reported for parameters R_0 , π , and δ in setting I and R_0 and δ in setting II.

Performances of Model Averaging and Model Selection for Prediction

Finally, we aimed to evaluate MA in the context of prediction, i.e., the capability to anticipate the effect of a change in the experimental setting. We focused on the prediction of the impact of an antiviral treatment limiting the viral production π with efficacy ε ($0 < \varepsilon < 1$) on the predicted proportion of patients with undetectable viral load ($10 \text{ copies mL}^{-1}$) at a given time point. We assumed that treatment was initiated at time $t = 6$ and lasted until $t = 20$ days, which coincides with the end of the follow-up. We considered 3 levels of efficacy on decreasing viral production with a factor $1 - \varepsilon$, namely $\varepsilon = 0.90$, 0.95 , and 0.99 , and we focused on the prediction at $t = 20$. For each model and each value of ε , Monte-Carlo simulations were used to the expected proportion of patients below the limit of detection noted $P_m^{\varepsilon,k} (\%) = P[V_m(t = 20, \hat{\Psi}_m^k, \varepsilon) < 10]$.

Following what has been done above, one can calculate, for each simulated dataset, the estimate that would be given by model selection, given by $P_{\text{MS}}^{\varepsilon,k} = P[V_{\text{MS}}(t = 20, \hat{\Psi}_{\text{MS}}^k, \varepsilon) < 10]$ or by model averaging $P_{\text{MA}}^{\varepsilon,k} = \sum_{m=1}^M w_m^k P[V_m(t = 20, \hat{\Psi}_m^k, \varepsilon) < 10]$. Likewise for the sake of comparison, one can also calculate the probability obtained by fitting the data under the true model, $P_{\text{TM}}^{\varepsilon,k} = P[V_m(t = 20, \hat{\Psi}_{\text{TM}}^k, \varepsilon) < 10]$. These values were summarized by calculating the bias and root mean square error (RMSE), given by $\frac{1}{3} \sum (P_{\text{MA}}^{\varepsilon,k} - P_m^{\varepsilon,k})$ and $\sqrt{\frac{1}{3} \sum (P_{\text{MA}}^{\varepsilon,k} - P_m^{\varepsilon,k})^2}$ in the case of MA (similar applies to calculate the bias and RMSE in the case of MS or TM). For the sake of graphical representation, proportions of patients below the limit of detection were presented as percentages and biases, and RMSE were therefore expressed in percentages.

RESULTS

Setting I

The first setting focused on the comparison between model averaging and model selection when parameters of the model (e.g., the eclipse phase, k , and the initial inoculum V_0) cannot be identified and are fixed to arbitrary values (see Table III).

Overall, the true set of parameter values was selected up to 62% of the simulations. The two parameters did not have the same rate of selection, with the correct values for k and V_0 being selected up to 71% and 96%, respectively (Fig. 2a). Although the true model was not systematically associated with the lowest AIC, it was

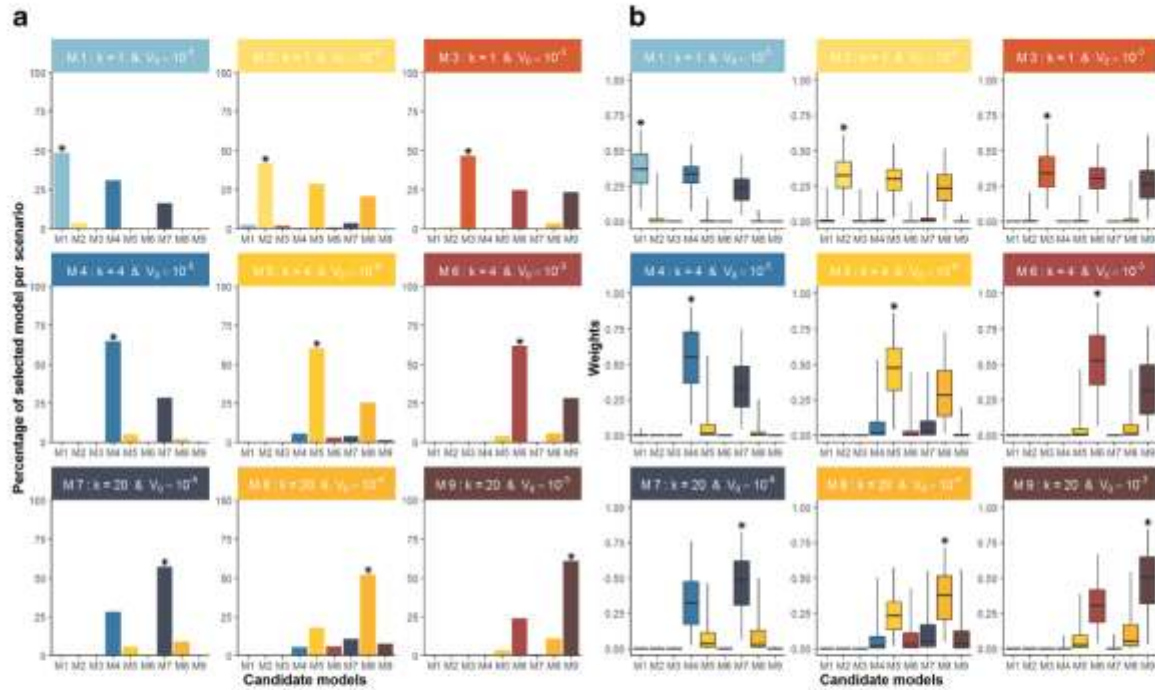


Fig. 2. Setting I. **a** For each scenario, the percentage of simulations where each candidate model was selected using AIC. Title of the facet indicates the true model. **b** Boxplots of weights (whiskers from the 2.5th to the 97.5th percentile) associated with each candidate model using AIC values. The asterisk denotes the true model in each scenario.

associated in all scenarios with the largest weight among the candidate models with a median value comprised between 0.32 and 0.55 (Fig. 2b). In all cases considered, at least two models had a weight greater than 0.20.

Next, we evaluated the impact of these results on parameter estimates and coverage rates. The estimation of R_0 using model selection was associated with a poor coverage rate between 0.46 and 0.63 (Fig. 3). Results for the loss rate of infected cells, δ , were better with a coverage rate ranging from 0.53 to 0.94 and was comprised in the nominal 0.95 coverage rate in 3 out of 9 scenarios. For the viral production π , MS showed coverage rates ranging from 0.68 to 0.96 and was comprised in the nominal 0.95 coverage rate in 5 out of 9 scenarios. Model averaging largely improved the coverage rates for all parameters and gave results close to those obtained with the true model. The coverage rates were between 0.91 and 0.98 for R_0 , between 0.72 and 0.95 for δ , and between 0.78 and 0.98 for π . Further, the coverage rates were comprised in the nominal 0.95 coverage rate in 7 out 9 scenarios for R_0 and 5 out of 9 scenarios for δ and π . All confidence intervals can be found in supplemental figures S1, S2, and S3.

Lastly, we explored the effect of simulating with less ($\omega=0.1$) or more ($\omega=1$) inter-subject variability. In both cases, MS provided subnominal coverage rates but MA corrected them (see Supplemental Figure S4). Eventually, we observed poorer coverage rates with $\omega=0.1$ and improved with $\omega=1$ compared with $\omega=0.3$.

Setting II

In the second setting, we assessed the properties of parameter estimates when several biological models can be proposed. We focused on models characterizing the effect of the immune response, considering that the immune response compartment could alternatively make cells refractory to infection, limit the production of virus, increase the elimination of infected cells, or increase the elimination of free virions (see Table III).

Unlike what was found in the previous setting, the chance of selecting the true model was largely dependent on the model considered. In fact, these chances were equal to 97% for the refractory model but this percentage could decrease to 58% with the cytotoxic model (Fig. 4a). Conversely, the models were also associated with a large rate of false selection with rates ranging from 3 to 10% for the refractory model, and up to 20% for the production inhibition model. In the case of the target cell limited model, the chances of correctly selecting it were equal to 88% and the rate of false selection were ranging from 1 to 19%. The median weight associated to the true model ranged from 0.43 to 0.99 (Fig. 4b).

Accordingly, MS provided satisfactory coverage rates for target cell limited and refractory model (Fig. 5); however, it failed to achieve the nominal coverage rate in all other models, with values ranging from 0.62 to 0.91 for R_0 and from 0.50 to 0.89 for δ . This could be improved by taking into account model uncertainty and using model averaging. Indeed, the coverage rates ranged

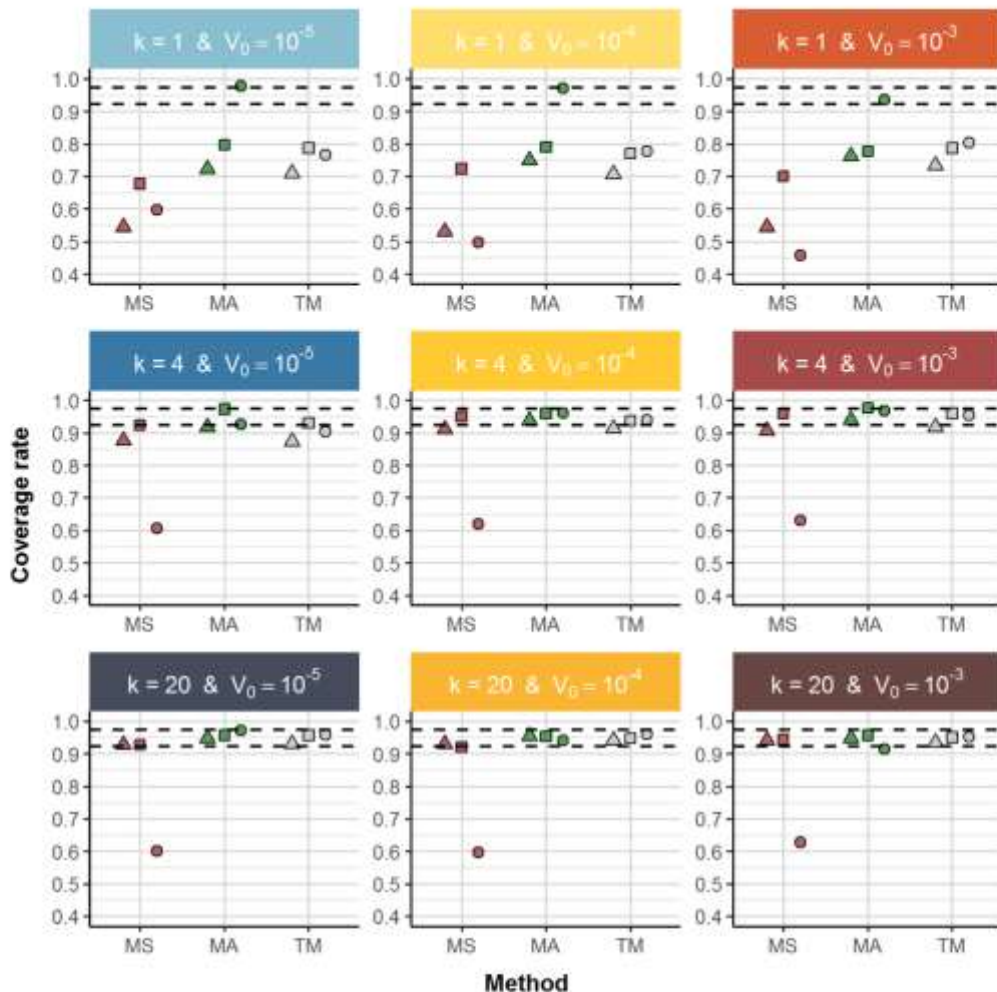


Fig. 3. Coverage rate of R_0 and δ in setting I. Coverage rate of the parameters R_0 (dots), π (squares), and δ (triangles) for each scenario using model selection, model averaging, or the true model. Dashed lines represents the prediction interval around 0.95

from 0.86 to 0.99 for both parameters in all models considered. In fact, MA had even better performances than the true model in some cases, which achieved subnominal coverage rate in 3 of the 5 considered scenarios (Fig. 5). All confidence intervals can be found in supplemental figures S5 and S6.

Finally, we compared the predictive performances of MS, MA, and the true model. For that purpose, we predicted the effect of a putative antiviral treatment on the proportion of patients having undetectable viremia at the end of follow-up (day 20). Here as well, the performances obtained using model selection and model averaging were compared. In all cases, the percentage of undetectable viral loads at end of treatment was accurately predicted for both MS and MA, with no more than 4% of bias in all cases considered (Fig. 6). In terms of precision of estimation, the results were also largely similar in most scenarios, with RMSE ranging from 0.4

to 30.5% in all cases. In one case, namely $\varepsilon = 0.95$, we found that MA outperformed the results obtained by MS. Here as well, the results obtained by model averaging were largely comparable with those obtained with the true model.

DISCUSSION

The objective of this study was to compare the estimation and the predictive performances of model selection and model averaging in the context of viral dynamic models. We explored two frequent issues encountered when developing viral dynamic models with uncertainty related to either (1) unidentifiable parameters or (2) the presence of several candidate biological models. In the two settings, MS provided poor coverage rates of typical parameters. This stems from the fact that MS neglects model uncertainty and focuses on one single

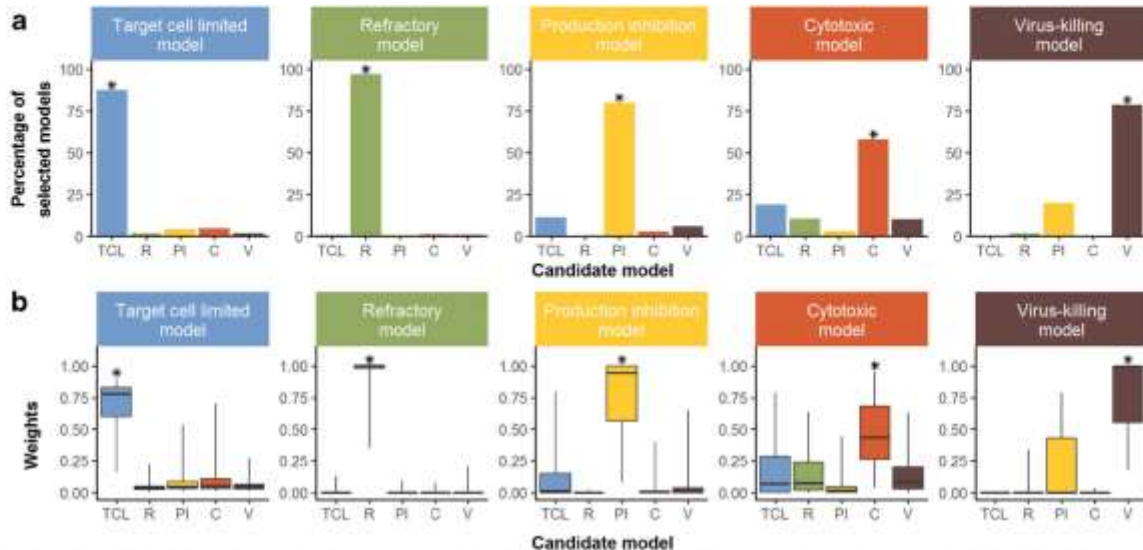


Fig. 4. Setting II. **a** For each scenario, the percentage of simulations where each candidate model was selected using AIC. Title of the facet indicates the true model. **b** Boxplots of weights (whiskers from the 2.5th to the 97.5th percentile) associated with each candidate model using AIC values. The asterisk denotes the true model in each scenario

"best model," leading to overconfidence in the parameter estimates. This can be corrected under certain conditions using MA, which provided better coverage rates and achieved the nominal coverage rate in most scenarios studied. MA can also be relevant to predict the effect of intervention, such as the percentage of patients that would achieve undetectable viral loads during treatment. Thus, extending results found in other contexts, in particular dose-finding studies [25, 35].

By offering a simple framework to take into account model uncertainty, MA accounts for the fact that in many situations several biological models are plausible. Our study shows the limitations of reporting only the best model. For instance, in the case of the target cell limited model, we found that the chance to conclude wrongly to an immune response controlling the infection was equal to 11%. In the case of the refractory model, which has been proposed as a driving force in several acute infection [33, 36], our results were more reassuring, with a rate of false

rejection of only 3%. This risk was larger with other models integrating an immune response, with rates of false rejection greater than 60% in some cases. By weighing the predictions of alternative models, MA avoids the caveat of MS. As advocated in other contexts [17, 37], MA can be used to more transparently discuss model uncertainty and to stimulate new data acquisition [13].

Although MA offers a simple alternative to MS, it also presents the defects of its virtue. As MA weighs the models according to their information criterion, using MA is relevant only if one model does not largely outperform the others. The weight value leading to "outperformance" is arbitrary and depends also on the number of candidate models. Accordingly, one may question the need to use weights when making predictions. As suggested by a reviewer, we conducted a simulation where all models having a weight greater than a given threshold (0.1 or 0.2) were considered as equally likely in the prediction, and this approach provided results close to those obtained

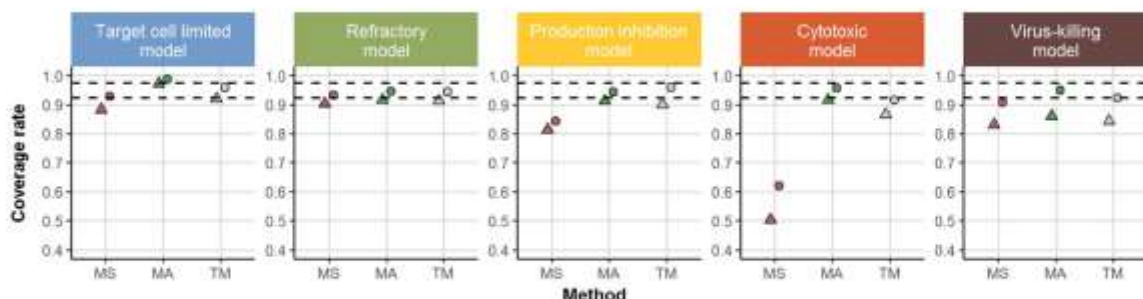


Fig. 5. Coverage rate of R_0 and δ in setting II. Coverage rate of the parameters R_0 (dots) and δ (triangles) for each scenario using model selection, model averaging, or the true model. Dashed lines represent the prediction interval around 0.95

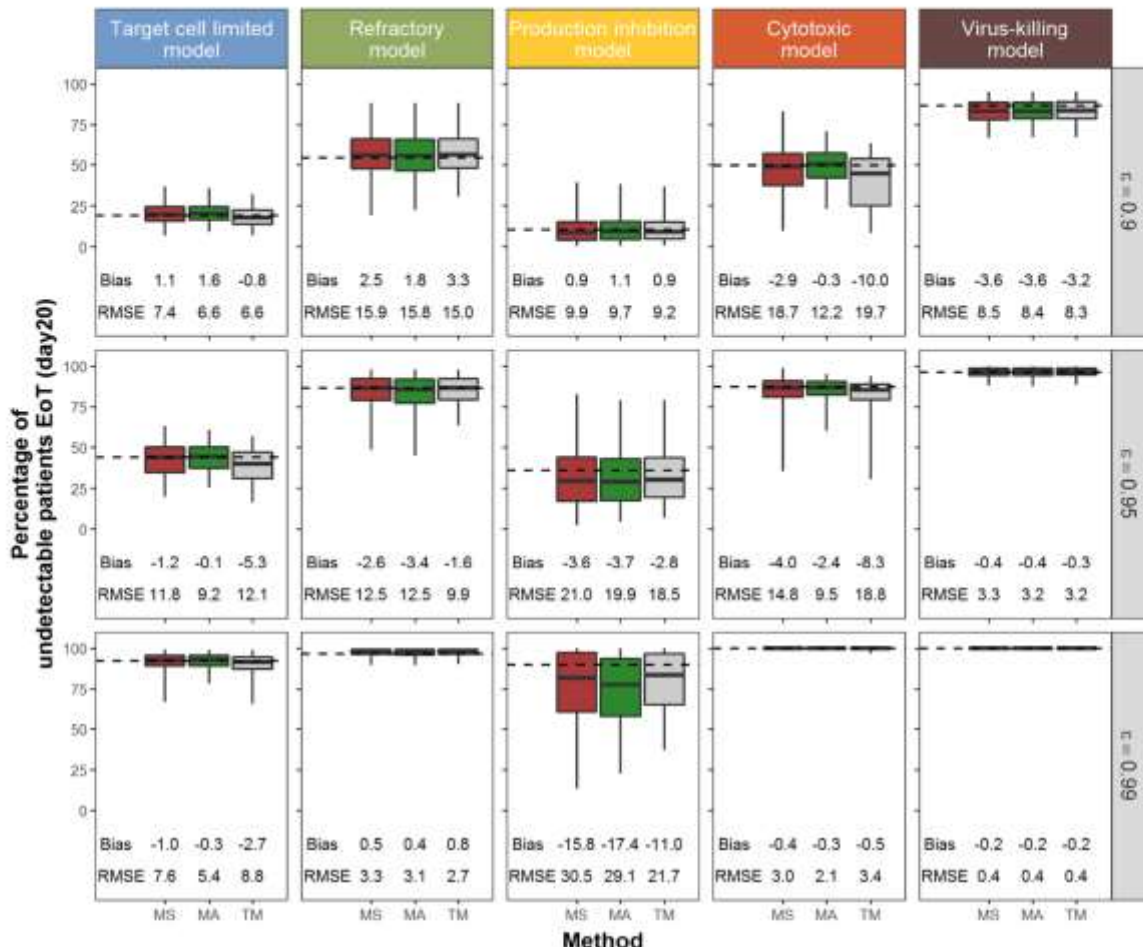


Fig. 6. Distribution of the expected proportion of patients below the limit of detection at day 20 using model selection (red), model averaging (green), or the true model (gray). For each scenario, whiskers represent the 2.5th to the 97.5th percentile, and each row corresponds to a different value of the treatment effect, noted s .

with MA (Supplemental Figure S7).

MA still requires to make important assumptions that need to be kept in mind. First, we used the asymptotic Gaussian approximations to calculate the standard errors. This assumption may not hold for all models, depending on their complexity and data paucity, as can been seen in some cases of Figs. 3 and 5. Other approaches have been proposed in the context of NLMEM to calculate the standard error more precisely, such as bootstrapping [38], sampling importance resampling [39], or Hamiltonian Monte-Carlo methods (HMC) [40]. Future work will be needed to evaluate in which contexts these methods, which are computationally demanding, are beneficial. Second, in our simulations, we assumed that there was a true model and that it was part of the candidate models. Although there is no “true model” in real data, we made this hypothesis to stress that MA should be performed only with biologically relevant models. Likewise, MA should not be used to “blindly” average predictions of any models and modelers should, prior to the analysis,

develop other models at hand and, if possible, discuss and perform new experiments to discriminate between them [13]. In that perspective, using MA to calculate CI is meaningful only if parameter has the same interpretation across the candidate models. This is the case for half-life or viral production rates but is less evident for derived parameters such the basic reproductive number R_0 [41, 42]. Finally, MA does not substitute to a proper analysis of parameter identifiability. In fact, the differences between MA and MS may simply reveal a poor practical identifiability, i.e., the fact that data available are not sufficient to precisely estimate parameters [8] and/or that the biological question is wrongly formulated [13]. This is also, what we observed here, with the wrong selection of models being in part due to the fact that the models had a poor practical identifiability, at least for some parameters. In order to be performant, MA requires that only a limited number of models are tested. It is only when a reasonable number of models remain that MA can be relevant, as an alternative to Bayesian approaches, that may be tedious in particular, a non-linear mixed effect framework.

ACKNOWLEDGMENTS

The authors also would like to acknowledge Hervé Le Nagard and Lionel de la Tribouille for the use of CATIBioMed calculus facility.

FUNDING INFORMATION

Antonio Gonçalves was funded by a grant from Roche Pharmaceutical Research and Early Development.

COMPLIANCE WITH ETHICAL STANDARDS

Conflict of interest The authors declare that they have no conflict of interest.

REFERENCES

- Ho DD, Neumann AU, Perelson AS, Chen W, Leonard JM, Markowitz M. Rapid turnover of plasma virions and CD4 lymphocytes in HIV-1 infection. *Nature*. 1995;373(6510):123–6.
- Wei X, Ghosh SK, Taylor ME, Johnson VA, Emini EA, Deutsch P, et al. Viral dynamics in human immunodeficiency virus type 1 infection. *Nature*. 1995;373(6510):117–22.
- Perelson AS, Ribeiro RM. Introduction to modeling viral infections and immunity. *Immunol Rev*. 2018;285(1):5–8.
- Perelson AS. Modelling viral and immune system dynamics. *Nat Rev Immunol*. 2002;2(1):28–36.
- Best K, Perelson AS. Mathematical modeling of within-host Zika virus dynamics. *Immunol Rev*. 2018;285(1):81–96.
- Ciupe SM. Modeling the dynamics of hepatitis B infection, immunity, and drug therapy. *Immunol Rev*. 2018;285(1):38–54.
- Lavielle M, Mentré F. Estimation of population pharmacokinetic parameters of saquinavir in HIV patients with the MONOLIX software. *J Pharmacokinet Pharmacodyn*. 2007;34(2):229–49.
- Guedj J, Thiebaut R, Commenges D. Practical identifiability of HIV dynamics models. *Bull Math Biol*. 2007;69(8):2493–513.
- Snoeck E, Chanu P, Lavielle M, Jacqmin P, Jonsson EN, Jorga K, et al. A comprehensive hepatitis C viral kinetic model explaining cure. *Clin Pharmacol Ther*. 2010;87(6):706–13.
- Nguyen T, Guedj J. HCV kinetic models and their implications in drug development: HCV kinetic models and their implications. *CPT Pharmacometrics Syst Pharmacol*. 2015;4(4):231–42.
- Handel A, Longini IM, Antia R. Towards a quantitative understanding of the within-host dynamics of influenza A infections. *J R Soc Interface*. 2010;7(42):35–47.
- Smith AM, Adler FR, Ribeiro RM, Gutenkunst RN, McAuley JL, McCullers JA, et al. Kinetics of coinfection with influenza A virus and *Streptococcus pneumoniae*. Grenfell BT, editor. *PLoS Pathogens*. 2013;9(3):e1003238.
- Ganusov VV. Strong inference in mathematical modeling: a method for robust science in the twenty-first century. *Front Microbiol*. 2016;7(1137):1–10.
- Buckland ST, Burnham KP, Augustin NH. Model selection: an integral part of inference. *Biometrics*. 1997;53(2):603.
- Boulesteix A-L. Ten simple rules for reducing overoptimistic reporting in methodological computational research. Lewitter F, editor. *PLoS Comput Biol*. 2015;11(4):e1004191.
- Kirk PDW, Babtie AC, Stumpf MPH. Systems biology (un)certainties. *Science*. 2015;350(6259):386–8.
- Burnham KP, Anderson DR. Model selection and multimodel inference: a practical information-theoretic approach. 2nd ed. [4. Printing]. New York: Springer; 2010. p. 488.
- Claeskens G, Hjort NL. Model selection and model averaging [internet]. Cambridge: Cambridge University Press; 2008. p. 332.
- Best K, Guedj J, Madelain V, de Lamballerie X, Lim S-Y, Osuna CE, et al. Zika plasma viral dynamics in nonhuman primates provides insights into early infection and antiviral strategies. *Proc Natl Acad Sci*. 2017;114(33):8847–52.
- Madelain V, Baize S, Jacquot F, Reynard S, Fizet A, Barron S, et al. Ebola viral dynamics in nonhuman primates provides insights into virus immuno-pathogenesis and antiviral strategies. *Nat Commun*. 2018;9(1):4013.
- Bertrand J, Comets E, Mentré F. Comparison of model-based tests and selection strategies to detect genetic polymorphisms influencing pharmacokinetic parameters. *J Biopharm Stat*. 2008;18(6):1084–102.
- Bozdogan H. Model selection and Akaike's information criterion (AIC): the general theory and its analytical extensions. *Psychometrika*. 1987;52(3):345–70.
- Anderson DR, Burnham KP. Understanding information criteria for selection among capture-recapture or ring recovery models. *Bird Study*. 1999;46(sup1):S14–21.
- Neath AA, Cavanaugh JE. The Bayesian information criterion: background, derivation, and applications: the Bayesian information criterion. *WIREs Comp Stat*. 2012;4(2):199–203.
- Buatois S, Ueckert S, Frey N, Retout S, Mentré F. Comparison of model averaging and model selection in dose finding trials analyzed by nonlinear mixed effect models. *AAPS J*. 2018;20(3):56.
- Aoki Y, Röshammar D, Hamrén B, Hooker AC. Model selection and averaging of nonlinear mixed-effect models for robust phase III dose selection. *J Pharmacokinet Pharmacodyn*. 2017;44(6):581–97.
- Kakizoe Y, Nakaoka S, Beauchemin CAA, Morita S, Mori H, Igashira T, et al. A method to determine the duration of the eclipse phase for *in vitro* infection with a highly pathogenic SHIV strain. *Sci Rep*. 2015;5(1):10371.
- Xia X, Moog CH. Identifiability of nonlinear systems with application to HIV/AIDS models. *IEEE Trans Autom Control*. 2003;48(2):330–6.
- Wu H, Zhu H, Miao H, Perelson AS. Parameter identifiability and estimation of HIV/AIDS dynamic models. *Bull Math Biol*. 2008;70(3):785–99.
- Miao H, Dykes C, Demeter LM, Cavanaugh J, Park SY, Perelson AS, et al. Modeling and estimation of kinetic parameters and replicative fitness of HIV-1 from flow-cytometry-based growth competition experiments. *Bull Math Biol*. 2008;70(6):1749–71.
- Dumont C, Lestini G, Le Nagard H, Mentré F, Comets E, Nguyen TT, et al. PFIM 4.0, an extended R program for design evaluation and optimization in nonlinear mixed-effect models. *Comput Methods Prog Biomed*. 2018;156:217–29.
- Baccam P, Beauchemin C, Macken CA, Hayden FG, Perelson AS. Kinetics of influenza A virus infection in humans. *J Virol*. 2006;80(15):7590–9.
- Pawelek KA, Huynh GT, Quinlivan M, Cullinan A, Rong L, Perelson AS. Modeling within-host dynamics of influenza virus infection including immune responses. *PLoS Comput Biol*. 2012;8(6):e1002588.
- Pinheiro J, Bornkamp B, Glimm E, Bretz F. Model-based dose finding under model uncertainty using general parametric models. *Statist Med*. 2014;33(10):1646–61.
- Schornig K, Bornkamp B, Bretz F, Dette H. Model selection versus model averaging in dose finding studies: K. SCHORNIG ET AL. *Stat Med*. 2016;35(22):4021–40.
- Saenz RA, Quinlivan M, Elton D, MacRae S, Blunden AS, Mumford JA, et al. Dynamics of influenza virus infection and pathology. *J Virol*. 2010;84(8):3974–83.
- Hoeting JA, Raftery AE, Madigan D. Bayesian model averaging: a tutorial. *Stat Sci*. 1999;14(4):382–417.
- Thai H-T, Mentré F, Holford NHG, Veayrat-Follet C, Comets E. Evaluation of bootstrap methods for estimating uncertainty of parameters in nonlinear mixed-effects models: a simulation

- study in population pharmacokinetics. *J Pharmacokinet Pharmacodyn.* 2014;41(1):15–33.
39. Dosne A-G, Bergstrand M, Harling K, Karlsson MO. Improving the estimation of parameter uncertainty distributions in nonlinear mixed effects models using sampling importance resampling. *J Pharmacokinet Pharmacodyn.* 2016 Dec;43(6):583–96.
40. Ueckert S, Riviere M-K, Mentré F. Alternative to resampling methods in maximum likelihood estimation for NLMEs by borrowing from bayesian methodology. www.page-meeting.org/?abstract=3632.
41. Lloyd AL. The dependence of viral parameter estimates on the assumed viral life cycle: limitations of studies of viral load data. *Proc Biol Sci.* 2001;268(1469):847–54.
42. Ribeiro RM, Qin L, Chavez LL, Li D, Self SG, Perelson AS. Estimation of the initial viral growth rate and basic reproductive number during acute HIV-1 infection. *J Virol.* 2010;84(12):6096–102.

PUBLISHER'S NOTE

Springer Nature remains neutral with regard to jurisdictional claims in published maps and institutional affiliations.

Supplementary material 1

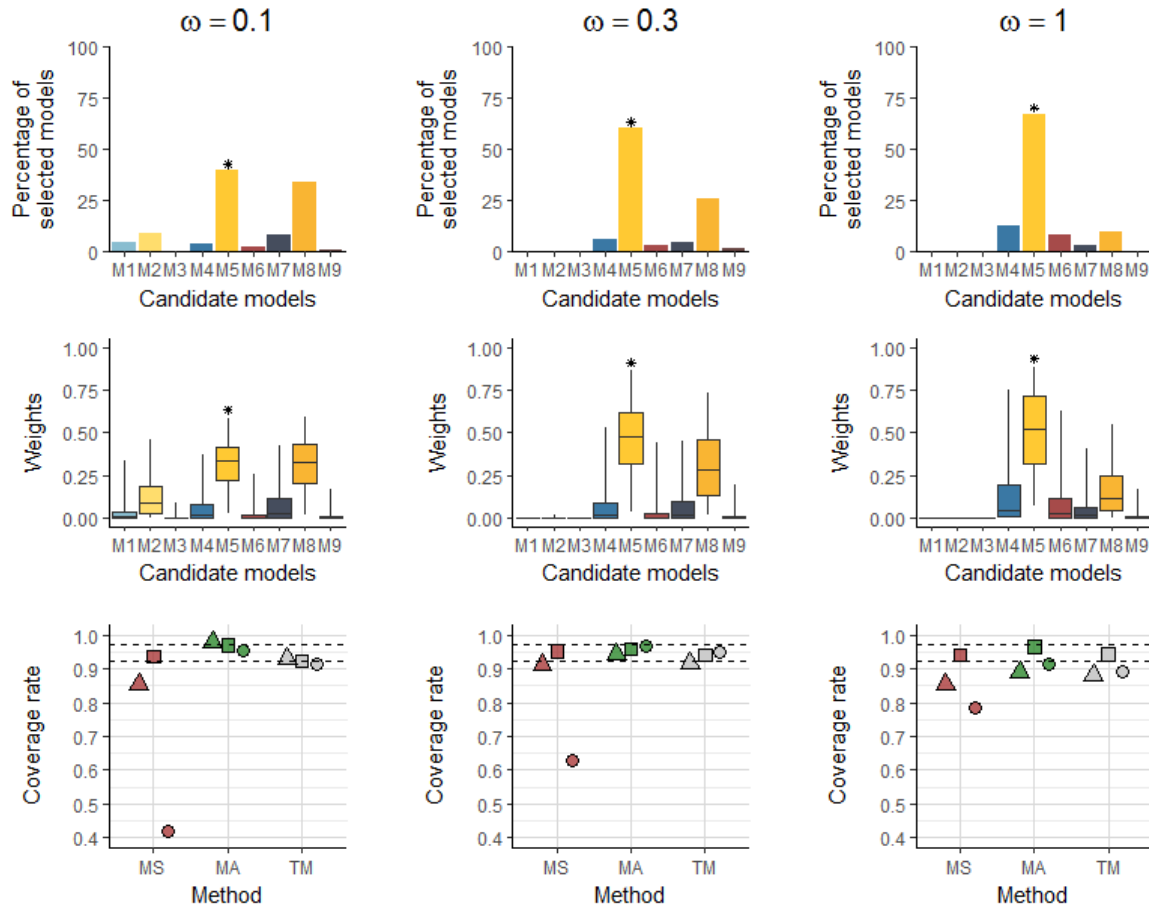


Figure S1. Influence of variability in model selection and model averaging procedures on model $k=4 \text{ d}^{-1}$ and $V_0=10^{-4} \text{ copies.mL}^{-1}$ (setting I). Top row shows the percentage of selected models using the AIC criterion. Middle row presents the boxplot of weights using the AIC criterion. Bottom row shows the coverage rates of parameters R_0 (dots), δ (triangles) and π (squares)

Le model averaging dans les modèles de cinétique virale

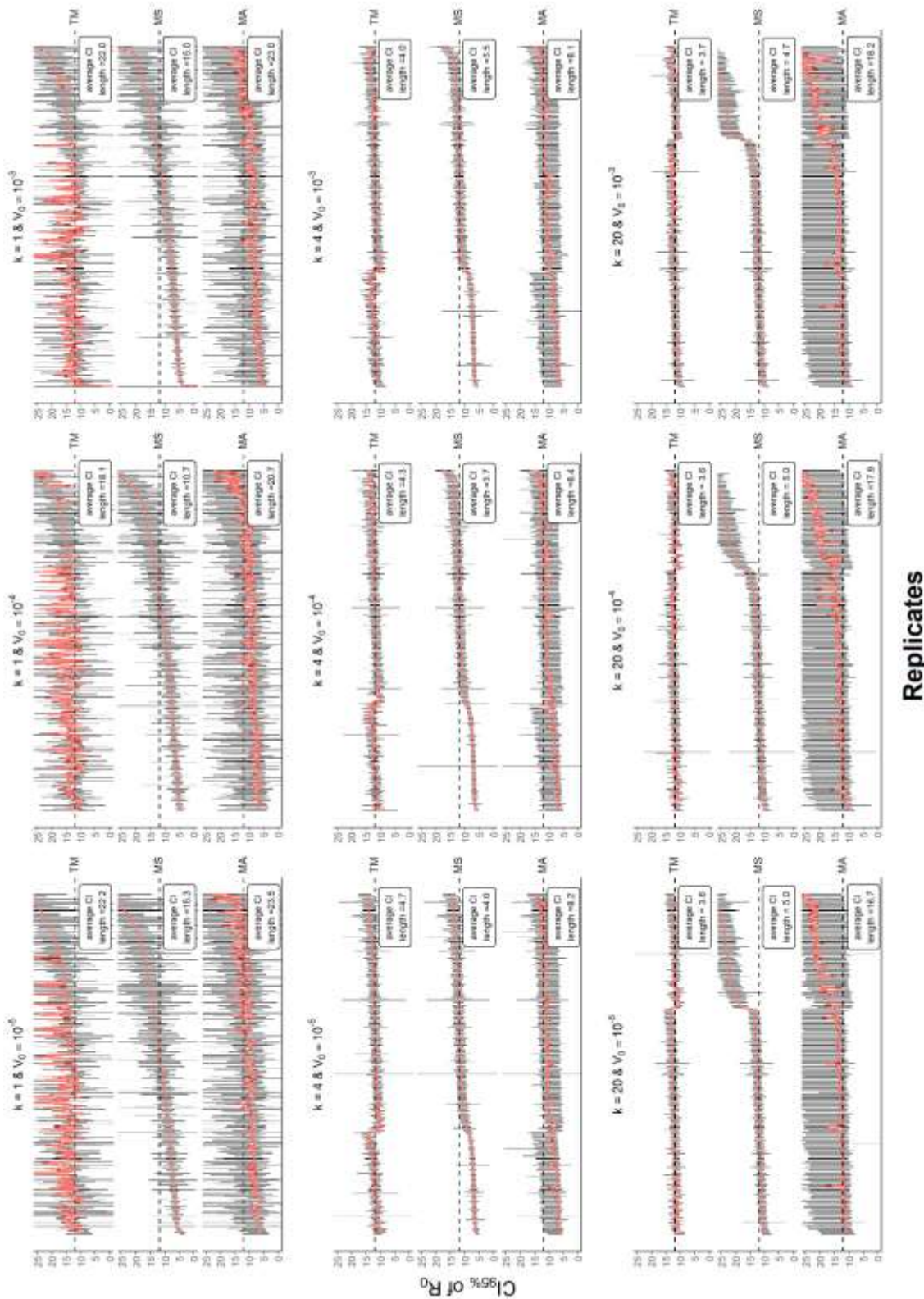
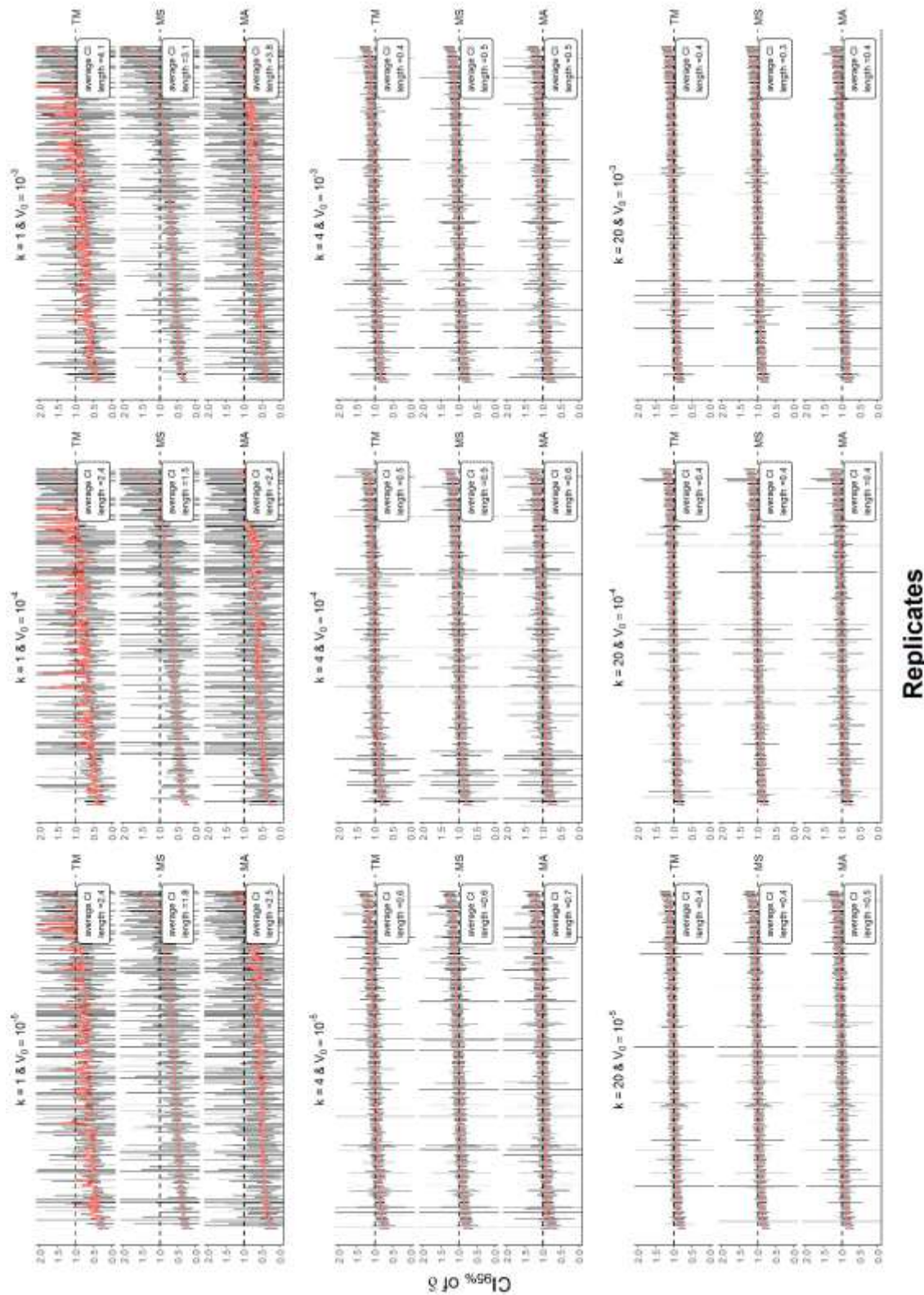


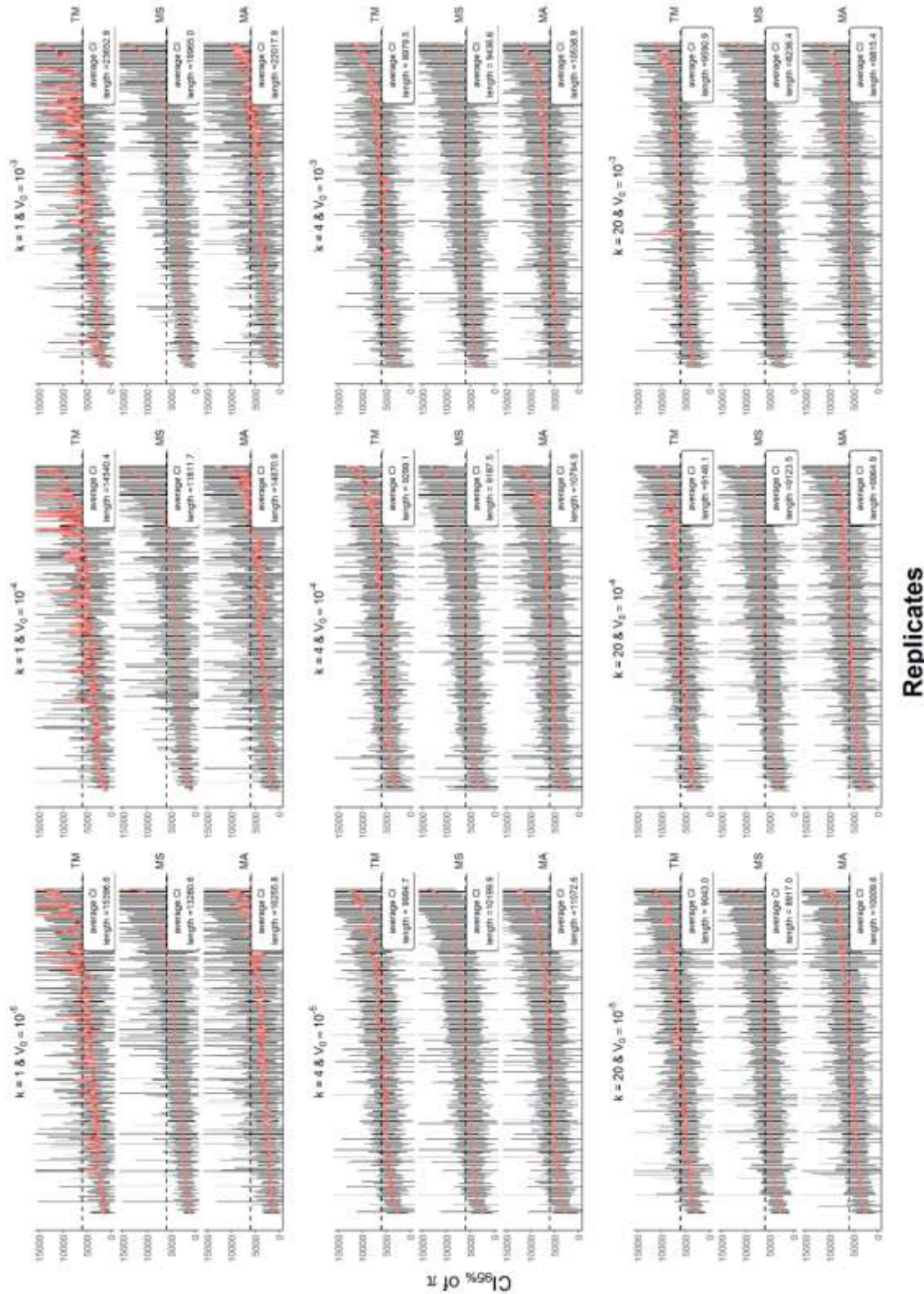
Figure S2. Confidence intervals at 95% of R_0 across models and for each modelling approach of setting I. Replicates are ordered by increasing median value found in MS. Dashed line corresponds to the true value of R_0



Replicates

Figure S3. Confidence intervals at 95% of δ across model and for each modelling approach of setting I. Replicates are ordered by increasing median value found in MS. Dashed line corresponds to the true value of δ

Le model averaging dans les modèles de cinétique virale



Replicates

Figure S4. Confidence intervals at 95% of π across model and for each modelling approach of setting I. Replicates are ordered by increasing median value found in MS. Dashed line corresponds to the true value of π

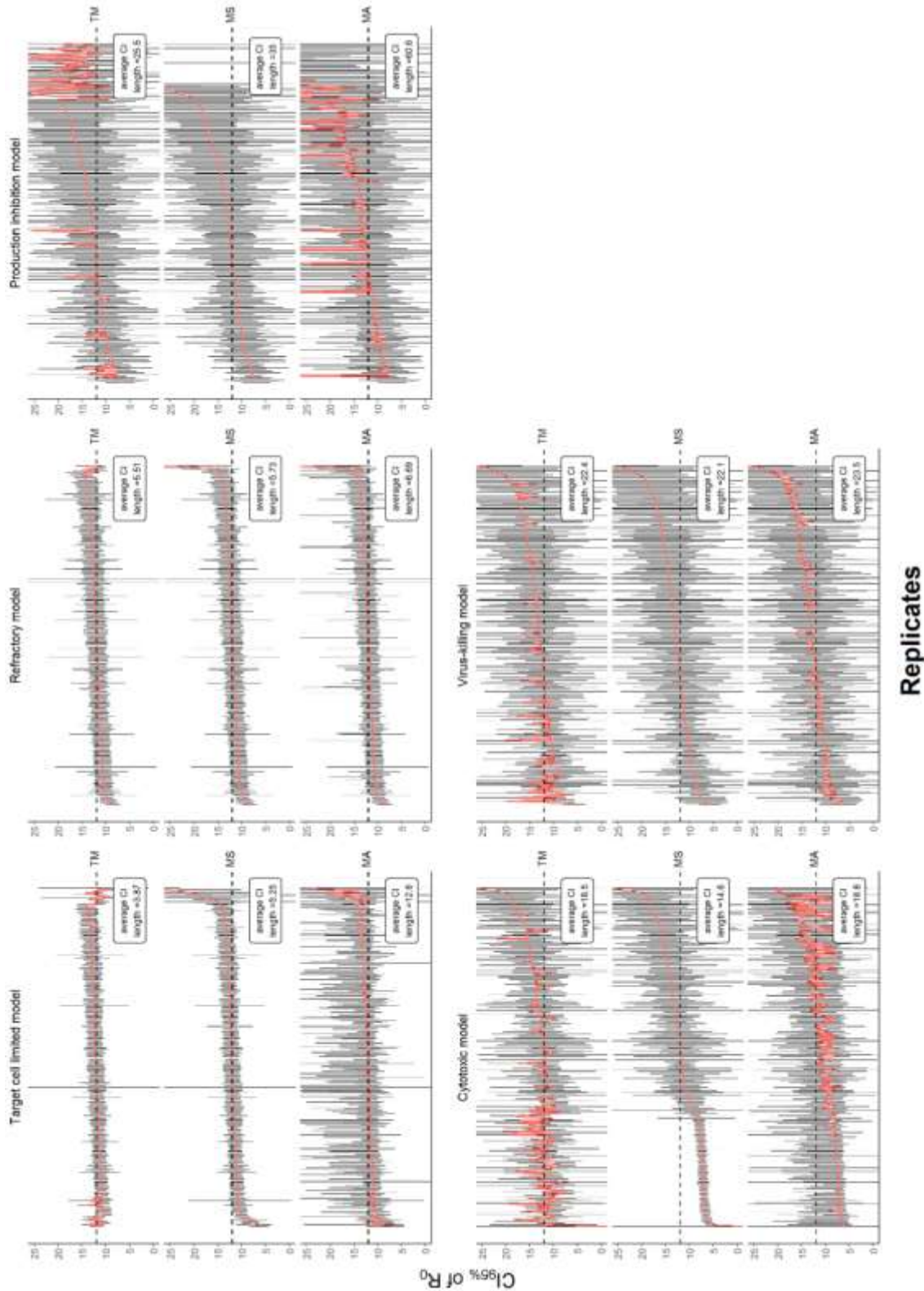


Figure S5. Confidence intervals at 95% of R_0 across model and for each modelling approach of setting II. Replicates are ordered by increasing median value found in MS. Dashed line corresponds to the true value of R_0

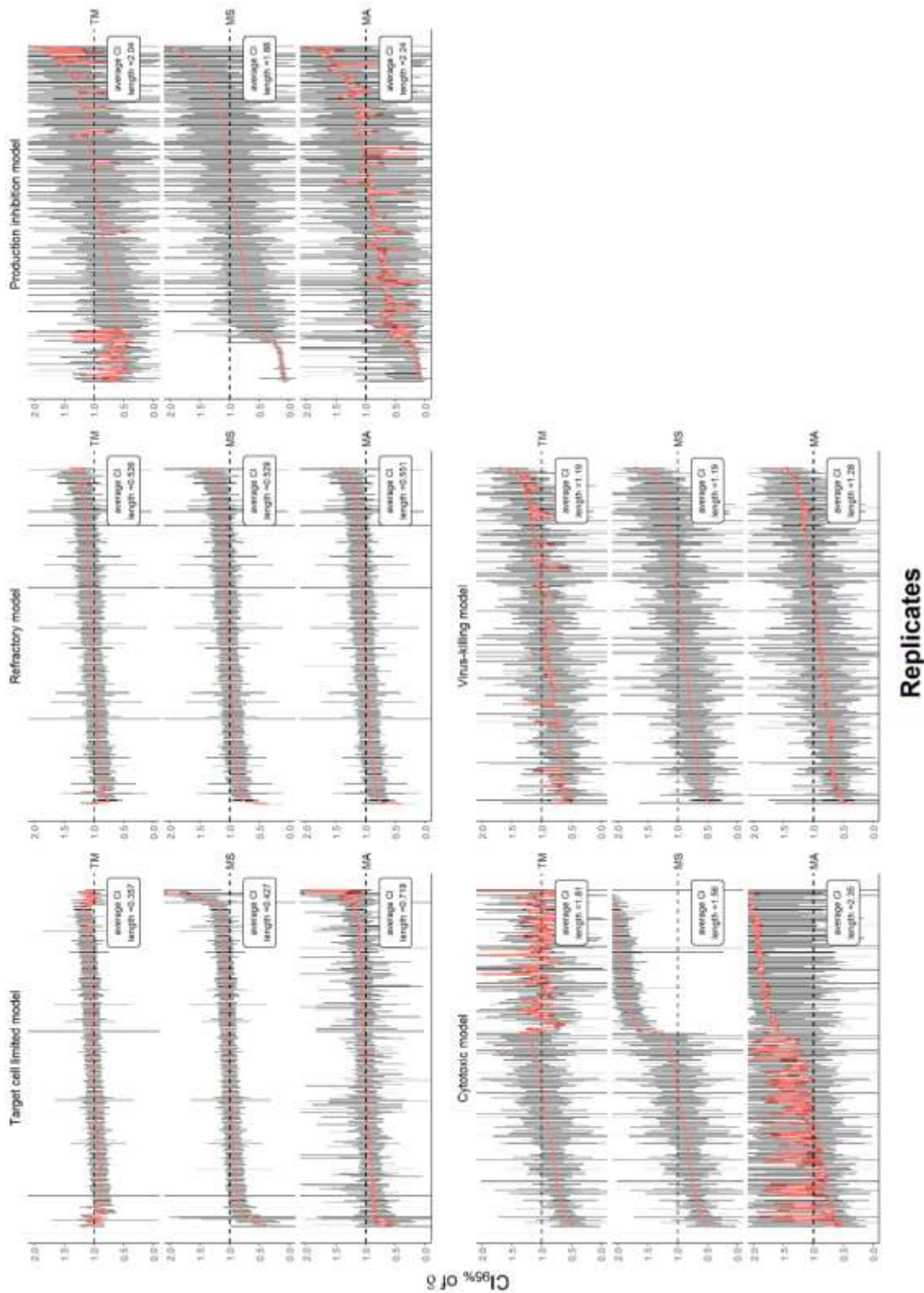


Figure S6. Confidence intervals at 95% of δ across model and for each modelling approach of setting II. Replicates are ordered by increasing median value found in MS. Dashed line corresponds to the true value of δ

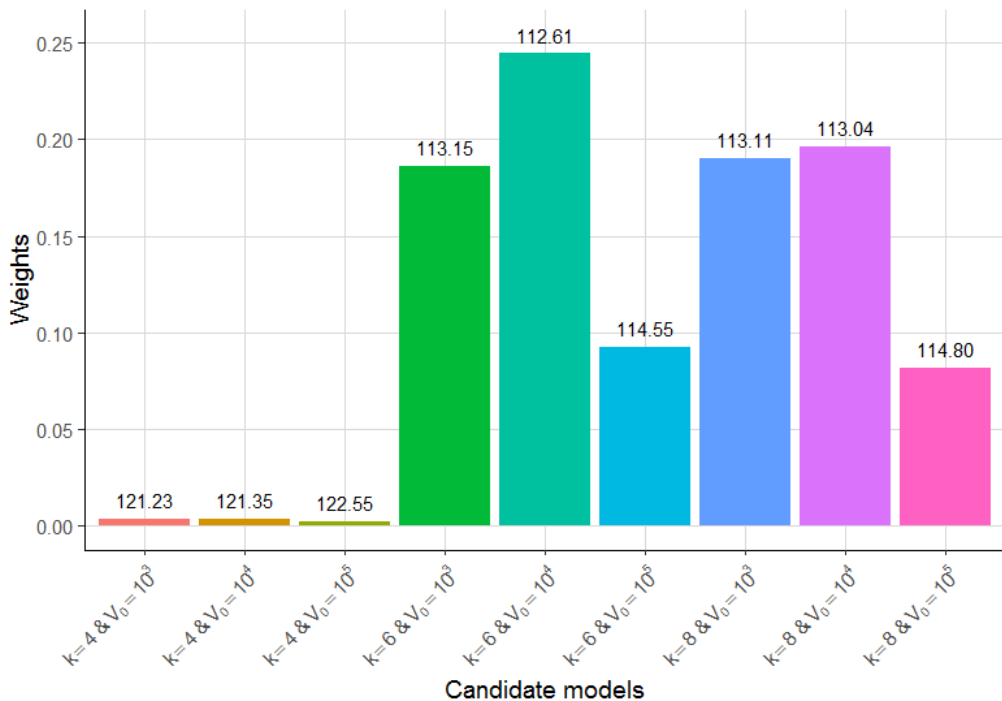


Figure S7. Distribution of weights given the data of Best et al. PNAS 2017. Nine candidate models were tested with values of k and V_0 ranging from 4 to 8 d^{-1} and 10^3 to 10^5 respectively

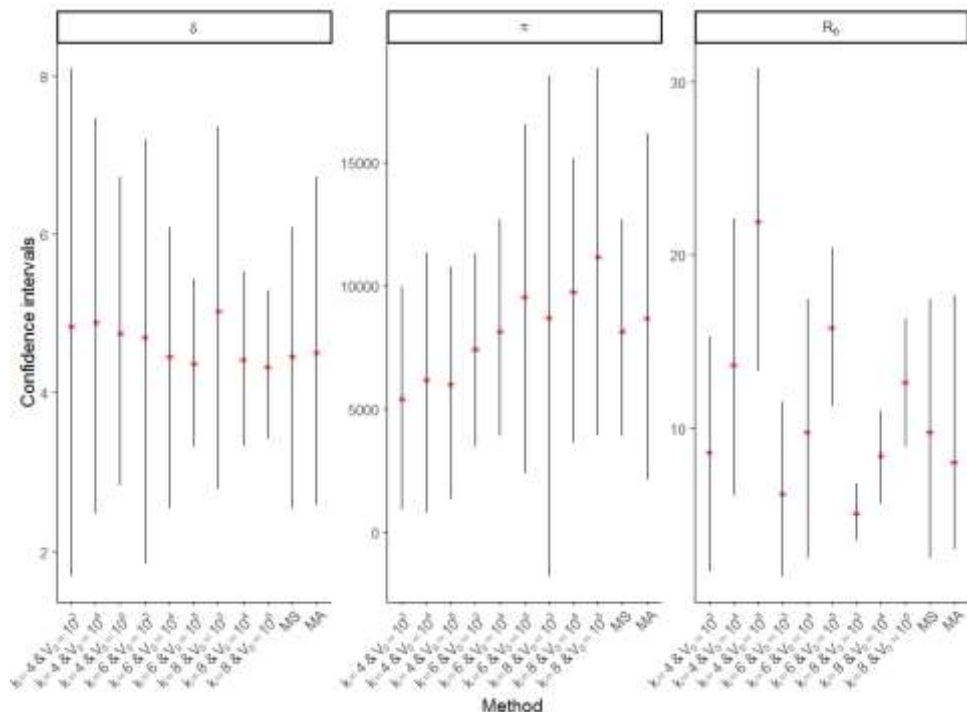


Figure S8. Confidence intervals of δ , π and R_0 for each candidate model, for the selected model (MS) and in model averaging (MA)

Chapitre 6. Discussion et conclusion

L'objectif principal de ces travaux de thèse était d'étudier l'effet de thérapies antivirales innovantes. Par le développement de modèles mécanistiques du VHB intégrant les mécanismes d'action de nouveaux traitements, nous avons pu étudier la cinétique de nouveaux marqueurs viraux. Dans un premier travail, nous avons développé un modèle décrivant l'action d'un agoniste du *toll-like* récepteur 7 sur la virémie, les sous particules virales et les anticorps anti-AgHBs. Dans un second travail, nous avons étudié l'effet d'un inhibiteur de capsid sur l'ADN et l'ARN VHB. Enfin dans un troisième travail nous avons évalué les performances prédictives et d'estimation fournies par la sélection de modèle et le *model averaging* dans les modèles de cinétique virale.

Ensemble ces travaux contribuent à une meilleure compréhension des mécanismes d'action des nouvelles thérapies et de la cinétique des marqueurs qu'elles ciblent. Ils ouvrent la voie au développement d'approches plus robustes pour l'estimation des paramètres et la prédiction, qui soutiendront les nouvelles générations de modèles de l'hépatite B dans le contexte de « HBV cure ».

6.1. Discussion

Jusqu'à présent, la modélisation de la cinétique virale dans l'hépatite B s'est limitée principalement à la description de l'ADN VHB, le seul produit viral inhibé par les traitements actuels (analogues nucléos(t)idiques et/ou interféron). Le développement de nouveaux traitements inhibant de nouveaux produits viraux requiert l'utilisation de modèles plus complexes qui permettront de soutenir leur utilisation clinique.

Dans un premier projet, nous avons caractérisé la cinétique conjointe de l'AgHBs et de la virémie chez la souris traitée par le RO7020531, un agoniste de TLR7. Nous avons montré que le RO7020531 inhibe la production d'ADN VHB et celle de sous particules virales (SVP), et stimule la réponse immunitaire. En utilisant ce modèle dans le cadre d'une infection humaine, notre modèle prédit un taux de guérison fonctionnelle (une charge virale indétectable, un AgHBs indétectable et la présence d'anticorps anti-AgHBs) pouvant aller jusqu'à 40% en 6

mois de traitement en utilisant les mêmes doses que chez la souris. Depuis l’initiation de cette thèse, des études cliniques de phase I ont évalué la tolérance et l’efficacité des agonistes du TLR7 en monothérapie (Janssen et al., 2018; Yuen et al., 2019a; Luk et al., 2020). Ces essais ont montré que les agonistes du TLR7 étaient bien tolérés et diminuaient la virémie chez les patients infectés. Le RO7020531 a montré une stimulation du système immunitaire entraînant la production d’IFN α et d’autres cytokines telles que l’IP10 ou l’ISG15 mais aucune diminution d’AgHBs n’a pu être observée à l’issue des 6 semaines de traitement (Yuen et al., 2019a; Luk et al., 2020). De fait, les doses de TLR7 ou TLR8 utilisée en clinique sont trop faibles pour entraîner un déclin de l’AgHBs (Janssen et al., 2018; Gane et al., 2020). Cependant la piste de ces agonistes et plus largement des immunomodulateurs reste à l’étude, particulièrement en combinaison avec des antiviraux directs comme les inhibiteurs de capsidé (CAM) qui permettent un contrôle virologique des patients (Dai et al., 2018).

Dans un second travail nous avons analysé les cinétiques virales de patients traités par un CAM : le RG7907. Les données, issues d’une étude de phase Ib et d’une durée de 4 semaines, ont été décrites grâce à un modèle multi-échelle intégrant la production intracellulaire d’ARN viral, la transcription en ADN ainsi que l’export dans la circulation sanguine. Nous avons estimé une efficacité du RG7907 sur la production de particules encapsidées de 99% en médiane. Cette efficacité se traduit par un déclin biphasique de l’ADN et d’ARN VHB. Après un déclin de 2 log₁₀ au cours de la première semaine de traitement, les deux marqueurs déclinent d’un log₁₀ supplémentaire à un taux de 0,13 j⁻¹. Un apport important de la modélisation réside dans l’interprétation biologique des pentes de déclin de la virémie. Alors que les modèles de cinétique virale du VHB développés jusque-là prédisent que la décroissance initiale de l’ADN VHB est un reflet de sa clairance naturelle dans le sang, notre modèle montre que le déclin initial pourrait aussi être influencé par les mécanismes intracellulaire de maturation et de sécrétion des particules. Nous avons estimé dans ce modèle que la première pente est due à l’export des particules encapsidées de l’ordre de 1 j⁻¹. Dans son article de 2006, Murray et al. fournissent une estimation similaire de la vitesse d’export (0.46 j⁻¹) en se basant sur la mesure d’ADN intracellulaire chez le chimpanzé (Murray et al., 2006). Ils estiment par ailleurs une demi-vie du virus courte et de l’ordre de 2 h. Cette estimation est proche de la nôtre (50 min) et concorde avec d’autres infections virales comme le VIH ou le VHC (0,5 – 3h). Afin de mieux estimer la clairance virale, il serait possible de réaliser une aphérèse chez des sujets infectés. La technique consiste à extraire le plasma contenant le virus. Une fois l’aphérèse terminée, la

virémie retourne à son état basal (pré-aphérèse) à un taux c , la clairance du virus. Dans le VHC et le VIH, ces expérimentations ont conduit à des estimations de la clairance plus grandes que celles fournies par les modèles de cinétique virale (Ramratnam et al., 1999). Des expériences similaires sont en cours de le VHB.

Une autre prédition de ce modèle est que le ratio ADN/ARN s'inverse au cours du traitement par analogues nucléos(t)idiques. Alors que l'ADN diminue dès l'initiation du traitement, nous prédisons que l'ARN VHB augmente transitoirement au cours des premiers jours de traitement avant de décliner à la même vitesse que l'ADN VHB (Wang et al., 2016). Une étude menée chez des patients traités par JNJ-6379, un autre CAM, semble confirmer ces résultats et montre une élévation continue de l'ARN VHB au cours des premières semaines de traitement (Janssen et al., 2020) bien que l'augmentation soit plus modeste que celle que nous prédisons ($0.2 \log_{10}$ contre $1.3 \log_{10}$ au 14^{ème} jour de traitement, respectivement). Cette prédition est dépendante des caractéristiques à l'inclusion et du statut antigénique des patients. Il paraît donc nécessaire d'inclure de telles informations dans les modèles afin d'élucider les mécanismes de cinétique précoces de l'ARN VHB.

Au cours de cette thèse, la compréhension des mécanismes d'action de ces nouvelles classes thérapeutiques s'est accompagnée du développement de modèles mécanistiques complexes intégrant de plus en plus de paramètres. De ce fait il devient encore plus important d'identifier les nouveaux paramètres du modèle et de savoir comment conclure en faveur d'un modèle plutôt qu'un autre au regard des données dont nous disposons. Dans notre troisième travail, nous avons proposé d'utiliser des approches de type *model averaging* pour apporter plus de robustesse aux prédictions. Nous avons montré que MS est moins performant que MA aussi bien en terme d'estimations des paramètres que de précisions des prédictions. Les résultats obtenus dans le cadre des modèles de cinétique virale rejoignent ceux obtenus dans d'autres domaines comme les études de recherche de dose optimale (*dose-finding studies*) (Schorning et al., 2016) où MS mène à la sélection d'un modèle plus complexe que celui ayant servi à générer les données simulées. Ceci montre les limites de MS dans le cas où le choix du meilleur modèle n'est pas évident et où plusieurs hypothèses alternatives fournissent des conclusions différentes. Avec le développement de modèles du VHB complexes intégrant de plus en plus de marqueurs viraux, cette problématique pourrait se poser plus fréquemment lors du développement clinique des médicaments. Ainsi des approches telles que le *model averaging*

pourraient être utilisées à l'avenir pour justifier le choix d'une dose et de la durée de traitement auprès des autorités réglementaires.

6.2. Perspectives

En clinique, l'objectif thérapeutique fixé par les sociétés savantes est la guérison fonctionnelle de la maladie (Lampertico et al., 2017), c'est-à-dire une charge virale indétectable et une perte de l'AgHBs associée ou non à l'apparition d'anticorps, persistante après l'arrêt du traitement. Compte-tenu des doses ou des durées de traitement, celle-ci n'a pu être observée au cours des études présentées dans cette thèse. Cependant, le potentiel antiviral de ces molécules doit être davantage étudié notamment en les combinant permettant ainsi la diminution de plusieurs marqueurs viraux et la restauration d'une immunité efficiente.

Le principal défi de ces traitements sera de comprendre les mécanismes liés à la persistance d'une activité transcriptionnelle du *cccDNA*. Pour les agonistes du TLR7, la stimulation de la production d'interféron- α endogène pourrait au long cours permettre une diminution de l'activité du *cccDNA* comme cela a pu être observé chez les patients traités par Peg-IFN. Concernant les CAM, ils pourraient limiter l'activité transcriptionnelle par inhibition de la boucle d'amplification du *cccDNA*. Par ailleurs, le lien entre la cinétique des marqueurs sous traitement et l'activité transcriptionnelle du virus n'a à ce stade pas été établi. La mesure du *cccDNA* est difficile : elle nécessite une biopsie ce qui rend la réalisation de prélèvements réguliers impossible. En revanche, il existe d'autres marqueurs viraux sériques qui sont corrélés à l'activité transcriptionnelle du virus et au niveau d'expression du *cccDNA*. En particulier l'AgHBcr (*core-related antigen*) a montré un bonne corrélation avec les niveaux d'ADN VHB, d'ARN pré-génomique, d'AgHBs et de *cccDNA* chez les patients traités (Testoni et al., 2019). L'étude de la cinétique de ce marqueur sous traitement pourrait permettre d'établir un lien entre les traitements utilisés et l'activité du *cccDNA*.

Les modèles présentés dans cette thèse ont permis une meilleure compréhension des mécanismes de déclin de l'ADN VHB. Ils montrent notamment que le déclin initial de la virémie sous traitement est dû à la sécrétion du virus dans la circulation générale. Toutefois ces modèles ne permettent pas d'expliquer le phénomène lié à la seconde pente de déclin de la virémie puisque le lent déclin de l'AgHBs, qui serait éliminé en plus de 50 ans (Chevaliez et

al., 2013), contredit la prédition d'une élimination des cellules infectées en quelques semaines. Ainsi, il est clair que les modèles, hérités du VHC et qui supposent que le déclin à long terme du virus est déterminé par la vitesse d'élimination des cellules infectées, sont trop réducteurs pour le VHB. Le cycle de réPLICATION du virus suggère l'existence d'autres marqueurs et/ou compartiments cellulaires qui pourraient expliquer la différence de déclin au long cours des marqueurs du VHB tels que le *cccDNA* et les cellules infectées avec de l'ADN intégré. Dans le premier projet nous avons initié le développement de modèles en distinguant deux sous populations cellulaires : l'une exprimant le *cccDNA* et une autre ne l'exprimant plus, soit par action de l'interféron soit par perte suite à la division cellulaire. Nous développons actuellement une extension de ce modèle sur des données historiques de patients traités par Peg-IFN±LAM. Le modèle distingue les cellules fortement productrices de particules virales complètes n'ayant pas subit l'étape d'intégration du génome viral et les cellules à demi-vie longue ayant subi l'intégration virale et à l'origine d'une forte production d'AgHBs (Cornberg et al., 2017; Tu et al., 2017; Wooddell et al., 2017). Ainsi, la diminution observée au cours des 4 premières semaines de traitement correspondrait à la mort des cellules à courte demi-vie, entraînant une forte diminution de la charge virale mais l'absence ou le faible déclin d'AgHBs. Les cellules à demi-vie longue persisteraient entraînant le maintien des niveaux d'AgHBs et de faibles niveaux de séroconversion malgré les traitements. Une autre hypothèse voudrait que l'ARN VHB soit une source de réinfection. En effet, les particules d'ARN VHB circulant contiennent en leur sein la reverse transcriptase, l'ARN pré-génomique nécessaire à la production de *cccDNA* (Liu et al., 2019). Le développement de modèles plus complexes intégrant ces compartiments est nécessaire pour expliquer le déclin au long cours des marqueurs viraux et prédire les chances de guérison avec les nouveaux traitements.

Dans cette thèse nous avons vu comment le *model averaging* permettait des estimations plus robustes. La problématique de l'identifiabilité des paramètres convient à l'application de méthodes bayésiennes dans lesquelles la connaissance *a priori* des paramètres est intégrée au modèle et dans le calcul de la vraisemblance. Nous envisageons d'utiliser l'algorithme *Hamiltonian Monte-Carlo* du logiciel Stan et permettant d'implémenter des modèles biologiques décrits par équations différentielles ordinaires et des modèles non linéaires à effets mixtes. Nous avons constaté la propagation de l'incertitude des paramètres sur la prédition d'un effet traitement en utilisant des lois asymptotiquement normales des paramètres. Néanmoins, d'autres méthodes de calcul des erreurs standard comme le *Sampling Importance*

Resampling et le *bootstrap* (Thai et al., 2014; Dosne et al., 2016) qui ne font pas d'hypothèse quant à la distribution des paramètres pourraient être à même de fournir une estimation non biaisée des paramètres du modèle et de l'effet traitement.

6.3. Conclusion générale

Depuis les années 90 et leur utilisation croissante dans les infections virales, les modèles de cinétique virale connaissent un important développement. Utilisés pour inférer l'efficacité d'un traitement, ceux-ci rendent compte des processus biologiques mis en jeu au cours de l'infection. Dans le cadre du virus de l'hépatite B, leur utilisation s'est limitée jusqu'à présent à la seule modélisation de la virémie.

Dans ce contexte, ces travaux de thèse présentent de nouveaux modèles du VHB intégrant les cibles pharmacologiques potentielles des nouveaux traitements et décrivant d'autres marqueurs vitaux produits au cours de l'infection. Le développement de ces modèles complexes a été rendu possible par l'utilisation d'algorithmes puissants et d'approches méthodologiques robustes comme le *model averaging*. Nous pensons que les modèles de cinétique virale de l'hépatite B permettront de mieux concevoir et d'optimiser les stratégies thérapeutiques futures en vue d'une guérison fonctionnelle de la maladie.

Chapitre 7. Une thèse pendant l'épidémie de COVID-19

En décembre 2019, une nouvelle infection virale a émergé en Chine dans la province de Wuhan (Huang et al., 2020). Rapidement l'épidémie s'est répandue, causant des millions de cas et plusieurs centaines de milliers de morts à travers le monde. Dès janvier 2020, la communauté scientifique a mobilisé ses ressources aussi bien humaines que matérielles. Ainsi, de mars à octobre 2020, j'ai participé à l'effort de recherche et mis mes connaissances et compétences en modélisation des infections virales à contribution.

Mes travaux de recherche se sont organisés autour de trois thématiques. Premièrement, il nous fallait caractériser cette infection virale émergente, notamment en estimer les paramètres clés tel que le taux de reproduction intra-hôte du virus R_0 permettant de définir les efficacités critiques nécessaires pour éradiquer le virus. Puis nous avons estimé les efficacités attendues des molécules repositionnées et évaluées en clinique. Enfin, nous avons évalué l'efficacité d'une de ces molécules *in vivo* dans un modèle primate de l'infection à SARS-CoV-2.

Dans un premier projet, nous modélisé les charges virales nasopharyngées d'une série de 13 patients hospitalisés à Singapour (Young et al., 2020). Nous avons utilisé le modèle usuel, dit limité par les cellules cibles, pour décrire la cinétique des patients infectés. Nous prédisons que la charge virale est maximale 5 jours après l'apparition des symptômes puis diminue à un taux de $0,6 \text{ j}^{-1}$ environ. Le modèle fournit également une première estimation du R_0 ($R_0 = 8,6$). Ces nombres nous renseignent sur l'efficacité ainsi que le moment optimal de l'initiation du traitement pour réduire la charge virale (Best et al., 2017; Friberg et Guedj, 2019). Nous prédisions qu'un traitement d'une efficacité de 90% et initié le jour de l'apparition des symptômes pourrait réduire le pic de charge virale de $2 \log_{10}$.

Cette efficacité prédictive a ensuite été comparée à celle prédictive pour les molécules alors étudiées dans l'essai DisCoVeRy (NCT04315948) : l'hydroxychloroquine, l'association lopinavir/ritonavir \pm IFN- β -1a et le remdesivir. Compte-tenu des caractéristiques pharmacocinétiques et pharmacodynamiques de ces molécules, il apparaissait peu probable que l'une d'entre elles ait une efficacité suffisante si elle est initiée après l'apparition des symptômes. Ces résultats ont depuis été confirmés par l'arrêt des bras hydroxychloroquine et lopinavir/ritonavir \pm IFN- β -1a en mai et juin dernier (Institut National de la Santé Et de la

Recherche Médicale, France, 2020). Ce travail a fait l'objet d'un article scientifique publié dans *CPT : Pharmacometrics and System Pharmacology*.

Dans un second projet, nous avons évaluer et caractériser l'infection dans un modèle primate de l'infection. Ce modèle, en permettant de mesurer le virus et les concentrations de médicament dans plusieurs compartiments de façon répétée, sont particulièrement adaptés à l'étude de la réponse au traitement (Williamson et al., 2020). Ainsi, nous avons modélisé les charges virales nasopharyngées et trachéales de 35 macaques cynomolgus infectés à des fortes doses de virus (10^6 pfu) et traités par hydroxychloroquine (HCQ) administrée seule ou combinaison avec l'azithromycine, avant ou après l'infection (Maisonnasse et al., 2020). Les singes ont développé une infection modérée de la maladie, similaire à celle observée chez l'homme, caractérisée par une toux persistante et peu de lésions pulmonaires.

Quel que soit le traitement et le moment de son initiation, les macaques présentaient des charges virales nasopharyngées et trachéales élevées, maximales à J2 post infection et détectables pendant 7 jours en moyenne suggérant l'absence d'un effet de l'HCQ dans l'infection au SARS-CoV-2. Ainsi, dans un second temps, les données recueillies ont été modélisées en négligeant l'effet de l'HCQ. Le modèle développé caractérise conjointement les cinétiques virales nasopharyngées et trachéales et permet d'estimer les paramètres clés de l'infection. Compte-tenu des faibles R_0 ($R_{0,N} = 4,0$ et $R_{0,T} = 5,9$) et des fortes doses du virus inoculé, nous prédisons que la charge virale augmente modestement dans les deux premiers jours de traitement avant de diminuer à un taux de $1,9 \text{ j}^{-1}$ correspondant à la mort des cellules infectées pour devenir indétectable vers J7. Nous avons ensuite étudié des protocoles expérimentaux explorant des doses de virus plus faibles et l'effet d'un traitement en prophylaxie et limitant la production virale. Quel que soit la dose de virus utilisée, le portage viral dure entre 10 et 12 jours ce qui concorde avec la durée de portage observée chez les sujets asymptomatiques (Sakurai et al., 2020). Ce travail fait l'objet d'une soumission dans *PLoS Computational Biology*.

ARTICLE

Timing of Antiviral Treatment Initiation is Critical to Reduce SARS-CoV-2 Viral Load

Antonio Gonçalves^{1*}, Julie Bertrand¹, Ruian Ke², Emmanuelle Comets¹, Xavier de Lamballerie³, Denis Malvy^{4,5}, Andrés Pizzorno⁶, Olivier Terrier⁶, Manuel Rosa Calatrava⁶, France Mentré¹, Patrick Smith⁷, Alan S. Perelson² and Jérémie Guedj^{1,*}

We modeled the viral dynamics of 13 untreated patients infected with severe acute respiratory syndrome-coronavirus 2 to infer viral growth parameters and predict the effects of antiviral treatments. In order to reduce peak viral load by more than two logs, drug efficacy needs to be > 90% if treatment is administered after symptom onset; an efficacy of 60% could be sufficient if treatment is initiated before symptom onset. Given their pharmacokinetic/pharmacodynamic properties, current investigated drugs may be in a range of 6–87% efficacy. They may help control virus if administered very early, but may not have a major effect in severely ill patients.

Study Highlights

WHAT IS THE CURRENT KNOWLEDGE ON THE TOPIC?

- Repurposed drugs are being evaluated in clinical trials but little is known about their efficacy on severe acute respiratory syndrome-coronavirus 2 viral kinetics.

WHAT QUESTION DID THIS STUDY ADDRESS?

- Our study aims to combine pharmacokinetic/pharmacodynamic and viral kinetics modeling to anticipate the effects of lopinavir/ritonavir, hydroxychloroquine (HCQ), IFN- β -1a, and remdesivir.

WHAT DOES THIS STUDY ADD TO OUR KNOWLEDGE?

- Given the predicted efficacy of lopinavir/ritonavir, HCQ, IFN- β -1a, and remdesivir, it is unlikely that these drugs will have a major effect on viral kinetics if they are administered as monotherapy after symptom onset.

HOW MIGHT THIS CHANGE DRUG DISCOVERY, DEVELOPMENT, AND/OR THERAPEUTICS?

- Our results suggest that these drugs should be evaluated in persons exposed to the virus but prior to appearance of the first symptoms.

The outbreak of severe acute respiratory syndrome coronavirus 2 (SARS-CoV-2), which originated in Wuhan, China, has become a global pandemic. By May 7, 2020, this virus had infected more than 3,700,000 people worldwide and caused more than 260,000 deaths. To readily propose a first line of defense and combat the virus in hospitalized patients, the World Health Organization relies on already existing drugs ("repurposed") that are immediately available in large quantities and have a good safety profile. In coordination with other European institutions, France is implementing a randomized clinical trial in hospitalized patients ("DisCoVery," NCT04315948) comparing the efficacy of lopinavir/ritonavir \pm IFN- β -1a, remdesivir, and hydroxychloroquine (HCQ) in hospitalized patients. However, the clinical efficacy of currently available therapies is unknown and could be limited.¹

Here, we fit mathematical models of viral dynamics to *in vivo* data to estimate parameters driving viral replication. We then use these models to predict the needed efficacy

of treatments.² By combining the expected drug concentrations and half-maximal effective concentration (EC_{50}) of drug candidates, we also use the model to predict the effects of various dosing regimens (doses and timing of treatment initiation) on viral load dynamics.

METHODS

Data used for fitting

We used published data from 13 untreated patients infected with SARS-CoV-2 that were followed in 4 Singapore hospitals.³ Patients were hospitalized in median at day 3 after onset of symptoms (range 1–10 days) and had a median symptomatic period of 12 days (range 5–24 days). Viral loads in nasopharyngeal swabs were measured by real-time reverse transcriptase polymerase chain reaction (lower limit of quantification: 38 cycles-threshold, CT) at multiple time points with an observed peak of viral load at day 5 post onset of symptoms (range 2–27 days).

¹Université de Paris, IAME, INSERM, Paris, France; ²Theoretical Biology and Biophysics, Los Alamos National Laboratory, Los Alamos, New Mexico, USA; ³Institut Hospitalo-Universitaire Méditerranée Infection, UMR "Emergence des Pathologies Virales" (EPV: Aix-Marseille University - IRD 190 - Inserm 1207 - EHESS), Marseille, France; ⁴Inserm, UMR 1219, Université de Bordeaux, Bordeaux, France; ⁵Centre Hospitalier Universitaire de Bordeaux, Bordeaux, France; ⁶CIRI, Centre International de Recherche en Infectiologie, (Team VirPath), Univ Lyon, Inserm, U1111, Université Claude Bernard Lyon 1, CNRS, UMR5308, ENS de Lyon, Lyon, France; ⁷Certara, Integrated Drug Development, Princeton, New Jersey, USA. *Correspondence: Antonio Gonçalves (antonio.goncalves@inserm.fr) and Jérémie Guedj (jeremie.guedj@inserm.fr)

Received: May 15, 2020; accepted: June 12, 2020. doi:10.1002/psp4.12543

Data presented in CT were transformed to \log_{10} copies/mL using a published relationship in Zou et al.⁴ and the model was fit to the \log_{10} viral load. Of note, the transformation from CT to \log_{10} copies/mL does not affect the estimates of parameters of interest, in particular R_0 and the death rate of productively infected cells. Time since infection was assumed to be 5 days before the onset of symptoms.⁵ In a sensitivity analysis, we also examined values of 2 and 10 days.

Model

Viral dynamics was fitted using a target cell limited model with an eclipse phase.

$$\begin{aligned}\frac{dT}{dt} &= -\beta VT \\ \frac{dI_1}{dt} &= \beta VT - kI_1 \\ \frac{dI_2}{dt} &= kI_1 - \delta I_2 \\ \frac{dV}{dt} &= \rho I - cV - \beta VT\end{aligned}\quad (1)$$

The model considers three populations of cells: target cells, T , infected cells in the eclipse phase, I_1 , and productively infected cells, I_2 . Given the timescale of the infection, we neglect target cell proliferation and natural death, and we focused on the process of cell depletion by virus infection. We assumed target cells become infected with rate constant β . After an average time of $1/k$, these cells start producing virus and are cleared with per capita rate δ . Virions are released from productively infected cells I_2 at rate ρ per cell and are cleared from the circulation at per capita rate c or lost by infecting a target cell. Based on this model, the basic reproduction number, R_0 , the average number of cells infected by a single infected cell at the beginning of the infection, is^{6,7}

$$R_0 = \frac{\rho \beta T_0}{\delta(c + \beta T_0)} \quad (2)$$

To determine the target cell concentration, the following calculation was done. We assumed that the total number of epithelial cells in the upper respiratory tract was 4×10^8 cells, distributed in a volume of 30 mL .⁸ Assuming that 1% of these cells express the ACE2 receptor and associated proteases needed for viral entry,⁹ the target cell concentration, T_0 , was fixed to 1.33×10^5 cells/mL. Following what was found in other viral infections, including acute infection,⁸ the clearance rate of virus, c , was assumed to be fast and equal to 10 day^{-1} but values of 5 and 20 day^{-1} were also evaluated.

Model building strategy

Because not all parameters can be identified when only viral load data are available, parameters V_0 and k were fixed at 10^{-1} copies/mL and 3 day^{-1} , respectively, which corresponds to an initiation of the viral production 8 hours after cell infection on average.¹⁰ A sensitivity analysis was also performed with different values of $k = \{1, 3, 5\} \text{ day}^{-1}$ and $V_0 = \{10^{-3}, 10^{-2}$,

$10^{-1}\}$ copies/mL to assess the robustness of the parameter estimates. The parameter R_0 was estimated instead of the infection rate β by a change of variables in Eq. 1.

Parameters were estimated in a nonlinear mixed-effect modeling framework using the SAEM algorithm implemented in Monolix (www.lixoft.com). The model providing the best description of the data was used for the predictions and the individual data fitting, and model averaging was used to correct for the model uncertainty when calculating confidence intervals of estimated parameters.¹¹

Predicting the effects of treatment according to the antiviral efficacy and the time of treatment initiation

We assumed that antivirals with a constant effectiveness ϵ could reduce R_0 by a factor $(1-\epsilon)$, with ϵ taking values from 50–99% in Eq. 2. We considered different times of treatment initiation, from the time of infection to 3 days after the symptom onset. For each treatment strategy, we calculated the reduction in viral load at the peak of infection in the absence of treatment (i.e., 5 days after symptom onset).

Model including an innate immune response

We also examined the possibility that cell infection is limited by an innate immune response that renders cells refractory to infection, as was proposed for other acute viral infections.^{8,12} In this model, two additional compartments are added, one for a cytokine (e.g., IFN) released in response to antigen, and one representing cells in an antiviral state that cannot be infected (Supplementary Information).

Pharmacokinetic/pharmacodynamic drug properties of lopinavir/ritonavir, HCQ, IFN- β -1a, and remdesivir

We relied on the literature to find pharmacokinetic (PK) population models and parameter values of lopinavir/ritonavir,¹³ plasma HCQ,¹⁴ IFN- β -1a,¹⁵ and remdesivir, as well as reported EC₅₀ values *in vitro* (see Table 1). For lopinavir EC₅₀, specific results were obtained as follows. Vero E6 cells were infected by SARS-CoV-2 (strain BetaCoV/France/IDF0571/2020) at a multiplicity of infection of 0.01 and treated with several concentrations of lopinavir 1 hour after infection. Supernatant samples were collected at 48 and 72 hours postinfection. Relative quantification of viral genome was performed by real-time quantitative polymerase chain reaction RT-qPCR from RNA extracted using QIAamp viral RNA Mini Kit (Qiagen). IC₅₀ values of lopinavir (5.246 μM and 4.941 μM at 48 and 72 hours postinfection, respectively) were calculated from dose-response curve using a four-parameter logistic regression model.

To determine the mean antiviral efficacy of these drugs, we simulated their plasma PK profiles considering clinical regimens used in the Discovery trial, namely 400–100 mg twice daily (b.i.d.) for lopinavir/ritonavir, 400 mg b.i.d. the first day (loading dose) followed by 400 mg once daily (q.d.) for HCQ and 12 MIU for IFN- β -1a. For each regimen, we simulated 100 PK profiles according to the reported parameter distributions. Then, we calculated for each simulated individual the mean inhibitory coefficient, sometimes called the mean antiviral effectiveness, $\epsilon = \frac{1}{T} \times \int_0^T \frac{C(t)}{C_{\text{inf}} + EC_{50}} dt$ during the first week of treatment, and the mean value over the N profiles are given in Table 1. For comparison purposes, we based the analysis

Table 1 PK/PD properties of candidate antiviral drugs

Drug	PK parameter	EC ₅₀	Dosing regimen D0–D7	$\bar{e} = \frac{1}{N} \times \frac{1}{T} \times \int_0^T \frac{C(u)}{C_0 + EC_{50}} du$
Lopinavir/ritonavir	Wang et al. ¹³	5.2 μ M (unpublished)	400/100 b.i.d.	66%
Hydroxychloroquine	Morita et al. ¹⁴	4.2 μ M ²⁷	400 mg b.i.d. at D0, followed by 400 mg q.d.	6%
β -IFN- β -1a	Hu et al. ¹⁵	175 IU/mL ²⁹	12 MIU at D0, D2, D5	18%
Remdesivir	EMEA guidelines ¹⁶	1 μ M ¹⁷	200 mg q.d. at D0, followed by 100 mg q.d.	87%

We assume that the total concentrations were the driver of efficacy, and we did not consider intracellular metabolites or free drug concentrations. D, day; EC₅₀, half-maximal effective concentration; EMEA, European Medicines Evaluation Agency; PK/PD, pharmacokinetic/pharmacodynamic.

on total plasma concentrations and did not adjust for plasma protein binding when computing efficacy.

Because the PK parameters of remdesivir have not been reported yet in humans, the same method could not be applied. We used the summary statistics reported in the summary for compassionate use of remdesivir filed by Gilead to the European Medicines Evaluation Agency (EMEA)¹⁶ to derive the mean concentration of the active metabolite in peripheral blood mononuclear cell, mean serum concentration (C_{mean}), using the area under the curve (AUC) after a loading dose of 200 mg and after repeated doses of 100 mg q.d., and we assumed that the EC₅₀ for the metabolite was equal to the EC₅₀ of the parent.¹⁷

RESULTS

We used a "target-cell limited" model with an eclipse phase,⁸ given by Eq. 1 to characterize the viral load

dynamics of 13 hospitalized patients in Singapore for which data obtained from frequent nasopharyngeal swabs were available.³ Because this model needs to incorporate a date of infection, an incubation period of 5 days was used as the most plausible date of infection in each patient.⁵ The model fitted the data well (Figure 1) and using a model-averaging approach to take into account model uncertainty,¹¹ the within-host basic reproductive number, R_0 , was found equal to 8.6 (95% confidence interval (CI) = 1.9–17.6), and the death rate of productively infected cells was estimated as 0.60 day⁻¹ (95% CI = 0.22–0.97), corresponding to a median half-life of 1.2 days (Table 2 and Figure S1). In influenza A, another respiratory infectious disease, estimates of the within host R_0 varied greatly, but the half-life of infected cells was shorter than 10 hours (see more details in ref. 18), suggesting a faster clearance of influenza-infected cells than SARS-CoV-2. The viral production rate p was also

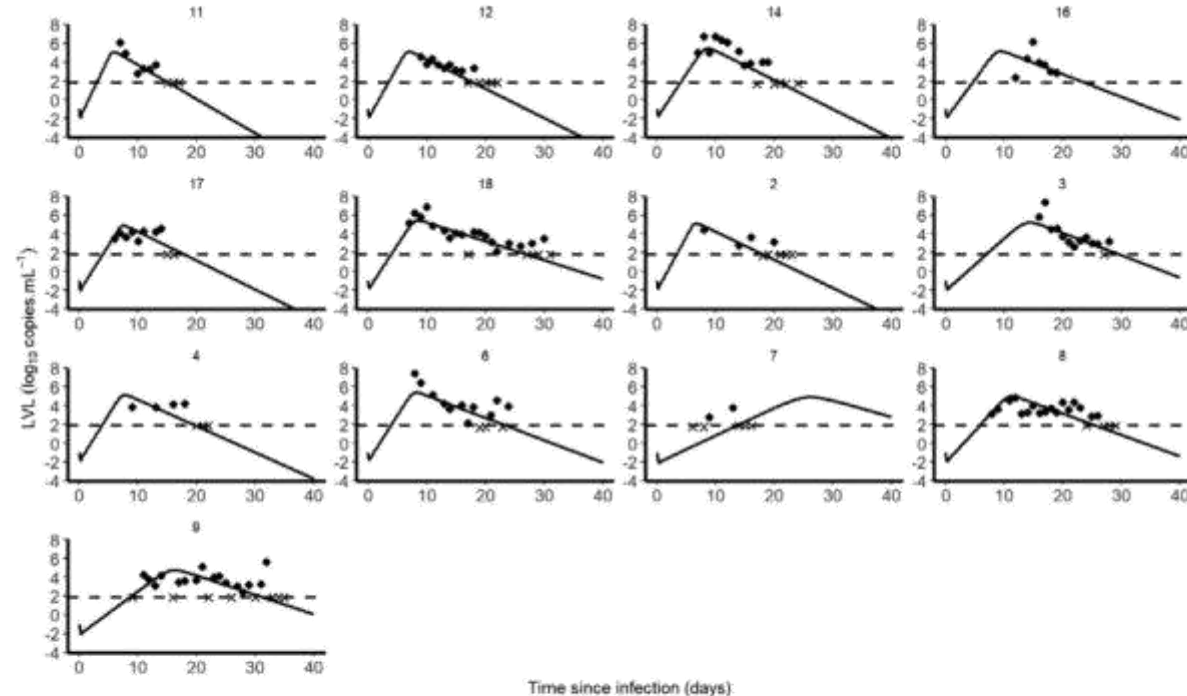


Figure 1 Individual predictions of severe acute respiratory syndrome-coronavirus 2 (SARS-CoV-2) of 13 untreated patients from Young et al.³

Timing of Treatment is Critical in SARS-CoV-2
Gonçalves et al.

512

Table 2 Median and confidence intervals of R_0 , δ , and p across models and following model averaging procedure

k (day^{-1})	V_0 (\log_{10} copies/mL)	R_0 [95% CI]	δ [95% CI] (day^{-1})	p [95% CI] (day^{-1})
1	10^{-1}	13.1 [5.1–21.8]	0.68 [0.44–0.9]	26.55 [0–57.32]
	10^{-2}	15.4 [7.9–23.2]	0.71 [0.46–0.94]	32 [8.38–56.26]
	10^{-3}	19.1 [10.3–28.8]	0.71 [0.46–0.94]	35.18 [12.46–60.06]
3	10^{-1}	8.2 [3.5–13.1]	0.6 [0.38–0.82]	21.36 [0–60.35]
	10^{-2}	9.8 [4.1–15.4]	0.58 [0.08–1.15]	20.37 [0–85.01]
	10^{-3}	12.5 [4.8–20]	0.58 [0.42–0.74]	23.37 [6.36–39.57]
5	10^{-1}	7.1 [0–13.9]	0.6 [0.19–1.06]	22.07 [0–58.57]
	10^{-2}	8.9 [4.7–13.2]	0.57 [0.43–0.74]	22.42 [1.9–41.84]
	10^{-3}	10.2 [4.8–16.2]	0.58 [0.46–0.71]	22.31 [5.48–41.46]
Model averaging		8.6 [1.9–17.6]	0.6 [0.22–0.97]	22.71 [0–59.64]

CI, confidence interval.

estimated as 22.7 copies/day (95% CI = 0–59.6; **Table 2**). However, as shown previously, p cannot be uniquely identified unless the initial target cell density T_0 is known.^{19,20} Therefore, the only quantity that can be reliably estimated is the product $p \times T_0$, equal to 3.0×10^6 copies/day (95% CI = $0\text{--}7.9 \times 10^6$). Parameter estimates and CIs were also consistent across models assuming a viral clearance c of 5 or 20 day⁻¹ (see **Table S1**).

Our model, along with the parameter estimates given above, also inform us both on the time to initiate antiviral treatment, and the level of efficacy that needs to be achieved to reduce viral load.⁶ As limited information is available on the mechanisms leading to viral clearance, and how they

may be modulated by treatment, we used our model to predict the effects of treatment at day 5 post-symptoms, which corresponds to the time the viral load tends to peak in the absence of treatment in these data.³ We considered a simple case where the drug effectiveness is assumed to be constant after therapy initiation (see Methods) and we calculated the minimal efficacy that would be needed to generate more than 2 logs of viral decline at peak viral load in the 13 studied patients (**Figure 2**). As predicted by viral kinetic modeling theory,² we found that the impact of treatment on peak viral load is inversely correlated with the time of treatment initiation. For a putative treatment blocking the viral production p and initiated at the time of infection, symptom

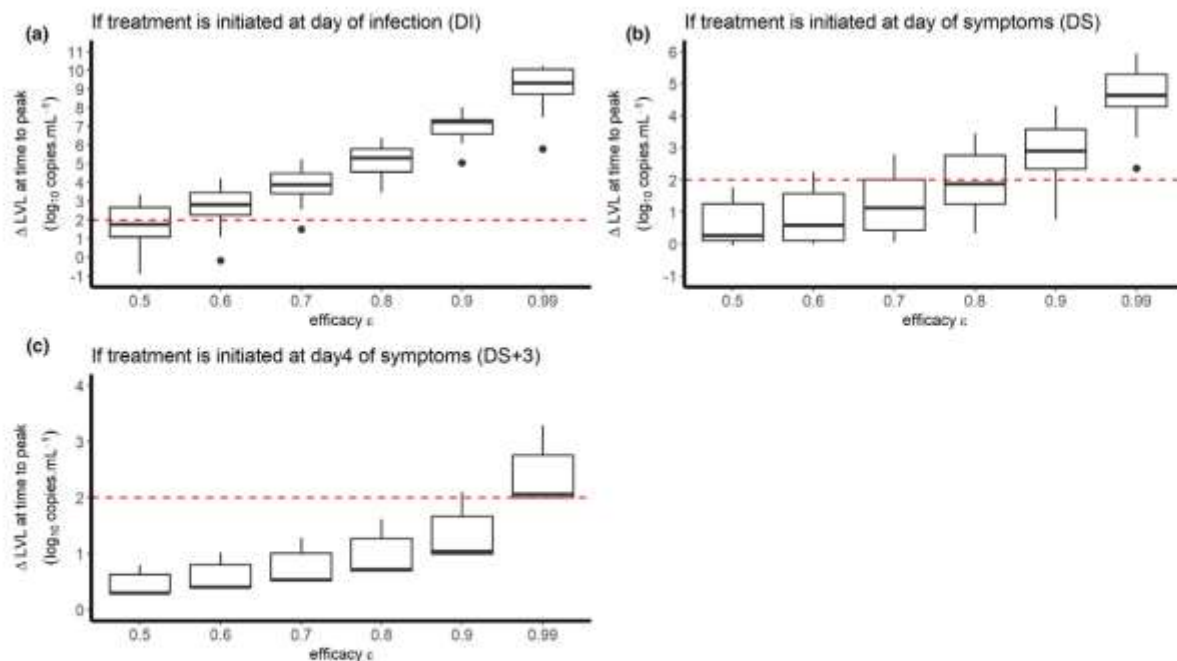


Figure 2 Reduction in viral load at day 5 post-symptom onset according to the level of antiviral effectiveness of a treatment blocking the viral production and the timing of treatment initiation (a) at time of infection; (b) at time of symptom onset; (c) 3 days after symptom onset. We assumed an incubation period of 5 days.

onset, or 3 days post-symptom onset, a median efficacy of at least 60%, 90%, and 99% in reducing viral replication would be needed, respectively, to generate more than 2 logs of decline in the peak viral load (**Figure 2**). The results obtained assuming 2 or 10 days of incubation are presented in **Figures S2 and S3**. We also considered the case of a drug like hydroxychloroquine blocking viral infection (parameter β in Eq. 1). Results were similar to those obtained before, as long as the treatment was initiated before or at symptom onset. However, initiating a treatment 3 days post-symptom onset could not reduce peak viral load, regardless of the drug effectiveness (see **Figure S4**).

The model, including an innate immune response, did not improve the data fitting and, therefore, was not selected for inclusion in the main text. However, the same analysis on viral dynamics and treatment was conducted and the conclusions remained unchanged (see **Figures S5, S6 and Table S2**).

How do these levels of effectiveness compare with the antiviral drugs that are currently being investigated? To study this question, we assumed that the treatment antiviral effectiveness at time t after treatment initiation, $\varepsilon(t)$, was related to the plasma total drug concentration, $C(t)$: $\varepsilon(t) = \frac{C(t)}{C_0 + EC_{50}}$ (except for remdesivir, see Methods) and the mean antiviral effectiveness during the first 7 days of treatment is given by $\bar{\varepsilon} = \frac{1}{N} \times \frac{1}{7} \times \int_0^7 \frac{C(u)}{C_0 + EC_{50}} du$. Given their PK and pharmacodynamic properties (**Table 1**), we calculated a mean antiviral effectiveness of up to 66% for lopinavir/ritonavir, 6% for hydroxychloroquine, 18% for IFN- β -1a, and 87% for remdesivir. Given these estimates, these compounds are unlikely to have a dramatic effect on peak viral load if administered after the onset of symptoms. In fact, the effective concentrations will presumably be lower in patients, as drug availability may be further limited by protein binding (in particular for lopinavir, which has a protein binding rate > 98%) or capability to penetrate respiratory compartments. Importantly, levels of antiviral efficacy of ~ 50% could nonetheless be relevant in a prophylactic setting, before symptom onset, to reduce viral replication in the upper respiratory tract and reduce the risk of large infiltration to the lungs before an effective immune response is mounted to clear the virus.² Note, above, we calculated the effectiveness of drugs administered in monotherapy for their usual dosing regimen. We did not consider drugs that could directly target infected cells and lead to their elimination, such as some monoclonal antibodies.

DISCUSSION

Overall, our results emphasize that the PK/pharmacodynamic properties of lopinavir/ritonavir, HCQ, IFN- β -1a, and remdesivir make them unlikely to have a dramatic impact on nasopharyngeal viral load kinetics if they are administered after symptom onset. However, these drugs may be relevant to reduce viral replication if administered early (i.e., as a pre-exposure or post-exposure prophylaxis). This conclusion, however, depends on a number of hypotheses that we discuss below.

First, we focused on the capability of drugs to reduce the peak viral load making the implicit hypothesis that reducing peak viral load would likely reduce symptoms and disease

severity. However, the relationship between viral kinetics and disease severity is still debated, with several studies suggesting that viral load did not differ between patients with severe and nonsevere disease.^{21,22} Related to this question, our study had some limitations. Our calculations relied on blood or plasma drug concentrations. Except for HCQ, for which the ratio of lung-to-plasma concentration is known to be high,^{23,24} the lung exposure of the other drugs that we considered is unknown, and their effect on viral load in the lower respiratory tract, as measured from broncho-alveolar aspirates, for instance, may differ. In addition, the drug EC_{50} that we used were determined on Vero E6 cells, an *in vitro* system that may not reflect the *in vivo* EC_{50} . For instance, we found in another study that HCQ had no antiviral activity in a more physiological model of reconstituted human airway epithelium, and this may explain the absence of antiviral of activity of HCQ *in vivo* against SARS-CoV-2.^{24,25} Finally, we focused solely on the antiviral effects of these drugs, and did not consider other potential effects of these drugs, such as their immunomodulatory effects. Such effects have been suggested for drugs that are not purely antivirals, such as HCQ and IFN- β -1a.^{26,27}

Another implicit implication of our work is the benefit of drugs used for prophylaxis (i.e., before exposure to the virus). In that case, the objective of the treatment may be to “flatten the peak viral load” (by analogy with the now popular terminology of epidemiological models) but also to prevent infection. Our deterministic, ordinary differential equation-based model, cannot reproduce virus extinction, but this can be captured using a stochastic version of the same model.²⁸

Our modeling provides estimates of viral kinetic parameters, in particular R_0 and the loss rate of infected cells, δ , and the limit of extrapolation of these parameters also need to be well understood. The advantage of studying this series of patients was the fact that viral load was sampled extremely frequently and early in the infection. However, the number of patients we studied was quite small (only 13), and the patients were rather young (37 years, range 31–56 years) and may not be representative of patients who typically evolve to have severe forms of the disease.²¹ Therefore, more data will be needed from various populations to estimate precisely the parameter distribution in the population of patients that are most in need of antiviral therapy. Finally, our estimate of the loss rate of free virus and infected cells are constant over time, which neglects the effects of the adaptive immune response. For instance, antibodies that emerge in the second week after symptom onset,^{29,30} may contribute to accelerate viral clearance or reduce viral infectivity. However, to include these effects would require more complex models and quantitative data on these antibodies and their *in vivo* effects, which are currently lacking. Further, our analysis of the antiviral effects of repurposed drugs focused on their ability to reduce the peak viral load, which typically occurs well before the antibody response emerges and, hence, the analysis we presented here should not be affected in any major way by our neglect of antibody responses.

Future models of drug efficacy may need to account for viral resistance, as it is possible that continued viral replication in the presence of drug will select for drug-resistant mutations,³¹ although coronaviruses are unusual in that they appear to have low mutation rates due to RNA proofreading capability.³² Drug combination therapy and more aggressive dosing, including

consideration of loading doses to rapidly achieve therapeutic exposures, may be beneficial to maximize efficacy of these repurposed antiviral agents.³³ For all these reasons, the outcome of randomized clinical trials remains urgently needed, and the analysis of their impacts not only on viral clearance but also on disease severity will be critical to design more potent drugs.

Supporting Information. Supplementary information accompanies this paper on the *CPT: Pharmacometrics & Systems Pharmacology* website (www.psp-journal.com).

Funding. Antonio Gonçalves is funded by a grant from Roche Pharmaceutical Research and Early Development. The study has received financial support of the national Research Agency (ANR) through the ANR-Flash calls for COVID-19 (TheraCoV ANR-20-COVI-0018). Portions of this work were done under the auspices of the US Department of Energy under contract 89233218CNA000001. We also gratefully acknowledge the support of the US Department of Energy through the LANL/LDRD Program for this work (A.S.P. and R.K.).

Conflict of Interest. J.G. has consulted for F. Hoffmann-La Roche. All other authors declared no competing interests for this work.

Author Contributions. A.G., R.K., A.S.P., and J.G. wrote the manuscript. A.G., R.K., X.D.L., F.M., D.M., A.S.P., and J.G. designed the research. A.G., R.K., J.B., E.C., A.P., O.T., M.R.C., P.S., A.S.P., and J.G. performed the research. A.G., R.K., J.B., E.C., A.P., O.T., M.R.C., P.S., A.S.P., and J.G. analyzed the data.

Ethical Statement. Data were originally provided in Young *et al.* (<https://doi.org/10.1001/jama.2020.3204>) where “waiver of informed consent for collection of clinical data from infected individuals was granted by the Ministry of Health, Singapore” and “written informed consent was obtained from study participants.”

Disclaimer. As Editor-in-Chief of *CPT: Pharmacometrics & Systems Pharmacology*, France Mentré was not involved in the review or decision process for this paper.

1. Cao, B. *et al.* A trial of lopinavir-ritonavir in adults hospitalized with severe Covid-19. *N. Engl. J. Med.* **382**, 1787–1799 (2020).
2. Friberg, L.E. & Guedj, J. Acute bacterial or viral infection—What’s the difference? A perspective from PKPD modelers. *Clin. Microbiol. Rev.* <https://doi.org/10.1128/cmr.00165-20>.
3. Young, B.E. *et al.* Epidemiologic features and clinical course of patients infected with SARS-CoV-2 in Singapore. *JAMA*. <https://doi.org/10.1001/jama.2020.3204>. [e-pub ahead of print].
4. Zou, L. *et al.* SARS-CoV-2 viral load in upper respiratory specimens of infected patients. *N. Engl. J. Med.* **382**, 1177–1179 (2020).
5. Laufer, S.A. *et al.* The incubation period of coronavirus disease 2019 (COVID-19) from publicly reported confirmed cases: estimation and application. *Ann. Intern. Med.* **172**, 577–582 (2020).
6. Best, K. *et al.* Zika plasma viral dynamics in nonhuman primates provides insights into early infection and antiviral strategies. *Proc. Natl. Acad. Sci. USA* **114**, 8847–8852 (2017).
7. Banerjee, S., Guedj, J., Ribeiro, R.M., Moses, M. & Perelson, A.S. Estimating biologically relevant parameters under uncertainty for experimental within-host murine West Nile virus infection. *J. R. Soc. Interface* **13**, 20160130 (2016).
8. Baccam, P., Beauchemin, C., Macken, C.A., Hayden, F.G. & Perelson, A.S. Kinetics of influenza A virus infection in humans. *J. Virol.* **80**, 7590–7599 (2006).
9. Muus, C. *et al.* Integrated analyses of single-cell atlases reveal age, gender, and smoking status associations with cell type-specific expression of mediators of SARS-CoV-2 viral entry and highlights inflammatory programs in putative target cells. *BioRxiv* (2020). <https://doi.org/10.1101/2020.04.19.049254>. [e-pub ahead of print].
10. Agostini, M.L. *et al.* Coronavirus susceptibility to the antiviral remdesivir (GS-5734) is mediated by the viral polymerase and the proofreading exonuclease. *MBio* **10**:e0221-18. [e-pub ahead of print].
11. Gonçalves, A., Mentré, F., Lemenuel-Diot, A. & Guedj, J. Model averaging in viral dynamic models. *AAPS J.* **22**, 22–48 (2020).
12. Pawelek, K.A. *et al.* Modeling within-host dynamics of influenza virus infection including immune responses. *PLoS Comput. Biol.* **8**, e1002588 (2012).
13. Wang, K. *et al.* Integrated population pharmacokinetic/viral dynamic modelling of lopinavir/ritonavir in treatment-naïve patients. *Clin. Pharmacokinet.* **53**, 361–371 (2014).
14. Morita, S., Takahashi, T., Yoshida, Y. & Yokota, N. Population pharmacokinetics of hydroxychloroquine in Japanese patients with cutaneous or systemic lupus erythematosus. *Ther. Drug Monit.* **38**, 259–267 (2016).
15. Hu, X. *et al.* COMPAREx: Pharmacokinetic profiles of subcutaneous peginterferon beta-1a and subcutaneous interferon beta-1a over 2 weeks in healthy subjects: pharmacokinetics of peginterferon beta-1a and s.c. interferon beta-1a. *Br. J. Clin. Pharmacol.* **82**, 380–388 (2016).
16. Francisco, E.M. EMA provides recommendations on compassionate use of remdesivir for COVID-19. European Medicines Agency <<https://www.ema.europa.eu/en/news/ema-provides-recommendations-compassionate-use-remdesivir-covid-19>> (2020). Accessed May 10, 2020.
17. Pizzorno, A. *et al.* Characterization and treatment of SARS-CoV-2 in nasal and bronchial human airway epithelia. *BioRxiv* [10.1101/2020.03.31.017889](https://doi.org/10.1101/2020.03.31.017889). [e-pub ahead of print].
18. Smith, A.M. Host-pathogen kinetics during influenza infection and coinfection: insights from predictive modeling. *Immunol. Rev.* **285**, 97–112 (2018).
19. Mao, H., Xia, X., Perelson, A.S. & Wu, H. On identifiability of nonlinear ode models and applications in viral dynamics. *SIAM Rev. Soc. Ind. Appl. Math.* **53**, 3–39 (2011).
20. Stafford, M.A. *et al.* Modeling plasma virus concentration during primary HIV infection. *J. Theor. Biol.* **203**, 285–301 (2000).
21. Zheng, S. *et al.* Viral load dynamics and disease severity in patients infected with SARS-CoV-2 in Zhejiang province, China, January–March 2020: retrospective cohort study. *BMJ*. <https://doi.org/10.1136/bmj.m1443>. [e-pub ahead of print].
22. Liu, S., Zhou, B., Valdes, J.D., Sun, J. & Guo, H. Serum hepatitis B virus RNA: a new potential biomarker for chronic hepatitis B virus infection. *Hepatology* **69**, 1816–1827 (2019).
23. Yao, X. *et al.* In vitro antiviral activity and projection of optimized dosing design of hydroxychloroquine for the treatment of severe acute respiratory syndrome coronavirus-2 (SARS-CoV-2). *Clin. Infect. Dis.* <https://doi.org/10.1093/cid/ciaa237>. [e-pub ahead of print].
24. Maisonnasse, P. *et al.* Hydroxychloroquine in the treatment and prophylaxis of SARS-CoV-2 infection in non-human primates. *Research Square* <https://doi.org/10.21203/rs.3.rs-27223/v1>[e-pub ahead of print].
25. Boulware, D.R. *et al.* A randomized trial of hydroxychloroquine as postexposure prophylaxis for Covid-19. *N. Engl. J. Med.* <https://doi.org/10.1056/NEJMoa2018638>. [e-pub ahead of print].
26. Liu, J. *et al.* Hydroxychloroquine, a less toxic derivative of chloroquine, is effective in inhibiting SARS-CoV-2 infection in vitro. *Cell Discov.* **6**, 1–4 (2020).
27. Ingraham, N.E. *et al.* Immunomodulation in COVID-19. *Lancet Respir. Med.* **8**, 544–546 (2020).
28. Czuppon, P. *et al.* Predicted success of prophylactic antiviral therapy to block or delay SARS-CoV-2 infection depends on the targeted mechanism medRxiv. <https://doi.org/10.1101/2020.05.07.20092965>. [e-pub ahead of print].
29. Woelert, R. *et al.* Clinical presentation and virological assessment of hospitalized cases of coronavirus disease 2019 in a travel-associated transmission cluster. *medRxiv* [10.1101/2020.03.05.20030502](https://doi.org/10.1101/2020.03.05.20030502). [e-pub ahead of print].
30. Wu, F. *et al.* Neutralizing antibody responses to SARS-CoV-2 in a COVID-19 recovered patient cohort and their implications. *medRxiv* [10.1101/2020.03.30.20047365](https://doi.org/10.1101/2020.03.30.20047365). [e-pub ahead of print].
31. Perelson, A.S., Rong, L. & Hayden, F.G. Combination antiviral therapy for influenza: predictions from modeling of human infections. *J. Infect. Dis.* **205**, 1642–1645 (2012).
32. Denison, M.R., Graham, R.L., Donaldson, E.F., Eckerle, I.D. & Baric, R.S. Coronaviruses. *RNA Biol.* **8**, 270–279 (2011).
33. Smith, P.F., Dodds, M., Bentley, D., Yeo, K. & Rayner, C. Dosing will be a key success factor in repurposing antivirals for COVID-19. *Br. J. Clin. Pharmacol.* <https://doi.org/10.1111/bcpt.14314>. [e-pub ahead of print].

© 2020 The Authors. *CPT: Pharmacometrics & Systems Pharmacology* published by Wiley Periodicals LLC on behalf of the American Society for Clinical Pharmacology and Therapeutics. This is an open access article under the terms of the Creative Commons Attribution-NonCommercial License, which permits use, distribution and reproduction in any medium, provided the original work is properly cited and is not used for commercial purposes.

SARS-CoV-2 viral dynamics in non-human primates

Antonio Gonçalves¹, Pauline Maisonnasse², Flora Donati^{3,3b}, Mélanie Albert^{3,3b}, Sylvie Behillil^{3,3b}, Vanessa Contreras², Thibaut Naninck², Romain Marlin², Caroline Solas⁴, Andres Pizzorno⁵, Julien Lemaitre², Nidhal Kahlaoui², Olivier Terrier⁵, Raphael Ho Tsong Fang², Vincent Enouf^{3,3b,9}, Nathalie Dereuddre-Bosquet², Angela Brisebarre^{3,3b}, Franck Touret⁷, Catherine Chapon², Bruno Hoen⁸, Bruno Lina^{5,6}, Manuel Rosa Calatrava⁵, Xavier de Lamballerie⁷, France Mentré¹, Roger Le Grand², Sylvie van der Werf^{3,3b}, and Jérémie Guedj¹

¹Université de Paris, IAME, INSERM, F-75018 Paris, France

²Université Paris-Saclay, Inserm, CEA, Center for Immunology of Viral, Auto-immune, Hematological and Bacterial diseases (IMVA-HB/IDMIT), Fontenay-aux-Roses & Le Kremlin-Bicêtre, France

³ Unité de Génétique Moléculaire des Virus à ARN, GMVR : Institut Pasteur, UMR CNRS 3569, Université de Paris, Paris, France.

^{3b}Centre National de Référence des Virus des infections respiratoires (dont la grippe), Institut Pasteur, Paris, France.

⁴Aix-Marseille Univ, APHM, Unité des Virus Emergents (UVE) IRD 190, INSERM 1207, Laboratoire de Pharmacocinétique et Toxicologie, Hôpital La Timone, 13005 Marseille, France

⁵CIRI, Centre International de Recherche en Infectiologie, (Team VirPath), Univ Lyon, Inserm, U1111, Université Claude Bernard Lyon 1, CNRS, UMR5308, ENS de Lyon, F-69007, Lyon, France

⁶Laboratoire de Virologie, Centre National de Référence des Virus des infections respiratoires (dont la grippe), Institut des Agents Infectieux, Groupement Hospitalier Nord, Hospices Civils de Lyon, 69004 Lyon, France

⁷Unité des Virus Emergents, UVE: Aix Marseille Univ, IRD 190, INSERM 1207, IHU Méditerranée Infection, 13005, Marseille, France.

⁸Emerging Diseases Epidemiology Unit, Institut Pasteur, Paris, France

⁹Plate-forme de microbiologie mutualisée (P2M), Pasteur International Bioresources Network (PIBnet), Institut Pasteur, Paris, France

Corresponding author: Antonio Gonçalves, antonio.goncalves@inserm.fr

IAME INSERM U1137,
16 rue Henri Huchard 75018, Paris, France
Tel: +33 1 57 27 75 39

Keywords

Viral dynamics; SARS-CoV-2; Hydroxychloroquine; non-human primates

Author contributions

AB: Performed RT-PCR viral quantification and analyzed the data. AG: Developed the mathematical model, analyzed the data and wrote the article AP: Performed in vitro evaluation of HCQ (Vero E6, HAE). BH: Contributed to study design, data analysis and article writing. BL: Contributed to study design and data analysis. CC: Contributed to study design and data analysis. CS: Supervised and coordinated the HCQ PK analysis, contributed to article writing. FD: Coordinated the viral load and infectious titers quantification FT: contributed to in vitro antivirals evaluation JG: Conceived the project, designed the study, data analysis and article writing. JL: contributed to clinical follow up of animals. MA: Coordinated the viral load and infectious titers quantification. MRC: Contributed to study design and data analysis. NDB: Contributed to the animal work and cytokine measurement, analyzed the data and coordinated IDMIT core activities. NE: Developed the qPCR assay and analyzed the data. NK: Contributed to study design and data analysis. OT: Contributed to data analysis. PM: Contributed to project conception and design of the study, contributed to coordination of the experiments and data analysis, and article writing. RHTF: Coordinated the animal core facility, contributed to study design and data analysis. RLG: Conceived the project, designed the study, analyzed the data and contributed to article writing. RM: Contributed to the design of the study, animal work, data analysis and contributed to article writing. SB: Performed RT-PCR viral quantification and analyzed the data. SVDW: Conceived the project, designed the study, provided the viral challenge stock, coordinated the viral load and infectious titers quantification, contributed to data analysis and article writing. TN: Performed CT acquisitions/CT quantification and contributed to article writing. VC: Contributed to data analysis and article writing. XDL: Contributed to study design and data analysis.

Competing interests

Funding for Antonio Gonçalves PhD grant has been provided by ROCHE Company.
Dr. Jérémie GUEDJ has worked as consultant for ROCHE Company.

Abstract

Non-human primates infected with SARS-CoV-2 exhibit mild clinical signs. Here we used a mathematical model to characterize in detail the viral dynamics in 31 cynomolgus macaques for which nasopharyngeal and tracheal viral load were frequently assessed. We identified that infected cells had a large burst size ($>10^4$ virus) and a within-host reproductive basic number of approximately 6 and 4 in nasopharyngeal and tracheal compartment, respectively. After peak viral load, infected cells were rapidly lost with a half-life of 9 hours, with no significant association between cytokine elevation and clearance, leading to a median time to viral clearance of 10 days, consistent with observations in mild human infections. Given these parameter estimates, we predict that a prophylactic treatment blocking 90% of viral production or viral infection could prevent viral growth.

In conclusion, our results provide estimates of SARS-CoV-2 viral kinetic parameters in an experimental model of mild infection and they provide means to assess the efficacy of future antiviral treatments.

Author summary

Non-human primates infected with SARS-CoV-2 develop a mild infection resembling asymptomatic human infection. Here we used viral dynamic modelling to characterize the nasopharyngeal and tracheal viral loads. We found that viral load rapidly declined after peak viral load despite the absence of association between model parameters and immune markers. The within-host reproductive basic reproduction number was approximately equal to 6 and 4 in nasopharynx and trachea suggesting that a prophylactic therapy blocking viral entry or production with 90% efficacy could be sufficient to prevent viral growth and peak viral load.

Introduction

The severe acute respiratory syndrome coronavirus 2 (SARS-CoV-2) which originated in Wuhan, China, at the end of December 2019, has spread rapidly around the world, resulting at the end of December 2020 in more than 1,600,000 deaths (1). Fortunately, the majority of infections do not lead to hospitalizations (2), and the vast majority of subjects infected with SARS-CoV-2 will experience asymptomatic or pauci-symptomatic infection characterized by specific (anosmia) or general symptoms (fever, fatigue) (3–5). In other acute or chronic viral diseases (HIV, HCV, influenza), the characterization of viral load kinetics has played an important role to understand the pathogenesis of the virus and design better antiviral drugs (6–8). In the case of SARS-CoV-2, viral kinetics has been found to be associated with mortality in hospitalized patients (9) but the association in less severe patients is unclear. This is due to the fact that many studies rely on large cross-sectional analyses with few patients having serial data points or, in contrary, on detailed small series of patients (10–12). In that perspective, the analysis of data generated in non-human primates is a unique opportunity to characterize in detail the viral dynamics during natural infection, and to study the effects of antiviral therapy (13–15).

Here, we used data generated on nonhuman primates (NHP) and treated with hydroxychloroquine (HCQ) ± azithromycine (AZTH) in either pre- or post-exposure prophylaxis (16) to develop a mathematical model of SARS-CoV-2 infection. Although our analysis did not reveal any significant antiviral efficacy of HCQ, the large data generated (31 cynomolgus macaques with frequent measurements of both nasopharyngeal and tracheal viral loads) allowed us to characterize in detail the key parameters driving the viral dynamics and to evaluate putative immune response mechanisms during the infection.

Material and Methods

Ethics statement

Cynomolgus macaques aged 37–40 months and originating from Mauritian AAALAC certified breeding centers were used in this study. Animals were housed under BSL-2 and BSL-3 containment when necessary (Animal facility authorization #D92-032-02, Prefecture des Hauts de Seine, France) and in compliance with European Directive 2010/63/EU, the French regulations and the Standards for Human Care and Use of Laboratory Animals, of the Office for Laboratory Animal Welfare (OLAW, assurance number #A5826-01, US).

The protocols were approved by the institutional ethical committee “Comité d’Ethique en Expérimentation Animale du Commissariat à l’Energie Atomique et aux Energies Alternatives” (CEtEA #44) under statement number A20-011. The study was authorized by the “Research, Innovation and Education Ministry” under registration number APAFIS#24434-2020030216532863v1.

Experimental procedure

Our study includes 31 cynomolgus macaques (16 male, 15 female) infected with 10^6 pfu (corresponding to 10^{10} total RNA copies) of a primary isolate of SARS-CoV-2 (BetaCoV/France/IDF/0372/2020). Each animal received 5 mL of the total inoculum: 90% (4.5 mL) were injected by the intra-tracheal route and 10% (0.5 mL) by the intra-nasal route (17,18). Nasopharyngeal and tracheal swabs were collected longitudinally at days 1, 2, 3, 4, 5, 7, 9, 11, 13, 16 and 20 post-infection (pi) and eluted in 3 mL of Universal transport medium (Copan) or Viral Transport Medium (CDC, DSR-052-01). Viral RNA levels were assessed in each sample

using a real-time PCR, with 8540 and 180 copies/mL as quantification and detection limits, respectively (**Fig. 1**)

The original study included 6 groups treated either by a high dosing regimen (Hi) of HCQ (90 mg/kg loading dose and 45 mg/kg maintenance dose) \pm AZTH (36 mg/kg of at 1 dpi, followed by a daily maintenance dose of 18 mg/kg), a low dosing regimen (Lo) of HCQ (30 mg/kg loading dose and 15 mg/kg maintenance dose) or a vehicle (water) as a placebo. Among the 23 treated animals, 14 were treated at 1 dpi with a Lo (n=4), Hi (n=5) dose of HCQ or HCQ+AZTH (n=5). A late treatment initiation was also investigated in 4 animals receiving a Lo dosing regimen. Finally, 5 animals received HCQ at the Hi dose starting at day 7 prior to infection as a pre-exposure prophylaxis (PrEP).

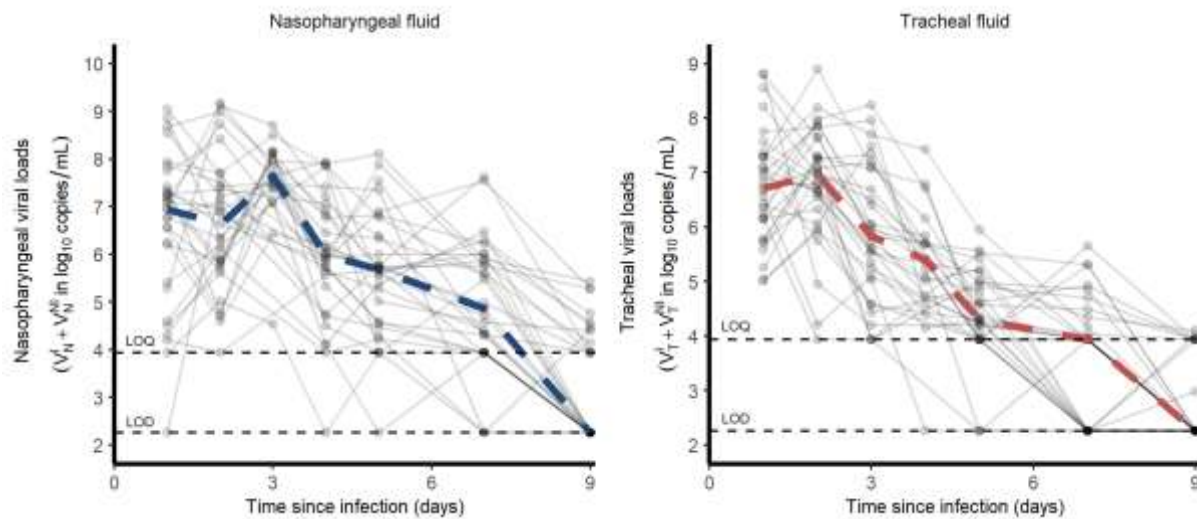


Figure 1: Nasopharyngeal and tracheal SARS-CoV-2 viral loads in infected cynomolgus macaques treated by a placebo or hydroxychloroquine \pm azithromycin. Dashed lines represent the lower limit of detection (LOD) and lower limit of quantification (LOQ).

Viral dynamic model of SARS-CoV-2

Model describing nasopharyngeal and tracheal swabs

Given that HCQ was not associated to any antiviral effect (16), we pooled the data from either treated and untreated groups. Thus, we consider all animals as controls in our primary analysis but we also investigated a potential effect of HCQ (see details in **supplementary information file 1**). Nasopharynx and trachea were considered as two distinct compartments of the upper respiratory tract (URT) where each one is described by a target cell limited model (13,19,20). In this model, susceptible cells (T) are infected by an infectious virus (V^I) at a rate β and generate non-productive infected cells (I_1). After an eclipse phase of duration $1/k$ on average, infected cells start to be productive (I_2) and produce both infectious and non infectious viruses at a rate μp and $(1-\mu)p$ respectively. Productive infected cells die at a rate δ and viruses are cleared at a rate c . The model is given by ordinary differential equations (1) to (5) where subscript X denotes the compartment of interest either nasopharynx or trachea. The basic reproduction number is $R_0 = \frac{\beta p T_0 \mu}{c \delta}$ and the burst-size is $N = \frac{p}{\delta}$.

$$\frac{dT_X}{dt} = -\beta_X T_X V_X^I \quad (1)$$

$$\frac{dI_{1,X}}{dt} = \beta_X T_X V_X^I - k I_{1,X} \quad (2)$$

$$\frac{dI_{2,X}}{dt} = k I_{1,X} - \delta_X I_{2,X} \quad (3)$$

$$\frac{dV_X^I}{dt} = p_X I_{2,X} \mu - c V_X^I \quad (4)$$

$$\frac{dV_X^{NI}}{dt} = p_X I_{2,X} (1 - \mu) - c V_X^{NI} \quad (5)$$

Fixed parameters

Because not all parameters can be estimated when only total viral RNA are measured, some parameters had to be fixed based on the experimental setting or the current literature. As only the product $p \times T_0$ is identifiable, we chose to fix T_0 , the initial concentrations of susceptible cells, as follows. We measured the surfaces (S) and volumes (V) of the nasopharynx and the trachea in one euthanized animal and obtained $V_N = 6.3 \text{ mL}$; $V_T = 1.2 \text{ mL}$; $S_N = 50 \text{ cm}^2$; $S_T = 9 \text{ cm}^2$. Assuming an apical surface of one epithelial cell of $s=4 \times 10^{-7} \text{ cm}^2/\text{cell}$ (21), the number of target cells exposed to the virus in the nasopharynx and the trachea are $\frac{S_N}{s \times V_N} = 1.98 \times 10^7 \text{ cells/mL}$ and $\frac{S_T}{s \times V_T} = 1.88 \times 10^7 \text{ cells/mL}$, respectively. Only a fraction of these cells expresses both angiotensin-converting enzyme 2 (ACE2) and the type II transmembrane serine protease (TMPRSS2), and we fixed this proportion to 0.1% i.e. $T_{N,0} = 1.98 \times 10^4$ and $T_{T,0} = 1.88 \times 10^4$ cells in nasopharynx and trachea, respectively. Also, we supposed that the eclipse phase duration was equal in the nasopharynx and in the trachea, and we set $k=3 \text{ d}^{-1}$ based on *in vitro* studies showing that virus release occurs 8 hours after infection (22). Third, we supposed the proportion of infectious virus μ remained constant over time. TCID₅₀ is a proxy for the infectious viruses. **Fig. 2B** shows that the ratio TCID₅₀/total viral loads is 10^{-5} (range $10^{-6} - 10^{-4}$). However, not all the infectious viruses present in the samples may be detected in Vero-E6 cells experiments. Hence, we fixed μ to 10^{-4} , the upper bound of the observed ratio of infectious virus. Finally the viral clearance c was fixed to 10 d^{-1} , consistent with the rapid viral clearance rate of influenza virus (20). Sensitivity analyses exploring the consequences of those different assumptions were performed, with c in a range $5-20 \text{ d}^{-1}$, μ in a range $10^{-5}-10^{-3}$ and the proportion of target cells being equal to 1% (see **supplementary information file 2**). Thus, the estimated parameters in each compartment were V_0 , p , β and δ .

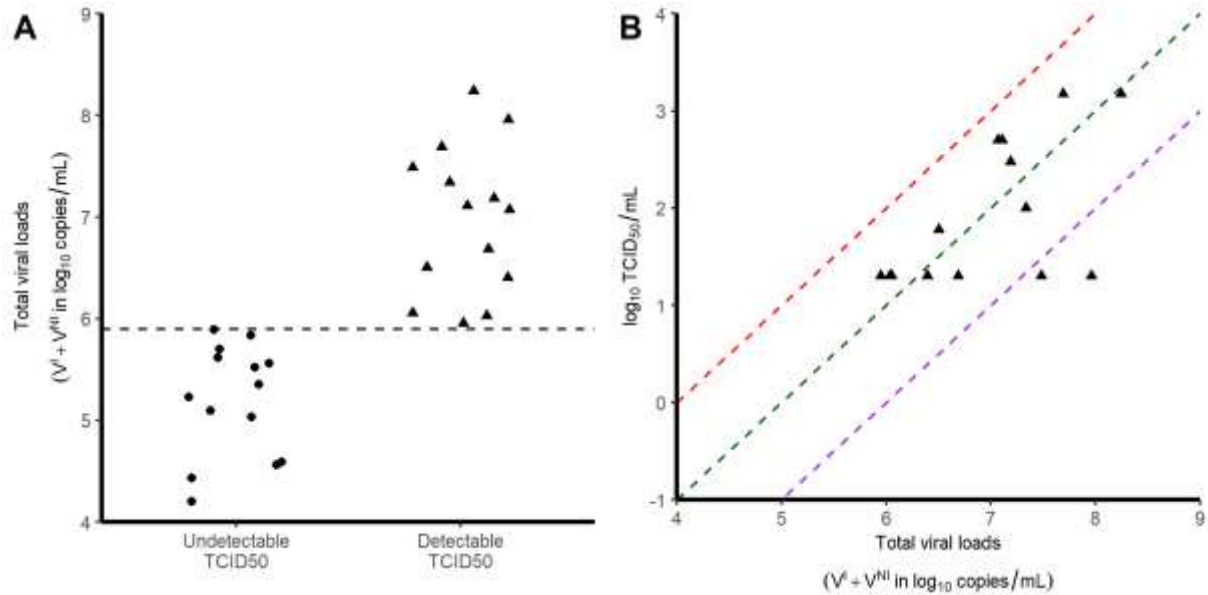


Figure 2: Relationship between TCID₅₀ and viral loads. Each symbol corresponds to a tracheal swab obtained at 3 dpi. A) Viral load levels in samples with no detectable infectious virus (circles) and those with detectable infectious virus (triangles). B) Correlation between the viral loads and the infectious virus, as measured by TCID₅₀. Red, green and purple dashed lines represent putative ratios of infectious virus of 10⁻⁴; 10⁻⁵ and 10⁻⁶ respectively.

Statistical model

The structural model used to describe the observed \log_{10} viral loads Y_{ijk} of the i^{th} animal at the j^{th} time point in the k^{th} compartment ($k=1$ for nasopharyngeal or $k=2$ for tracheal) is

$$Y_{ijk} = f(\theta_{ik}, t_{ijk}) + e_{ijk} \quad (6)$$

Where f is the function describing the total viral loads dynamics over time ($V^I(t) + V^{NI}(t)$); θ_{ik} is the vector of parameters of subject i in the k^{th} compartment and e_{ijk} is the additive residual error. Individual parameters θ_{ik} are supposed to follow a log-normal distribution with a median value that depends on the compartment:

$$\theta_{ik} = \gamma \times \exp(\eta_i) \times \exp(\alpha \times I_{k=2}) \quad (7)$$

where γ indicates the fixed effects and η_i the individual random effects, which are supposed to follow a normal distribution of mean zero and standard deviation ω , and $\exp(\alpha)$ is the vector of the ratio values between the nasal and tracheal compartments. The residual error e_{ijk} is assumed to follow a normal distribution of mean zero and constant standard deviation σ_k . Standard errors were calculated by drawing parameters in the asymptotic distribution of the parameter estimators. For each parameter, we calculated the 2.5 and 97.5% percentile to derive the 95% confidence interval.

Modelling strategy

As a first step, we considered nasopharynx and trachea parameters as two distinct compartments and we then tested whether the virus could migrate from one compartment to the other at a constant first order migration rate g . Parameter g was set to 0 if it did not improve the fit to the data or could not be precisely estimated. In order to reduce the number of remaining parameters, we fixed the ratio of effective inoculum, $V_{0,T}/V_{0,N}$, to 9. Then we tested the possibility for estimated parameters to be equal in both nasopharynx and trachea (e.g., $\alpha=0$) and tested then if their variances could be set to 0 (e.g., $\omega=0$). To do this, we used a backward selection procedure and stopped once the BIC did not decrease anymore. Lastly, based on the Empirical Bayes Estimates (EBE), we screened the random effects for correlations. Only correlations with a Pearson's coefficient >0.8 were implemented in the model. All models tested are presented and compared in **supplementary information file 3**.

Viral titers determination on Vero-E6 cells

Vero-E6 cells (mycoplasma-free) were seeded in 24-well plates (2×10^5 cells/well) and cultured in DMEM (Thermo Fisher Scientific) containing 1% PS (Penicillin 10,000 U/mL; Streptomycin 10,000 µg/mL) supplemented with 5% FBS (Foetal Bovine Serum) and incubated at 37°C in the presence of 5% CO₂. The next day, cells were inoculated in triplicate with 100µL per well of the tracheal swab dilutions (1:2, 1:10, 1:50, 1:250) in DMEM, 1% PS, 0.1% TPCK trypsin and incubated for 1 hour at 37°C. After removal of the inoculum, 1mL of DMEM, 1% PS, 0.1% TPCK trypsin was added in each well before incubation at 37°C in the presence of 5% CO₂ for 72 hrs. The presence of a cytopathic effect (CPE) was visualized under the microscope and the TCID₅₀ i.e. the tissue culture infective dose leading to 50% of the maximal cytopathic effect, was calculated using the method of Reed and Münch. All experiments were conducted under strict BSL3 conditions.

Plasma cytokine analysis

In all 31 macaques, the concentration of 30 cytokines were measured at 0, 2, 5, 7 and 9 dpi. Among them, CCL11, CCL2, IFN-α, IL-15, IL-1Ra and IL-2 were of particular interest as their kinetic changed during the infection. To identify the cytokines to be incorporated in the model, we correlated the area under the cytokine curve (AUC, calculated by the linear trapezoidal method) with the AUC of log₁₀ viral loads predicted by the model.

Models assuming a compartment for the innate immune response

We considered additional models incorporating a compartment for an antigen-dependent immune response, F, given by $\frac{dF_X}{dt} = qI_{2,X} - d_F F_X$. In these models, F could either i) reduce

viral infectivity ii) and iii) put target cells into a refractory state, iv) reduce viral production and v) increase the loss of infected cells (see **supplementary information file 4**).

Simulations of a prophylactic treatment

We used the median estimated parameter values of the model to simulate the effects of an antiviral treatment, initiated before infection, on the viral kinetics. We explored the effects of 10 to 100 fold lower viral inoculum (corresponding to doses of 10^5 and 10^4 pfu) as well as the effects of drugs acting on viral production, viral entry or the proportion of infectious virus. For each scenario, we also calculated the 95% confidence interval of the median time to viral clearance, using the method described above.

Parameter estimation

Parameters were estimated with the SAEM algorithm implemented in MONOLIX software version 2018R2 allowing to handle the left censored data (23). Likelihood was estimated using the importance sampling method and the Fisher Information Matrix (FIM) was calculated by stochastic approximation. Graphical and statistical analyses were performed using R version 3.4.3.

Results

SARS-CoV-2 viral kinetics

In our experiment, cynomolgus macaques developed a rapid infection, with viral loads peaking 2 days post infection (dpi) in both nasopharyngeal and tracheal compartments. Afterwards, both nasopharyngeal and tracheal viral loads rapidly declined exponentially, with a similar median

rate of 1.9 d^{-1} , corresponding to a daily reduction of $0.8 \log_{10} \text{ copies/mL}$ (Fig. 1). Because the viral load peaked later and higher in the nasopharynx than in the trachea (7.9 and $7.2 \log_{10}$, respectively), the median time to unquantifiable viral load nonetheless occurred later in the nasopharynx than in the trachea (9 and 7 dpi, respectively).

Overall, the area under the viral load curve (AUC) was larger in the nasopharynx than in the trachea (45 vs $38 \log_{10} \text{ copies.day/mL}$, $p < 10^{-4}$). In addition to viral RNA, we also measured virus titers in Vero-E6 cells using tracheal swabs obtained at 3 dpi (see methods). All samples contained more than $4 \log_{10} \text{ copies/mL}$ however viral growth was observed only in those having more than $6 \log_{10} \text{ copies/mL}$ (Fig. 2A). In those for which viral culture could be obtained, the ratio of TCID₅₀ (median tissue culture infective dose) to the total number of RNA copies ranged between 10^{-4} to 10^{-6} (Fig. 2B).

Viral dynamic model

Importantly, there was no antiviral effect in animals receiving various doses of HCQ compared to those receiving vehicles, even after adjustment on the mean HCQ exposure (16). Thus, the effect of treatment was neglected as a first approximation. We later challenged this hypothesis but found no significant effect of HCQ in reducing viral production or viral infectivity (see **supplementary information file 1**).

Physiologically, viruses can migrate from the nasopharynx to the trachea through respiration and movements of ciliary cells at the mucosal surface. Thus, we tested the possibility for viruses to move from nasopharyngeal to tracheal compartment and *vice versa* by linking both with a bidirectional rate constant g . However, possibly due to data paucity, the parameter g was not significantly different from 0 (CI_{95%} included 0) and was therefore set to 0 in the following.

Then, using a backward selection procedure we found that the infectivity rate β and the viral production p were different between nasopharyngeal and tracheal compartments (**Table 1**). The final model well fitted the data and allowed the estimation of several parameters of the infection (**Fig. 3**). We estimated the effective initial viral load to 1.7×10^6 and 8.0×10^7 copies/mL in tracheal and nasal compartments, respectively, which corresponds to a total inoculum of approximately 10^8 total RNA, i.e., about 1% of the total injected dose (see methods). We found estimates of β of 1.2×10^{-3} (CI_{95%} $0.5 \times 10^{-3} - 2.8 \times 10^{-3}$) and 1.8×10^{-3} (CI_{95%} $0.6 \times 10^{-3} - 5.6 \times 10^{-3}$) mL/virion/day ($p < 10^{-4}$) in nasopharynx and trachea, respectively, while p was estimated to 4.8×10^4 (CI_{95%} $1 - 8.8 \times 10^4$) and 2.2×10^4 (CI_{95%} $0.7 - 4.1 \times 10^4$) virions/cell/day ($p < 0.05$). Consequently the product $p \times T_0$ was equal to 9.5×10^8 (CI_{95%} $2.0 - 17 \times 10^8$) and 3.9×10^8 (CI_{95%} $1.2 - 17.7 \times 10^8$) virions/mL/day in nasopharynx and trachea, respectively.

The loss rate of infected cells, δ , was not found different between the two compartments and estimated to 1.9 (CI_{95%} $1.6 - 2.3$) d⁻¹ corresponding to an infected cell half-life of 9 (CI_{95%} $7 - 13$) hours. These parameter estimates allow us to derive the basic reproduction number R_0 corresponding to the number of infected cells generated by a single infected cell at the beginning of the infection. We found $R_{0,N}$ equal to 5.6 (CI_{95%} $1.3 - 21$) and $R_{0,T}$ equal to 3.8 (CI_{95%} $0.7 - 18$) in the nasopharynx and the trachea, respectively. One can also derive the viral burst size N corresponding to the number of viruses produced by an infected cell over its lifespan. We found $N_N = 25,000$ (CI_{95%} $5,900 - 72,000$) virions and $N_T = 11,000$ (CI_{95%} $4,000 - 19,000$) virions.

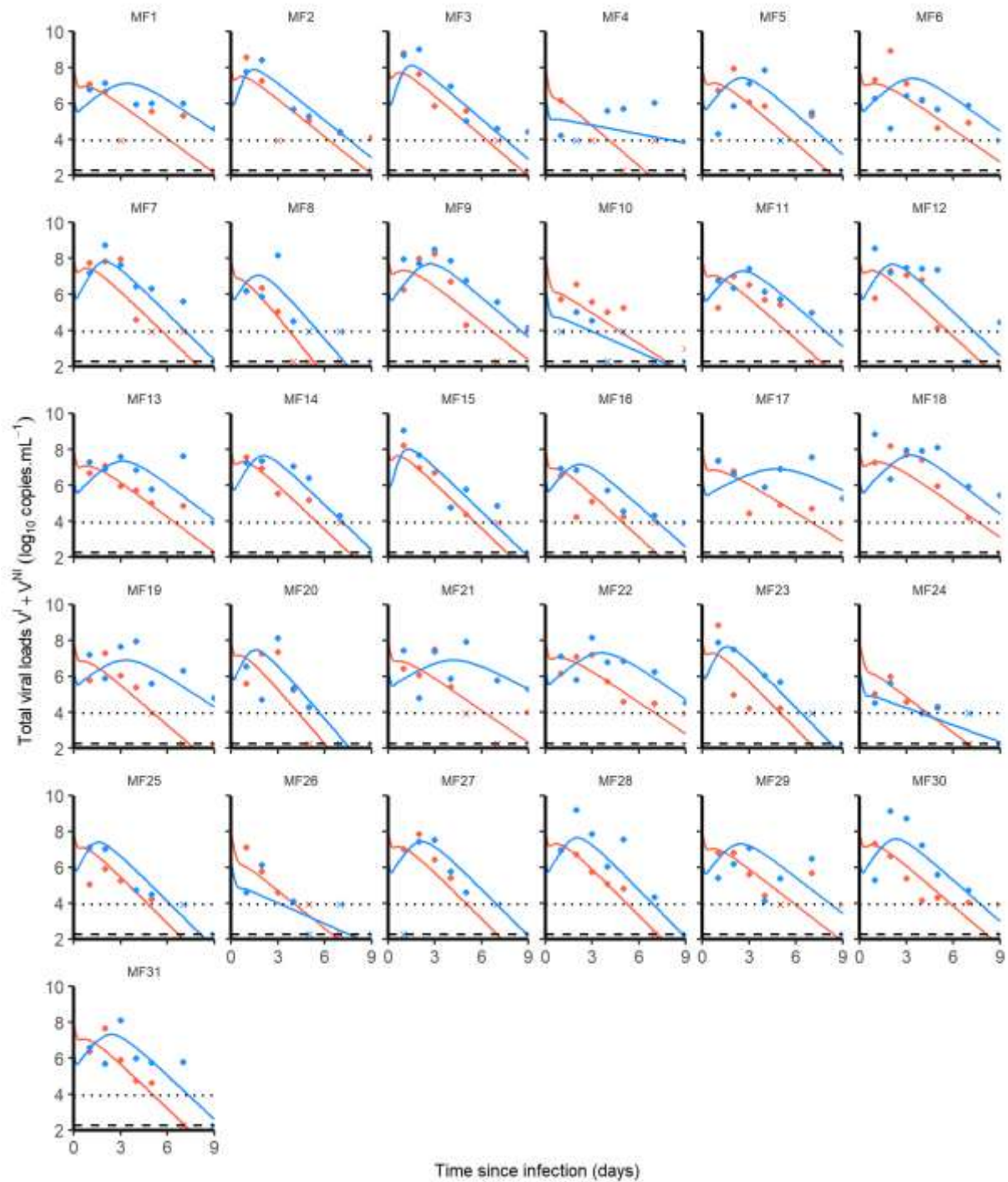


Figure 3: Nasopharyngeal (blue) and tracheal (red) individual predicted dynamics by the model described in equations (1) to (5). Full dots are the quantifiable viral loads and crosses the observation below the limit of quantification. The dotted line represents the limit of quantification and the dashed line the limit of detection.

Table 1: Population parameter estimates of the final model described by equation (1) to (5). Numbers in parenthesis are the relative standard error expressed in percentage (RSE%) associated either to the fixed or the standard deviation (SD) of random effects.

Parameters (units)	Fixed effects (RSE%)	SD of random effects (RSE%)
β_T (mL.copie/d)	1.8×10^{-3} (42)	0.3 (33)
β_N (mL.copie/d)	1.2×10^{-3} (12)	
p_T (copies/cell/d)	2.2×10^4 (49)	1.0 (27)
p_N (copies/cell/d)	4.8×10^4 (40)	
$V_{T,0}$ (copies/mL)	8.0×10^7 (9)	-
$V_{N,0}$ (copies/mL)	1.7×10^6 (9)	-
δ (1/d)	1.9 (9)	0.2 (37)
c (1/d)	10 (fixed)	-
μ (unitless)	10^{-4} (fixed)	-
k (1/d)	3 (fixed)	-
$T_{T,0}$ (cells/mL)	1.88×10^4 (fixed)	-
$T_{N,0}$ (cells/mL)	1.98×10^4 (fixed)	
σ_T	1.06 (6)	-
σ_N	1.19 (6)	-

Sensitivity analysis

In our main analysis, the viral clearance c and the proportion of infectious virus μ were fixed. We tested the robustness of our results to different values of these parameters (see **supplementary information file 2**) and we used model averaging (MA) to compute the averaged parameters values following a methodology presented in (24). Overall, models were broadly undistinguishable as they provided a Bayesian Information Criterion within a 4 points range. Model averaged parameter estimates of δ , $R_{0,N}$ and $R_{0,T}$ were equal to 1.9 ($CI_{95\%}$ 1.5 – 2.3) d^{-1} , 6.8 ($CI_{95\%}$ 1.3 – 29) and 4.4 ($CI_{95\%}$ 1 – 26), respectively.

Immune markers during SARS-CoV-2 infection

Among the 30 cytokines tested, 6 greatly varied during the infection and peaked at 2 dpi (namely CCL11, CCL2, IFN- α , IL-15, IL-1RA and IL-2) but there was no association between cytokine and viral loads (**Fig. 4**). A model assuming an effect of the immune response in cell protection resulted in a reduced BIC of 6 points. However, the gain in fitting criterion was entirely due to 3 individuals (see **supplementary information file 4**) and led to more uncertainty in parameter estimates due to increased complexity (see **Table S2**). Moreover none of the cytokines measured during the experiments, including IFN- α , showed a correlation with viral dynamics (**Fig. 5**). Thus, overall, there was no clear evidence in these data that a more complex model improved the understanding of viral dynamics over a simple target cell model.

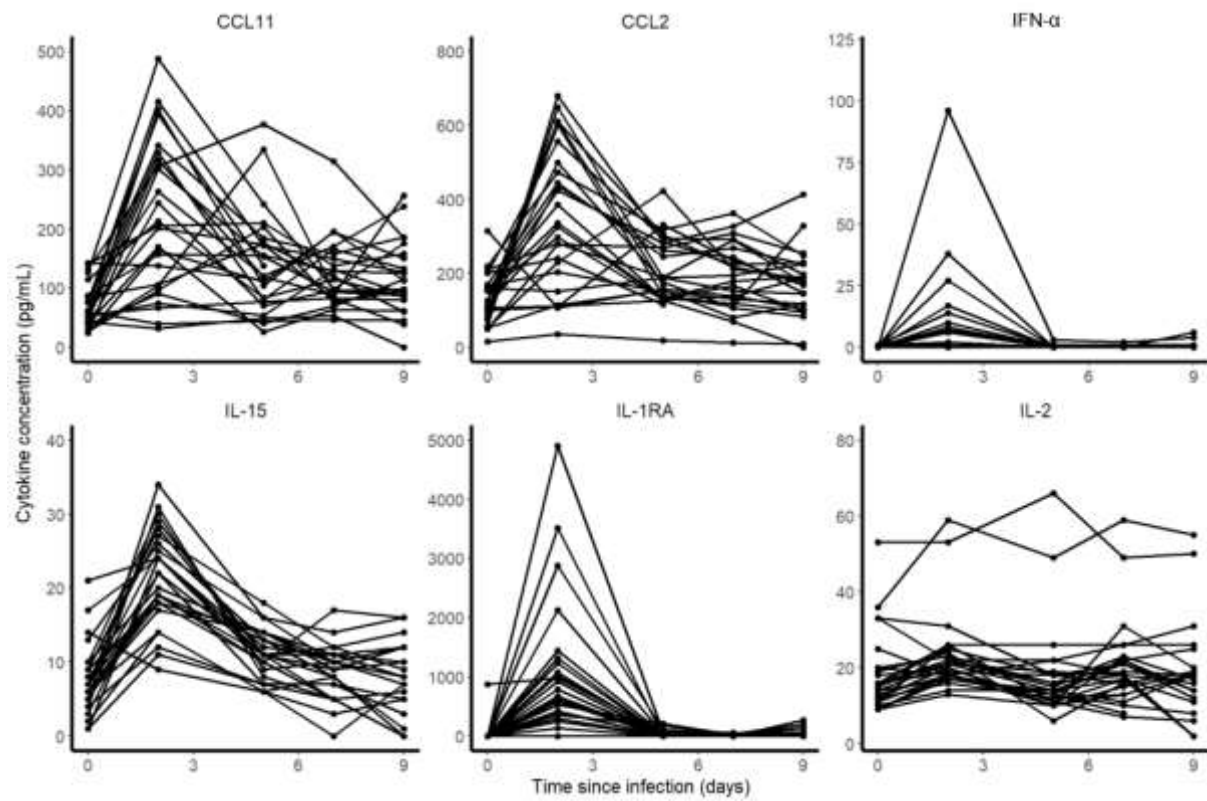


Figure 4: Cytokine concentrations during SARS-CoV-2 infection.

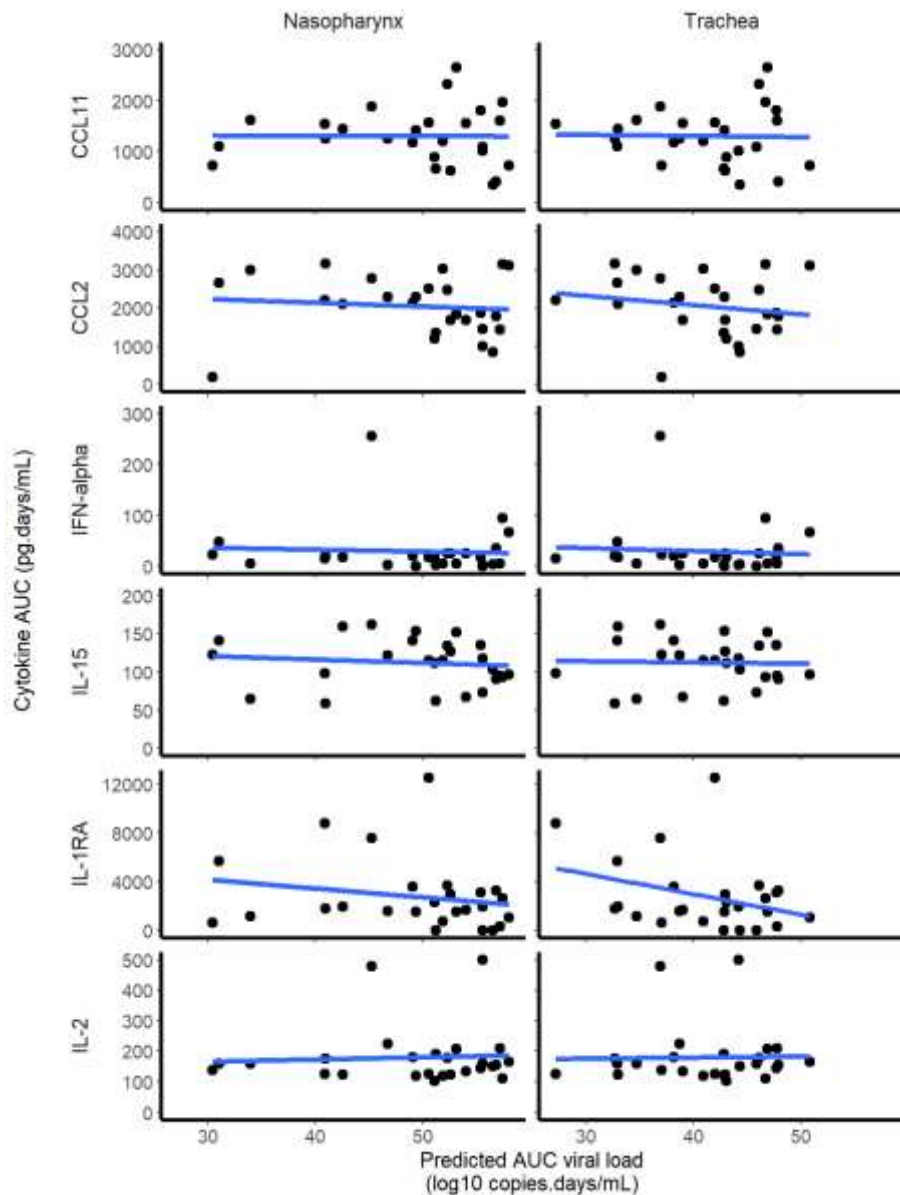


Figure 5: Correlation between the individual predicted AUC \log_{10} viral load and cytokine AUC. None of the 6 cytokines that increased during the infection was significantly correlated with the predicted viral load AUC in the nasopharynx or the trachea.

Expected profiles with prophylaxis treatments

We used estimated parameter values of the model to simulate the effects of an antiviral treatment, initiated before infection, on the viral kinetics. We explored different viral inoculum (ranging from 10^4 to 10^6 pfu), drugs mechanisms of action (blocking viral production, viral entry, or infectious virus production), with different levels of antiviral efficacy. As the conclusions were not sensitive to the mechanism of action, we present below the results for a prophylactic drug blocking viral entry (**Fig. 6**). Other mechanisms of action are presented in **supplementary information file 5**.

In both compartments, the median time to viral clearance increased with lower doses of inoculum, and ranged from 10.1 (CI_{95%} 8.4 – 14.7) days with 10^6 pfu to 11.7 (CI_{95%} 9.5 – 19.0) days with 10^4 pfu in the nasopharynx. A 90% effective antiviral treatment administered upon infection would dramatically reduce peak viral load in all scenario and maintain virus below the threshold level of infectivity of $6 \log_{10}$ copies/mL (see **Fig. 2A**). A 99% effective antiviral treatment could in addition abrogate viral load viral load, with time to viral clearance ranging from 3.5 (CI_{95%} 1.9 – 6.2) days with 10^6 pfu to 0.5 (CI_{95%} 0.2 – 2.5) days with 10^4 pfu in the nasopharynx.

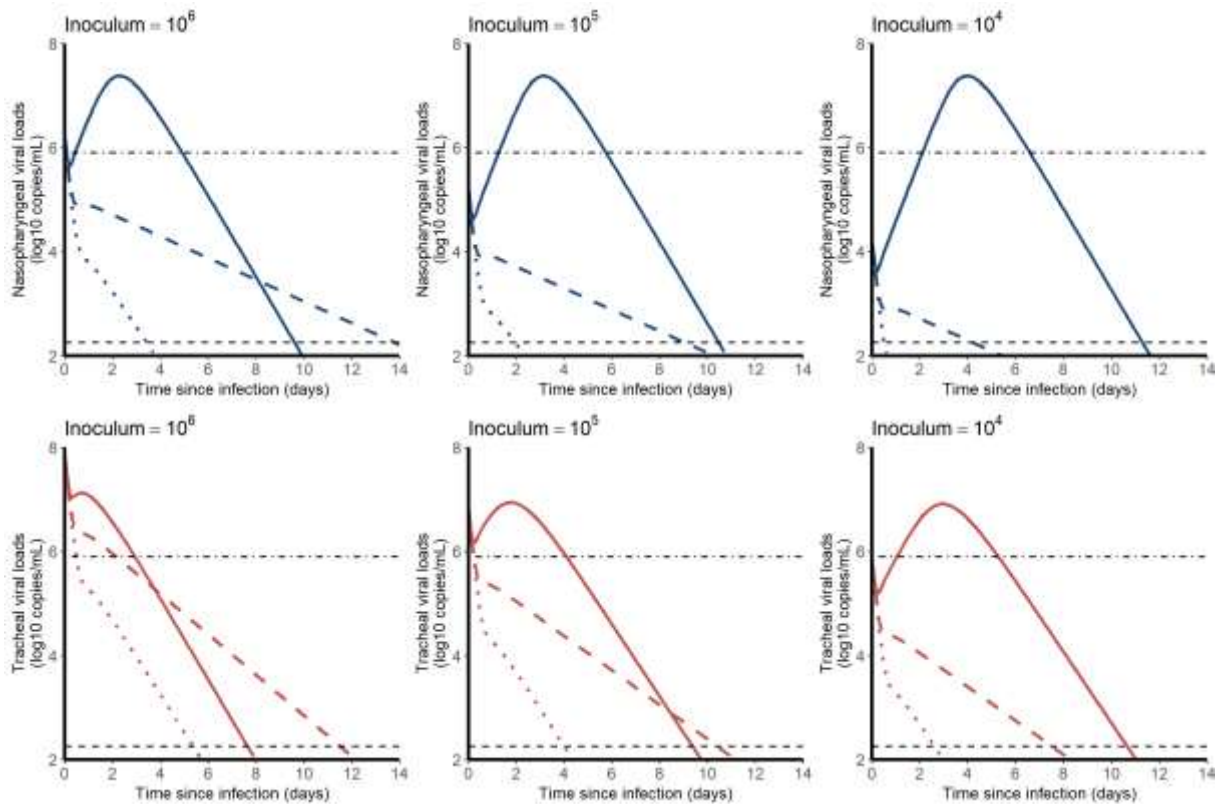


Figure 6: Median viral kinetic profiles in the nasopharynx (blue) and the trachea (red) according to the inoculum size and the level of an antiviral initiated in prophylaxis and blocking viral entry β . Treatment efficacy of 0% (no treatment, solid line), 90% (dashed line) and 99% (dotted lines) were considered. Point-dotted line represents the threshold below which no virus could be cultured in vitro (see Fig. 2).

Discussion

We here developed a mathematical model for SARS-CoV-2 viral dynamics using nasopharyngeal and tracheal swabs obtained in 31 infected macaques. Using this model we could estimate key parameters of virus pathogenesis, in particular the viral infectivity rate (equal to 1.2×10^{-3} and 1.8×10^{-3} in tracheal and nasopharyngeal compartments, respectively), and the loss rate of infected cells, estimated to 1.9 d^{-1} in both compartments (e.g., a half-life of 9 hours). Consequently, we estimated the number of secondary cell infection resulting from one infected cells, R_0 , to approximately 4 and 6 in tracheal and nasopharyngeal compartments, respectively. This value of R_0 , together with the large viral inoculum used in this experimental model (10^6 pfu), explains that tracheal viral loads barely increased post-infection and that nasopharyngeal viral loads rapidly peaked at 3 dpi. After peak viral load, the rapid loss rate of infected cells was sufficient to explain that clearance of the virus occurred around day 10 in both compartments, and we did not find evidence in this model for a role of an immune response mediated by cytokines in accelerating the viral clearance.

Although the number of animals and the very detailed kinetic data allowed the precise estimation of several parameters, some limitations exist. First, animals were infected with a large inoculum (10^6 pfu, i.e. 10^{10} RNA copies) which rapidly saturate target cells making the estimation of β less robust and difficult to distinguish the processes of clearance of the inoculum from those of *de novo* viral infections. In the future, the analysis of subgenomic RNA, that quantifies intracellular viral transcription, will provide important information to distinguish these two processes and provide a more precise estimate of R_0 (25,26). Second, a number of unknown parameters were fixed to ensure identifiability, in particular the proportion of infectious virus, μ , and the number of target cells available in each compartment, T_0 . In this model, $p \times T_0$ is the only reliable quantity since the estimate of p depends on the number of

susceptible cells. We here estimated the number of alveolar type II cells by analysis of the size of the tissues of one euthanized animal and we assumed that 0.1% of these cells could be target for the virus. Although this value led to more coherent parameter estimates (see supplementary file 2), this is higher than the value of 1% of cells expressing the ACE2 receptor and serine protease TMPRSS2 found in humans (27,28). Specific experiments will be needed to estimate the proportion of target cells in the URT of macaques. Third, we relied only on measures in both compartments of the upper respiratory tract, which may not reflect the kinetics in the lower respiratory tract. It is in particular possible that the kinetics of both the virus and the immune response may be different in the lung, and that both cytokine responses and the lesions as observed by CT scans may be associated with viral loads in the lungs. In our experiments the first viral load measurements in bronchoalveolar lavages (BAL) was made at 6 dpi, and were all below the limit of detection at the next available data point at day 14, precluding a more detailed analysis of the kinetics in the lungs.

We also aimed to evaluate whether more complex models including an antigen-dependent immune response could improve the data fitting. A model assuming that cells could be put in an antiviral state improved the BIC (see supplementary file 3), however this improvement was due to 3 individuals, and this came to the expense of a deteriorated precision of parameter estimates. Further, none of the observed cytokines were found associated with viral dynamics (**Fig. 5**), suggesting that this improvement in data fitting was not supported by our data. In addition, none of the animals had detectable antibodies until day 7, and only 25% had detectable antibodies by day 14, suggesting that the humoral response played a minor role in viral clearance. The role of the immune response in this experimental model of mild infection is unclear, but our findings are consistent with data obtained in patients with an asymptomatic infection, in which the immune response and the cytokine response remained low throughout

the infection period (29). Accordingly our estimate of the duration of viral shedding was between 10 and 12 days in the nasopharynx, depending on the initial inoculum, very close to the values of 9 days (*Diamond Princess* (30)) and 12 days (11) estimated in mild or asymptomatic individuals. From an experimental setting, the analysis of viral dynamics in animals infected with different size of viral inoculum could also bring insights on the need to use more complex models (31).

Finally, we used the model to inform on the use of prophylactic drugs in this macaque model. Given our estimate of R_0 , a 90% effective treatment should be able to prevent virus growth and would maintain the viral load levels below 10^6 copies/mL at all times, making the chance of detecting infectious virus very limited, consistent with our modeling predictions in humans ((32), submitted).

Acknowledgments

We thank Peter Czuppon (Collège de France & Sorbonne Université), François Blanquart (Collège de France & INSERM UMR1137) and Alan S. Perelson (Los Alamos National Laboratory) for critical reading and expertise on the analysis.

References

1. Weekly epidemiological update - 22 December 2020 [Internet]. [cité 11 janv 2021]. Disponible sur: <https://www.who.int/publications/m/item/weekly-epidemiological-update---22-december-2020>
2. Lapidus N, Paireau J, Levy-Bruhl D, Lamballerie X de, Severi G, Touvier M, et al. Ready for a BASE jump? Do not neglect SARS-CoV-2 hospitalization and fatality risks in the middle-aged adult population. medRxiv. 7 nov 2020;2020.11.06.20227025.
3. Chen N, Zhou M, Dong X, Qu J, Gong F, Han Y, et al. Epidemiological and clinical characteristics of 99 cases of 2019 novel coronavirus pneumonia in Wuhan, China: a descriptive study. The Lancet. 15 févr 2020;395(10223):507-13.
4. Yang X, Yu Y, Xu J, Shu H, Xia J, Liu H, et al. Clinical course and outcomes of critically ill patients with SARS-CoV-2 pneumonia in Wuhan, China: a single-centered, retrospective, observational study. The Lancet Respiratory Medicine. 1 mai 2020;8(5):475-81.
5. Wu F, Wang A, Liu M, Wang Q, Chen J, Xia S, et al. Neutralizing antibody responses to SARS-CoV-2 in a COVID-19 recovered patient cohort and their implications. medRxiv [Internet]. 6 avr 2020 [cité 2 juin 2020]; Disponible sur: <http://medrxiv.org/lookup/doi/10.1101/2020.03.30.20047365>
6. Guedj J, Bazzoli C, Neumann AU, Mentré F. Design evaluation and optimization for models of hepatitis C viral dynamics. Statistics in Medicine. 10 mai 2011;30(10):1045-56.
7. Lovern M, Minton SK, Patel K, Xiong Y, Kirkpatrick CM, Smith PF. Applications of Influenza Viral Kinetic Modeling in Drug Development. Curr Pharmacol Rep. 1 oct 2017;3(5):294-300.
8. Hill AL, Rosenbloom DIS, Nowak MA, Siliciano RF. Insight into treatment of HIV infection from viral dynamics models. Immunol Rev. sept 2018;285(1):9-25.
9. Néant et al. N. Modeling SARS-CoV-2 viral kinetics and association with mortality in hospitalized patients from the French Covid cohort. PNAS. 2020;
10. Zheng S, Fan J, Yu F, Feng B, Lou B, Zou Q, et al. Viral load dynamics and disease severity in patients infected with SARS-CoV-2 in Zhejiang province, China, January-March 2020: retrospective cohort study. BMJ [Internet]. 21 avr 2020 [cité 9 mai 2020];369. Disponible sur: <https://www.bmjjournals.com/content/369/bmj.m1443>
11. Young BE, Ong SWX, Kalimuddin S, Low JG, Tan SY, Loh J, et al. Epidemiologic Features and Clinical Course of Patients Infected With SARS-CoV-2 in Singapore. JAMA [Internet]. 3 mars 2020 [cité 29 mars 2020]; Disponible sur: <https://jamanetwork.com/journals/jama/fullarticle/2762688>
12. Woelfel R, Corman VM, Guggemos W, Seilmäier M, Zange S, Mueller MA, et al. Clinical presentation and virological assessment of hospitalized cases of coronavirus disease

- 2019 in a travel-associated transmission cluster. medRxiv [Internet]. 8 mars 2020 [cité 2 juin 2020]; Disponible sur: <http://medrxiv.org/lookup/doi/10.1101/2020.03.05.20030502>
13. Best K, Guedj J, Madelain V, de Lamballerie X, Lim S-Y, Osuna CE, et al. Zika plasma viral dynamics in nonhuman primates provides insights into early infection and antiviral strategies. *Proceedings of the National Academy of Sciences*. 15 août 2017;114(33):8847-52.
14. Madelain V, Baize S, Jacquot F, Reynard S, Fizet A, Barron S, et al. Ebola viral dynamics in nonhuman primates provides insights into virus immuno-pathogenesis and antiviral strategies. *Nat Commun*. déc 2018;9(1):4013.
15. Guedj J, Piorkowski G, Jacquot F, Madelain V, Nguyen THT, Rodallec A, et al. Antiviral efficacy of favipiravir against Ebola virus: A translational study in cynomolgus macaques. *PLOS Medicine*. 27 mars 2018;15(3):e1002535.
16. Maisonnasse P, Guedj J, Contreras V, Behillil S, Solas C, Marlin R, et al. Hydroxychloroquine in the treatment and prophylaxis of SARS-CoV-2 infection in non-human primates. *Nature* [Internet]. 6 mai 2020 [cité 3 juin 2020]; Disponible sur: <https://www.researchsquare.com/article/rs-27223/v1>
17. Kobasa D, Jones SM, Shinya K, Kash JC, Copps J, Ebihara H, et al. Aberrant innate immune response in lethal infection of macaques with the 1918 influenza virus. *Nature*. 18 janv 2007;445(7125):319-23.
18. Cillóniz C, Shinya K, Peng X, Korth MJ, Proll SC, Aicher LD, et al. Lethal influenza virus infection in macaques is associated with early dysregulation of inflammatory related genes. *PLoS Pathog*. oct 2009;5(10):e1000604.
19. Pawelek KA, Huynh GT, Quinlivan M, Cullinane A, Rong L, Perelson AS. Modeling within-host dynamics of influenza virus infection including immune responses. *PLoS Comput Biol*. 28 juin 2012;8(6):e1002588.
20. Baccam P, Beauchemin C, Macken CA, Hayden FG, Perelson AS. Kinetics of influenza A virus infection in humans. *J Virol*. août 2006;80(15):7590-9.
21. Fedoseev G, Geharev S. Basic defence mechanisms of bronchio-lung system. In Outov NV. Vol. vol 1 Medicina. Moscow, Russia; 1989. p 112-144.
22. Agostini ML, Andres EL, Sims AC, Graham RL, Sheahan TP, Lu X, et al. Coronavirus Susceptibility to the Antiviral Remdesivir (GS-5734) Is Mediated by the Viral Polymerase and the Proofreading Exoribonuclease. *mBio* [Internet]. 6 mars 2018 [cité 7 mai 2020];9(2). Disponible sur: <https://www.ncbi.nlm.nih.gov/pmc/articles/PMC5844999/>
23. Samson A, Lavielle M, Mentré F. Extension of the SAEM algorithm to left-censored data in nonlinear mixed-effects model: Application to HIV dynamics model. *Computational Statistics & Data Analysis*. déc 2006;51(3):1562-74.
24. Gonçalves A, Mentré F, Lemenuel-Diot A, Guedj J. Model Averaging in Viral Dynamic Models. *AAPS J*. mars 2020;22(2):48.

25. Baum A, Ajithdoss D, Copin R, Zhou A, Lanza K, Negron N, et al. REGN-COV2 antibodies prevent and treat SARS-CoV-2 infection in rhesus macaques and hamsters. *Science*. 27 nov 2020;370(6520):1110-5.
26. Chandrashekhar A, Liu J, Martinot AJ, McMahan K, Mercado NB, Peter L, et al. SARS-CoV-2 infection protects against rechallenge in rhesus macaques. *Science*. 14 août 2020;369(6505):812-7.
27. Muus C, Luecken MD, Eraslan G, Waghray A, Heimberg G, Sikkema L, et al. Integrated analyses of single-cell atlases reveal age, gender, and smoking status associations with cell type-specific expression of mediators of SARS-CoV-2 viral entry and highlights inflammatory programs in putative target cells. *bioRxiv*. 21 avr 2020;2020.04.19.049254.
28. Bezara MEO, Thurman A, Pezzulo AA, Leidinger MR, Klesney-Tait JA, Karp PH, et al. Heterogeneous expression of the SARS-CoV-2 receptor ACE2 in the human respiratory tract [Internet]. *Cell Biology*; 2020 avr [cité 26 juin 2020]. Disponible sur: <http://biomedrxiv.org/lookup/doi/10.1101/2020.04.22.2056127>
29. Long Q-X, Tang X-J, Shi Q-L, Li Q, Deng H-J, Yuan J, et al. Clinical and immunological assessment of asymptomatic SARS-CoV-2 infections. *Nat Med* [Internet]. 18 juin 2020 [cité 26 juin 2020]; Disponible sur: <http://www.nature.com/articles/s41591-020-0965-6>
30. Sakurai A, Sasaki T, Kato S, Hayashi M, Tsuzuki S, Ishihara T, et al. Natural History of Asymptomatic SARS-CoV-2 Infection. *N Engl J Med*. 12 juin 2020;NEJM2013020.
31. Li Y, Handel A. Modeling inoculum dose dependent patterns of acute virus infections. *Journal of Theoretical Biology*. avr 2014;347:63-73.
32. Czuppon P, Débarre F, Gonçalves A, Tenaillon O, Perelson AS, Guedj J, et al. Predicted success of prophylactic antiviral therapy to block or delay SARS-CoV-2 infection depends on the targeted mechanism. 12 mai 2020; Disponible sur: <http://medrxiv.org/lookup/doi/10.1101/2020.05.07.20092965>.

Chapitre 8. Bibliographie

- Abe A, Inoue K, Tanaka T, Kato J, Kajiyama N, Kawaguchi R, et al. Quantitation of Hepatitis B Virus Genomic DNA by Real-Time Detection PCR. *Journal of Clinical Microbiology*. 1999;37(9):2899-903.
- Agarwal K, Fung SK, Nguyen TT, Cheng W, Sicard E, Ryder SD, et al. Twenty-eight day safety, antiviral activity, and pharmacokinetics of tenofovir alafenamide for treatment of chronic hepatitis B infection. *Journal of Hepatology*. 2015;62(3):533-40.
- Aoki Y, Röshammar D, Hamrén B, Hooker AC. Model selection and averaging of nonlinear mixed-effect models for robust phase III dose selection. *Journal of Pharmacokinetics and Pharmacodynamics*. 2017;44(6):581-97.
- Balsitis S, Gali V, Mason PJ, Chaniewski S, Levine SM, Wichroski MJ, et al. Safety and efficacy of anti-PD-L1 therapy in the woodchuck model of HBV infection. *PloS One*. 2018;13(2):e0190058.
- Beasley RP, Trepo C, Stevens CE, Szmuness W. The e antigen and vertical transmission of hepatitis B surface antigen. *American Journal of Epidemiology*. 1977;105(2):94-8.
- van den Berg F, Limani SW, Mnyandu N, Maepa MB, Ely A, Arbuthnot P. Advances with RNAi-Based Therapy for Hepatitis B Virus Infection. *Viruses*. 2020;12(8).
- Bergstrand M, Hooker AC, Wallin JE, Karlsson MO. Prediction-Corrected Visual Predictive Checks for Diagnosing Nonlinear Mixed-Effects Models. *The AAPS Journal*. 2011;13(2):143-51.
- Berke JM, Dehertogh P, Vergauwen K, Van Damme E, Mostmans W, Vandyck K, et al. Capsid Assembly Modulators Have a Dual Mechanism of Action in Primary Human Hepatocytes Infected with Hepatitis B Virus. *Antimicrobial Agents and Chemotherapy*. 2017;61(8).
- Bertoletti A, Ferrari C. Innate and adaptive immune responses in chronic hepatitis B virus infections: towards restoration of immune control of viral infection. *Gut*. 2012;61(12):1754-64.
- Best K, Guedj J, Madelain V, de Lamballerie X, Lim S-Y, Osuna CE, et al. Zika plasma viral dynamics in nonhuman primates provides insights into early infection and antiviral strategies. *Proceedings of the National Academy of Sciences*. 2017;114(33):8847-52.
- van Bömmel F, Bartens A, Mysickova A, Hofmann J, Krüger DH, Berg T, et al. Serum hepatitis B virus RNA levels as an early predictor of hepatitis B envelope antigen seroconversion during treatment with polymerase inhibitors. *Hepatology (Baltimore, Md)*. 2015;61(1):66-76.

Bibliographie

- Bornkamp B, Ohlssen D, Magnusson BP, Schmidli H. Model averaging for treatment effect estimation in subgroups. *Pharmaceutical Statistics*. 2017;16(2):133-42.
- Boulesteix A-L. Ten simple rules for reducing overoptimistic reporting in methodological computational research. Lewitter F, éditeur. *PLOS Computational Biology*. 2015;11(4):e1004191.
- Brendel K, Comets E, Laffont C, Laveille C, Mentré F. Metrics for external model evaluation with an application to the population pharmacokinetics of gliclazide. *Pharmaceutical Research*. 2006;23(9):2036-49.
- Bruss V. Hepatitis B virus morphogenesis. *World Journal of Gastroenterology*. 2007;13(1):65-73.
- Buatois S, Ueckert S, Frey N, Retout S, Mentré F. Comparison of model averaging and model selection in dose finding trials analyzed by nonlinear mixed effect models. *The AAPS journal*. 2018;20(3):56.
- Buckland ST, Burnham KP, Augustin NH. Model selection: an integral part of inference. *Biometrics*. 1997;53(2):603.
- Cantell K. The story of interferon: the ups and downs in the life of a scientist. Singapore ; New York: World Scientific; 1998.
- Casella G. An Introduction to Empirical Bayes Data Analysis. *The American Statistician*. 1985;39(2):83-7.
- Chang T-T, Gish RG, de Man R, Gadano A, Sollano J, Chao Y-C, et al. A Comparison of Entecavir and Lamivudine for HBeAg-Positive Chronic Hepatitis B. *New England Journal of Medicine*. 2006;354(10):1001-10.
- Chang T-T, Liaw Y-F, Wu S-S, Schiff E, Han K-H, Lai C-L, et al. Long-term entecavir therapy results in the reversal of fibrosis/cirrhosis and continued histological improvement in patients with chronic hepatitis B. *Hepatology*. 2010;52(3):886-93.
- Chen C-H, Hung C-H, Wang J-H, Lu S-N, Hu T-H, Lee C-M. Long-term incidence and predictors of hepatitis B surface antigen loss after discontinuing nucleoside analogues in noncirrhotic chronic hepatitis B patients. *Clinical Microbiology and Infection*. 2018;24(9):997-1003.
- Chen Y, Cheng G, Mahato RI. RNAi for Treating Hepatitis B Viral Infection. *Pharmaceutical Research*. 2008;25(1):72-86.
- Chevaliez S, Hézode C, Bahrami S, Grare M, Pawlotsky J-M. Long-term hepatitis B surface antigen (HBsAg) kinetics during nucleoside/nucleotide analogue therapy: Finite treatment duration unlikely. *Journal of Hepatology*. 2013;58(4):676-83.
- Ciupe SM, Ribeiro RM, Perelson AS. Antibody responses during hepatitis B viral infection. *PLoS Comput Biol*. 2014;10(7):e1003730.

Bibliographie

- Colombatto P, Civitano L, Bizzarri R, Oliveri F, Choudhury S, Gieschke R, et al. A multiphase model of the dynamics of HBV infection in HBeAg-negative patients during pegylated interferon-alpha2a, lamivudine and combination therapy. *Antiviral Therapy*. 2006;11(2):197-212.
- Cornberg M, Wong VW-S, Locarnini S, Brunetto M, Janssen HLA, Chan HL-Y. The role of quantitative hepatitis B surface antigen revisited. *Journal of Hepatology*. 2017;66(2):398-411.
- Dai L, Yu Y, Gu L, Zhao J, Zhu L, Yun H, et al. Combination treatment of a TLR7 agonist RO7020531 and a capsid assembly modulator RO7049389 achieved sustainable viral load suppression and HBsAg loss in an AAV-HBV mouse model. *Journal of Hepatology*. 2018;68:S17-8.
- Dane DS, Cameron CH, Briggs M. Virus-like particles in serum of patients with Australia-antigen-associated hepatitis. *Lancet (London, England)*. 1970;1(7649):695-8.
- Dartois C, Lemenuel-Diot A, Laveille C, Tranchand B, Tod M, Girard P. Evaluation of uncertainty parameters estimated by different population PK software and methods. *Journal of Pharmacokinetics and Pharmacodynamics*. 2007;34(3):289-311.
- Davidian M, Giltinan DM. Nonlinear Models for Repeated Measurement Data. 1995;
- Delyon B, Lavielle M, Moulines E. Convergence of a stochastic approximation version of the EM algorithm. *Annals of Statistics*. 1999;27(1):94-128.
- Deres K, Schröder CH, Paessens A, Goldmann S, Hacker HJ, Weber O, et al. Inhibition of hepatitis B virus replication by drug-induced depletion of nucleocapsids. *Science (New York, NY)*. 2003;299(5608):893-6.
- Dosne A-G, Bergstrand M, Harling K, Karlsson MO. Improving the estimation of parameter uncertainty distributions in nonlinear mixed effects models using sampling importance resampling. *Journal of Pharmacokinetics and Pharmacodynamics*. 2016;43(6):583-96.
- Fan J-H, Wang J-B, Jiang Y, Xiang W, Liang H, Wei W-Q, et al. Attributable Causes of Liver Cancer Mortality and Incidence in China. *Asian Pacific Journal of Cancer Prevention*. 2013;14(12):7251-6.
- Fanning GC, Zoulim F, Hou J, Bertoletti A. Therapeutic strategies for hepatitis B virus infection: towards a cure. *Nature Reviews Drug Discovery*. 2019;
- Feld JJ, Colledge D, Sozzi V, Edwards R, Littlejohn M, Locarnini SA. The phenylpropenamide derivative AT-130 blocks HBV replication at the level of viral RNA packaging. *Antiviral Research*. 2007;76(2):168-77.
- Féray C, Gigou M, Samuel D, Reyes G, Bernau J, Reynes M, et al. Hepatitis C virus RNA and hepatitis B virus DNA in serum and liver of patients with fulminant hepatitis. *Gastroenterology*. 1993;104(2):549-55.

Bibliographie

- Food and Drug Administration. Chronic Hepatitis C Virus Infection: Developing Direct-Acting Antiviral Drugs for Treatment. *Chronic Hepatitis C Virus*. 2017;40.
- Friberg LE, Guedj J. Acute bacterial or viral infection—What's the difference? A perspective from PKPD modellers. *Clinical Microbiology and Infection*. 2019;S1198743X19306639.
- Gane E, Dunbar PR, Brooks A, Zhao Y, Tan S, Lau A, et al. Efficacy and safety of 24 weeks treatment with oral TLR8 agonist, selgantolimod, in virally-suppressed adult patients with chronic hepatitis B: a phase 2 study. *Journal of Hepatology*. 2020;73:S52.
- Gane E, Liu A, Yuen M-F, Schwabe C, Bo Q, Das S, et al. RO7049389, a core protein allosteric modulator, demonstrates robust anti-HBV activity in chronic hepatitis B patients and is safe and well tolerated. *Journal of Hepatology*. 2018;68:S101.
- Gane E, Yuen M-F, Bo Q, Schwabe C, Tanwandee T, Das S, et al. FRI-219-RO7049389, a core protein allosteric modulator, demonstrates robust decline in HBV DNA and HBV RNA in chronic HBV infected patients. *Journal of Hepatology*. 2019;70(1):e491.
- Ganem D, Prince AM. Hepatitis B Virus Infection — Natural History and Clinical Consequences. *New England Journal of Medicine*. 2004;350(11):1118-29.
- Ganusov VV. Strong inference in mathematical modeling: a method for robust science in the twenty-first century. *Frontiers in Microbiology*. 2016;7(1137):1-10.
- Ge Z, J. Bickel P, A. Rice J. An approximate likelihood approach to nonlinear mixed effects models via spline approximation. *Computational Statistics & Data Analysis*. 2004;46(4):747-76.
- Gibbert K, Schlaak J, Yang D, Dittmer U. IFN- α subtypes: distinct biological activities in anti-viral therapy. *British Journal of Pharmacology*. 2013;168(5):1048-58.
- Giersch K, Allweiss L, Volz T, Dandri M, Lütgehetmann M. Serum HBV pgRNA as a clinical marker for cccDNA activity. *Journal of Hepatology*. 2017;66(2):460-2.
- Gonzalez SA. Hepatitis B Virus - Infectious Disease and Antimicrobial Agents. 2017;
- Guedj J, Dahari H, Rong L, Sansone ND, Nettles RE, Cotler SJ, et al. Modeling shows that the NS5A inhibitor daclatasvir has two modes of action and yields a shorter estimate of the hepatitis C virus half-life. *Proceedings of the National Academy of Sciences*. 2013;110(10):3991-6.
- Guedj J, Perelson AS. Second-phase hepatitis C virus RNA decline during telaprevir-based therapy increases with drug effectiveness: Implications for treatment duration. *Hepatology*. 2011;53(6):1801-8.
- Guedj J, Thiébaut R, Commenges D. Practical identifiability of HIV dynamics models. *Bulletin of Mathematical Biology*. 2007;69(8):2493-513.

Bibliographie

- Ho DD, Neumann AU, Perelson AS, Chen W, Leonard JM, Markowitz M. Rapid turnover of plasma virions and CD4 lymphocytes in HIV-1 infection. *Nature*. 1995;373(6510):123-6.
- Hong M, Bertoletti A. Tolerance and immunity to pathogens in early life: insights from HBV infection. *Seminars in Immunopathology*. 2017;39(6):643-52.
- Hou J, Liu Z, Gu F, others. Epidemiology and prevention of hepatitis B virus infection. *Int J Med Sci*. 2005;2(1):50-57.
- Hu J, Liu K. Complete and Incomplete Hepatitis B Virus Particles: Formation, Function, and Application. *Viruses*. 2017;9(3):56.
- Huang C, Wang Y, Li X, Ren L, Zhao J, Hu Y, et al. Clinical features of patients infected with 2019 novel coronavirus in Wuhan, China. *Lancet (London, England)*. 2020;395(10223):497-506.
- Huang Y-H, Fang C-C, Tsuneyama K, Chou H-Y, Pan W-Y, Shih Y-M, et al. A murine model of hepatitis B-associated hepatocellular carcinoma generated by adenovirus-mediated gene delivery. *International Journal of Oncology*. 2011;39(6):1511-9.
- Huang Y-W, Chayama K, Tsuge M, Takahashi S, Hatakeyama T, Abe H, et al. Differential effects of interferon and lamivudine on serum HBV RNA inhibition in patients with chronic hepatitis B. *Antiviral Therapy*. 2010;15(2):177-84.
- Huang Y-W, Takahashi S, Tsuge M, Chen C-L, Wang T-C, Abe H, et al. On-treatment low serum HBV RNA level predicts initial virological response in chronic hepatitis B patients receiving nucleoside analogue therapy. *Antiviral Therapy*. 2015;20(4):369-75.
- Hyams KC. Risks of chronicity following acute hepatitis B virus infection: a review. *Clinical Infectious Diseases: An Official Publication of the Infectious Diseases Society of America*. 1995;20(4):992-1000.
- Inoue T, Tanaka Y. Hepatitis B virus and its sexually transmitted infection - an update. *Microbial Cell*. 2016;3(9):420-37.
- Institut National de la Santé Et de la Recherche Médicale, France. Multi-centre, Adaptive, Randomized Trial of the Safety and Efficacy of Treatments of COVID-19 in Hospitalized Adults. clinicaltrials.gov; 2020 juill. Report No.: NCT04315948.
- Janssen H, Brunetto MR, Kim YJ, Ferrari C, Massetto B, Nguyen A-H, et al. Safety, efficacy and pharmacodynamics of vesatolimod (GS-9620) in virally suppressed patients with chronic hepatitis B. *Journal of Hepatology*. 2018;68(3):431-40.
- Janssen H, Hou J, Asselah T, Chan H, Zoulim F, Tanaka Y, et al. Efficacy and safety results of the phase 2 JNJ-56136379 JADE study in patients with chronic hepatitis B: Interim week 24 data. *Journal of Hepatology*. 2020;73:S129-30.

Bibliographie

- Janssen H, van Zonneveld M, Senturk H, Zeuzem S, Akarca US, Cakaloglu Y, et al. Pegylated interferon alfa-2b alone or in combination with lamivudine for HBeAg-positive chronic hepatitis B: a randomised trial. *Lancet (London, England)*. 2005;365(9454):123-9.
- Jo J, Tan AT, Ussher JE, Sandalova E, Tang X-Z, Tan-Garcia A, et al. Toll-Like Receptor 8 Agonist and Bacteria Trigger Potent Activation of Innate Immune Cells in Human Liver. *PLOS Pathogens*. 2014;10(6):e1004210.
- Kirk PDW, Babtie AC, Stumpf MPH. Systems biology (un)certainties. *Science*. 2015;350(6259):386-8.
- Köck J, Rösler C, Zhang J-J, Blum HE, Nassal M, Thoma C. Generation of Covalently Closed Circular DNA of Hepatitis B Viruses via Intracellular Recycling Is Regulated in a Virus Specific Manner. *PLoS Pathogens*. 2010;6(9).
- Kramvis A, Kostaki E-G, Hatzakis A, Paraskevis D. Immunomodulatory Function of HBeAg Related to Short-Sighted Evolution, Transmissibility, and Clinical Manifestation of Hepatitis B Virus. *Frontiers in Microbiology*. 2018;9.
- Kuhn E, Lavielle M. Maximum likelihood estimation in nonlinear mixed effects models. *Computational Statistics & Data Analysis*. 2005;49(4):1020-38.
- Kwon SY, Lee CH. Epidemiology and prevention of hepatitis B virus infection. *The Korean Journal of Hepatology*. 2011;17(2):87-95.
- Lahlali T, Berke JM, Vergauwen K, Foca A, Vandyck K, Pauwels F, et al. Novel Potent Capsid Assembly Modulators Regulate Multiple Steps of the Hepatitis B Virus Life Cycle. *Antimicrobial Agents and Chemotherapy*. 2018;62(10):e00835-18, /aac/62/10/e00835-18.atom.
- Lampertico P, Agarwal K, Berg T, Buti M, Janssen HLA, Papatheodoridis G, et al. EASL 2017 Clinical Practice Guidelines on the management of hepatitis B virus infection. *Journal of Hepatology*. 2017;67(2):370-98.
- Lampertico P, Soffredini R, Viganò M, Minola E, Cologni G, Rizzi M, et al. 5-year entecavir treatment in nuc-naïve, field-practice patients with chronic hepatitis b showed excellent viral suppression and safety profile but no prevention of hcc in cirrhotics. *Journal of Hepatology*. 2013;58:S306-7.
- Lanford RE, Guerra B, Chavez D, Giavedoni L, Hodara VL, Brasky KM, et al. GS-9620, an Oral Agonist of Toll-Like Receptor-7, Induces Prolonged Suppression of Hepatitis B Virus in Chronically Infected Chimpanzees. *Gastroenterology*. 2013;144(7):1508-1517.e10.
- Lau GK, Piratvisuth T, Luo KX, Marcellin P, Thongsawat S, Cooksley G, et al. Peginterferon Alfa-2a, lamivudine, and the combination for HBeAg-positive chronic hepatitis B. *New England Journal of Medicine*. 2005;352(26):2682-2695.

Bibliographie

- Lavielle M. Mixed Effects Models for the Population Approach: Models, Tasks, Methods and Tools. CRC Press; 2014.
- Lavielle M, Mentré F. Estimation of population pharmacokinetic parameters of saquinavir in HIV patients with the MONOLIX software. *Journal of Pharmacokinetics and Pharmacodynamics*. 2007;34(2):229-49.
- Levrero M, Zucman-Rossi J. Mechanisms of HBV-induced hepatocellular carcinoma. *Journal of Hepatology*. 2016;64(1):S84-101.
- Lewin SR, Ribeiro RM, Walters T, Lau GK, Bowden S, Locarnini S, et al. Analysis of hepatitis B viral load decline under potent therapy: complex decay profiles observed. *Hepatology (Baltimore, Md)*. 2001;34(5):1012-20.
- Lindstrom MJ, Bates DM. Nonlinear Mixed Effects Models for Repeated Measures Data. *Biometrics*. 1990;46(3):673-87.
- Liu S, Liu Z, Li W, Zhou B, Liang X, Fan R, et al. Factors associated with the biphasic kinetics of serum HBV RNA in patients with HBeAg-positive chronic hepatitis B treated with nucleos(t)ide analogues. *Alimentary Pharmacology & Therapeutics*. 2020;52(4):692-700.
- Liu S, Zhou B, Valdes JD, Sun J, Guo H. Serum Hepatitis B Virus RNA: A New Potential Biomarker for Chronic Hepatitis B Virus Infection. *Hepatology*. 2019;69(4):1816-27.
- Locarnini S, Mason WS. Cellular and virological mechanisms of HBV drug resistance. *Journal of Hepatology*. 2006;44(2):422-31.
- Lok AS, Zoulim F, Dusheiko G, Ghany MG. Hepatitis B cure: From discovery to regulatory approval. *Journal of Hepatology*. 2017;67(4):847-61.
- Lok ASF, McMahon BJ, Brown RS, Wong JB, Ahmed AT, Farah W, et al. Antiviral therapy for chronic hepatitis B viral infection in adults: A systematic review and meta-analysis. *Hepatology (Baltimore, Md)*. 2016;63(1):284-306.
- Lucifora J, Protzer U. Attacking hepatitis B virus cccDNA--The holy grail to hepatitis B cure. *Journal of Hepatology*. 2016;64(1 Suppl):S41-8.
- Luk A, Jiang Q, Glavini K, Triyatni M, Zhao N, Racek T, et al. A Single and Multiple Ascending Dose Study of Toll-Like Receptor 7 Agonist (RO7020531) in Chinese Healthy Volunteers. *Clinical and Translational Science*. 2020;13(5):985-93.
- Luo J, Li X, Wu Y, Lin G, Pang Y, Zhang X, et al. Efficacy of Entecavir Treatment for up to 5 Years in Nucleos(t)ide-Naïve Chronic Hepatitis B Patients in Real Life. *International Journal of Medical Sciences*. 2013;10(4):427-33.
- Luo Z, Li L, Ruan B. Impact of the implementation of a vaccination strategy on hepatitis B virus infections in China over a 20-year period. *International journal of infectious diseases: IJID: official publication of the International Society for Infectious Diseases*. 2012;16(2):e82-88.

Bibliographie

- Ma et al. Interim safety and efficacy results of the ABI-H0731 phase 2a program exploring the combination of ABI-H0731 with Nuc therapy in treatment-naïve and treatment-suppressed chronic hepatitis B patients [abstract LBO-06]. *J Hepatol* 70,. 2019;e130.
- MacLachlan JH, Cowie BC. Hepatitis B Virus Epidemiology. *Cold Spring Harbor Perspectives in Medicine*. 2015;5(5).
- Maisonnable P, Guedj J, Contreras V, Behillil S, Solas C, Marlin R, et al. Hydroxychloroquine in the treatment and prophylaxis of SARS-CoV-2 infection in non-human primates. 2020;
- Marcellin P, Bonino F, Yurdagun C, Hadziyannis S, Moucari R, Kapprell H-P, et al. Hepatitis B surface antigen levels: association with 5-year response to peginterferon alfa-2a in hepatitis B e-antigen-negative patients. *Hepatology International*. 2012;7(1):88-97.
- Marcellin P, Heathcote EJ, Buti M, Gane E, de Man RA, Krastev Z, et al. Tenofovir Disoproxil Fumarate versus Adefovir Dipivoxil for Chronic Hepatitis B. *New England Journal of Medicine*. 2008;359(23):2442-55.
- Marcellin P, Lau GKK, Bonino F, Farci P, Hadziyannis S, Jin R, et al. Peginterferon Alfa-2a Alone, Lamivudine Alone, and the Two in Combination in Patients with HBeAg-Negative Chronic Hepatitis B. *New England Journal of Medicine*. 2004;351(12):1206-17.
- McMahon BJ, Alward WL, Hall DB, Heyward WL, Bender TR, Francis DP, et al. Acute hepatitis B virus infection: relation of age to the clinical expression of disease and subsequent development of the carrier state. *The Journal of Infectious Diseases*. 1985;151(4):599-603.
- Mentré F, Escolano S. Prediction discrepancies for the evaluation of nonlinear mixed-effects models. *Journal of Pharmacokinetics and Pharmacodynamics*. 2006;33(3):345-67.
- Michel M-L, Pol S, Brechot C, Tiollais P. Immunotherapy of chronic hepatitis B by anti HBV vaccine: from present to future. *Vaccine*. 2001;19(17):2395-9.
- Mouzannar K, Liang TJ. Hepatitis B virus – recent therapeutic advances and challenges to cure. *Journal of Hepatology*. 2020;73(3):694-5.
- Murray JM, Purcell RH, Wieland SF. The half-life of hepatitis B virions. *Hepatology*. 2006;44(5):1117-21.
- Murray JM, Wieland SF, Purcell RH, Chisari FV. Dynamics of hepatitis B virus clearance in chimpanzees. *Proceedings of the National Academy of Sciences of the United States of America*. 2005;102(49):17780–17785.
- Neumann AU. Hepatitis B viral kinetics: A dynamic puzzle still to be resolved. *Hepatology*. 2005;42(2):249-54.

Bibliographie

- Neumann AU, Lam NP, Dahari H, Gretch DR, Wiley TE, Layden TJ, et al. Hepatitis C viral dynamics in vivo and the antiviral efficacy of interferon-alpha therapy. *Science (New York, NY)*. 1998;282(5386):103-7.
- Nguyen T, Mouksassi M-S, Holford N, Al-Huniti N, Freedman I, Hooker A, et al. Model Evaluation of Continuous Data Pharmacometric Models: Metrics and Graphics: Evaluation Graphs for Population PK/PD Models. *CPT: Pharmacometrics & Systems Pharmacology*. 2017;
- Nguyen THT, Mentré F, Levi M, Yu J, Guedj J. A Pharmacokinetic–Viral Kinetic Model Describes the Effect of Alisporivir as Monotherapy or in Combination With Peg-IFN on Hepatitis C Virologic Response. *Clinical Pharmacology & Therapeutics*. 2014;96(5):599-608.
- Niu C, Li L, Daffis S, Lucifora J, Bonnin M, Maadadi S, et al. Toll-like receptor 7 agonist GS-9620 induces prolonged inhibition of HBV via a type I interferon-dependent mechanism. *Journal of Hepatology*. 2018;68(5):922-31.
- Nowak MA, Bonhoeffer S, Hill AM, Boehme R, Thomas HC, McDade H. Viral dynamics in hepatitis B virus infection. *Proceedings of the National Academy of Sciences*. 1996;93(9):4398–4402.
- Papatheodoridis GV, Dimou E, Papadimitropoulos V. Nucleoside analogues for chronic hepatitis B: antiviral efficacy and viral resistance. *The American Journal of Gastroenterology*. 2002;97(7):1618-28.
- Perelson AS, Neumann AU, Markowitz M, Leonard JM, Ho DD. HIV-1 dynamics in vivo: virion clearance rate, infected cell life-span, and viral generation time. *Science (New York, NY)*. 1996;271(5255):1582-6.
- Pillonel J, Saura C, Couroucé AM. Dépistage des marqueurs d'une infection par le VIH et les virus des hépatites B et C chez les donneurs de sang en France et risque résiduel de transmission de ces virus par transfusion sanguine. *Eurosurveillance*. 1998;3(7):76-9.
- Pinheiro JC, Bates DM, éditeurs. Fitting Nonlinear Mixed-Effects Models. In: Mixed-Effects Models in S and S-PLUS. New York, NY: Springer; 2000. p. 337-421. (Statistics and Computing).
- Plan EL, Maloney A, Mentré F, Karlsson MO, Bertrand J. Performance comparison of various maximum likelihood nonlinear mixed-effects estimation methods for dose-response models. *The AAPS journal*. 2012;14(3):420-32.
- Polaris Observatory Collaborators. Global prevalence, treatment, and prevention of hepatitis B virus infection in 2016: a modelling study. *The Lancet Gastroenterology & Hepatology*. 2018;3(6):383-403.
- Raftery AE. Bayesian Model Selection in Social Research. *Sociological Methodology*. 1995;25:111.

Bibliographie

- Ramratnam B, Bonhoeffer S, Binley J, Hurley A, Zhang L, Mittler JE, et al. Rapid production and clearance of HIV-1 and hepatitis C virus assessed by large volume plasma apheresis. *The Lancet*. 1999;354(9192):1782-5.
- Rokuhara A, Matsumoto A, Tanaka E, Umemura T, Yoshizawa K, Kimura T, et al. Hepatitis B virus RNA is measurable in serum and can be a new marker for monitoring lamivudine therapy. *Journal of Gastroenterology*. 2006;41(8):785-90.
- Rydell GE, Prakash K, Norder H, Lindh M. Hepatitis B surface antigen on subviral particles reduces the neutralizing effect of anti-HBs antibodies on hepatitis B viral particles in vitro. *Virology*. 2017;509:67-70.
- Sakurai A, Sasaki T, Kato S, Hayashi M, Tsuzuki S, Ishihara T, et al. Natural History of Asymptomatic SARS-CoV-2 Infection. *New England Journal of Medicine*. 2020;NEJMc2013020.
- Savic RM, Karlsson MO. Importance of Shrinkage in Empirical Bayes Estimates for Diagnostics: Problems and Solutions. *The AAPS Journal*. 2009;11(3):558-69.
- Schorning K, Bornkamp B, Bretz F, Dette H. Model selection versus model averaging in dose finding studies: K. SCHORNING ET AL. *Statistics in Medicine*. 2016;35(22):4021-40.
- Schurich A, Pallett LJ, Lubowiecki M, Singh HD, Gill US, Kennedy PT, et al. The Third Signal Cytokine IL-12 Rescues the Anti-Viral Function of Exhausted HBV-Specific CD8 T Cells. *PLOS Pathogens*. 2013;9(3):e1003208.
- Seeger C, Mason WS. Hepatitis B Virus Biology. *Microbiology and Molecular Biology Reviews*. 2000;64(1):51-68.
- Sheiner LB, Rosenberg B, Melmon KL. Modelling of individual pharmacokinetics for computer-aided drug dosage. *Computers and Biomedical Research*. 1972;5(5):441-59.
- Shekhtman L, Cotler SJ, Hershkovich L, Uprichard SL, Bazinet M, Pantea V, et al. Modelling hepatitis D virus RNA and HBsAg dynamics during nucleic acid polymer monotherapy suggest rapid turnover of HBsAg. *Scientific Reports*. 2020;10(1):7837.
- Simon N. Analyse pharmacocinétique et pharmacodynamique par approche de population estimation, évaluation, simulation. Marseille: Solal; 2011.
- Smedile A, Farci P, Verme G, Caredda F, Cargnel A, Caporaso N, et al. Influence of delta infection on severity of hepatitis B. *Lancet (London, England)*. 1982;2(8305):945-7.
- Snoeck E, Chanu P, Lavielle M, Jacqmin P, Jonsson EN, Jorga K, et al. A comprehensive Hepatitis C viral kinetic model explaining cure. *Clinical Pharmacology & Therapeutics*. 2010;87(6):706-13.
- Stevens CE, Beasley RP, Tsui J, Lee W-C. Vertical Transmission of Hepatitis B Antigen in Taiwan. *New England Journal of Medicine*. 1975;292(15):771-4.

Bibliographie

- Stevens CE, Neurath RA, Beasley RP, Szmuness W. HBeAg and anti-HBe detection by radioimmunoassay: correlation with vertical transmission of hepatitis B virus in Taiwan. *Journal of Medical Virology*. 1979;3(3):237-41.
- Sypsa V-A, Mimidis K, Tassopoulos NC, Chrysagis D, Vassiliadis T, Moulakakis A, et al. A viral kinetic study using pegylated interferon alfa-2b and/or lamivudine in patients with chronic hepatitis B/HBeAg negative. *Hepatology*. 2005;42(1):77-85.
- Talal AH, Ribeiro RM, Powers KA, Grace M, Cullen C, Hussain M, et al. Pharmacodynamics of PEG-IFN α differentiate HIV/HCV coinfecting sustained virological responders from nonresponders. *Hepatology*. 2006;43(5):943-53.
- Testoni B, Lebossé F, Scholtes C, Berby F, Miaglia C, Subic M, et al. Serum hepatitis B core-related antigen (HBcrAg) correlates with covalently closed circular DNA transcriptional activity in chronic hepatitis B patients. *Journal of Hepatology*. 2019;70(4):615-25.
- Thai H-T, Mentré F, Holford NHG, Veyrat-Follet C, Comets E. Evaluation of bootstrap methods for estimating uncertainty of parameters in nonlinear mixed-effects models: a simulation study in population pharmacokinetics. *Journal of Pharmacokinetics and Pharmacodynamics*. 2014;41(1):15-33.
- Tong S, Revill P. Overview of hepatitis B viral replication and genetic variability. *Journal of Hepatology*. 2016;64(1):S4-16.
- Tu T, Budzinska MA, Shackel NA, Urban S. HBV DNA Integration: Molecular Mechanisms and Clinical Implications. *Viruses*. 2017;9(4).
- Wang J, Shen T, Huang X, Kumar GR, Chen X, Zeng Z, et al. Serum hepatitis B virus RNA is encapsidated pregenome RNA that may be associated with persistence of viral infection and rebound. *Journal of Hepatology*. 2016;65(4):700-10.
- Whalley SA, Murray JM, Brown D, Webster GJM, Emery VC, Dusheiko GM, et al. Kinetics of Acute Hepatitis B Virus Infection in Humans. *Journal of Experimental Medicine*. 2001;193(7):847-54.
- Williamson BN, Feldmann F, Schwarz B, Meade-White K, Porter DP, Schulz J, et al. Clinical benefit of remdesivir in rhesus macaques infected with SARS-CoV-2. *Microbiology*; 2020 avr.
- Wolfinger R. Laplace's approximation for nonlinear mixed models. *Biometrika*. 1993;80(4):791-5.
- Wooddell CI, Yuen M-F, Chan HL-Y, Gish RG, Locarnini SA, Chavez D, et al. RNAi-based treatment of chronically infected patients and chimpanzees reveals that integrated hepatitis B virus DNA is a source of HBsAg. *Science Translational Medicine*. 2017;9(409):eaan0241.

Bibliographie

- Wu H-L, Huang L-R, Huang C-C, Lai H-L, Liu C-J, Huang Y-T, et al. RNA interference-mediated control of hepatitis B virus and emergence of resistant mutant. *Gastroenterology*. 2005;128(3):708-16.
- Yan H, Zhong G, Xu G, He W, Jing Z, Gao Z, et al. Sodium taurocholate cotransporting polypeptide is a functional receptor for human hepatitis B and D virus. *elife*. 2012;1:e00049.
- Yang D, Liu L, Zhu D, Peng H, Su L, Fu Y-X, et al. A mouse model for HBV immunotolerance and immunotherapy. *Cellular & Molecular Immunology*. 2014;11(1):71-8.
- Young BE, Ong SWX, Kalimuddin S, Low JG, Tan SY, Loh J, et al. Epidemiologic Features and Clinical Course of Patients Infected With SARS-CoV-2 in Singapore. *JAMA*. 2020;
- Yuen, Balabanska RI, Agarwal K, Zhu YH, Grippo J, Jin YY, et al. Safety, pharmacokinetic, pharmacodynamic and viral data after 6-weeks of dosing with TLR7 agonist RO7020531 in chronic hepatitis B patients. 2019a;;
- Yuen et al. Short term RNA interference (RNAi) therapy in chronic hepatitis B (CHB) using JNJ-3989 brings majority of patients to HBsAg <100 IU/ml threshold. *Journal of Hepatology*. 2019b;;
- Yuen MF, Gane EJ, Kim DJ, Weilert F, Yuen Chan HL, Lalezari J, et al. Antiviral Activity, Safety, and Pharmacokinetics of Capsid Assembly Modulator NVR 3-778 in Patients with Chronic HBV Infection. *Gastroenterology*. 2019c;156(5):1392-1403.e7.
- Zhou X, Zhou Y, Tian X, Shen F, Yang G, Zhu W, et al. In vitro and in vivo antiviral characterization of RO7049389, a novel small molecule capsid assembly modulator for the treatment of chronic hepatitis B. *Journal of Hepatology*. 2018;68:S770.
- Zoulim F. Hepatitis B virus resistance to antiviral drugs: where are we going? *Liver International*. 2011;31 Suppl 1:111-6.
- Zoulim F, Lenz O, Vandenbossche JJ, Talloen W, Verbinnen T, Moscalu I, et al. JNJ-56136379, an HBV Capsid Assembly Modulator, Is Well-Tolerated and Has Antiviral Activity in a Phase 1 Study of Patients With Chronic Infection. *Gastroenterology*. 2020;159(2):521-533.e9.
- Zoulim F, Locarnini S. Hepatitis B virus resistance to nucleos(t)ide analogues. *Gastroenterology*. 2009;137(5):1593-1608.e1-2.
- Zoulim F, Luangsay S, Durantel D. Targeting innate immunity: a new step in the development of combination therapy for chronic hepatitis B. *Gastroenterology*. 2013;144(7):1342–1344.

Abstract

Covalently closed circular DNA (cccDNA) and integrated DNA are stable forms of HBV virus that makes it difficult to treat. Current therapies such as nucleosidic analogs (NA) and pegylated interferon (Peg-IFN) reduce the viral loads but fail to trigger those intracellular forms of DNA. Since cccDNA remains transcriptionally active, viral products such as subviral particles, (SVP) and HBV RNA continue to be produced, and contribute to the disease burden. Hence, therapies with different mechanisms of action are being developed such as immunomodulators, triggering both innate and adaptive immune response, and capsid inhibitors reduction the production of encapsidated particles.

Since its use in HIV and HCV infection, viral dynamic models have helped to gain knowledge on antiviral efficacy and brought novel insight of the biological processes of the infection. This approach is based on nonlinear mixed effect models, has allowed to characterize the biphasic decline of HBV DNA in infected patients treated by NA and/or Peg-IFN.

In this thesis, we extended the current models of HBV dynamics and described the mechanisms of action of novel drugs affecting other markers in addition to HBV DNA. First, we evaluated the effects of a TLR7 agonist, an immunomodulator affecting the dynamics of the HBs antigen through the stimulation of the immune response. Second, we studied a capsid inhibitor, a direct antiviral treatment destabilizing the encapsidation step. The development of complex models goes along with a number of models tested but only the one providing the best description of the data is carried forward. However, this current approach called model selection ignores model uncertainty and may lead to wrong biological conclusions. Hence, we finally evaluated model averaging as an alternative approach to take into account model uncertainty.

We showed how modelling can help to better understand HBV infection and describe the mechanisms of action of drugs under development. This work initiates the development of comprehensive models of HBV infection and it may be used to evaluate and optimize future treatment strategies.

Keywords

Hepatitis B virus ; Viral kinetics ; Nonlinear mixed effect models ; HBs antigen ; HBV RNA ; capsid inhibitors ; immunomodulators.

Résumé

La difficulté à traiter l'infection au virus de l'hépatite B (VHB) réside dans la complexité de son cycle de réPLICATION. En particulier, le virus persiste dans les hépatocytes sous une forme stable appelée ADN circulaire super-enroulé (*cccDNA*). Or les traitements actuels tels que les analogues nucléos(t)iques (NUC) et l'interféron pégylé (Peg-IFN) réduisent la virémie mais ne permettent pas l'éradication du *cccDNA*. Ainsi certaines particules comme l'antigène de surface (AgHBs) ou l'ARN VHB demeurent produites, traduisant la persistance d'une activité transcriptionnelle. C'est dans ce cadre que de nouveaux traitements sont en cours d'évaluation. Parmi les molécules testées, on distingue les immunomodulateurs stimulant la réponse immunitaire, ou encore des antiviraux directs réduisant la production d'ADN et d'ARN VHB.

Comme cela a été fait dans le cadre de l'infection au VIH ou au VHC, les modèles de cinétique virale ont permis d'estimer l'efficacité des nouveaux traitements et d'apporter une compréhension mécanistique de l'infection. Basées sur des modèles non linéaires à effets mixtes (MNLEM), ces approches ont déjà permis de caractériser la décroissance biphasique de l'ADN viral chez les patients traités par NUC ou Peg-IFN.

Dans le cadre de cette thèse, nous avons développé de nouveaux modèles décrivant la dynamique d'autres marqueurs en parallèle de celle de l'ADN VHB. Dans un premier travail, nous avons évalué les effets chez la souris d'un agoniste du TLR7, un immunomodulateur stimulant la production d'anticorps anti-HBs. Dans un second travail, nous avons étudié la dynamique de l'ARN VHB chez des patients traités par inhibiteurs de capside, un nouvel antiviral agissant sur la production des particules encapsidées. Au cours de tels développements, de nombreux modèles alternatifs sont testés, puis écartés, au profit de celui produisant la meilleure description statistique des données. Or cette approche, appelée sélection de modèle, peut mener à des prédictions erronées voire à de fausses conclusions biologiques. Ainsi, dans un troisième travail nous avons évalué les performances prédictives d'une approche alternative nommée *model averaging* prenant en compte l'incertitude liée au modèle.

Ces travaux ont montré l'apport de la modélisation dans la compréhension de l'infection au VHB et des mécanismes d'action des traitements. Ils ouvrent la voie à l'élaboration de modèles complets de l'infection permettant d'évaluer et d'optimiser les stratégies thérapeutiques futures.

Mots-clés

Virus de l'hépatite B ; Cinétique virale ; Modèles non linéaires à effets mixtes ; antigène HBs ; ARN VHB ; inhibiteurs de capside ; immunomodulateurs.